HARVARD UNIVERSITY
Graduate School of Arts and Sciences

DISSERTATION ACCEPTANCE CERTIFICATE

The undersigned, appointed by the

Department of Physics

have examined a dissertation entitled

Diamond nanophotonic quantum networks
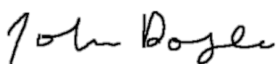
presented by   Mihir Keshav Bhaskar

candidate for the degree of Doctor of Philosophy and hereby
certify that it is worthy of acceptance.

Signature _____

Typed name: Professor Mikhail Lukin, Chair

Signature _____

Typed name: Professor John Doyle

Signature _____

Typed name: Professor Hongkun Park

Date: January 26, 2021

Diamond nanophotonic quantum networks

Thesis advisor: Professor Mikhail D. Lukin   Mihir Keshav Bhaskar

Diamond nanophotonic quantum networks

ABSTRACT

Technologies that employ the laws of quantum mechanics for information processing tasks could unlock transformational new advances in computing, metrology, and communication. These devices would rely on individual quantum bits (qubits) that can be isolated from their environment, accurately controlled, and made to interact with extreme precision. A coherent interface between optical photons and long-lived matter qubits can form the basis for a broad range of such quantum devices. We realize this interface using inversion symmetric color-centers integrated into diamond nanophotonic devices at millikelvin temperatures. This thesis documents the characterization of the resulting high-cooperativity spin-photon interface and its application in the study of quantum nonlinear optics and proof-of-principle quantum networking protocols. The diamond nanophotonic platform presented here can be fabricated en-masse and exhibits a unique combination of long coherence times, high-fidelity control, strong light-matter interactions, and efficient photon out-coupling. These properties enable the first experimental demonstration of memory-enhanced quantum communication, establishing this system as a leading platform for the construction of a large-scale quantum internet.

Contents

vi

vii

Acknowledgments

First, I thank my advisor Misha Lukin for his unwavering support throughout graduate school. His unique creativity and intuition have always been an inspiration. I am especially grateful for the faith he placed in our team when we ventured into unknown territory and began our quantum optics experiments inside dilution refrigerators. His trust in us enabled us to make rapid experimental progress despite embarking on a new technical and scientific direction, and has helped me to become an independent researcher.

I also thank Hongkun Park for his enthusiastic support of our project. I greatly appreciate both his expertise in nanoscale physics and chemistry, as well as the professional advice and support he has provided me throughout my time at Harvard. I thank John Doyle for his advice and assistance particularly regarding dilution refrigerator cryogenics. I have always enjoyed coming to John for discussions, as his expertise, wit, and good nature make every conversation enjoyable.

I have also been fortunate to be a part of several fruitful collaborations that have made my thesis work possible. The first is with the group of Marko Lončar, whose expertise in diamond nanofabrication laid the foundations for this project. I am especially thankful to Mike Burek, who pioneered the first generation of diamond nanophotonic devices for quantum optical experiments. His dedication towards realizing a variety of diamond nanophotonic structures enabled many of the early experiments in this thesis. I was also fortunate to engage in many enjoyable discussions with Srujan Meesala and Haig

Atikian, who have worked in Marko's group on related projects.

Next, I have had the opportunity to collaborate with the group of Fedor Jelezko at Ulm University. Fedor's unique expertise and wisdom were essential in our understanding of group-IV complexes in diamond, and enabled a new generation of experiments. I truly appreciate Fedor's generosity in sharing his scientific wisdom and capabilities, as this has truly enabled our project to make many advances that would not have been possible otherwise, in particular in the early days of exploring new color-centers, and understanding their spin physics. In particular, I have enjoyed fruitful discussions with his group members, particularly Lachlan Rogers, Mathias Metsch, Petr Siyushev, and Katharina Senkalla.

Additionally, I would like to acknowledge Lily Childress and Erika Janitz, who I met at various confernces and had the pleasure of collaborating with on their exciting experiments involving GeV centers in membranes, as well as a very timely review on cavity QED systems in diamond.

Finally, I would also like to acknowledge the excellent collaboration with Dirk Englund, his group, and the optical communications team at MIT Lincoln Laboratory. I have always enjoyed discussions with Dirk, who is very gifted at approaching complex problems with the big picture in mind, while still maintaining a clear grasp on the technical details. Under Dirk's guidance, it has been a pleasure working with Eric Bersin, Benjamin Dixon, and Ryan Murphy to try and perform a true long-distance networking experiment. I am extremely optimistic that their hard work will allow us to deploy this

technology to enable quantum communication in the greater Boston area.

Next, I am indebted to several Lukin group graduate students and postdocs who have mentored me throughout my time in graduate school. I am especially grateful to Alp Sipahigil, Ruffin Evans, and Denis Sukachev, who taught me the majority of what I learned during graduate school. I was fortunate enough to work closely with Alp, whose keen intuition, curiosity, and intensity were a model for how I conducted experiments for the rest of my PhD. Most importantly, I learned from Alp by example how to constantly critically evaluate the direction of the experiment to make sure we always understood what we were doing, and why we were doing it. I also cannot understate Ruffin's role as an advisor to me; his shrewd, all-rounded knowledge of the field has been invaluable. The experiments Ruffin and I carried out together during my second and third years were some of the most fun times in the lab, as well as some of the most valuable in terms of my graduate education. During most of my PhD, I have also been incredibly fortunate to work directly with Denis, who taught me most of what I know about optics and cryogenics. Denis is an incredibly shrewd and skillful experimentalist, as well as an excellent lab-mate, and I have enjoyed working with him immensely.

I was also fortunate to interact with several other members of the Lukin group. In particular, I would like to acknowledge Johannes Borregaard, who was and continues to be an extremely generous, approachable, and helpful theory collaborator, the extremely knowledgeable Kristiaan de Greve, who is always enjoyable to consult for various issues ranging from technical to theoretical, and Dominik Wild, who, in addition to being a

fantastic theorist, was an excellent office-mate and internet scavenger. I also had numerous enjoyable and fruitful interactions with various other group members, including Emma Rosenfeld, Jan Gieseler, Arthur Safira, Giovanni Scuri, Bo Dwyer, Elana Urbach, Nabeel Aslam, Alexei Bylinskii, Trond Andersen, Po Samutpraphot, Tamara Djordjevic, Conner Williams, Kyle Fridberg, Wenjie Gong, Pasha Stroganov, Grace Zhang, Hannes Bernien, Ahmed Omran, Alex Keesling, Harry Levine, Tamara Sumarac, Aditya Venkatramani, Mike Goldman, Emil Khabibouline, Sasha Zibrov, and Hannes Pichler.

I am incredibly thankful for the time spent in the lab with the other members of the silicon-vacancy team. First, I would like to thank Christian Nguyen for being an excellent lab partner for many years. Christian is an incredibly patient and kind person, and his positive attitude and incredible programming skills continually pushed our experiments forward. Next, I would like to acknowledge Bart Machielse, the extremely skilled fabrication expert on our team who made all of these experiments possible with his unyielding efforts both inside and outside of the cleanroom. Bart has always been an extremely selfless researcher, constantly going above and beyond to assist on a number of projects in parallel, and I have been extremely fortunate to work with him for many years. Finally, I have benefited immensely from working with Ralf Riedinger, whose unique perspective and selfless advising have been extremely helpful in guiding both the general progress in the lab as well as my own scientific development in recent years.

I have also been very fortunate to work with a number of extremely talented and engaging newly arriving students and postdocs, including Can Knaut, Daniel Assumpcao,

supported me unconditionally throughout my time in graduate school. Finally, I would like to thank Catherine for being an unwavering pillar throughout my PhD. She has been there to help pick me up during some of the most difficult struggles along the way, as well as to celebrate the greatest successes. This thesis is dedicated to my parents, Meera, and Catherine.

To my parents, my sister Meera, and Catherine.

Citations to previously published work

Parts of this dissertation cover research reported in the following articles:

Chapter 2, in its entirety, has been published as

"Cavity quantum electrodynamics with color centers in diamond", E. Janitz, M. K. Bhaskar, L. Childress, *Optica* 7 (10): 1232-1252 (2020).

Chapter 4, in its entirety, has been published as

"Quantum nonlinear optics with a germanium-vacancy color center in a nanoscale diamond waveguide", M. K. Bhaskar, D. D. Sukachev, A. Sipahigil, R. E. Evans, M. J. Burek, C. T. Nguyen, L. J. Rogers, P. Siyushev, M. H. Metsch, H. Park, F. Jelezko, M. Lončar, M. D. Lukin, *Physical Review Letters* 118 (22): 223603 (2017).

Chapter 5, in its entirety, has been published as

"Photon-mediated interactions between quantum emitters in a diamond nanocavity", R. E. Evans, M. K. Bhaskar, D. D. Sukachev, C. T. Nguyen, A. Sipahigil, M. J. Burek, B. Machielse, G. H. Zhang, A. S. Zibrov, E. Bielejec, H. Park, M. Lončar, M. D. Lukin, *Science* 362 (6415): 662-665 (2018).

Chapter 6, in its entirety, has been published as

"Quantum network nodes based on diamond qubits with an efficient nanophotonic interface", C. T. Nguyen, D. D. Sukachev, M. K. Bhaskar, B. Machielse, D. S. Levonian, E. N. Knall, P. Stroganov, R. Riedinger, H. Park, M. Lončar, M. D. Lukin, *Physical Review Letters* 123 (18): 183602 (2019).

Chapter 7, in its entirety, has been published as

"An integrated nanophotonic quantum register based on silicon-vacancy spins in diamond", C. T. Nguyen, D. D. Sukachev, M. K. Bhaskar, B. Machielse, D. S. Levonian, E. N. Knall, P. Stroganov, C. Chia, M. J. Burek, R. Riedinger, H. Park, M. Lončar, M. D. Lukin, *Physical Review B* 100 (16): 165428 (2019).

Chapter 8, in its entirety, has been published as

1

Introduction

At present, we are in the midst of an explosion of growth in the development of new technologies that utilize quantum mechanics for a wide range of applications. The idea to use the quantum mechanical behavior of collective systems in such a way has already given rise to transformative tools that have shaped the modern era, including magnetic resonance imaging (MRI) [1], global positioning systems (GPS) [2], and lasers [3]. The current wave of interest in quantum science in technology is driven by relatively recent advances in the isolation and precise control of individual quantum systems across a growing variety of physical platforms, including neutral atoms [4–6], ions [7–9], photons [10, 11], superconducting circuits [12, 13], and electronic and nuclear spins in solids [14–20]. The growing degree of control over quantum matter in such a diverse set of systems has resulted in the creation of a number of subfields of *quantum information*

science [21–23], most notably quantum computing [24, 25], quantum metrology [26, 27], and quantum communication [28–30]. Each of these subfields seeks to utilize high-fidelity control of quantum systems to implement quantum logic operations that rely on unique features such as superposition or entanglement to accomplish tasks that might otherwise be impossible, such as the hardware efficient factorization of large numbers [31], unprecedented gains in the precision of timekeeping systems [32], and the unconditionally secure distribution of cryptographic keys [33, 34].

Despite the rapidly advancing degree of control over quantum systems, as well as recent experimental demonstrations of advantages of quantum devices over their classical counterparts [35, 36], quantum information science has yet to result in a practical technological breakthrough. Numerous challenges and open questions remain about what applications such devices will be useful for, and whether the size and scale of well-controlled quantum systems can be expanded to the level of technological relevance without operational errors eclipsing any practical advantage. While the exact applications of future quantum machines remains uncertain, it is clear that noisy experiments in state-of-the-art quantum science laboratories do not yet meet the criteria for useful technological exploit [25]. Fortunately, quantum error correction (QEC) protocols promise to enable the scaling of faithful quantum information processes to arbitrary sizes, once the requisite hardware achieves a certain fidelity threshold [37]. Whether the task is metrology [38], communication [39], or computation [40, 41], large-scale deployment will likely require implementation of some form of QEC.

While QEC provides a clear motivation to continue to improve the underlying quantum hardware modules, it does not provide any guideline on how to indefinitely scale the scope and size of a machine given realistic, physical constraints such as the cooling capacity of a single cryogenic refrigerator or the field of view of an optical microscope. Given the nature of quantum systems, which require simultaneous isolation from the environment as well as precise, high-fidelity control, scaling up quantum hardware also presents a major challenge. Building quantum systems that operate on truly large scales, either in terms of number of quantum bits (qubits) or physical distances will therefore also likely require implementation of new, creative architectures for engineering robust and scalable connections between various quantum modules.

1.1 Quantum networks

One such architecture for building a large-scale quantum system that can extend over long distances is a *quantum network* [42]. A quantum network consists of a collection of individual *quantum nodes*, or small processors where quantum information can be locally initialized, stored, manipulated, read out using a collection of stationary qubits. In a quantum network, nodes can be connected over potentially long distances using *quantum channels*, which can support flying qubits. By far the most common choice of flying qubit is the optical photon,[1] which can be transmitted either through free space

---

[1]Other proposals exist (see e.g. [43]), but no experimental progress has yet been made in this direction.

or routed through optical fibers for long-distance communication [44]. The quantum memories at each node can be used as end nodes that encoding or decode quantum information transmitted throughout the network, or as intermediate repeater stations to relay information between distant nodes [45]. *Quantum repeaters* [46–48], which transduce the quantum information between transient flying qubits on the quantum channels and stationary memory qubits at the quantum nodes, are needed in order to connect two end nodes at large distances beyond which single photons cannot transmit due to inescapable channel losses (Chapter 8) [49, 50]. The key task in constructing a quantum network node is therefore to engineer an interface between stationary and flying qubits, often referred to as a *spin-photon* interface. Such an interface, which can coherently and reversibly transduce quantum information between matter and light, is a foundational element of a wide array of quantum information technologies [22, 51].

The ability to send quantum bits across long distance can be used to distribute entanglement among remote parties [52]. When distant communicating parties share entangled particles, they can perform quantum communication secured by Bell's theorem, which can certify that no third-party eavesdropper has successfully obtained information about their message [33, 53, 54]. If the entanglement can be prepared with high-fidelity in quantum memories, this communication process can even be made device independent: the end users of the communication channel can directly verify the security of the channel themselves, without making assumptions about the details of the device [34, 55]. If widely deployed, such a concept could have a transformative impact on privacy in

4

information sharing, a concept with rapidly growing implications given our increasing reliance on cloud-based systems for general-purpose communications, computing, and storage.

The establishment of secure, long-distance quantum key distribution (QKD) channels is currently the primary motivation for studying and building quantum networks. This is in large part due to the fact that QKD systems cannot be realized with classical technology, yet can be carried out using a relatively low resource requirement. In fact, several field tests of QKD - albeit with device-specific assumptions required to guarantee security - have already been demonstrated in real-world conditions [29, 30, 56, 57]. More complex quantum networks may also enable related security technologies involving more than two parties, including secret sharing [58, 59], which could be useful in reporting of sensitive information such as health care data, and certified, anonymous quantum voting [60], which could address concerns about voter fraud in modern-day electoral processes. A handful of other promising long-term applications beyond the realm of security may also be enabled by the development of robust spin-photon interfaces. For example, distributed entanglement can be used for more efficient sensing of faint astronomical sources using quantum enhanced long-baseline interferometry [61, 62]. Additionally, a network of entangled distant atomic clocks could be used to improve the precision of worldwide timekeeping standards and GPS [63].

Progress in quantum networking is also a necessary counterpart to the flourishing field of quantum computing. Just as our interactions with modern day computers are

inextricably tied to their ability to communicate and network both locally and globally, it is likely that quantum networks will play an important role in the development and deployment of truly scalable quantum computing technology.

Access to quantum computers over a fully-fledged quantum network could enable blind quantum computing [64, 65], a protocol for privately encoding, running, and interpreting the results of an algorithm on a distant quantum computer in such a way that the owner of the quantum computer cannot access the inputs, outputs, or even the algorithm itself. Foreseeable prototypes of quantum computers are likely to be located in select research laboratories at elite universities or private companies; blind quantum computing could help reduce inequality associated with access to quantum computers and democratize their use, helping to spur the responsible growth, development, and testing of new quantum algorithms by a more diverse group of quantum computer scientists.

Most importantly, quantum networks may also play an essential role in the functionality of quantum computers themselves. At its core, a quantum network describes an architecture to link small quantum processors into a larger quantum machine over which entanglement can be distributed. By combining entanglement distribution between separate quantum modules with local control and measurement within the modules, distributed quantum logic can be achieved [66, 67]. Quantum networks therefore present a promising, modular architecture to enable scaling quantum processors to arbitrary sizes [68] in a way that can overcome technical limitations such as cryogenic capacity. For

this reason, some of the leading quantum computing platforms have already begun developing quantum network interfaces, recently demonstrating teleported quantum gates and transfer of entanglement over small quantum networks [69–71].

Achieving a high-fidelity, efficient spin-photon interface adds significant overhead to the already formidable task of building a small, fault-tolerant quantum computing module. However, this addition may prove to be key in enabling practical, cost-effective scaling of quantum machines to arbitrary sizes, as predicted in the early days of quantum computing [51]. The incredible wave of interest in quantum computing therefore justifies a corresponding surge of effort in constructing spin-photon interfaces. However, while the usefulness of future quantum computers remains uncertain, one can argue that secure quantum communication is currently the most mature and technologically justifiable subfield of all of quantum information science, since real-world demonstrations of point-to-point networks have already successfully deployed, and commercial quantum communication systems already exist on the market today [57, 72, 73]. Consequently, as long as there continues to be significant interest in the construction of commercially viable quantum technologies of any sort, quantum scientists and engineers must continue to develop and improve quantum network interfaces.

1.2 OVERVIEW

This thesis presents experiments utilizing color-centers in diamond structures as a spin-photon interface for quantum network applications [50, 74–78]. The idea to use color-centers in such a way dates back over a decade, to the early days of coherent quantum control of nitrogen-vacancy (NV) centers [79–81]. While early experiments made rapid progress in developing the NV center as a spin-photon interface, the sub-optimal optical properties of the NV (chapter 2.3.2) illustrated the importance of integration into efficient photonic structures to enhance the relevant zero-phonon-line (ZPL) optical transition (chapter 2.2). However, despite remarkable advances in the nanofabrication of free-standing diamond photonic structures, incorporation of optically coherent NV centers into such devices proved to be a formidable challenge [82].[2] Instead, the negatively charged group IV color-centers[3] were shown to have superior optical coherence properties [85], even when incorporated into heavily fabricated structures [86], enabling the first coherent cQED experiments with color-centers in diamond nanophotonic devices [87].

This thesis documents the subsequent progress towards technologically relevant quantum network nodes based on color-centers in diamond integrated into nanofabricated photonic structures. Chapter 2 provides the necessary context and overview for under-

---

[2]For an overview of such efforts prior to the work in this thesis, see chapter 2 of [83]

[3]This thesis will not provide a first principles description of the physics of negatively charged group IV color-centers. An excellent treatment is provided in chapter 2 of [84].

standing experimental cQED with color-centers in diamond. Chapter 2.2 introduces the physics of cQED, with specific attention to phenomena and parameter regimes unique to experiments involving solid-state emitters. Chapter 2.3 gives an overview of the properties of various color-centers in diamond in the context of incorporation into cQED systems. Chapter 2.4 presents an overview of various techniques used to fabricate nanophotonic structures in diamond.

Chapter 3 provides technical detail for the experiments described in the following chapters. Here, we highlight the important details and discoveries that enabled the rest of the experiments described in the thesis. These are essential techniques and concepts that are often overlooked or not present in published material. The discussion in chapter 3 is intended to serve as a technical reference for researchers who work on related systems. I draw specific attention to Chapter 3.3.3, which compares the SiV center to other related platforms and discusses the unique advantages of the SiV-nanophotonic platform for near-term experiments and technologies (an additional perspective on these prospects are also provided in the conclusion, chapter 9).

The subsequent chapters document quantum optical experiments with color-centers in diamond nanostructures. Chapter 4 describes a series of experiments with germanium vacancy color-centers in diamond waveguides, which illustrate the presence of a family of defects for which coherent spin-photon interfaces should be possible, serving as the foundation for a recent wave of research interest [88, 89]. Chapter 5 documents the observation of photon-mediated interactions between multiple quantum emitters coupled

9

strongly to a single cavity, marking the first step towards experiments involving multiple nanocavity-integrated color-centers.

Chapter 6 describes the operation of a fully functional quantum network node consisting of an SiV center and nearby ^{13}C nuclear spin coupled to a nanophotonic cavity with high cooperativity at millikelvin temperatures. It describes the protocol used for establishing spin-photon entanglement, the fundamental ingredient in quantum networking, as well as operations between SiV centers and nearby nuclear spins. Following this, chapter 7 is the most detailed chapter of this thesis, describing the working principles of the quantum network node. The implications of all external parameters, including temperature, magnetic field, crystal strain, cQED coupling and loss rates, and nuclear spin environment are discussed in detail. Additional information about experimental techniques for achieving coherent electron and nuclear spin control as well as spin-photon gates at millikelvin temperatures are also provided. In combination with the additional technical information highlighted in chapter 3, this chapter serves to provide a detailed guide to using the SiV-cavity system as a spin-photon interface for quantum networks.

These advances culminate in the experimental demonstration of memory-enhanced quantum communication, described in chapter 8. This experiment is an important step towards integration of quantum memory devices into realistic long-distance quantum networks, since it marks the first demonstration of a quantum advantage of using memories for quantum communication. Together with the supporting material in the other sections of this thesis documenting the full range of functionality of the diamond

10

nanophotonic platform, this chapter signals the maturity of such devices for use in near-future technologies.

2

Cavity quantum electrodynamics with color-centers in diamond

2.1 INTRODUCTION

Optical photons play a critical role in quantum networks because they interact very weakly with surrounding media, making them the ideal carrier of quantum information over long distances. However, these weak interactions pose a significant impediment for engineering gates between photons, and make it difficult to interface photons with information storage and processing nodes. Cavity quantum electrodynamics (cQED) offers a paradigm to overcome these challenges: by confining photons inside a high quality factor optical resonator, vastly enhanced interactions with material systems

can be obtained [16, 90–94], enabling a broad range of relevant quantum information tasks [52, 95, 96]. For example, cavity-coupled emitters can be used as bright sources of the indistinguishable photons [97, 98] needed for photonic quantum computation [99, 100], or even employed to mediate interactions between photons [101]. The most exciting opportunities emerge when the material system possesses long-lived internal degrees of freedom, such as electron or nuclear spin sublevels, in addition to its optical transitions [an example is shown in Fig. 2.1(b)]. Such long-lived states can be used to realize a quantum memory for light [102–105], spin-photon entanglement [106–111], spin-photon switches [17, 112], or quantum gates between asynchronous photons [113–115]. While some of these capabilities can be realized without cavities (e.g. using optically dense ensembles [116, 117]), cQED can enhance the efficiency of probabilistic protocols, and even enable near-deterministic interactions between single photons and individual quantum bits.

The likely impact of cQED systems on quantum networks is exemplified by their potential role in quantum repeaters, which compensate for photon loss to enable transmission of quantum states or secret keys over long distances [46, 118, 119]. The simplest repeater schemes distribute entanglement over long distances via a chain of spins linked by photonic channels [46], generating a resource that can be purified [120–122] and used to teleport quantum information [123, 124] or generate a secret key [33]. Such schemes often employ heralded entanglement generation [125–132], which exploits entanglement between spins and indistinguishable outgoing photons, such that a detected

13

photon could have originated from either of two distant spins. Conditioned on a detection event, the spins are projected onto an entangled state, and photon loss errors result only in reduced success probability. Cavity coupling can vastly increase the efficiency of these protocols by increasing photon emission rates into a well-defined cavity-coupled mode [90, 133]; for strongly-coupled cQED systems, even deterministic remote entanglement generation can be possible [52, 134]. In the longer term, one-way repeater schemes promise much faster communication by transmitting entangled multi-photon states that encode quantum information in a photon-loss-tolerant structure [135, 136], potentially incorporating error correction [137], and without the need for long-term quantum memory [47, 138, 139]. In this context, cavity-coupled emitters play an essential role: by maintaining a coherent quantum memory during repeated interactions with light, an emitter can generate entanglement between sequentially emitted photons [140–143] and be used for efficient re-encoding at one-way repeater stations [48]. While these are just a subset of quantum repeater and networking functionalities being actively pursued, they illustrate the key role played by cavity-coupled spin-photon interfaces in near-term quantum information applications [144].

A wide variety of physical platforms for realizing cQED are currently being explored, aimed at achieving interaction rates between the quantum emitter and cavity mode that exceed relevant losses. Cavity-enhanced interfaces between optical photons and individual quantum emitters began with neutral atoms [94] and quickly expanded to other systems including quantum dots [145], molecules [146], and trapped ions [147, 148].

In particular, there has been a recent interest in cavity coupling to atomic-like solid-state systems [18, 149], most notably defects in diamond [150–152], but also rare-earth ions [153, 154], defects in silicon carbide [155], and potentially others [156]. These defect-based systems aim to combine the atomic-like advantages of a predictable structure, optical selection rules and long spin coherence times with a robust solid-state platform compatible with integration into micro- or nano-scale cavities. The various host materials and defect structures carry different strengths, as discussed in recent reviews [18, 149]. Here, we focus on the most well-studied platform for defect-based, optically-active spin qubits: diamond.

Indeed, diamond's large bandgap and nearly nuclear-spin-free lattice make it an appealing host for such defects [157]. Of these, the best known is the nitrogen-vacancy (NV) center, which exhibits long spin coherence times, access to nearby nuclear spins for ancilla qubits [19], and well-understood spin-selective optical transitions [158, 159]. Thanks to these properties, cavity-coupled NVs form the basis for many quantum information proposals [79, 160–162]. Moreover, even without cavity coupling, NVs have already been used to achieve landmark proof-of-principle quantum network experiments demonstrating loophole-free Bell inequality violation [53], unconditional teleportation [163], entanglement distillation [122], and entanglement distribution faster than entanglement loss [164], all of which would exhibit vastly improved efficiency using cavity coupling. At the same time, novel defects such as the silicon vacancy (SiV) have been found to exhibit superior optical properties [152] and the potential for long spin

15

coherence times [165–167]. These advances have helped to motivate development of cQED systems in diamond.

2.2 Cavity QED with solid-state emitters

Cavity QED enhances the coherent coupling rate between a quantum emitter and cavity-confined photons, thereby improving the efficiency with which indistinguishable photons (within the same spatial, spectral, and temporal mode) can interact with individual color center quantum memories. This can approach a deterministic process when the emitter-photon interaction rate exceeds cavity losses and dephasing of the emitter optical transition. In this section, we examine the figures of merit for cQED with imperfect emitters, and consider different regimes for quantum applications.

In the absence of a cavity, emitter-photon interactions scale with the spontaneous emission rate γ_0 along the desired optical transition. In the case of color centers (see chapter 2.3.2), this is typically a transition within the zero phonon line (ZPL), and the rate γ_0 is often weak compared to the overall rate of dephasing of the optical transition (γ). The total dephasing rate γ comprises both γ_0 and all other decay pathways (γ_1), including nonradiative decay or emission into the phonon sideband (PSB), as well as pure dephasing (γ_d), with $\gamma = \gamma_0 + \gamma_1 + \gamma_d$ [Fig. 2.1(b)].

When an emitter is placed inside of an optical cavity, the local photonic density of states can be strongly enhanced at the cavity resonance frequency, enabling rapid

16
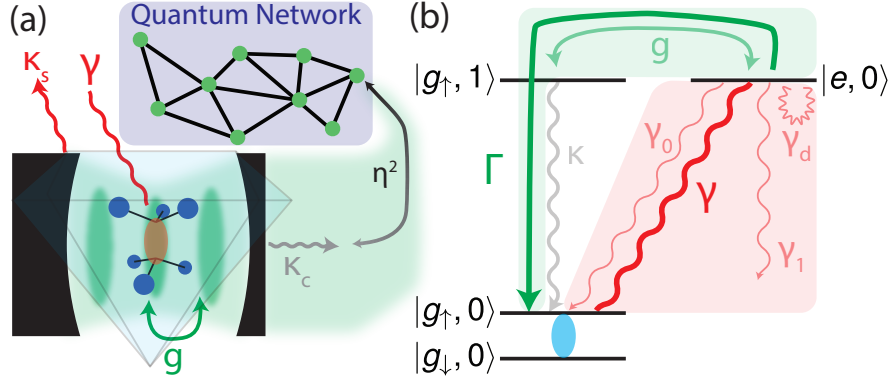
Figure 2.1: (a) Schematic of diamond cQED system. Cavity photons are coherently coupled to the color center at rate g and can scatter out of the cavity at rate κ_s, or into a collected mode at rate κ_c. Optical decoherence of the color center occurs at rate γ. Indistinguishable photons in the collected mode are matched into a single-mode fiber with efficiency η^2. (b) Detailed diagram for one instance of relevant cQED energy levels, comparing coherent coupling rates (green) to decoherence rates (gray, red). Quantum information (blue oval) is stored in the color center spin states $|g_\downarrow, 0\rangle, |g_\uparrow, 0\rangle$, where $g(e)$ indicates the ground (excited) state, $\uparrow, \downarrow$ indicate spin, and the final integer indicates cavity photon number. $|e, 0\rangle$ couples spin-selectively to $|g_\uparrow, 1\rangle$ at rate g, leading to an effective cavity-enhanced emission rate Γ. The cavity dissipates at overall decay rate $\kappa = \kappa_s + \kappa_c$ and the emitter dephases at overall rate γ, which comprises desired emission (γ_0), undesired decay (γ_1), and pure dephasing (γ_d).

emitter-photon interactions when the cavity is tuned to the emitter optical transition.

This enhancement can be characterized using the *Purcell factor*

$$\mathcal{P} = \frac{\Gamma}{\gamma_0}, \tag{2.1}$$

which compares Γ, the new rate of emission via the cavity, to γ_0, the original free-space emission rate along the relevant transition. Note that definitions of the Purcell factor vary, especially for non-ideal emitters, and we have chosen this definition to clearly differentiate the regimes of cQED with broadened emitters. When the emitter

17

is on resonance with the cavity, and the cavity decay κ is the dominating rate, $\Gamma \approx 4g^2/\kappa$. Here $g = \vec{\mu} \cdot \vec{\mathcal{E}}_0/\hbar$ is the rate of interaction between the dipole moment $\vec{\mu}$ of the optical transition of interest and the cavity mode vacuum field $\vec{\mathcal{E}}_0$ at the emitter location. Notably, since $\gamma_0 \propto \mu^2$, μ drops out of $\mathcal{P}$, and for an optimally oriented and located emitter the Purcell factor is determined entirely by the properties of the cavity [133, 168],

$$\mathcal{P} = \frac{3}{4\pi^2}\left(\frac{\lambda}{n}\right)^3\left(\frac{Q}{V}\right), \tag{2.2}$$

where $Q = \omega/\kappa$ is the quality factor of the cavity, ω is its resonance frequency, λ is the corresponding wavelength in free space, n is the index of refraction within the cavity (assumed constant), and the cavity mode volume V emerges from $\mathcal{E}_0 = \sqrt{\hbar\omega/2\epsilon_0 V}$. The scaling of $\mathcal{P} \propto Q/V$ naturally motivates the use of high quality-factor cavities with minimal mode volume.

$\mathcal{P}$ quantifies the enhancement of radiative emission on resonance with the cavity. However, for most solid-state emitters, the resonant optical emission γ_0 only accounts for a fraction of their total decay processes $\gamma_0 + \gamma_1$, implying that $\mathcal{P}$ does not describe the increase in the overall excited state decay rate. Furthermore, $\mathcal{P}$ does not specify the absolute probability of coherent atom-photon interaction per attempt; this depends on the cooperativity C, where

$$C = \frac{4g^2}{\kappa\gamma} = \mathcal{P}\left(\frac{\gamma_0}{\gamma}\right) \equiv \frac{\Gamma}{\gamma}. \tag{2.3}$$

Here, the final equivalence (valid in the large-κ limit), gives a physical picture of C: the cooperativity compares the rate of radiation via the cavity to all emitter dephasing mechanisms. More generally, when $C > 1$, the coherent coupling between the emitter and cavity photons is stronger than the decoherence mechanisms, leading to near-deterministic atom-photon interactions [94, 144].

Unlike the Purcell factor $\mathcal{P}$, the cooperativity C captures the effects of the sub-optimal optical characteristics of solid-state emitters. In the case of an ideal, radiatively broadened two-level system, $\gamma_0/\gamma = 1$, and $C = \mathcal{P}$ exactly. However, in the case of solid-state emitters, where typically $\gamma_0/\gamma \ll 1$, a cQED system can have a Purcell factor $\mathcal{P} > 1$ but still be in the regime $C < 1$. There are scenarios where this intermediate regime can offer useful enhancements. For highly broadened emitters ($\gamma \gg \kappa$), such as diamond defects at room temperature, the cavity can funnel otherwise broadband emission into the relatively narrow resonator mode, creating a frequency-tunable source of narrow-band single photons [169–173]. More typically, low temperature solid-state cQED systems operate in the $\kappa \gg \gamma$ limit, with emitters still dominated by pure dephasing $\gamma_d \gg \gamma_0, \gamma_1$. In this case, the brightness of the optical transition of interest is enhanced by $\mathcal{P}$, and when Γ becomes larger than $\gamma_1 + \gamma_0$, the lifetime of the emitter begins to decrease significantly, increasing the overall rate of photon emission. However, as long as $C < 1$, the emitter linewidth is still determined primarily by γ_d, requiring detection during a short time window $\delta t \sim 1/\gamma_d$ to render the photons indistinguishable [174, 175]. Nevertheless, as the cavity coupling rate Γ increases, so does the probability of photon emission within

19

δt. Hence Purcell-enhanced emission, in combination with spin-selective optical transitions [88, 176–181], coherent qubit manipulation [165, 176], and efficient outcoupling [182–184], could already greatly enhance the rate of remote entanglement generation [53, 122, 126, 130, 162, 164].

In contrast, the high cooperativity regime $C > 1$ corresponds to conditions of near-deterministic interactions, where the emitter has a high probability to interact with a cavity photon before it dephases. High cooperativity is a prerequisite for protocols involving deterministic, cavity-mediated quantum information processing with spins and photons [52, 113, 144]. For example, in the high-cooperativity regime, single, indistinguishable cavity photons can be generated on demand [97]. Since this interaction is coherent and reversible, single photons injected into the cavity can also be completely absorbed by the emitter, enabling transduction of quantum states from light to matter [52, 94, 185]. Alternatively, the spin state of a single quantum emitter can fully modulate the amplitude or phase of a photon reflected from the cavity, enabling deterministic interactions with (or among) transient photons [113, 186, 187]. Finally, strongly-coupled cavity photons can be used to mediate spin-spin interactions in a cavity or between distant, resonant cavities, enabling implementation of near-deterministic distributed quantum logic operations [52, 68, 95, 188, 189]. Notably, the efficiency and fidelity of such near-deterministic protocols can generally be improved by increasing C, motivating the development of cQED systems that can reach $C \gg 1$ [144].

A final consideration in cavity engineering of solid-state emitter properties is the

efficient in- and out-coupling of light. In particular, the cavity-confined mode must be engineered to critically- or over-couple into a propagating mode that can be guided into a single-mode fiber with high efficiency [Fig. 2.1(a)]. This is equivalent to the condition $\kappa_c \geq \kappa_s$, where $\kappa_c + \kappa_s = \kappa$ and κ_c and κ_s are the cavity leakage rates into the collected and scattered modes respectively. Beyond ensuring efficient photon collection, $\kappa_c \geq \kappa_s$ is a prerequisite for certain deterministic quantum logic operations between spins and photons [113, 144]. Once coupled out of the cavity via κ_c, the photons should be mode-matched with high overlap η into a single-mode fiber, either for detection or for distribution to distant quantum network nodes.

In summary, in order to achieve high cooperativity, the coherent interaction between the emitter and cavity photons must be made stronger than all decoherence mechanisms by maximizing the ratio Q/V while minimizing undesirable dephasing γ. Accomplishing this is a central challenge of experimental cQED, and requires careful consideration of both cavity and emitter properties.

2.3 Choosing an Emitter

There exist a multitude of crystallographic defects with optical transitions within the bandgap of diamond [157], some of which have optically accessible spin degrees of freedom. An important class of defects comprises an impurity atom and single vacancy [199], of which the most studied are the negatively charged nitrogen-vacancy (NV) [Fig.

Defect	Symmetry	ZPL wavelength	DW Factor (ξ)	lifetime (τ)	$\hbar\Delta_{GS}/k_b$ [†]
NV	C_{3v}	637 nm	0.03 [190]	11-13 ns [176, 191]	N/A
SiV	D_{3d}	737 nm	0.7 [192]	1.6-1.7 ns [86, 193, 194]	2.4 K [179]
GeV	D_{3d}	602 nm	0.6 [195]	6 ns [75]	7.3 K [75]
SnV	D_{3d}	619 nm	0.6 (5K) [196]	4.5-4.8 ns [88, 181]	41 K [197]
PbV	D_{3d}^{*}	520-552 nm [89, 198]	unknown	>3 ns [89, 198]	$200 - 270$ K [89, 198]
SiV0	D_{3d}	946 nm	0.9 [166]	1.8 ns [166]	N/A

Table 2.1: Summary of emitter properties (see text for details). ∗ PbV symmetry is unconfirmed experimentally, † temperature corresponding to exponential suppression of phonon-induced spin dephasing.

2.2(a)] and negatively charged silicon-vacancy (SiV) centers [Fig. 2.2(d)]. In addition, several emerging color centers have recently gained traction in the field, such as the neutral charge state of the silicon vacancy (SiV0), as well as negatively charged group-IV defects based on heavier impurities such as the germanium-vacancy (GeV), tin-vacancy (SnV), and lead-vacancy (PbV) centers. An ideal emitter for quantum information applications would combine deterministic fabrication with coherent, bright optical transitions that couple to long-lived spin states. This section provides a survey of such properties as well as other experimental considerations that are relevant in choosing a color center.

2.3.1 FABRICATION

Efficient cavity coupling requires accurate emitter placement within the cavity mode as well as high optical coherence. Simultaneously achieving these requirements poses a significant challenge, and has spurred development of advanced techniques for emitter creation [200].

The best placement accuracy is obtained using ion implantation and annealing [201–203]. Standard blanket implantation forms a two-dimensional layer of impurities at a depth determined by the acceleration energy [204], while three-dimensional precision can be achieved using a focused ion beam (FIB) [205–208], or via blanket implantation through a lithographically aligned mask [209–212]. Combining shallow masked implantation and diamond overgrowth [213] could further aid 3D localization by limiting implantation straggle. Subsequent high-temperature, high-vacuum annealing repairs lattice damage and mobilizes vacancies to form the desired color center with sub-unity conversion efficiency [202, 214, 215]. Particularly for larger implanted species, annealing at higher temperatures ($> 1200°$ C) or pressures may be important to mitigate unwanted defects formed due to implantation damage [197, 216].

In contrast to implantation, fabrication techniques based on as-grown impurities offer less control over position but generate defects with better optical properties. This was clearly illustrated by a recent study comparing as-grown and implanted NV centers in the same sample, where the former displayed superior optical coherence [Fig. 2.2(b) [217]]. As-grown NV centers can be formed using the non-negligible native nitrogen impurity levels present in electronic grade diamond. Other impurities can be introduced in high pressure, high temperature (HPHT) [195, 218, 219] or chemical vapor deposition (CVD) diamond synthesis [194, 220], and delta-doping techniques have been used to further localize emitters into a single layer [221, 222]. In addition, precise boron doping has been critical in engineering the Fermi level of diamond to stabilize the SiV0 charge

23

state [166]. Following impurity incorporation, techniques such as electron irradiation [223–225] or laser writing [226] can be used to generate vacancies, which, upon annealing, can recombine with implanted or as-grown impurities to form emitters.

2.3.2 OPTICAL PROPERTIES

Cavity-coupled quantum information technologies require a high rate of emission on a coherent optical transition. For diamond defects, such transitions lie within the ZPL. Moreover, to eliminate thermal broadening of the ZPL itself, experiments must be conducted at cryogenic temperatures (typically at ~ 10 K or below [193, 227]).

The ZPL radiative emission rate (γ_0) is determined by a combination of the excited state state lifetime (τ), Debye-Waller factor (ξ), and quantum efficiency (QE) according to

$$\gamma_0 = \frac{\xi}{\tau} QE, \tag{2.4}$$

neglecting for simplicity any fine structure within the ZPL (see Table 2.1 for a comparison of emitter properties). While emitter lifetimes vary by less than an order of magnitude, the Debye-Waller factor, or the fraction of radiative emission that occurs within the ZPL, is much lower for the NV than for group-IV emitters [228, 229]. This is due to a change in the NV electronic wavefunctions (or charge distributions) between the ground and excited states, such that photon emission is accompanied by a significant shift in nuclear spin coordinates.
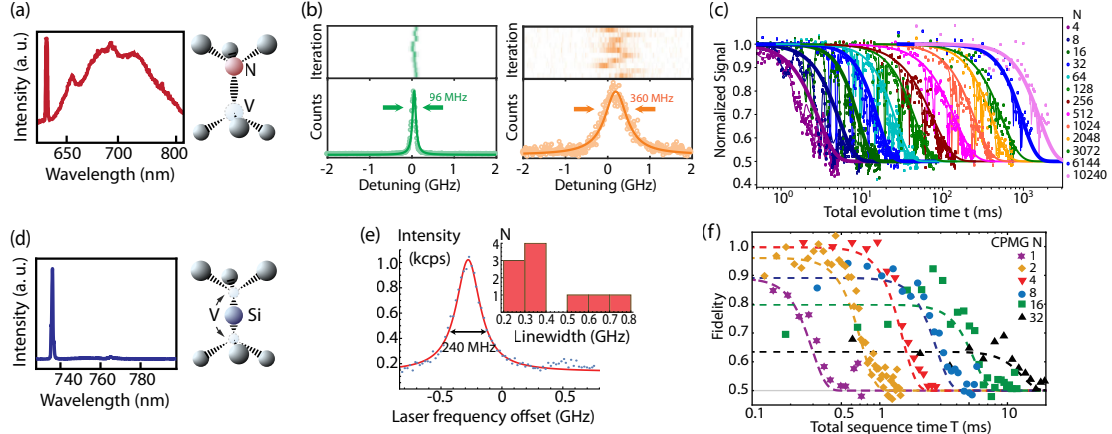
Figure 2.2: (a) NV center structure and low temperature emission spectrum (spectrum adapted with permission from [230], copyright Wiley-VCH Verlag GmbH & Co. KGaA). (b) Representative NV photoluminescence excitation (PLE) data at 4 K for each nitrogen isotope (green: ^{14}NV; orange: ^{15}NV). The sample is implanted with ^{15}N, and the ^{14}N are as-grown impurities. Individual scans of the ZPL reveal the linewidth free from spectral diffusion. The summation of many repeated scans shows spectral diffusion (adapted with permission from [217], copyrighted by the American Physical Society). (c) Decoherence of an NV electronic spin at 3.7 K with tailored decoupling sequences employing pulse numbers from N = 4 to N = 10,240 (adapted with permission from [231] in accordance with creativecommons.org/licenses/by/4.0/legalcode). (d) SiV center structure and low temperature emission spectrum. (e) Linewidth of a representative implanted SiV at 4 K inside a nano-waveguide measured by PLE spectroscopy (blue points: data; red line: Lorentzian fit). Inset: histogram of emitter linewidths in nanostructures. Most emitters have linewidths within a factor of four of the lifetime limit (94 MHz) (adapted with permission from [86], copyrighted by the American Physical Society). (f) Spin coherence of an SiV electronic spin at 100 mK using CPMG sequences with N = 1, 2, 4, 8, 16, and 32 pulses. The longest measured T_2 time is 13 ms for N = 32 (adapted with permission from [165], copyrighted by the American Physical Society).

Quantum efficiency refers to the radiative fraction of total excited state decay, which can also include direct phonon relaxation [193, 232]. In general, QE is challenging to extract directly from emitter brightness due to confounding factors that can reduce fluorescence detection rates, including the presence of metastable dark states and imperfect calibration of collection and detection efficiency. Instead, QE can be most precisely

estimated by measuring the response of the emitter's excited state lifetime to a controlled change in the local photonic density of states [233]. This technique has been used to show that the NV QE is close to unity in bulk diamond [234]. Unfortunately, this method is not as precise for emitters with QE substantially less than 1, since their lifetimes do not depend as sensitively on their local photonic environment. This is the case for the SiV center [86], which is believed to have $QE \approx 0.1$ at 4 K (see supplementary of [87]). Indeed, the SiV's relatively short and temperature-dependent lifetime of $\sim 1.6(1.0)$ ns at 4(300) K [193] is consistent with strong nonradiative processes. On the other hand, the GeV center has a slightly longer, temperature-independent lifetime of 6 ns that is very sensitive to its local photonic environment [75], and single GeVs can induce coherent extinction of waveguide transmission [75, 235]. These measurements suggest a relatively high $QE \gtrsim 0.4$. However, this estimate is in conflict with a $QE < 0.1$ extrapolated using detected count rates from GeV centers in bulk diamond [236]. There is even more uncertainty regarding the QE of other emerging color centers including the SnV, PbV, and SiV0; however, it is worth noting that photon count rates in experiments involving SnV and SiV0 are consistent with a high QE comparable to that of the NV center [166, 197].

Another consideration in choosing an emitter is the ZPL emission frequency. Working at longer wavelengths simplifies nanofabrication by allowing larger feature sizes with lower sensitivity to surface roughness. Furthermore, the GeV, SnV, and PbV ZPL wavelengths occur in the 520-620 nm range, where it is challenging to obtain stable,

26

high-power lasers.

In addition, resonant cavity coupling relies on spectral stability of the emitter, which is strikingly different for the NV center compared to group-IV defects owing to their different symmetries. While all of these color centers occur along the $\langle 111 \rangle$ family of crystal axes, the nitrogen of the NV center sits in place of a missing carbon atom, resulting in a defect with C_{3v} symmetry. Its lack of inversion symmetry permits inequivalent electric dipole moments in the ground and excited states; consequently, the NV center ZPL frequency is strongly impacted by electric field noise on nearby surfaces, causing spectral diffusion, or variation in frequency over time, particularly when illuminated by the green light used to reinitialize the negative NV charge state [191, 237]. This effect is especially severe for implanted NV centers in nanostructures, which typically exhibit spectral diffusion of many GHz, far beyond the ~ 15 MHz lifetime limit [82]. Encouragingly, NV centers formed from native nitrogen impurities and electron irradiation have achieved spectral diffusion linewidths of < 250 MHz in a few-microns-thick diamond membrane [238]. Moreover, by applying pulses of green light until the NV transition matches a desired frequency [239], the effects of pump-induced spectral diffusion can be mitigated, and the majority of single-scan linewidths are below 100 MHz in such membrane samples [238]. Conversely, the electric field sensitivity of the NV can be viewed as a resource for tuning the ZPL frequency via the DC Stark effect, which has been used to actively compensate for both spectral diffusion (effectively reducing γ_d) and spectral mismatch of different defects [240–242].

27

In contrast to the NV center, group-IV defects take a split-vacancy configuration described by the point group D_{3d}, which includes inversion symmetry, leading to a vanishing permanent electric dipole moment. Such defects are insensitive to surface noise to first order; indeed, both as-grown [194] and implanted [86] SiV centers can display nearly lifetime-limited linewidths, even in nanostructures [86, 208] [Fig. 2.2(e)]. Other group-IV color centers such as the GeV [75, 180], SnV [88], and SiV0 [166] exhibit similar spectral stability, although this has not yet been observed in nanofabricated cavities. The insensitivity of group-IV emitters to electric fields precludes Stark shift tuning of the ZPL frequency; instead, two photon Raman transitions [87, 243] and dynamic control of the strain environment [244, 245] are promising approaches for wavelength tuning and spectral stabilization.

Finally, it is desirable to minimize inhomogeneous broadening, or the variation in ZPL emission frequency from emitter to emitter. The inhomogeneous distribution scales with implantation damage, increasing with the size and energy of the ion, but can be mitigated to varying degrees via post-implantation treatment. NV and SiV centers can exhibit inhomogeneous linewidths down to 0.17 nm [203] and 0.03 nm [86] respectively when annealed at high temperatures. Much larger linewidths of 30 nm have been observed for implanted SnV centers [88], although subsequent high-pressure, high-temperature annealing was shown to achieve distributions down to 6 nm [197]. Furthermore, the spectral features attributed to the PbV ZPL around 520 nm exhibit a narrow distribution of only 0.12 nm; however, unidentified emission lines over a ~ 100 nm range

28

could be evidence of a much larger inhomogeneous distribution or intermediate defect formation [89], meriting further investigation. In practice, it is likely that a combination of improved inhomogeneous broadening and spectral tuning will be necessary to realize spectrally indistinguishable emitters.

2.3.3 SPIN PROPERTIES

Many quantum information applications rely on spin-photon transduction via state-selective optical transitions within the ZPL [88, 176, 178, 180, 181]. These spin states, in combination with proximal nuclear spins coupled by magnetic dipolar interactions, can serve as an additional resource for storing or processing information [246] and performing local error correction [247].

In practice, the NV and SiV0 spins are easiest to work with due to their orbital singlet, $\mathcal{S} = 1$ ground states. A spin qubit can be realized between the $m_s = 0$ and either of the $m_s = \pm 1$ spin states, which are naturally separated in energy by a zero-field splitting. Coherent spin manipulation can be achieved via microwave fields [248], and NV centers have demonstrated the longest coherence times for a single electron spin qubit in any system ($T_2 > 1$ s) [Fig. 2.2(c)] [231]. So far, only ensemble spin resonance has been demonstrated for the novel SiV0 center; nevertheless, these defects exhibit coherence times as long as $T_2 = 255$ ms at 4 K [166, 249, 250].

In contrast, color centers based on negatively-charged group-IV defects exhibit a doubly-degenerate ground state in both orbit and spin ($\mathcal{S} = 1/2$), with orbital de-

29

generacy lifted by Δ_{GS} due to a combination of spin-orbit interaction and dynamic Jahn-Teller effect [179, 251]. In an external magnetic field aligned with the $\langle 111 \rangle$ axis, the lowest energy spin-1/2 manifold can be addressed using highly cycling, spin-selective optical transitions [178, 179, 252, 253]. The major challenge in working with the spins of negatively charged group-IV defects is rapid ground state dephasing caused by single-phonon transitions between orbital states. This motivates qubit operation at temperatures well below $\hbar\Delta_{GS}/k_B$ (see Table 2.1) to reduce phonon occupation, thereby exponentially increasing spin coherence times. As a result, the SiV exhibits a 4-5 order of magnitude increase in spin coherence times at T < 500 mK [$T_2 > 10$ ms [165], Fig. 2.2(f)] compared to 4 K ($T_2 \sim 100$ ns [254]). A complementary approach for improving spin coherence involves increasing the ground state splitting through the application of strain [244, 255]. For instance, strain tuning of SiVs in nanostructures has demonstrated an order-of-magnitude increase in orbital splitting, resulting in the highest reported SiV coherence time of $T_2 = 250$ ns at 4 K [255]. Moreover, defects based on heavier group-IV ions exhibit larger Δ_{GS}, which could facilitate operation at higher temperatures. Indeed, the PbV orbital splitting is estimated to be in the THz regime, suggesting the possibility of long-lived spin coherence at 4 K [89, 198].

A final consideration is the ability to couple to proximal nuclear spins of either the defect impurity or ^{13}C carbon isotopes in diamond. Impressively, the NV center has been used to control a 10-qubit quantum register with coherence times of > 75 s [19]. Single-site nuclear spin manipulation has also been demonstrated with the SiV [77, 167],

30

but multi-nuclear-spin registers have not yet been realized.

2.3.4 DISCUSSION

Thus far, state-of-the-art cavity experiments with diamond defects have used either the NV or SiV. While the NV center is the best understood defect, exhibiting excellent spin coherence, its optical properties are poor. In particular, the difference in permanent electric dipole moments between the ground and excited states degrades optical coherence for near-surface emitters. Open Fabry-Perot microcavities containing bulk-like diamond membranes are therefore especially promising for these color centers as they can be situated far from interfaces. In contrast, the SiV has poor spin properties at 4 K, requiring operation at dilution refrigerator temperatures to realize a long-lived spin qubit, but has superior optical coherence. Crucially, its inversion symmetry inhibits sensitivity to surfaces, allowing for incorporation into heavily fabricated nanoscale resonators with high Q/V (see chapter 2.4).

In addition, we discussed the potential of emerging group-IV color centers. Negatively-charged group-IV emitters based on larger ions appear to share the attractive optical properties of the SiV with the added potential for improved spin coherence times at 4 K, although these emitters are harder to fabricate and are not as well understood. The recently discovered SiV0 could potentially combine excellent optical and spin properties at liquid helium temperatures, but it requires specially-doped diamond to stabilize the neutral charge state and is one of the least explored of the defects considered here.

31

Finally, recent progress in ab initio [251, 256, 257] and machine learning [258, 259] techniques suggests it may soon be possible to predict new emitters with superior properties to those discussed in this section.

2.4 Diamond nanophotonics

In contrast to open-geometry cavities, nanophotonic resonators can readily achieve submicron mode volumes by using refractive-index contrast to confine light to volumes of order $(\lambda/n)^3$ or smaller [260–263]. Additionally, nanophotonic structures are naturally desirable for long-term scalability, since they can be fabricated en masse and utilize on-chip photon routing [11, 264]. For a general, platform-agnostic overview of nanophotonic systems we direct the reader to an alternate reference [265].

With its high index of refraction $n = 2.4$, diamond is a natural candidate for such systems, and in the absence of scattering or absorption losses, diamond nanophotonic resonators could theoretically achieve $\mathcal{P} \sim 10^5$ [266], or $Q/V_0 > 10^6$, where $V_0 = V(n/\lambda)^3$ is the mode volume relative to a cubic wavelength in the diamond. A wide variety of cQED structures have been fabricated in diamond [267], including whispering gallery mode resonators [268, 269], ring resonators [270, 271], and photonic crystal cavities (PCCs) [272–275].

The typical approach for nanoscale fabrication of high-quality photonic devices begins with single crystal thin films (~ 100 nm) grown heteroepitaxially, such as silicon-on-

insulator, which can then be processed into undercut photonic structures using standard lithography and wet-etching techniques [276]. Unfortunately, this relatively straightforward approach to engineer optically isolated photonic structures does not translate effectively to the fabrication of diamond. Despite immense progress in the field of diamond growth, heteroepitaxial single-crystal thin films of diamond cannot yet be produced with defects at or below the parts-per-billion level, as required for quantum optical experiments involving single emitters [277–281]. Additionally, diamond is resilient to all forms of wet etching. Instead, less controllable plasma-based dry etching techniques [282] must be used in combination with sophisticated lithography masks [269, 283]. Initial successes in nanofabrication of diamond [for example, see Fig. 2.3(a-b)] overcame these challenges using creative techniques to engineer nanoscale diamond membranes with sub-micron thickness, either via ion-beam implantation and liftoff or mechanical polishing and subsequent reactive-ion etch thinning, but both techniques struggled with low resulting cavity and emitter quality [82, 271, 272, 284–286].

Rather than membrane-based fabrication, underetching of structures defined in bulk, electronic-grade, single-crystal substrates [287] has recently enabled high-quality nanophotonic devices [Fig. 2.3(c-m)]. Unlike most nanoscale membrane structures, devices undercut from bulk substrates can achieve high quality factors due to their optical isolation from the bulk and are compatible with annealing and acid-cleaning post-processing steps required for incorporation of high-quality single emitters (chapter 2.3.1). Underetching was first implemented by using an angled etch to undercut one-dimensional structures

33

predefined with electron-beam lithography and top-down etching, leaving behind free-standing diamond nanobeams with a triangular cross-section [Fig. 2.3(h), steps I-III]. The angled etch was initially accomplished by placing samples inside a triangular Faraday cage within the reactive-ion etcher [266, 288]. More recently, a similar angled etch has been achieved using ion-beam milling at a well-controlled angle of incidence, resulting in more reliable etch profiles [289]. Both of these techniques have proven extremely effective for fabricating freestanding one-dimensional PCCs out of electronic-grade diamond substrates, such as those shown in Fig. 2.3(c-i), with high ratios of $Q/V_0 > 10^4$ [78, 266].

Underetched devices can also be fabricated out of bulk single-crystal diamond using a selective crystallographic etch to achieve a flat lower surface, as illustrated in Fig. 2.3(l) [269, 291]. This etching technique was initially developed to fabricate high Q/V_0 whispering gallery mode resonators [Fig. 2.3(m)] [268, 269], and has now been adapted to fabricate freestanding PCCs with a rectangular cross-section [292], enabling two-dimensional PCCs in single-crystal diamond [Fig. 2.3(j-k)] [290]. While the crystallographic-etch technique is somewhat less mature than the angled etch, it allows for rectangular device geometries similar to conventional photonic platforms. This should enable fabrication of waveguides with arbitrary relative spacing, allowing for implementation of freestanding diamond-waveguide based beamsplitters and electromechanical switches for on-chip photon routing [11, 264]. Furthermore, this technique has a largely unexplored parameter space available, making it possible to optimize the mask and etching procedure to
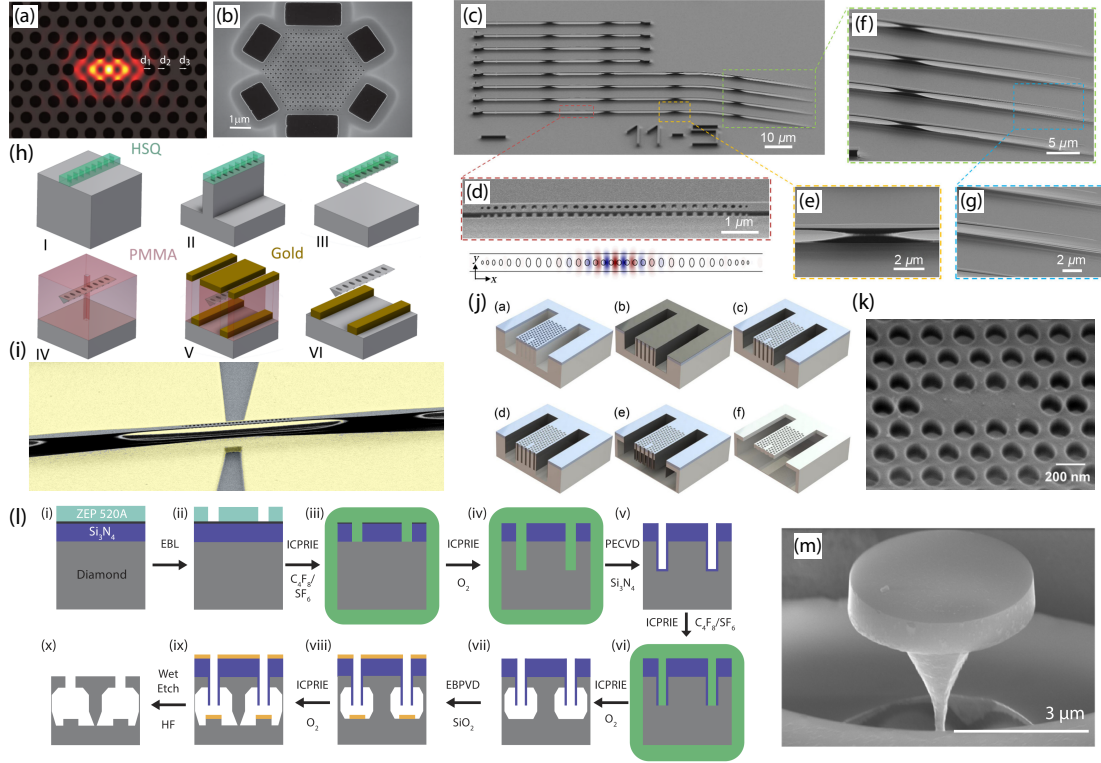
Figure 2.3: Diamond nanophotonic devices. (a) Mode simulation and (b) SEM of 2D PCC fabricated from an ultra-thin diamond membrane (reprinted with permission from Ref. [82], copyrighted by the American Physical Society). (c) SEM of an array of free-standing PCCs created by angled reactive ion etching, highlighting (d) 1D PCC region, (e) support anchor connecting waveguide to substrate, and (f-g) tapered waveguide region for adiabatic single-mode fiber coupling (reprinted with permission from Ref. [184], copyrighted by the American Physical Society). (h) Fabrication procedure for angle-etched devices (steps I-III), including targeted implantation through a mask (IV) and microwave electrode deposition (V-VI) (reprinted with permission from Ref. [78], copyrighted by the American Physical Society). (i) SEM of resulting devices with gold coplanar waveguide for microwave spin control (false color added, adapted with permission from [77], copyrighted by the American Physical Society). (j) Rectangular cross-section PCC fabrication procedure using an anisotropic crystallographic etch and (k) SEM of a freestanding 2D PCC (reprinted with permission from Ref. [290], AIP Publishing). (l) Optimized procedure to fabricate microdisk resonators using the crystallographic etch and (m) resulting high Q/V_0 device (reprinted with permission from Ref. [269], AIP Publishing).

achieve a wide variety of surface properties [269, 293].

In order to utilize low-mode-volume cavities for cQED experiments, color centers must

be placed at the mode-field maximum of the cavity with sub-100 nm precision. This has been accomplished with SiV centers using a variety of techniques (chapter 2.3.1), including delta doping [294], FIB implantation [206–208] and blanket ion implantation through lithographically aligned masks [209–211]. By implanting several ions and utilizing spectral selection of individual emitters, these techniques have enabled deterministic nanoscale PCC coupling of single SiV centers [76, 77, 87].

Once fabricated, nanoscale cavities can be optically interrogated using free-space optics [82, 270] or a transient coupler such as a tapered fiber [295, 266]. Coupling can also be made indirectly by means of a waveguide in which the photonic crystal cavity is integrated [for example, see Fig. 2.3(c, d, i)]. In this case, the cavity design is adjusted to damp preferentially into the diamond waveguide mode (see chapter 2.2, [260]), which can subsequently be outcoupled into a single-mode fiber by various techniques. Even a small defect in the waveguide, such as a deliberately introduced notch, induces scattering into free-space modes that can be coupled into a single-mode fiber via a high-numerical-aperture objective, albeit with limited $\eta^2 \sim 1\%$ efficiency [87, 243, 294]. Alternatively, grating structures [271, 296] can enable $\eta^2 \sim 10\%$ coupling efficiency by improving mode matching, and can be made broadband using optimized photonic design principles [297].

Nanophotonic structures can also be directly integrated into single-mode fiber networks. This has been done extremely efficiently using adiabatically tapered diamond waveguides coupled to similarly tapered optical fibers using van der Waals forces, yielding efficiencies close to unity [184, 298]. Currently, this technique requires precise

nanopositioning of the adiabatically tapered fiber, which can be challenging and costly to implement in cryogenic conditions where experimental access is limited [76, 78]. Instead, permanent and efficient integration into large-scale photonic circuits will likely be necessary to scale up nanophotonic cQED experiments. The first steps in this direction have recently been demonstrated using a pick-and-place technique to integrate diamond structures with aluminium nitride photonic circuits, enabling access to group-IV color centers in 72 separate diamond nanophotonic waveguides [235].

3

Millikelvin quantum nanophotonics with SiV centers

In this chapter, we review some technical details regarding low-temperature quantum optics experiments involving color-centers in diamond nanophotonic devices. The aim of this chapter is to supplement the other chapters of the thesis, most of which are already published in the literature, in order to provide a complete picture of how these experiments can be performed, some of the main experimental obstacles, and how to overcome them. This is meant to be a resource to experimental researchers performing similar solid-state cQED experiments. While there is some overlap with the published material in the other sections, this section will highlight important technical points that

are either commonly overlooked, or not included in the published works explicitly for brevity.

3.1 Nanophotonics

3.1.1 Device fabrication

In this thesis, we focus on nanoscale diamond waveguides and photonic crystal cavities fabricated using angled ion etching, either via the Faraday cage technique or the ion beam milling technique described above. All devices included a tapered diamond waveguide to which light could efficiently be coupled using a tapered optical fiber. All devices were fabricated at the Center for Nanoscale Systems at Harvad by Mike Burek and Bart Machielse. The high quality of the devices they fabricated, along with the conventional cleanroom equipment used, can provide a false sense of simplicity regarding diamond nanofabrication for quantum optics experiments. This could not be further from the truth - in practice, many years and hundreds of iterations went into perfecting the techniques used to produce the high quality devices described in the rest of this thesis. For details on the exact processes, I refer the reader to the references [245, 283] and Chapter 7.2. The difficulty of diamond nanofabrication is simultaneously a limitation on experimental progress and also one of the main reasons for optimism about this technology. The steady advancements in device cooperativity and functionality documented in this thesis are a testament to how much room to improve these integrated diamond

nanostructures have in the near future.

3.1.2 EFFICIENT TAPERED FIBER COUPLING

For published details regarding the physics of tapered fiber coupling, I recommend the reference [298], and for technical details on the tapered diamond waveguide, tapered fiber interface, I recommend the reference [184]. The success of the efficient tapered fiber interface was key to many of the scientific developments reported in this thesis. Below, I summarize a few key technical points that have enabled its success, which may not be obvious at first glance in the literature.

First, the tapered diamond waveguides have a tendency to bend and even "snap down" to the surface of the diamond when dried out of solution during fabrication [184]. It is very challenging to raise the diamond tapers once they had snapped down to the substrate, and found that coupling efficiency was typically limited to less than 30% for snapped-down tapers. Instead, if the sample is always removed from solution by extracting it from a solvent at the critical point, using a critical point dryer, this nearly deterministically prevents the taper from bending down and touching the substrate [245].

Second, the fabrication and handling of tapered fibers is quite challenging and can be a source of great frustration and a low yield step, if not carried out carefully. The HF etching procedure used for fabricating these fibers is described in [184], and in addition we have learned a few key points in the years following. First, it is crucial to properly

remove the acrylic coating around the fiber. Typical blade-based fiber-strippers can be used, but have a tendency to damage the fiber itself, often times in a way that is hard to diagnose. By switching to using a boiling sulfuric acid solution to selectively remove this coating without etching or damaging the fiber core or cladding prior to the HF step, the fibers are less likely to break during the fabrication, or shortly after the fabrication while handling the fibers.

Despite this, the tapered fibers remain extremely sensitive, and great care must be taken when handling and mounting them. In particular, sharp jerking movements (such as when removed from an adhesive such as a piece of tape) have a tendency to result in a broken or dull fiber tip. Additionally, whenever possible, tapered fibers should be stored in vacuum or a dry environment, as this appears to prolong their lifetime. Lower quality tapered fibers result in a measurably lower coupling efficiency (typically $< 50\%$). While difficult to evaluate directly without testing fiber-coupling efficiency, a reasonable metric for the quality of a tapered fiber can be obtained under a 100x optical microscope; if a rounded tip of the fiber is clearly visible under this magnification, near-unity coupling efficiencies are unlikely. With free-standing tapers, we found that after on average ~ 100 coupling attempts, we eventually break the diamond taper due to the repeated forces of coupling and de-coupling from the device. By switching to diamond tapered waveguides supported at the end, this problem can be addressed.

Stabilizing the tapered fiber in cryogenic conditions can also be challenging. Often times, vibrations from a cryostat's pulse tube or other ambient noise can couple to the

41

tapered fiber, which serves as an antenna and becomes very unstable and nearly impossible to controllably couple to nanoscale devices. We find that this problem is exacerbated particularly at low temperatures, regardless of the vibrational environment. This could either be due to a low temperature property of the piezoelectric positioners used for moving the fiber, thermal contractions involving the components used to mount the fiber, or combined thermal and mechanical properties of the fiber itself. By minimizing the length of the fiber that is free-standing to be on the order of $\sim 5\,\mathrm{mm}$ or less, one can largely mitigate vibrations of the tapered fiber and successfully couple to nanostructures in cryogenic conditions. Future developments utilizing ultraviolet-curing adhesives will be crucial to enable mechanical reinforcement or even permanent packaging of fibers to devices, greatly improving yield, robustness, and overall scalabiltiy [299].

Finally, characterization of the exact tapered fiber coupling efficiency is in general not straightforward. In order to characterize the efficiency, one must inject slightly-detuned light into the device and measure the reflected intensity when the fiber is coupled to the device. In all experiments presented in this thesis, this is done with a network of beamsplitters. For example experimental schematics used to characterize the efficiency, see figures B.2 and D.3(b). By measuring the input power and comparing it to the reflected power, one can extract the additional loss due to tapered fiber coupling.

This technique makes a number of assumptions. First, it assumes that the losses in the rest of the fiber network (insertion losses of beamsplitters and splices) is negligible. This is in general not a good assumption, as even the best fiber beamsplitters (manu-

42

factured by Evanescent Optics using fiber polishing techniques) still result in roughly 0.2 dB excess loss. Additionally, each fiber splice can introduce on average 0.05 dB excess loss at the visible wavelengths used in these experiments. In practice, one can either measure and calibrate these losses, or treat the extracted coupling efficiency as a lower-bound on the precise fiber-device coupling efficiency. Second, this method also assumes that the photonic crystal cavity reflects all of the light. This is a reasonable assumption if the wavelength of the light is within the bandgap of the PCC (but not on resonance with the cavity mode), and that the light is TE polarized. As such, polarization controllers are needed to control the input polarization in order to maximize the device reflectivity. Finally, small reflections in the fiber network due to imperfect splices, fiber beamsplitters, and imperfect tapered fiber coupling can result in an etalon effect which can cause significant ($> 10\%$) variations in the reflected signal as a function of wavelength. Therefore, in order to characterize the system, one must either look at a particular wavelength of interest, scan the laser wavelength over a large enough range, or use a somewhat more broadband source (but still within the bandgap of the PCC).

Using these techniques, with the best tapered fibers and devices, we observe coupling efficiencies with a lower bound exceeding 90%. Details about optimal position of the fiber are given in [184]. We typically use an approach angle of 5-7 degrees, and sometimes have to iterate to precisely align the fiber angle in the plane of the sample to be coaligned with the devices. Typically, all 3 axes needed to be optimized iteratively in order to achieve maximum coupling, although initial mechanical contact is achieved, the axis

43

along the taper is the most sensitive.

3.1.3 Gas tuning of cavity resonances

Due to variations and imperfections in the diamond nanofabrication process, PCC resonance frequencies have a large distribution on a single sample and vary from sample to sample. As a result, we fabricate devices with various scaling factors across a single chip, with larger scaling factors producing red-shifted devices, and smaller factors producing blue-shifted devices. A subset of these devices are in a suitable wavelength range for use in the experiments. Future progress in improving the reliability of the fabrication process, in particular the uniformity and thickness of the lithography mask, as well as the reproducibility of the diamond etch, could help improve the consistency of resonance wavelengths and improve the overall yield of usable devices.

Due to this uncertainty in device wavelength, a precisely controllable resonance tuning technique is required, compatible with cryogenic device conditions. In order to accomplish this, we condense gas (typically nitrogen, but other gases such as Argon and Xenon have also been used) on the sample surface at low temperatures. The gas condenses on the diamond PCC, locally increasing the index of refraction of the previously vacuum regions, resulting in an overall device redshift. In typical conditions, we can achieve a total redshift of more than $10 - 15$ nm. As a result, we would typically target a wavelegnth range of $725 - 735$ nm in order to access the SiV resonance at 737 nm. One can achieve a larger range (> 20 nm) of quasi-permanent device red-shift by precisely

depositing alumina using ALD after sample fabrication. However, we find that this reduces overall device quality factors and have some evidence (see Chapter 7.8) that this may result in the introduction of impurity spins that reduce coherence times.

Depositing the gas in cryogenic conditions, in particular in a dilution refrigerator, is technically challenging due to the thermal shielding necessary to operate the cryostat at base temperature. For example, the Blue Fors LD-250 dilution refrigerator used for these experiments, has fully closed shields at $60\,\mathrm{K}$, $4\,\mathrm{K}$, and $1\,\mathrm{K}$ stages, and line of site ports are usually blocked off with thermally anchored feedthroughs to prevent radiation leaks. In order to deliver nitrogen gas to the sample, attached to the mixing chamber of the dilution refrigerator (chapter 7.3), we anchor a copper tube to the 4K plate of the fridge and thread it through line-of-site ports at each, while only anchoring it with non-conducting materials (teflon and nylon) at $T < 4$ K stages. The end of the tube points directly at the sample, with a large solid angle for gas leaving the tube to be deposited on the sample. By attaching a $60\,\mathrm{W}$ cartridge heater (Lakeshore) to the tube, we can heat the tube to a temperature exceeding the nitrogen boiling point while keeping the sample at $T < 10$ K, which is below the nitrogen boiling point in high vacuum. On the higher temperature end, the copper tube is eventually connected to a standard gas/liquid vacuum feedthrough (Lesker), through which nitrogen is supplied via a leak valve. The gas tuning system is illustrated in part of the schematic shown in Fig. B.1.

The gas tuning procedure is as follows. Once the sample is at $4\,\mathrm{K}$ temperature (cooled

by the pulse tube, but while keeping the ^{3}He/^{4}He mix in the storage tank), we apply the heater in closed-loop mode with temperature readout on the copper tube nearby. Depending on the position of the temperature sensor relative to the heater, we calibrate the sensor temperature necessary to reach the boiling point of nitrogen along the entire tube, which ranged from $50\,$K to $100\,$K at the position of the sensor. The temperature of the sample and the other parts of the fridge do warm up slightly during this procedure, but never exceed $10\,$K. Once the temperature has stabilized (usually after about 15 minutes), we begin to slowly flow gas using the leak valve, while measuring the cavity reflection spectrum with a broadband source at low excitation power ($< 1\,$W) and a spectrometer. We stop the gas flow and turn off the heaters when the cavity reaches an acceptable wavelength.

Since this method of tuning is only precise to about ~ 5 cavity linewidths, typically several hundred GHz, and cannot be performed while the fridge is at base temperature, we typically tune well past the longest cavity wavelength we need for an experiment. Once the gas is deposited, it can subsequently be removed locally by sending in light through the tapered fiber to heat the cavity region and evaporate off any excess gas, without causing significant load on the entire fridge. Power on the scale of $1-10\,$W at the device can be used for this local back-tuning. By controlling the power and duration of the tuning light precisely, and by simultaneously monitoring the cavity reflection spectrum using a wideband source and a spectrometer, extremely high cavity tuning accuracy can be achieved, limited only by the spectrometer resolution. Interestingly,

46

under such illumination, the cavity initially redshifts, before eventually blueshifting. This suggests there is a nontrivial spatial distribution of temperatures along the beam. Under normal operating conditions, we find that the cavity resonance does not drift over timescales of months. However, we did occasionally notice discrete jumps in the cavity resonance, likely due to an overload of power (either optical or microwave) that caused gas to boil off somewhere on chip.

3.2 Quantum optics in a dilution refrigerator

Prior to the work carried out in this thesis, there was relatively little collective experience in carrying out solid-state quantum optics and electron spin resonance experiments in dilution refrigerator conditions. The need to shield out thermal radiation at many stages (see Sec. 3.1.3), as well as the very low cooling power of these systems (typically $\sim 10\,\mathrm{W}$ at $10\,\mathrm{mK}$ and $< 1\,\mathrm{mW}$ at $100\,\mathrm{mK}$) makes experiments involving free-space optical access and strong optical, microwave, and radio frequency control pulses very challenging. However, with proper consideration of experimental techniques, we have shown that it is possible to perform quantum nanophotonics experiments at millikelvin temperatures. This section highlights a few key considerations that are important to the success of such experiments.

47

3.2.1 SAMPLE MOUNTING

First, the diamond sample must be properly thermally anchored to the mixing chamber of the dilution refrigerator. Ideally, this should be done using gold-plated copper parts fastened tightly with brass screws and nuts. The thermal conductivity of oxygen-free copper is substantially better than that of aluminum and brass at low temperatures, and a gold plated layer (usually a few m) on the surface of the copper allows for better thermal and mechanical contact between surfaces and prevents oxidation at the surface, which can dramatically reduce thermal conductivity at an interface [300].[1] Furthermore, for cryo-magenetic experiments such as the ones described here, the gold-plated layer should ideally be deposited without any nickel undercoat if possible. Additionally, brass screws contract more than copper and therefore tighten when cooled down, whereas other materials such as stainless steel may actually loosen at lower temperatures. As a consequence, however, one must be careful to check upon several thermal-cycles that the brass screws are still tight, as they can come loose due to the repeated contraction and expansion as the system cycles.

Auxiliary parts that do not directly connect the sample to the mixing chamber can be made of different (ideally still non-magnetic) materials, such as aluminum and brass, in order to save cost or for ease of machinability. If the sample is placed on positioners, such as in our first dilution refrigerator setup described in Fig. 7.3, annealed copper braids or

---

[1]"Matter and Methods at Low Temperatures" by Pobell [300] is an excellent all-around reference for experimentalists working on demanding cryogenic experiments.

soft copper foil should be used to thermalize the sample on top of the positioners while still allowing for proper stepping motion. This is because the positioners themselves are typically made from poorly conductive materials such as titanium and ceramics, and involve bearings that have very poor interface thermal conductivity. In fact, even if the materials on top of the positioner are not temperature critical, the top stage of each positioner should still be thermalized with braids in order to reduce the cooldown time and prevent long-term drifts, since the interface between the base of the positioner which is fixed and the moving stage is typically very highly insulating. As a result, we assemble our own three-axis systems from the individual positioners with intermediate mounting plates to which copper braids or foil could easily be attached (see item 18 in Fig. B.1), ensuring that the entire positioner thermalizes to the base temperature quickly.

The sample itself should ideally be mounted using indium solder to a gold plated copper piece. While we did not perform substantial tests of alternative mounting techniques, we did find that this technique consistently allows us to obtain the sufficiently low sample temperatures (as inferred by the decoherence and decay rates of various ground-state transitions), whereas direct clamping of the diamond to gold-plated copper yielded inconsistent results. Soldering can be performed by heating the gold-plated copper sample holder to an appropriate temperature just above the melting point of indium, placing a small piece of indium wire on the sample until it melts, applying a small amount of flux to the indium (taking care that the flux residue does not splatter

49

onto the sample), and pressing the sample down on the indium, rubbing it in a circular motion for several seconds to allow it to thermalize and for the indium to properly wet the backside of the diamond. Once attached, the sample holder can be removed from the heat and allowed to cool. In future, optimized tools for holding and aligning the sample to the sample holder during this soldering process might be benefical, to avoid human error in the sample mounting process. However, we find that the sample mounting step, while challenging, almost always succeeded without damage to the sample, and therefore was not close to being a yield limiting step in our experimental process. While indium becomes a superconducter at low temperature, due to the extremely low critical field, we find that it retains its normal state and is able to effectively conduct heat between the diamond sample and the copper substrate.

3.2.2 Cryogenic optics

Achieving high resolution optical access to cryogenic samples is also especially challenging given the amount of radiation shielding present in dilution refrigerator systems, which dramatically reduces optical access. However, properly thermally anchored glass (UV fused silica) does not transmit infrared heat radiation, and can be used at room temperature and $60\,\mathrm{K}$ to prevent thermal radiation from higher temperatures from reaching the sample. In order to prevent reflections which would reduce the efficiency and introduce etalon effects to the system, the glass pieces should be suitably AR coated for the wavelength of interest, or wedged. In our experience, introduction of glass windows

rather than solid metallic plates in the 40 mm line-of-sight ports of the Blue Fors LD-250 only increased the base temperature by about 5 mK from 10 mK to 15 mK. In order to thermally anchor the glass plates, they were clamped with a copper piece using soft indium wire as an intermediate layer to prevent cracking of the glass while still enabling good thermal contact.

Additionally, in order to achieve a simultaneously high resolution and large field of view of the sample, a telescope is used, either to relay the image of the sample onto a CCD for wide-field imaging, or to relay the deflection from a galvonometric mirror onto the back aperture of the objective in a confocal microscope. Due to the long working distance from the top of the fridge to the sample, some of the lenses of the telescope must be located inside the fridge. A custom-machined "cage" system of rods that attached to the native threaded holes of the Blue-Fors LD-250 was constructed to enable mounting of the lenses perfectly cocentric with the line-of-site port of the fridge. Lenses are clamped between two copper pieces using a similar indium wire technique as above, and holes are drilled in the copper pieces to make it compatible with this cage system. We have used both ahcromatic cemented doublets and standard convex lenses in the telescope, and did not find any degradation in quality of the lenses after many (several tens of) thermal cycles, even in the case of the cemented lenses. The position of the lenses is also optimized to be close to individual flanges of the fridge, to reduce the number of additional glass windows needed for thermal shielding. Furthermore, the 8f telescope used in the setup described in Fig. B.1 is designed to place the 4f focal point

51

exactly at the 4 K stage, enabling use of a small aperture as opposed to a window for improved thermal shielding at this stage.

For the final lens, it is desirable to use a high-NA microscope objective. However, standard high-NA objectives used in ambient conditions are typically not vacuum and cryogenically compatible: they are quite expensive, and degrade over time in such conditions. Additionally, they are particularly poorly suited for repeated thermal cycling, which can deteriorate adhesive used in the assembly of the objective. Finally, they are quite heavy, and typically cannot be moved by standard, compact piezoelectric positioners. Instead, a very limited selection of low-temperature compatible objectives can be used (such as the Attocube LT-APO). However, these are also extremely expensive and have a poorer performance in terms of correcting for chromatic and spherical aberration. As a compromise, a standard aspheric objective lens with high NA can be used, if the imaging system is used at a single wavelength. This provides reasonable overall performance, but introduces some spherical aberrations compared to a proper imaging objective.

One major challenge in achieving high resolution is the stability of the imaging system under cryogenic pulse tube operation. Without significant optimization, we typically see vibrations with an amplitude $< 1\,\mathrm{m}$, which is suitable for imaging the nanostructures and performing laser excitation of the nanostructures for transmission measurements, such as those described in chapter 5. We find that the stability is usually limited by the least stable optical component, which is usually the objective lens assembly

52

connected to the piezo positioners by an intentionally lightened aluminium L-shaped bracket. Sturdier piezoelectric positioner assemblies may help in achieving diffraction limited performance.

Additional optical access can be achieved using optical fibers. We construct optical fiber feedthroughs using two methods. The first is to drill a very small ($< 1\,\mathrm{mm}$) hole in a blank vacuum flange and thread the fiber through, coating it with Torr-Seal adhesive at the location of the hole to fill the hole. Several holes can be drilled in a single KF16 or KF40 flange, enabling feedthrough of many fibers. For a slightly higher stability and more organized solution, a KF to Swagelok tubing adapter can be used, and multiple fibers can be threaded through the swagelok tubing, with a small amount of Torr-Seal used to seal the Swagelok connector. The room-temperature ends of the fiber can then be threaded through Swagelok-compatible tubing and transferred across the lab in such tubes to an optical table, allowing for robust mechanical shielding and higher polarization stability of the potentially long fiber link. Inside the cryostat, we find that thermalization of the fiber at various stages is not necessary, due to the low thermal conductivity of the fiber. Like other cryogenic wire, the fiber can be secured with cryogenically compatible tape or nylon string. Additional fiber connections can be made by splicing within the dilution refrigerator. Although not technically cryogenically and vacuum compatible, standard fiber heat shrink can be used without any noticeable adverse effects for our experiments inside the cryostat.

3.2.3 Experiment control challenges

The experiments described in subsequent chapters require precisely timed sequences of optical and electronic input and output signals to and from the apparatus. The pulse sequence timescales and signal frequencies for these experiments range over many orders of magnitudes, from picoseconds to seconds and megahertz to terahertz respectively, making experimental control quite complex compared to many other physical systems. Due to the lack of specialized equipment for such control signals, a number of pieces of general-purpose lab equipment were used in concert to enable the experiments in this thesis. For an example experimental configuration, see Fig. D.3(a).

The core of such an experiment is a field-programmable-gate-array (FPGA) into which a particular experiment sequence can be programmed and delivered in the form of a waveform of pulses on several digital channels. In the experiments described here, this was a 32-channel National Instruments high-speed digital input/output (HSDIO) device, which was programmed in Labview. Digital signals from such a device can be used in a number of ways. First, they can trigger digitally gated equipment which have two relevant experimental states (such as "on" and "off"). Often, these digital flags would be used to generate precisely timed analog control signals, such as those required for driving acousto-optic modulators (AOMs), electro-optic modulators (EOMs), or microwave and radio-frequency pulses, using external analog circuits or pre-programmed, external arbitrary waveform generators (see Fig. D.3 for an example configuration). The

54

signals could also be used in external digital circuits for logical experiment control and processing, for example to digitally "gate" photon counts to accept counts during a readout pulse, and reject counts at other times. An FPGA based device like the HSDIO can also accept digital inputs and perform feedback based on experimental results, such as active branching or decision making, to modify an experimental control sequence in hardware time (sub-microsecond). Common examples of such experimental control processes are described below in Sec. 3.3.1, or feedback based initialization, described in Tables D.1 and D.2.

In general, while this experimental architecture was quite flexible and enabled a wide variety of experiments, it did so at the expense of considerable complexity in the scope of the control equipment. Integration of the various components of the experiment, including digital to analog converters, local oscillators and mixers, amplifiers, high-extinction switches and filters, and time-tagging electronics into a single FPGA-based device would improve ease of such experiments greatly. Furthermore, control software can play a limiting role in the types of experiments possible. One major obstacle is the programming of FPGA-based devices, which is extremely challenging at the level of a research laboratory without dedicated FPGA engineerse. A flexible environment in which FPGA functionality can be accessed at the level of a scientific programming language such as python is extremely desirable. Additionally, complex experiments with tens of pieces of equipment distributed across a large laboratory require flexible control structures, such as that afforded by a modular client-server control architecture, rather than a single

thread of programming commands for all experimental procedures. Furthermore, the ability for physicists and engineers to rapidly develop and prototype new code is crucial, and becomes extremely challenging the more complex the experiment. While the experiments performed here used a relatively inflexible set of Labview control software, we have in recent months developed a client-server, python-based laboratory control infrastructure specifically designed to address these challenges,[2] which will hopefully enable more demanding distributed quantum network experiments in the near future.

3.3 Emitter properties

3.3.1 Stabilizing charge state and optical frequency

A key advance that enbaled the experiments presented in this thesis was the ability to consistently measure narrow emitter linewidths and perform various complex experiments in a regime where line broadening was not a dominant effect. This can be challenging with solid-state defects, which typically experience broadening of several orders of magnitude beyond their natural linewidths, sometimes known as spectral diffusion (see chapter 2.3.2). Even group IV defects, which exhibit inversion symmetry, demonstrate significant spectral diffusion in nanostructures (see chapters 4 and 7.5.2 and appendix A for examples) which can be an impediment to certain experiments, such as the realization of a high-fidelity spin-photon interface at a well-defined optical

---

[2]For details, see pylabnet.

56

frequency. Undesired ionization of the color-center, often referred to as blinking, can be another obstacle in achieving a reliable optical interface.

Both of these effects appear to scale quite dramatically with applied incident optical power. One leading theory is that high-powered optical fields can excite nearby defects in the environment, changing local electric field or strain configurations and inducing spectral and charge diffusion. If a high illumination intensity is used, as is typical in inefficient free-space confocal excitation of defects, the timescales for spectral diffusion and blinking can be quite short (millisecond or less), even for nominally insensitive defects. With an efficient optical interface, such as that afforded by the fiber-coupled cQED system discussed in this thesis, optical spectroscopy could often be performed with very low powers, enabling clear resolution of narrow lines on timescales significantly longer than the characteristic diffusion or ionization timescale. In other experiments however, where higher intensities are needed, a stop-gap solution used in early work [87] is to randomize the emitter position and probabilistically initialize the charge state using a green (520 nm) laser pulse before each experiment. Depending on the intensity and duration of the green pulse, the emitter's charge and frequency state could be reset in a stochastic fashion (see Supplementary information of [87]). While this technique is reasonably effective for ensuring charge state initialization, it simply randomizes the emitter's optical frequency, rather than locking it to a narrow value.

The most reliable technique for ensuring narrow lines is preselection [75, 301]. In this technique, the color-center is briefly probed with a narrow-band, resonant laser. If

57

the color-center is in the correct charge state and at the appropriate frequency position resonant with the laser, it will scatter above (or below) a certain threshold of photons which can be pre-calibrated, and the experiment can proceed. This threshold can also be adjusted to obtain a desired linewidth: a more stringent threshold will generally result in a narrower linewidth at the expense of a lower experiment duty cycle. If the threshold is not passed, a feedback procedure can be implemented to reinitialize the charge and frequency of the color-center before proceeding to the experiment. The most primitive technique is to shine the 520 nm laser to randomize the frequency and reset the charge state. While this works remarkably well, it has a relatively low success probability and yields a lower experiment duty cycle. Additioally, we find that not all SiV centers respond identically to 520 nm illumination; some may be more or less sensitive to it. Alternatively, the frequency of the near-resonant probe laser can be scanned and used to actively find the new resonance frequency. This works very well for emitters that are stable on timescales significantly longer than the time it takes for the line-finding procedure, which is often the case for SiV centers inside nanoscale diamond PCCs [50]. Finally, active feedback on the actual frequency of the emitter, for example using electromechanical control of the local strain [245], is a very promising long-term solution for emitter stabilization. Control of the local strain environment can also have other potential uses in optimizing the spin-photon interface (chapter 7.4), but presents a significant nano-optoelectronic integration challenge.

58

3.3.2 Emitter properties in nanostructures

The remarkable aspect of group IV color-centers is that in general, they maintain nearly lifetime-limited linewidths - at least on some measureable timescale - even inside of nanophotonic structures [75, 86]. However, in general, their properties can degrade as a function of the specific nanophotonic environment. While we did not perform any specific quantitative analysis, over the course of the studies presented in this thesis we found that emitters implanted in standard waveguides without PCCs had better optical properties (narrower linewidths) than those implanted in PCCs. This is an important distinction, since the first results with new defects inside nanostructures tend to be in simple structures such as waveguides. While positive results regarding linewidths in waveguides are encouraging, they do not necessarily imply straightforward translation to small mode-volume PCCs.

This discrepancy could be for two primary reasons. First, the pattern of holes that form a PCC introduces additional surfaces near the defect, which might result in defects which can produce electric field noise (which only couples to second order to the optical transition), or configurationally unstable defects which could produce strain noise which could linearly affect the optical transition.

Second, and perhaps more compelling, is the fact that the density of ions implanted to create defects in PCCs is naturally higher than in typical waveguide samples, due to the need to localize emitters in a very small mode volume in the PCC. Typical densities of

ion implantation in PCC experiments were 5×10^{12} ions per cm^2, compared to 1×10^9 in waveguide experiments. The hypothesis is that residual damage from ion implantation that is not repaired by annealing procedures leads to the formation of defects, either impurity complex defects, or larger vacancy clusters [302]. These defects might couple to the color-center either producing fluctuation strain or electric fields, and could be located within the diamond lattice itself, in very close proximity ($\sim$ nm) to the color-center. Such nearby defects have even been sensed in double-electron-electron resonance in these samples (chapter 7.8). Additionally, we noticed that GeV centers tended to be less stable than SiV centers under identical nanophotonics and implantation density conditions. Assuming the internal symmetry of the GeV provides a similar level of protection to environmental noise, this would be consistent with the hypothesis that residual damage from ion implantation is responsible for the degradation of optical properties, since germanium is a heavier element and thus must be implanted at higher energies to achieve similar depths, leading to more lattice damage. This phenomenon could have significant implications for the prospects of similar experiments with heavier tin and lead vacancy emitters [88, 89].

3.3.3 ADVANTAGES OF SIV CENTERS COMPARED TO OTHER SYSTEMS

In this section, we compare the SiV center platform described in most of this thesis to other systems with potential for building quantum network nodes, including trapped atoms in macroscopic cavities and near nanostructures, self-assembled quantum dots,

and other defect-based centers in diamond and related materials. Here, we focus on the SiV center; for a broader, more complete overview of spin-photon interfaces, please see the reviews [18, 94, 144, 303].

TRAPPED ATOM AND ION SYSTEMS have the best optical and spin coherence properties, due to the ability to isolate them from environmental noise and cool them to ultra-low temperatures. Additionally, in the absence of external fields, each atomic species of a given isotope is identical to a very high precision, making the generation of indistinguishable photons from different atoms or ions relatively straightforward. However, compared to solid-state platforms, there is a serious overhead associated with cooling and trapping atoms and ions, both introducing experimental complexity and reducing operational duty cycles. Despite this, canonical experiments with atoms and ions have been carried out in macroscopic cavities [304, 305], and there have also been advances in the trapping of neutral atoms near nanostructures [306–308]. Perhaps most promising is the emerging intermediate platform of fiber cavities, which are a compromise of small mode volume and ease of trapping, and have recently achieved record cooperativites [309].

Many factors are often cited as advantages or disadvantages of solid-state systems compared to atoms. Here, we focus on a few key factors which are subtle and often misunderstood. The first is the compatibility for en-masse fabrication and integration into photonic circuits. While compelling and often cited as a key advantage of solid-state

systems, this argument is not necessarily the most straightforward, as atomic systems have also been coupled to nanostructures, and atomic arrays are arguably one of the leading platforms for scaling to the ~ 100 qubit regime. In the case of the SiV specifically however, this argument holds due to the fact that it can be deterministically and permanently integrated into the mode-field maximum of a nanostructure with relative ease, and such nanostructures can be fabricated with a very high density.

Additionally, the complexity in trapping and cooling atoms and ions is often cited as a disadvantage compared to solid-state systems. This is a subtle point - on one hand, solid-state systems typically require cryogenic operation, which also introduces a non-negligible amount of complexity and cost. On the other hand, a major disadvantage of these systems which is related but rarely considered directly in the literature is the difficulty in rapidly prototyping the system. Trapped atom experiments require ultra-high vacuum (UHV) chambers which typically take on the order of weeks to cycle and pump back down to a suitable vacuum level, and there tends to be a large amount of inertia involved in opening a vacuum chamber once a suitably functional experiment is already inside. In the early stage of quantum network technology, this is a major disadvantage, as the ability to rapidly prototype and test various types of devices and techniques is key. This can more easily be done in solid-state systems in which qubits are trapped in a lattice rather than suspended in vacuum. Even dilution refrigerators can be cycled on the 2-3 day timescale, which is significantly faster and easier than a UHV glass cell. The ability to constantly change the experimental apparatus to add

new functionality has been a key enabling feature throughout the course of the work described in this thesis.

Finally, the typically broad inhomogeneous distributions of solid-state systems are often viewed as the biggest disadvantage of solid-state systems compared to their atomic counterparts. However, state of the art experiments involving spin-photon interfaces have only been carried out with at most two remote nodes so far. The bottleneck so far has been efficiency of the spin-photon interface, rather than resonance matching. Once spin-photon interfaces are made to be more efficient, scaling them up will require solving the resonance matching problem somehow. However, many solid-state systems, including the SiV center, have already demonstrated wideband resonance tuning [245, 310], which can completely address this issue, and further provide an additional tuning knob not as easily accessible to atomic systems, for example to switch resonant interactions on and off. Additionally, the ability to span multiple frequencies will likely serve as a key feature in the long run, enabling efficient frequency multiplexing along single communication channels [311].

SELF-ASSEMBLED QUANTUM DOTS are in many ways a model solid-state quantum emitter, as they can be fabricated with high quality using molecular-beam epitaxy or droplet-etch epitaxy and straightforwardly embedded into micro- or nano-cavities made directly from the GaAs host material. Several canonical cQED experiments were carried out using such systems, enabling the exploration of light-matter interactions in photonic

nanostructures which enable incredibly high-bandwidth operation [16]. Over a decade of work has also led to a detailed understanding of the spin properties of quantum dots, which are in general limited to timescales of 1 s due to the dense nuclear spin environment in the surrounding GaAs crystal [312].

The SiV platform shares many of the advantages with quantum dots in regards to integrability into nanostructures. While diamond fabrication is perhaps more involved than fabrication of GaAs, the resulting device qualities and cooperativities are on par. One advantage of the SiV is the ability to introduce high quality defects at a deterministic location using targeted implantation. Such spatial localization is not possible with quantum dot samples, which typically require post-growth analysis prior to fabrication of optical cavities. The most clear advantage of the SiV is the long spin coherence possible at low temperatures ($T_2 > 1$ ms at $T < 500$ mK).

DEFECTS IN OTHER MATERIALS are emerging as promising candidates for building quantum network nodes. Here I will discuss a few relevant platforms and discuss their merits, and how they compare specifically to the SiV.

Rare earth ions in crystals are perhaps one of the most interesting systems, since the combine some of the advantages of atomic-level coherence properties with opportunities such as nanophotonic integration and frequency multiplexing. While the optical lifetimes of such defects tend to be quite long, leading to relatively weak photon emission, recent work has pushed this platform into the $C > 1$ regime, making it a promising spin

photon interface [153]. One key possible advantage over the SiV and other systems could be in the use of select ions such as erbium which provide a direct telecommunications spin-photon interface [154]. Another is the natural inhomogeneous distribution commonly present in samples, that have enabled applications involving atomic frequency combs and might enable multiplexed application in a future quantum network [311]. However, the intrinsic bandwidths of this system are relatively low due to the long natural lifetimes of the emitters. It is still an open question whether or not all decoherence effects can be overcome, leading to robust spin-photon entanglement at rates suitable for quantum networking applications. For example, long spin coherences may be challenging to achieve due to the presence of magnetic impurities in the host material, which is not a problem in diamond.

Similarly, emitters in silicon carbide hold great promise and have many of the advantages that diamond has. Additionally, defects in SiC, in particular the silicon-vacancy in SiC, have been shown to have good spin properties at liquid helium temperatures and be relatively insensitive to electric field noise, despite the lack of inversion symmetry in the SiC crystal [20]. However, deterministic incorporation into nanostructures has yet to be demonstrated. Additionally, the silicon-vacancy in SiC lacks a cycling transition, and has a relatively narrow-band spin-photon interface that cannot be easily tuned using, for example, external magnetic fields. On the other hand, SiV spin-selective optical transitions can be split on the GHz level using external magnetic fields, enabling fine-tuning of the spin-photon interface.

A number of emerging defects in other materials are now being studied. Perhaps most exciting is the new class of defects in silicon [313], which is a material for which a wealth of scalable nanofabrication expertise already exists. Such systems are still not at the same level of maturity as the SiV for use in quantum networking devices, as questions still remain about the ability to fabricate single centers determinstically, optical and spin coherence properties, and a robust spin-photon interface. However, if such defects can be shown to possess a suitable spin photon interface in the near future, they hold enormous promise.

OTHER GROUP IV COLOR CENTERS are perhaps the most challenging to differenti-ate from the SiV. These centers have the same D_{3d} symmetry and the same resulting electronic structure. The argument about inversion symmetry therefore holds, making these centers promising spin photon interfaces that might be suitable for incorporation into nanophotonic structures. Additionally, many of the same schemes and techniques developed from the SiV may directly translate onto these color-centers. For a detailed comparison of the properties of color-centers in diamond, including the neutral SiV and the NV, see chapter 2.3. Here, I will describe the subtle considerations in choosing between the very similar negatively charged group IV color-centers.

The first consideration is the optical transition frequency. The SiV is resoundingly the most convenient in this regard. First and foremost, it is the longest wavelength optical transition, meaning that resonant optical nanostructures can be fabricated with

66

larger feature sizes compared to the shorter wavelength counterparts. This typically results in higher quality factor devices. Additionally for the SiV, there exists a convenient combination of wavelengths (1630 and 1350 nm), which can be used in sum and difference frequency generation for wavelength conversion to enable efficient propagation in telecommunications fibers at 1350 nm. Most crucially, generation of a 737 nm photon from a 1350 nm photon can be done with a lower energy 1630 nm pump, which should result in fewer noise photons at 737 nm. Perhaps equally crucially, there exists a wealth of convenient and high quality laser technology for 737 nm. Both pulsed and continuous wave Ti:Sapphire lasers can easily reach this wavelength, enabling high quality, high power sources for research grade experiments. However, standard commercial diodes exist in the range of $720 - 730$ nm, which can be thermally tuned and incorporated into external cavities to enable narrow-band sources at 737 nm that are both cheap and potentially scalable in future. On the other hand, the GeV and SnV are at wavelengths inaccessible by both Ti:Sapphire lasers and standard diodes, and require either expensive or increasingly complex frequency conversion setups, or high-maintenance dye lasers. Practically speaking, performing detailed spectroscopy and actively developing new quantum optical protocols often requires or benefits enormously from the availability of multiple independent near-resonant lasers, so the ability to acquire inexpensive but functional lasers is a serious factor in the ease of development of a particular system. Our own experiences with GeV centers were hampered by the need to use a home-built frequency conversion setup in order to achieve even a single resonant tone.

The next consideration is the quantum efficiency (QE) of the transition. The GeV and SnV appear to have higher intrinsic quantum efficiency than the SiV. While the cause of this is unknown, one possible explanation would be the higher optical transition energy, which could cause direct multi-phonon decay to be less likely. It is widely believed that QE is an essential parameter in evaluating the performance of a spin photon interface. However, as established in Chapter 2.2, the final cooperativity of the system is the true figure of merit in evaluating a spin-photon interface. Thus, one should look at how the QE affects the cooperativity of the system. Observing equation 2.3 for the cooperativity, the QE would influence C by way of introducing $\gamma = \gamma_r + \gamma_{nr}$, where γ_r and γ_{nr} are the radiative and nonradiatve rates. In this example, if one emitter has a low QE, this means that nonradiative decay is dominant ($\gamma_{nr} > \gamma_r$). However, in practice, as explained in chapter 2.2, solid state systems are typically limited by additional broadening effects $\gamma_d > \gamma_r, \gamma_{nr}$. In this case, the exact quantum efficiency is not important, since the linewidth is determined by other factors, such as spectral diffusion. In other words, γ_d, the spectral diffusion, typically ends up limiting the cooperativity, not γ_{nr}, the nonradiative decay (low QE).

There is, however, an exception to this analysis. Spectral diffusion is largely believed to be a non-Markovian broadening mechanism. In other words, the transition is not instantaneously broadened, but instead wanders on a timescale that could in principle be measured and tracked. If this tracking were implemented effectively enough (see appendix D.4) for an example protocol using frequency tracking on a slow timescale),

and γ_d were eliminated completely, then the QE could again become the limiting factor on cooperativity, potentially providing additional motivation for studying the higher QE emitters. However, inside high quality PCCs we have not yet been able to observe narrow linewidths using GeV centers for timescales long enough to enable effective preselection and tracking.

The next consideration, and most widely cited, is the difference in spin-orbit coupling constant. The heavier the ion, the larger the spin orbit coupling, leading to a larger splitting between the two lowest energy orbitals. It is known that thermal phonon coupling between these two orbitals is responsible for decoherence of negatively charged group-IV color-centers at elevated temperatures. This mechanism limits the SiV coherence time to $\sim 200\,\mathrm{ns}$ at the readily accessible temperature of $4\,\mathrm{K}$. A primary motivation for moving to larger centers, therefore, is to increase this splitting and thereby increase the temperature of relevant phonons. While the SiV requires temperatures roughly below $500\,\mathrm{mK}$ to achieve ms coherence times, it is believed that the SnV and the PbV might be able to access these at temperatures of $\approx 1\,\mathrm{K}$ and $\approx 4\,\mathrm{K}$ respectively. Achieving a similar spin photon interface as described in this thesis but at temperatures accessible by cheaper and more scalable cryogenic systems would be a major milestone.

At the same time, there is one subtle challenge associated with the larger spin-orbit coupling defects that will need to be addressed. When spin orbit coupling is the dominant perturbation in the ground state, the magnetic dipole transition between the qubit states is not allowed, due to the necessity to flip both the orbital and spin components.

69

Only when sufficient strain is applied does this transition become allowed and straightforward to drive in cryogenic conditions. Additionally, the orbital states are sensitive to strain fluctuations and experience much more diffusion and drift as compared to the purely magnetic spin sublevels. As a result, experiments with SiV centers involving high-fidelity microwave control have primarily been done with high strain emitters. The regime of high strain however, requires that the strain should be larger than or comparable to the spin orbit coupling. In the case of the SiV, this condition is often met for implanted emitters in nanostructures. The same may not be the case for the emitters with larger spin orbit coupling energies. As a result, microwave driving may prove difficult for these emitters. On the other hand, the ability to work at higher temperatures may afford higher cooling powers, enabling driving of microwave transitions nonetheless. Aside from the SiV and GeV centers, complete coherent control has not yet been achieved for the heavier group IV elements.

The final consideration is defect fabrication. As mentioned in chapter 3.3.2, we have observed a qualitative trend of decreasing emitter properties with increasing implantation energy. As increasing enegies are required to embed heavier ions into diamond structures at a given depth, this implies that it will be more challenging to achieve low spectral diffusion and narrow inhomogeneous distributions for heavier emitters. As a result, the SiV seems to be the most advantageous of the group IV centers as it is the lightest. However, it is possible that advances in defect incorporation and post-implantation annealing at higher temperatures could remedy the lattice damage [216],

70

improving defect properties even in the case of heavier ions.

IN SUMMARY there are number of competing platforms with various widely capitulated merits relative to the SiV center in diamond. However, in general, the SiV center has proven to be a more convenient platform in almost every possibly way for developing a toolset for quantum networking components. The ease of integration into nanostructures, the relative optical stability of its transitions despite ion implantation and fabrication, the ability to drive coherent microwave transitions and achieve long coherence times, and the ability to rapidly prototype experiments and obtain cheap yet high quality lasers for resonant control, have enabled the SiV to undergo a rapid metamorphosis from a spectroscopic curiosity to perhaps the leading platform for the construction of large-scale quantum networks. On the other hand, the multitude of systems available, including those still being discovered in new materials platforms such as silicon, as well as the amount of progress remaining until functional quantum networks are realized, means that another platform could possibly become a more practical long-term choice in the near future. In any case, the lessons learned and toolset developed by using the SiV as a testbed for primitive quantum networking experiments will hopefully lay the foundation for realistic quantum network technologies.

4

Quantum nonlinear optics with a germanium-vacancy color center in a nanoscale diamond waveguide

4.1 Introduction

Efficient coupling between single photons and coherent quantum emitters is a central element of quantum nonlinear optical systems and quantum networks [16, 42, 314]. Several atom-like defects in the solid-state are currently being explored as promising candidates for the realization of such systems [315], including the nitrogen-vacancy (NV) center in diamond, renowned for its long spin coherence at room temperature [316]; and

the silicon-vacancy (SiV) center in diamond, which has recently been shown to have strong, coherent optical transitions in nanostructures [86, 87, 317, 318]. The remarkable optical properties of the SiV center arise from its inversion symmetry [179], which results in a vanishing permanent electric dipole moment for SiV orbital states, dramatically reducing their response to charge fluctuations in the local environment. A large family of color centers in diamond are predicted to have inversion symmetry [199] and therefore may be expected to have similarly favorable optical properties. In this Letter, we demonstrate an efficient optical interface using negatively-charged germanium-vacancy (GeV) color centers integrated into nanophotonic devices with optical properties that are superior to those of both NV and SiV centers. These properties result in high interaction probabilities between individual GeV centers and photons in a single-pass configuration, even without the use of cavities or other advanced photonic structures.

4.2 GeV centers in diamond nanophotonic waveguides

The GeV center is a new optically active color center in diamond [195, 218, 319, 320]. Its calculated structure, shown in Fig. 4.1(a), is similar to that of the SiV center with D_{3d} symmetry [199, 319]. The Ge impurity occupies an interstitial site between two vacancies along the $\langle 111 \rangle$ lattice direction [199, 319, 320], resulting in inversion symmetry. Fig. 4.1(b) depicts the electronic level structure of the GeV [319, 320] with a zero-phonon line (ZPL) transition at $602\,\mathrm{nm}$ which constitutes about 60% of the total

73
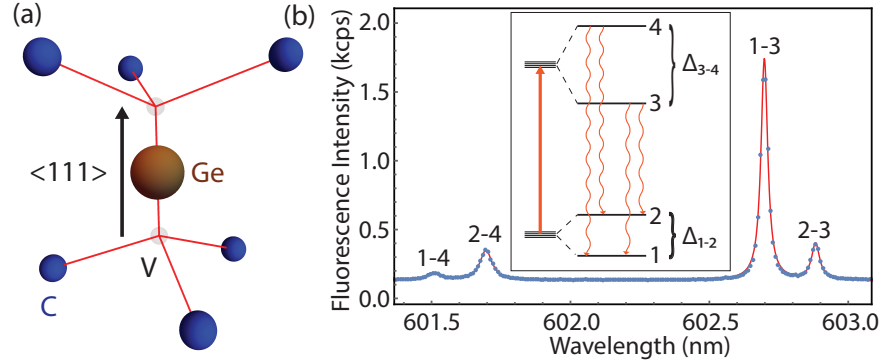
Figure 4.1: (a) Molecular structure of the GeV center. (b) Photoluminescence spectrum of the GeV at $T = 50\,\mathrm{K}$, revealing the four optical transitions predicted by the GeV electronic structure (inset) [195]. $\Delta_{1-2} = 152\,\mathrm{GHz}$ and $\Delta_{3-4} = 981\,\mathrm{GHz}$ are the measured ground and excited state orbital splittings respectively. The solid curve is a fit to four Lorentzians.

emission spectrum [195]. Similar to the negatively-charged SiV center [178, 179], the ground state of the GeV center is a spin-doublet ($S = 1/2$) [180] with double orbital degeneracy. The ground and excited orbital states of the GeV are split by spin-orbit coupling, forming a four-level system visible in its cryogenic photoluminescence (PL) spectrum [Fig. 4.1(b)] [195, 218, 320]. As demonstrated in the complementary Letter [180], this electronic structure allows one to directly control both orbital and electronic spin degrees of freedom using optical and microwave fields.

We achieve efficient coupling of individual GeV centers with single photons by incorporating them into one-dimensional waveguides [Fig. 4.2(a)] with transverse dimensions on the order of the single-atom scattering cross-section [87, 321–323]. Waveguides have a width of $480\,\mathrm{nm}$, and are nanofabricated from diamond [184, 266]. GeV centers are incorporated into devices at low density using $^{74}\,\mathrm{Ge}^+$ ion implantation ($10^9\,\mathrm{Ge}^+\,\mathrm{cm}^{-2}$)
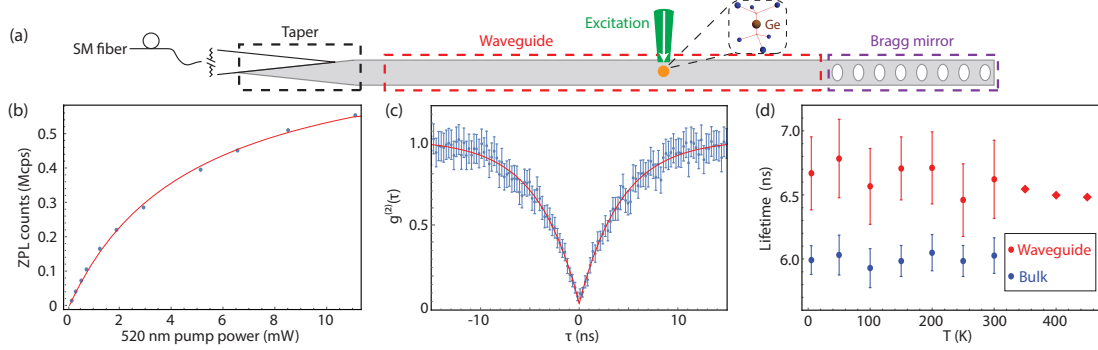
Figure 4.2: (a) Schematic of a diamond nanophotonic device. Devices are 100 m long and 480 nm wide and consist of a waveguide (red box), a partially-reflective Bragg mirror (purple box), and a taper (black box) for coupling to a tapered single-mode optical fiber. (b) Saturation response for a single GeV under continuous-wave, 520 nm excitation at $T = 300$ K, measured as a function of optical power at the microscope objective. The solid curve is a fit to a two-level saturation model (appendix A.2). (c) Intensity autocorrelation demonstrates antibunching of $g^{(2)}(0) = 0.08 \pm 0.02$. The solid curve is a single-exponential fit. (d) GeV excited state lifetime measurement at different temperatures in waveguides (red) and bulk diamond (blue). Error bars represent standard deviation of measured lifetimes of seven different emitters. For $T > 300$ K, the lifetime was measured for a single GeV in a waveguide (red diamonds).

and subsequent high temperature annealing at 1200 °C, leading to spatially-resolvable single emitters [86, 319]. We couple a single-mode tapered optical fiber to the waveguide with $\sim 50\%$ coupling efficiency by positioning it in contact with a tapered section of the diamond [87, 184, 298]. We implement this technique under a confocal microscope (described in [87] and appendix A.1), enabling both free-space and fiber-based collection of fluorescence from GeV centers.

We first measure the ZPL emission of a single GeV in a waveguide under continuous-wave 520 nm off-resonant excitation at room temperature [Fig. 4.2(b)]. Collecting via the tapered fiber, we observe a maximum single-photon detection rate of 0.56±0.02 Mcps (million counts per second) on the narrowband ZPL around 602 nm, limited by excitation

laser power. The single-photon nature of the emission is verified by antibunching of ZPL photons [Fig. 4.2(c)], measured at $I/I_{sat} \sim 0.5$ where I and I_{sat} (4.7±0.2 mW at 520 nm) are applied and saturation intensities respectively. To better understand the optical properties of the GeV, we measure its excited state lifetime at different temperatures with 532 nm pulsed excitation [Fig. 4.2(d)]. The GeV lifetime does not display significant temperature dependence up to $T = 450$ K at which local vibrational modes with $\sim$ 60 meV energy [195, 320] have finite occupation ($\bar{n} \sim 0.27$). This demonstrates that multi-phonon relaxation paths play a negligible role in determining the excited state lifetime [193], suggesting a high radiative quantum efficiency. A statistically significant difference in lifetime for waveguide (6.6±0.3 ns) and bulk (6.0±0.1 ns) emitters implies a high sensitivity to the local photonic density of states [183, 324, 325], providing further evidence of a high radiative quantum efficiency.

4.3 Optical coherence properties

To study coherence properties of single GeV centers in a waveguide, we use resonant excitation on transition 1-3 [Fig. 4.1(b)] at $T = 5$ K. We scan the frequency of the laser over the GeV resonance and record the fluorescence in the phonon-sideband (PSB) collected into the tapered fiber. This technique yields a linewidth of 73±1 MHz after 5 minutes of averaging at low excitation intensity [Fig. 4.3(a)]. The measured linewidth of a GeV in a nanophotonic structure is within a factor of 3 of the lifetime-broadened
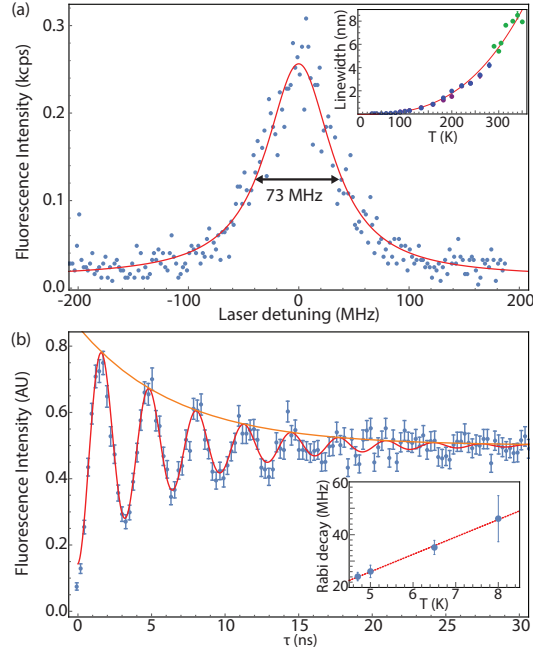
Figure 4.3: (a) Transition 1-3 linewidth of a GeV in a waveguide at $T = 5\,\mathrm{K}$, taken under resonant excitation at $I/I_{sat} \sim 0.01$. The solid curve is a Lorentzian fit. (Inset) Linewidth as a function of temperature, PL spectrum measured on a spectrometer under $520\,\mathrm{nm}$ excitation. Different colored points correspond to different emitters. The solid curve is a fit to a T^3 model (appendix A.3). (b) Optical Rabi oscillations. Fluorescence is measured on the PSB under resonant excitation. The solid curves are fits to a two-level model (appendix A.4). (Inset) The Rabi oscillation decay rate scales linearly as a function of temperature for $T < 10\,\mathrm{K}$.

limit, $\gamma_0/(2\pi) = 26 \pm 1$ MHz (appendix A.3). The measured linewidth increases with

temperature up to $T = 300\,\mathrm{K}$ [inset of Fig. 4.3(a)], due to phonon broadening that scales

as $a + b(T - T_0)^3$ [$a = 0.0 \pm 0.2$ nm, $b = (1.9 \pm 0.5) \times 10^{-7}$ nm K^{-3}, $T_0 = (-13 \pm 23)$ K]

for $T > 50\,\mathrm{K}$. The T^3 scaling suggests that optical coherence is limited by a two-phonon

orbital relaxation process for $T > 50\,\mathrm{K}$, similar to the case of the SiV [193].

In Fig. 4.3(b) we demonstrate coherent control over the GeV optical transition 1-3 by

applying a resonant 40-ns pulse and observing optical Rabi oscillations using photons

77

detected on the PSB. At high excitation power, the GeV optical transition undergoes spectral diffusion of roughly 300 MHz about the original resonance frequency. In order to mitigate spectral diffusion at high excitation intensities, we use an active feedback sequence [130, 326] that stabilizes the GeV resonance frequency while maintaining a high duty cycle on resonance (appendix A.4). This procedure enables high contrast oscillations at a Rabi frequency of 310 ± 2 MHz with a decay time of 6.59 ± 0.02 ns at 5 K, close to the excited state lifetime of 6.1 ± 0.2 ns. The decay rate of Rabi oscillations increases linearly with temperature [inset in Fig. 4.3(b)], suggesting that a single-phonon orbital relaxation process limits optical coherence at low temperatures between $T = 5$ K and $T = 10$ K, again similar to the case of the SiV [193].

4.4 SINGLE-PHOTON NONLINEARITY

These excellent optical properties allow us to observe the extinction of resonant transmission through a single GeV center in a waveguide, as demonstrated in Fig. 4.4. We focus the excitation on the Bragg mirror in order to scatter laser light into the waveguide. We collect the light transmitted through the GeV into the tapered fiber, separating the transmitted and fluorescence (PSB) components using a bandpass filter [Fig. 4.4(a)]. We find that on resonance, a single GeV reduces waveguide transmission by $18 \pm 1\%$ [Fig. 4.4(b)]. The extinction of resonant light by a single quantum emitter is an effective measure of the strength of emitter-photon interactions, and is related to the emitter-
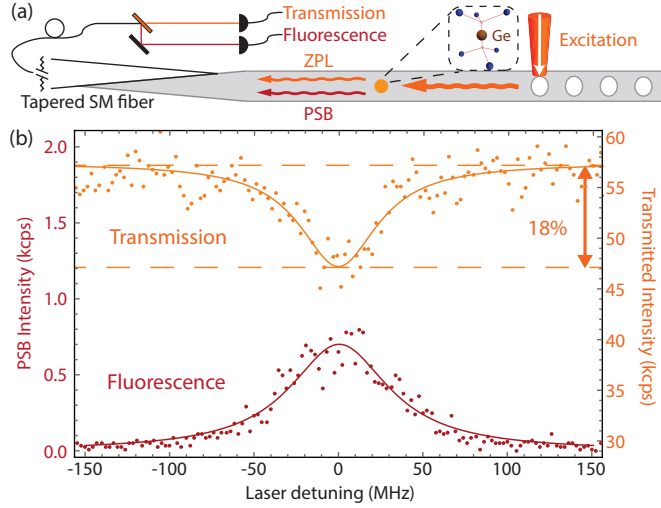
Figure 4.4: (a) Schematic for single-pass transmission measurement. The resonant excitation ($I/I_{sat} \sim 0.02$) is focused on the Bragg mirror to scatter light into the waveguide. We collect transmitted light into the tapered optical fiber and subsequently separate the transmission and fluorescence (PSB) using a bandpass filter. (b) Transmission spectrum of the GeV-waveguide device, showing $18 \pm 1\%$ extinction on resonance. Transmission is shown on top (right axis) in orange and PSB fluorescence is shown on the bottom (left axis) in red. The solid curves are Lorentzian fits.

waveguide cooperativity $C = \Gamma_{1D}/\Gamma'$, the ratio of the decay rate into the waveguide Γ_{1D}, to the sum of atomic decay rates to all other channels and dephasing Γ' [321, 322]. From the measured extinction from a single GeV, we directly obtain the GeV-waveguide cooperativity of $C \geq 0.10 \pm 0.01$ (appendix A.5). Because the GeV is a multi-level system with finite thermal population in level 2 at $T = 5\,\mathrm{K}$, the cooperativity extracted from transmission of light resonant with transition 1-3 is a lower bound and can be improved by initializing the GeV in state 1 by optical pumping [87].

The extinction of resonant light results from destructive interference between the driving field (a local oscillator) and resonance fluorescence from the GeV, and in general

79
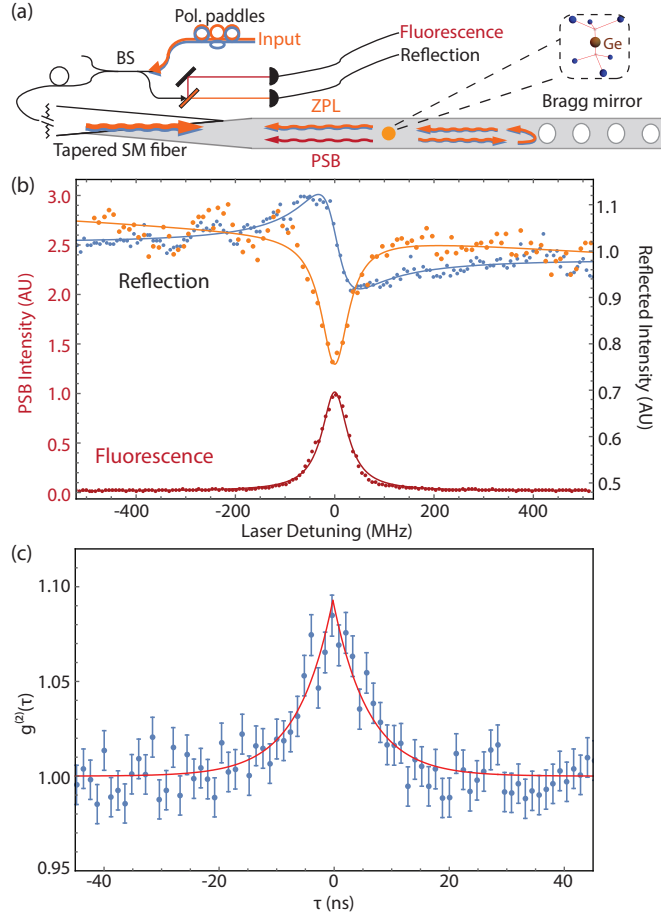
Figure 4.5: (a) Schematic for homodyne interferometer. We excite $(I/I_{sat} \sim 0.02)$ and collect through two ports of a fiber beamsplitter (BS). We use polarization paddles to change the excitation polarization. (b) Homodyne interfererometry with a single GeV. The reflected signal is shown on top (right axis) at two different input polarizations (orange and blue). PSB fluorescence is shown on the bottom (left axis) in red. The solid red curve is a Lorentzian fit and the solid blue and orange curves are fits to a phenomenological model (appendix A.6). (c) Autocorrelation measurement. We perform Hanbury Brown-Twiss interferometry on the reflected field in the case of destructive interference for single photons. We measure bunching of $g^{(2)}(0) = 1.09 \pm 0.03$ with a decay time $\tau_b = 6.2 \pm 2.7$ ns. The solid curve is an exponential fit (appendix A.6).

depends on the relative phase between them [327]. This phase can be controlled in a

homodyne measurement involving a laser field and GeV resonance fluorescence in the

80

stable nanophotonic interferometer depicted in Fig. 4.5(a). Here, the laser light is injected through one port of a fiber beamsplitter connected to the tapered fiber and collected via a second beamsplitter port. The reflected field at ZPL wavelengths consists of interference between GeV resonance fluorescence and the near-resonant excitation laser light reflected back into the fiber by the Bragg mirror, which acts as a local oscillator. We vary the relative amplitude and phase of the local oscillator with respect to the GeV resonance fluorescence by modifying the polarization of input laser light (for details, see (appendix A.6). Using this technique, we observe the change in lineshape of the output light from symmetric, corresponding to destructive interference (orange), to dispersive (blue) [Fig. 4.5(b)].

Finally, Fig. 4.5(c) demonstrates the quantum nonlinear character of the coupled GeV-waveguide system. In the homodyne measurement, the local oscillator is a weak coherent state with non-negligible single and two-photon components, whereas the GeV resonance fluorescence consists of only single photons. In the case of large single atom-photon interaction probability, a single photon in the waveguide mode can saturate the GeV center and a single GeV can alter the photon statistics of the output field [321]. As an example, in the case of destructive interference between the two fields, the output field consists preferentially of two-photon components from the local oscillator, resulting in photon bunching. We probe the photon statistics of the homodyne output field using Hanbury Brown-Twiss interferometry and observe, in the case of destructive interference, $g^{(2)}(0) = 1.09 \pm 0.03$ [Fig. 4.5(c)]. This observation provides direct evidence of device

81

nonlinearity at the level of a single photon [87, 321, 323].

4.5 CONCLUSION

We next turn to the discussion of our experimental observations. The GeV excited state lifetime [Fig. 4.2(d)] sets a theoretical upper bound on the single-photon flux from a GeV center of roughly 160 Mcps. From the saturation curve in Fig. 4.2(b), we infer that the maximum possible ZPL single-photon detection rate is 0.79 ± 0.02 Mcps in our experiment. Accounting for the ZPL branching ratio and setup inefficiencies, we estimate that per excitation, the probability of emission of a photon into the waveguide mode is at least 0.1 (appendix A.2) [183]. These measurements demonstrate that a single GeV center in a diamond waveguide is an efficient source of narrowband single photons.

The cooperativity measured in the transmission experiment (Fig. 4.4) is reduced by a combination of line-broadening mechanisms and multi-level dynamics [87, 321]. Since the branching ratios of the GeV optical transitions are not yet known, it is difficult to develop a comprehensive model of the population dynamics. Using a simple three-level model, we estimate the phonon relaxation rate using $\gamma_p = 2\gamma_{Rabi} - \frac{3}{2}\gamma_0$ [326], where γ_{Rabi} is the decay rate of Rabi oscillations, and γ_0 (γ_p) is the excited state (phonon) relaxation rate. Using the measured value of $\gamma_{Rabi}/(2\pi) = 24 \pm 0.1$ MHz from Fig. 4.3(b), we infer that phonon relaxation leads to $\gamma_p/(2\pi) = 9 \pm 2$ MHz of Markovian line-broadening at

$T = 5\,\mathrm{K}$. Therefore, the observed $73\,\mathrm{MHz}$ linewidth is limited at $5\,\mathrm{K}$ by a combination of phonon relaxation and residual spectral diffusion and can likely be reduced further at lower temperatures, as demonstrated for GeV centers in bulk diamond [180].

The present observations, together with recent advances involving SiV centers [87], demonstrate significant potential for the realization of quantum nanophotonic devices using the family of color centers in diamond with inversion symmetry [199]. The negatively-charged GeV center investigated here also has an electronic spin ($S = 1/2$) degree of freedom that can be manipulated using optical and microwave fields, making it a promising spin-photon interface [180]. As in the case of the SiV, coherence between GeV orbital and spin sublevels is limited by phonon relaxation at finite temperatures. Ongoing efforts to suppress these relaxation processes at lower temperatures should result in long spin coherence times [193].

Our observations also point to some key differences in the optical properties of GeV and SiV centers. In particular, the GeV excited state lifetime [Fig. 4.2(d)] shows negligible temperature dependence and high sensitivity to changes in the local photonic density of states, indicating the primarily radiative nature of the decay. By contrast, the excited state lifetime of the SiV has strong temperature dependence [193] and does not respond as sensitively to changes in the local photonic density of states [86]. These observations demonstrate that the GeV has a higher quantum efficiency than the SiV and directly result in the strong extinction of light in a single-pass, without the need for a slow-light waveguide or cavity. In particular, the large extinction observed from

a single GeV is competitive with single-pass transmission experiments using trapped atoms [328], ions [329], molecules [330], and quantum dots [331].

These observations open up exciting prospects for the realization of coherent quantum optical nodes with exceptionally strong atom-light coupling. In particular, the high quantum efficiency of the GeV, when integrated into diamond nanocavities with previously demonstrated quality factor-mode volume ratios $Q/V > 10^4$ [184, 266], could enable device cooperativities $C > 100$, leading to deterministic single atom-photon interactions. GeV orbital and spin coherence properties can be improved by cooling devices below $1\,\mathrm{K}$, potentially yielding long-lived quantum memories [193]. Arrays of such strongly-coupled GeV-nanophotonic devices could be used as a basis for the realization of integrated quantum optical networks with applications in quantum information science [42] and studies of many-body physics with strongly interacting photons [314].

5

Photon-mediated interactions between quantum emitters in a diamond nanocavity

5.1 Introduction

Photon-mediated interactions between quantum emitters are an important building block of quantum information systems, enabling entanglement generation and quantum logic operations involving both stationary qubits and photons [52, 188]. Progress in cavity quantum electrodynamics (QED) with trapped atoms and ions [332], superconducting qubits [333] and self-assembled quantum dots [16] has created possibilities for

engineering such interactions. In particular, coherent multi-qubit interactions mediated via a cavity have been demonstrated in the microwave domain using circuit QED [334]. Extending such interactions to the optical domain could enable key protocols in long-distance quantum communication [52, 335]. This goal is challenging due to the difficulty of achieving strong cavity coupling and individual control of multiple resonant quantum emitters. Recently, cavity-modified collective scattering has been observed in two-ion [336] and two-atom [337] systems. Signatures of cavity-mediated interactions between quantum dots have also been reported [338, 339]. However, the realization of controlled, coherent optical interactions between solid-state emitters is difficult due to inhomogeneous broadening and decoherence introduced by the solid-state environment [16, 339].

5.2 High-cooperativity nanophotonic interface to multiple SiV centers

We realize controllable optically-mediated interactions between negatively-charged silicon-vacancy (SiV) color centers coupled to a diamond photonic crystal cavity (Fig. 5.1A) [87]. SiV centers in diamond are atom-like quantum emitters featuring nearly lifetime-limited optical linewidths with low inhomogeneous broadening, both in bulk [85] and in nanostructures [86]. We integrate SiV centers into devices consisting of a one-dimensional diamond waveguide with an array of holes defining a photonic crystal cavity with qual-

86

ity factor $Q \sim 10^4$ and simulated mode volume $V \sim 0.5 \left(\frac{\lambda}{n=2.4}\right)^3$ (Fig. 5.1B) [184]. SiV centers are positioned at a single spot in these devices with $40\,\text{nm}$ precision by targeted implantation using a focused beam of ^{29}Si ions, yielding around 5 SiV centers per device [87]. The diamond waveguide is tapered and adiabatically coupled to a tapered single-mode fiber, enabling collection efficiencies from the waveguide into the fiber of more than 90% [184]. These devices are placed in a dilution refrigerator with an integrated confocal microscope (appendix B.1.1). At $85\,\text{mK}$, SiV centers are completely polarized into the orbital ground state [165]. Here, we use optical transitions between the lowest-energy orbital states in the electronic ground and excited states. The SiV electronic spin degeneracy is lifted by applying a magnetic field up to $10\,\text{kG}$ [165, 179]. The cavity resonance frequency ω_c is tuned using gas condensation (appendix B.1.4).

The coupling between SiV centers and the cavity is characterized by scanning the frequency of a laser incident on one side of the device from free space while monitoring the transmitted intensity in the collection fiber. The resulting transmission spectrum (Fig. 5.1C) reveals strong modulation of the cavity response resulting from the coupling of spectrally-resolved SiV centers to the cavity mode. For instance, two SiV centers near the cavity resonance each result in almost-full extinction of the transmission through the cavity (Fig. 5.1C), lower spectrum) [186]. In contrast, when the cavity is detuned from the SiV by several cavity linewidths (κ), the spectrum shows a narrow peak near each SiV frequency (Fig. 5.1D), corresponding to an atom-like dressed state of the SiV-cavity system with high transmission [334]. The resonance linewidth (Γ) changes by

more than an order of magnitude depending on the SiV-cavity detuning ($\Delta = \omega_c - \omega_{\mathrm{SiV}}$). This can be understood through Purcell enhancement, which predicts $\Gamma(\Delta) \approx \gamma + \frac{4g^2}{\kappa} \frac{1}{1+4\Delta^2/\kappa^2}$ where g is the single-photon Rabi frequency, κ is the cavity energy decay rate and γ is twice the decoherence rate due to free-space spontaneous emission and spectral diffusion. For the strongest-coupled SiV in the device used in Fig. 5.1, linewidths range from $\Gamma(0) = 2\pi \times 4.6$ GHz on resonance to $\Gamma(7\kappa) = 2\pi \times 0.19$ GHz $\approx \gamma$ when the cavity is far detuned. The measured $\Gamma(0)$ corresponds to an estimated lifetime of 35 ps compared to the natural SiV lifetime of 1.8 ns [87]. These measurements give cavity QED parameters $\{g, \kappa, \gamma\} = 2\pi \times \{7.3, 48, 0.19\}$ GHz, corresponding to a cooperativity (the key cavity-QED figure of merit) $C = \frac{4g^2}{\kappa\gamma} \sim 23$ (appendix B.3.2). This order-of-magnitude improvement in SiV-cavity cooperativity over previous work [87, 294] primarily results from the decreased cavity mode volume [184].

5.3 Photon-mediated interactions between two SiVs

As is evident from Fig. 5.1C, SiV centers are subject to inhomogeneous broadening, resulting predominantly from strain within the device [86, 244]. This broadening is smaller than that of other solid-state emitters compared to their lifetime-limited linewidths [16, 338, 339]. In fact, the frequencies of some SiV centers within the same devices are nearly identical. We study the cavity-mediated interaction between a pair (SiV 1 and SiV 2 in Fig. 5.1) of such nearly-resonant SiV centers (SiV-SiV detuning $\delta = 2\pi \times$
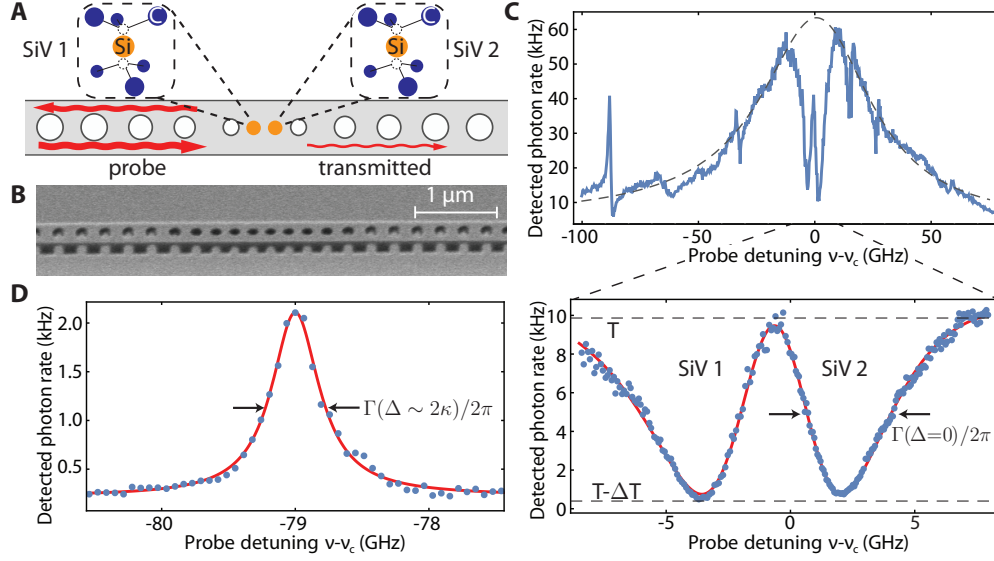
Figure 5.1: High cooperativity SiV-photon interface. **(A)** Schematic of a diamond nanocavity containing two SiV centers. **(B)** Scanning electron micrograph of a nanocavity. **(C)** Transmission spectrum of the coupled SiV-cavity system (blue). The broad Lorentzian response of an empty cavity (dashed) is modulated by cavity-coupled SiVs. Near the cavity resonance (lower panel), two SiVs each result in greater than 95% extinction in transmission and are broadened by the Purcell effect ($\Gamma(\Delta = 0) = 2\pi \times 4.6\,\text{GHz}$). **(D)** In the dispersive regime ($\Delta = 2\pi \times 79\,\text{GHz} \sim 2\kappa$), SiVs appear as narrow peaks in transmission ($\Gamma(\Delta) = 2\pi \times 0.5\,\text{GHz}$). The solid lines in (D) and the lower panel of (C) are fits to a model (appendix B.3).

0.6 GHz) coupled to the cavity in the dispersive regime, that is, with large SiV-cavity detuning ($\Delta = 2\pi \times$ 79 GHz $> \kappa$, Fig. 5.1A). To identify resonances associated with individual SiV centers, we selectively ionize either SiV into an optically-inactive charge state by applying a resonant laser at powers orders-of-magnitude higher than those used to probe the system(appendix B.4.1). This allows measurement of each of the SiV centers' spectra individually, with the other parameters (such as Δ) fixed (Fig. 5.2A, gray data).

When both SiV centers are in the optically-active charge state, the splitting between
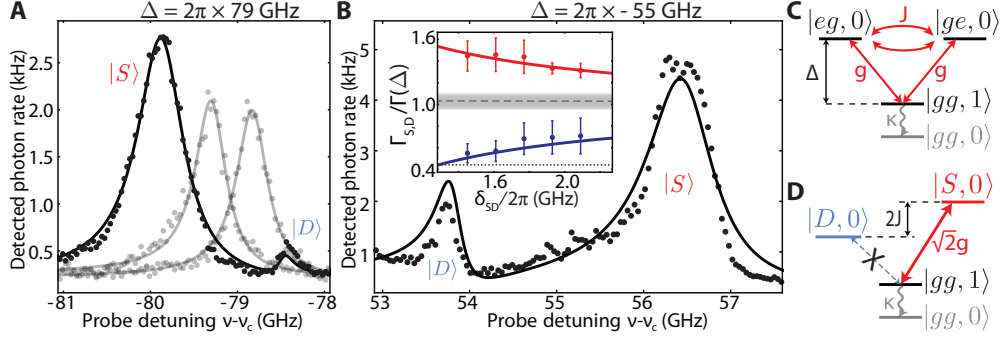
Figure 5.2: Cavity mediated SiV-SiV interactions. (A) Transmission spectrum of two nearly-resonant SiVs ($\delta = 2\pi \times 0.56$ GHz) at cavity detuning $\Delta = 2\pi \times 79$ GHz. When both SiVs are coupled to the cavity, superradiant (bright) $|S\rangle$ and subradiant (dark) $|D\rangle$ states are formed (black). Spectra of non-interacting SiVs are shown in gray. **(B)** Transmission spectrum of the same SiVs at $\Delta = 2\pi \times -55$ GHz and $\delta = 2\pi \times 2$ GHz. Inset: ratio of $|S\rangle$ (red) and $|D\rangle$ (blue) state linewidths to the single-SiV linewidth at $\Delta = 2\pi \times 79$ GHz as a function of δ_{SD}. The resonance frequencies of these SiVs slowly drift due to spectral diffusion [86], allowing us to measure the linewidths of $|S\rangle$ and $|D\rangle$ at different δ_{SD}. The gray dashed line and shaded region are the average and standard deviation of the single-SiV linewidths. The dotted line corresponds to the SiV linewidth γ without Purcell enhancement, demonstrating that $|D\rangle$ at minimum δ_{SD} is almost completely decoupled from the cavity. Solid lines in (A) and (B) are predictions based on independently-measured SiV parameters (appendix B.4). **(C)** Energy diagram of two SiV centers coupled to a cavity mode. Interaction via exchange of cavity photons at rate $J = g^2/\Delta$ leads to collective $|S\rangle$ and $|D\rangle$ eigenstates **(D)**.

the resonances increases. The new resonances (Fig. 5.2A, black data) also display different amplitudes compared with the single-SiV resonances, and are labeled as bright ($|S\rangle$) and dark ($|D\rangle$) states. The linewidths of $|S\rangle$ ($|D\rangle$) are also enhanced (suppressed) compared to those of the individual SiV centers (Fig. 5.2B, inset). At a cavity detuning of the opposite sign ($\Delta = 2\pi \times -55$ GHz), the sign of the energy splitting δ_{SD} between $|S\rangle$ and $|D\rangle$ is reversed (Fig. 5.2B). The observation that Δ affects δ_{SD} indicates that this effect arises from the cavity.

To understand these observations, we describe the system of two SiV centers coupled

to a cavity mode using the Hamiltonian [334, 340]:

$$\hat{H}/\hbar = \omega_c \hat{a}^\dagger \hat{a} + \omega_1 \hat{\sigma}_1^\dagger \hat{\sigma}_1 + \omega_2 \hat{\sigma}_2^\dagger \hat{\sigma}_2 + \hat{a}^\dagger \left(g_1 \hat{\sigma}_1 + g_2 \hat{\sigma}_2\right) + \hat{a}(g_1^* \hat{\sigma}_1^\dagger + g_2^* \hat{\sigma}_2^\dagger)$$

where ω_i is the frequency of the ith SiV center and $\hat{a}$ and $\hat{\sigma}_i$ are the cavity photon annihilation and i^{th} SiV center's electronic state lowering operators. Coherent evolution under $\hat{H}$ is modified by cavity (κ) and SiV (γ) decay and decoherence (appendix B.2). In the dispersive regime, $\hat{H}$ yields an effective Hamiltonian for two resonant ($\delta = 0$) SiV centers [334, 340]: $\hat{H}_{\text{eff}}/\hbar = J \left(\hat{\sigma}_1 \hat{\sigma}_2^\dagger + \hat{\sigma}_1^\dagger \hat{\sigma}_2\right)$ where $J = \frac{g^2}{\Delta}$ (in our system, $g_1 \approx g_2 \equiv g$). Thus, the two SiV centers undergo a flip-flop interaction at rate J mediated by the exchange of cavity photons (Fig. 5.2C). This interaction hybridizes the two SiV centers, forming collective eigenstates from the SiV ground ($|g\rangle$) and excited ($|e\rangle$) states which, for $\delta = 0$, are $|S\rangle = \frac{1}{\sqrt{2}}(|eg\rangle + |ge\rangle)$ and $|D\rangle = \frac{1}{\sqrt{2}}(|eg\rangle - |ge\rangle)$ and are split by $2J$ (Fig. 5.2D) [334]. The symmetric superradiant state $|S\rangle$ has an enhanced coupling to the cavity of $\sqrt{2}g$ (making it "bright" in transmission) and an energy shift of $2J = 2\frac{g^2}{\Delta}$, whereas the antisymmetric combination $|D\rangle$ is completely decoupled from the cavity ("dark" in transmission) and has zero energy shift [334, 339]. As δ/J increases, $|D\rangle$ becomes visible and the individual SiV eigenstates are eventually recovered. The energy shift of state $|S\rangle$ is away from the cavity resonance, explaining the reversed energy difference δ_{SD} upon changing the sign of Δ (Fig. 5.2B). By comparing the data in Fig. 5.2 to theory accounting for finite δ (Fig. 5.2, solid curves), the SiV-SiV interaction

strength $J = 2\pi \times 0.6\,\text{GHz}$ is extracted. The splitting δ_{SD} (which is at least $2J$) is larger than the measured linewidths (for a single SiV, $\Gamma(\Delta = 79\,\text{GHz}) = 2\pi \times 0.4\,\text{GHz}$), allowing these states to be spectrally resolved.

5.4 Cavity interface to SiV electronic spin degree of freedom

Next, the SiV center's long-lived electronic spin degree of freedom [179] is used to control the SiV-cavity transmission and two-SiV interaction. We apply a magnetic field to lift the degeneracy of the spin sublevels in the ground (spin states $|\uparrow\rangle$ and $|\downarrow\rangle$) and optically-excited ($|\uparrow'\rangle$ and $|\downarrow'\rangle$) states. The Zeeman shifts are different for each orbital state and depend on the magnitude and orientation of the field with respect to the SiV center's symmetry axis, yielding spectrally-distinguishable spin-selective optical transitions at frequencies $\omega_\uparrow$ and $\omega_\downarrow$ (Fig. 5.3A). In general, the splitting between these frequencies is maximized for off-axis magnetic fields [179]. Any off-axis magnetic field also prevents the optical transitions from being perfectly cycling, allowing the SiV center to be initialized into $|\uparrow\rangle$ by pumping at $\omega_\downarrow$ and vice versa [252, 253]. Coupling spin-selective transitions to the cavity mode enables high-contrast spin-dependent modulation of the cavity transmission [341].

We demonstrate this effect using an SiV center in the dispersive regime ($\Delta \sim 2\kappa$). Here, the optical transition linewidth is narrow, allowing us to resolve these transitions in a $9\,\text{kG}$ field well-aligned with the SiV center's symmetry axis where the transitions

92
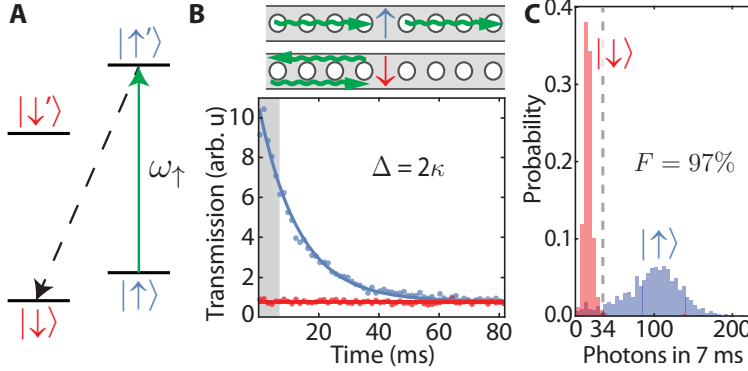
Figure 5.3: Cavity-assisted spin initialization and readout. (A) Simplified level structure of the SiV in a magnetic field. An optical transition at frequency $\omega_\uparrow$ (green arrow) initializes the SiV spin into $|\downarrow\rangle$ by optical pumping via a spin-flipping transition (dashed line). **(B)** Spin-dependent optical switching in the dispersive regime. State $|\downarrow\rangle$ is not coupled to the probe at frequency $\omega_\uparrow$ which is therefore reflected (red). Initialization into $|\uparrow\rangle$ results in transmission of the probe field (blue). **(C)** Photon number distributions for transmission in the dispersive regime for initialization into $|\uparrow\rangle$ (blue) and $|\downarrow\rangle$ (red) are well-resolved (mean $n_\uparrow = 96$, $n_\downarrow = 16$) in a 7 ms window (gray region in **(C)**), demonstrating single-shot spin-state readout with 97% fidelity.

are highly cycling (branching fraction $\sim 1 - 10^{-4}$) [165]. The spin is initialized in $|\downarrow\rangle$ or $|\uparrow\rangle$ via optical pumping and the system is probed in transmission. When the spin is in $|\downarrow\rangle$, the interaction with the probe at $\omega_\uparrow$ is negligible and the probe is reflected by the detuned cavity (Fig. 5.3B, red curve). When the spin is in $|\uparrow\rangle$, single photons at frequency $\omega_\uparrow$ are transmitted via the SiV-like dressed state (blue curve) for a time (12 ms) determined by the cyclicity of the transition [165]. The distribution of photon counts detected in a 7 ms window when the spin is initialized in $|\uparrow\rangle$ (red) versus $|\downarrow\rangle$ (blue) (Fig. 5.3D) are well-resolved, allowing the spin state to be determined in a single shot with 97% fidelity (appendix B.5). We also perform this experiment in the resonant-cavity regime and observe spin-dependent transmission switching with 80% contrast

(appendix B.6).

5.5   Spin-dependent photon-mediated interaction between two SiV centers

The combination of spin control, high-cooperativity coupling and a small inhomogeneous distribution of SiVs enables controllable optically-mediated interactions between multiple SiV centers. We focus on two SiV centers (SiV 1 and SiV 2 in Fig. 5.1) in the dispersive regime ($\Delta = 2\pi \times 109\,\mathrm{GHz}$) with $\{g_1 \approx g_2, \kappa, \gamma_1 \approx \gamma_2\} = 2\pi \times \{7.3, 39, 0.5\}\,\mathrm{GHz}$ ($C \approx 11$) and an initial two-SiV detuning $\delta = 2\pi \times 5\,\mathrm{GHz}$ (appendix B.7). We sweep the magnitude of a magnetic field oriented almost orthogonal to the SiV symmetry axis and tune transitions $|\uparrow_1\rangle \to |\uparrow_1'\rangle$ and $|\downarrow_2\rangle \to |\downarrow_2'\rangle$ (which have opposite Zeeman shifts) in and out of resonance (Fig. 5.3A). At each magnetic field, a continuous field Ω_1 or Ω_2 is used to optically pump either SiV 1 or SiV 2 into the spin state resonant with a weak probe field Ω_p measuring the transmission spectrum of the system, thus enabling control measurements where only one spin is addressed by Ω_p at a time (Fig. 5.4B, gray). The single-spin transmission spectra at each field are summed to form a composite spectrum of the two-SiV system (Fig. 5.4C), which displays an energy level crossing of the two SiV transitions characteristic of non-interacting systems.

Measurements were then made in the interacting regime by preparing the spins into $|\uparrow_1\rangle |\downarrow_2\rangle$ by simultaneously applying Ω_1 and Ω_2. The two-SiV transmission spectrum

94
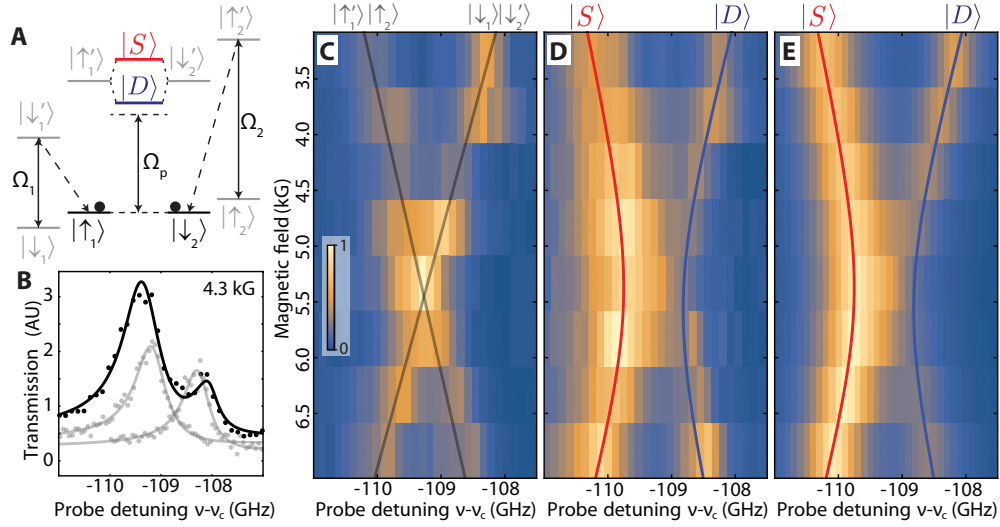
Figure 5.4: Deterministic control of photon-mediated interactions via SiV spin states. (A) Energy diagram of two SiV centers in a magnetic field. The spins can be initialized in $|\uparrow_1\rangle |\downarrow_2\rangle$ with Ω_1 and Ω_2 and probed by sweeping Ω_p. When $\Omega_1(\Omega_2)$ is off, Ω_p is sufficiently strong to ensure initialization in $|\downarrow_1\rangle$ ($|\uparrow_2\rangle$) as it sweeps across the relevant SiV 1 (2) transition. **(B)** Spin-dependent transmission spectra at $4.3\,\text{kG}$. Gray: Spectra of single SiVs in the noninteracting combinations of spin states. Black: Spectrum of two interacting SiVs, demonstrating formation of $|S\rangle$ and $|D\rangle$. **(C)** Composite spectrum of the system at different two-SiV detunings, demonstrating a level crossing characteristic of non-interacting systems. The solid lines are the fitted single-SiV energies of $|\uparrow_1'\rangle |\uparrow_2\rangle$ and $|\downarrow_1\rangle |\downarrow_2'\rangle$ as a function of magnetic field. **(D)** An avoided crossing is visible in cavity transmission when the spins are prepared in the interacting state $|\uparrow_1\rangle |\downarrow_2\rangle$. **(E)** Predicted spectrum. The red and blue lines in (D) and (E) are predicted energies of $|S\rangle$ and $|D\rangle$(appendix B.7).

demonstrates the formation of superradiant and subradiant states (Fig. 5.4B, black) that exist only for this combination of spin states. Spectra as a function of applied magnetic field (Fig. 5.4D) demonstrate an avoided crossing arising from spin-dependent interactions between the two SiV centers [334]. These experimental observations agree with an analysis based on a complete microscopic model of the system (appendix B.2) including independently-measured SiV-cavity parameters (Fig. 5.4E). For these exper-

95

iments (Fig. 5.4), an active preselection sequence is used to stabilize the SiV spectral positions (appendix B.7.1). Similar observations were reproduced in a separate device on the same chip(appendix B.7.5).

5.6 Conclusion

This optically-mediated interaction between quantum emitters could be used to realize key quantum information protocols, including cavity-assisted entanglement generation [188, 335, 340], efficient Bell-state measurements [186, 342] and robust gates between emitters in distant cavities [52]. To implement these schemes with high fidelity, qubits should be encoded in long-lived electronic spin states. Recent work has demonstrated that the SiV spin can be used as a long-lived quantum memory [165] that can be manipulated with microwave [165, 254] and optical fields [343]. Although the present work relies on magnetic field tuning of the SiV frequencies, recently-developed techniques including strain [244] or Raman tuning [87] can be applied to individual devices, allowing our approach to be extended to the chip scale. The infidelity associated with many deterministic cavity-mediated operations scales as $C^{-1/2}$ [342] or C^{-1} [335] and can therefore be mitigated with improved cooperativity. While the cooperativity $C \sim 20$ achieved here is among the largest demonstrated in the optical domain, it can be improved by at least an order of magnitude by increasing the cavity Q/V and by reducing sources of spectral diffusion limiting γ (appendix B.4.2). Alternatively, the cooperativ-

ity could be enhanced by using different quantum emitters, such as the GeV [75] or SnV [197] centers in diamond with higher quantum efficiencies [75]. Near-unity fidelities can also be achieved with existing cooperativities using heralded schemes where errors can be suppressed via error detection with an auxiliary qubit [342]. Furthermore, our system could be used to efficiently generate non-classical states of light [344], which are useful in, for example, measurement-based quantum computing. On-chip integration and GHz-level bandwidths make our system well-suited for exploring potential applications in quantum networking, including the implementation of efficient quantum repeaters [342] and distributed quantum computing.

6

An integrated diamond nanophotonic

quantum network node

6.1 INTRODUCTION

The realization of quantum networks is one of the central challenges in quantum science
and engineering with potential applications to long-distance communication, non-local
sensing and metrology, and distributed quantum computing [42, 61, 63, 68, 80]. Practi-
cal realizations of such networks require individual nodes with the ability to process and
store quantum information in multi-qubit registers with long coherence times, and to ef-
ficiently interface these registers with optical photons. Cavity quantum electrodynamics
(QED) is a promising approach to enhance interactions between atomic quantum memo-

ries and photons [16, 94, 332, 345, 346]. Trapped atoms in optical cavities are one of the most developed cavity QED platforms for quantum processing, and have demonstrated gates between atoms and photons [347] as well as interactions between multiple qubits mediated by the optical cavity [348]. While these experiments have demonstrated all of the individual components needed for a quantum network, combining them to realize a full-featured node remains an outstanding challenge.

Nanophotonic cavity QED systems with solid-state emitters are appealing candidates for realizing quantum nodes as they can be interfaced with on-chip electronic control and photonic routing, making them suitable for integration into large-scale networks [16, 349]. Numerous advances towards the development of such nodes have been made recently. Self-assembled quantum dots in GaAs have been efficiently interfaced with nanophotonic structures, enabling a fast, on-chip spin-photon interface [16, 17]. Nitrogen-vacancy color centers in diamond (NVs) have demonstrated multi-qubit quantum processors with coherence times approaching one minute [19], and have been used to implement quantum error correction [350] and teleportation [163]. Despite this rapid progress, functional nodes combining all the necessary ingredients in a single device have not yet been realized. For example, quantum memory times in quantum dots are limited to a few s by the dense bath of surrounding nuclear spins [312]. Conversely, an efficient nanophotonic interface to NVs remains elusive, in part due to the degradation of their optical properties inside nanostructures arising from electrical noise induced by the fabrication [82, 238].
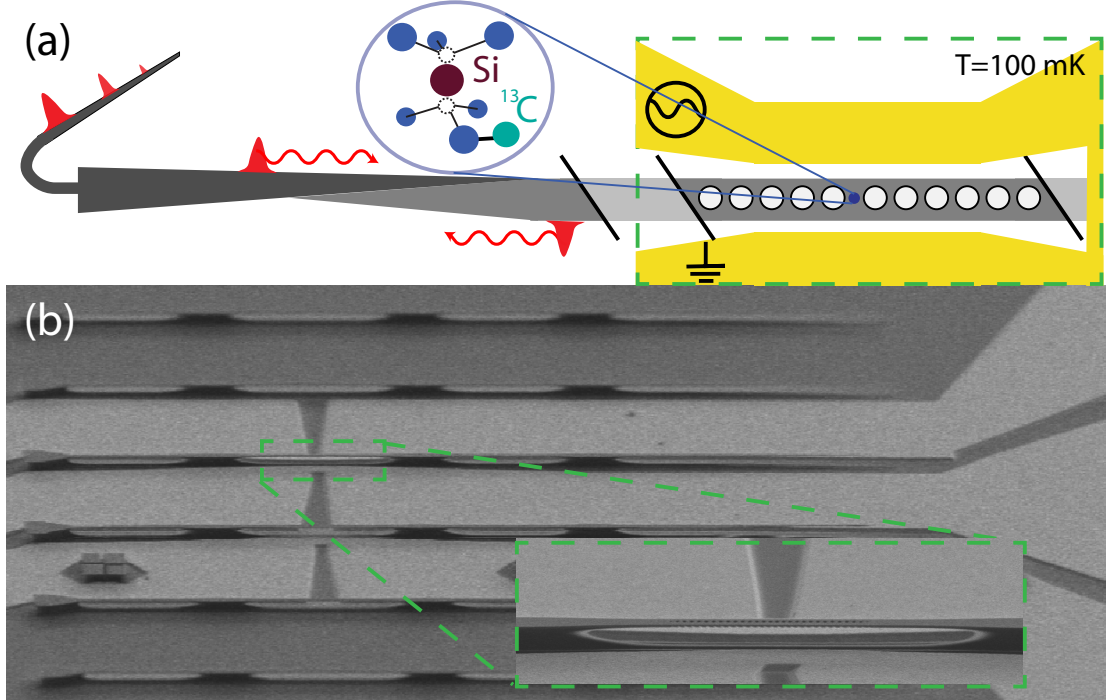
Figure 6.1: (a) Schematic of a SiV-nanophotonic quantum register. A diamond nanostructure with embedded SiV centers and ancillary ^{13}C nuclei are coupled via a waveguide to a fiber network. Spins are controlled by an on-chip microwave CPW at 0.1 K. (b) Scanning electron micrograph of several devices. The gold CPW is designed to localize microwave fields around the cavity center (green inset).

In this Letter, we demonstrate an integrated network node combining all key ingredients required for a scalable quantum network. This is achieved by coupling a negatively charged silicon-vacancy color-center (SiV) to a diamond nanophotonic cavity and a nearby nuclear spin, illustrated schematically in Fig. 6.1(a). The SiV is an optically active point defect in the diamond lattice [178, 179]. Its D_{3d} inversion symmetry results in a vanishing electric dipole moment of the ground and excited states, rendering optical transitions insensitive to electric field noise typically present in nanofabricated structures

[85, 87]. We enhance interactions between SiVs and optical photons by incorporating them into nanocavities (chapter 7), which are critically coupled to on-chip waveguides. Itinerant photons in a fiber network are adiabatically transferred to this waveguide, allowing for the collection of reflected photons with efficiencies exceeding 90% [184]. After an initial optical characterization of the devices, a shorted, gold coplanar waveguide (CPW) is deposited in close proximity to a small subset of cavities [Fig. 6.1 (b), inset] (chapter 7.2). This enables coherent microwave manipulation of the SiV ground state spin in a cryogenic environment ($T < 0.1\,\mathrm{K}$), where phonon-mediated dephasing and relaxation processes are mitigated [165, 193, 254].

In what follows, we characterize these devices in the context of the three key ingredients of a quantum network node: (i) an efficient spin-photon interface, (ii) a long-lived quantum memory, and (iii) access to multiple interacting qubits.

6.2 Deterministic optical interface to highly coherent spin states

The efficient spin-photon interface is enabled by coupling to a diamond nanophotonic cavity. For critically-coupled cavities, the presence of an SiV modulates the bare nanocavity reflection spectrum with the strength of this modulation parametrized by the cavity cooperativity $C = 4g^2/(\kappa\Gamma) \sim 38$ (with the single photon Rabi frequency, cavity, and atomic energy decay rate $\{g, \kappa, \gamma\} = 2\pi \times \{5.6, 33, 0.1\}$ GHz). For $C > 1$, we expect high-contrast modulation for a small detuning (Δ) between the cavity and the
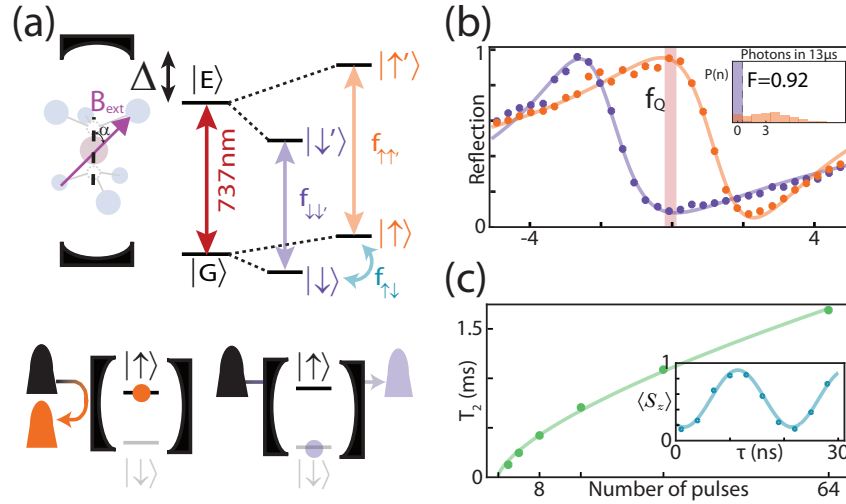
Figure 6.2: (a) Level structure of SiV spin-cavity system. The SiV optical transition at 737 nm is coupled to the nanocavity with detuning Δ. Spin conserving transitions (purple, orange) are split by an external magnetic field ($\mathbf{B}_{\text{ext}}$), at an angle α with respect to the SiV symmetry axis. Photons are only reflected by the cavity when the SiV is in state $|\uparrow\rangle$. Microwave fields at frequency $f_{\uparrow\downarrow}$ coherently drive the qubit states. (b) Spin-dependent reflection spectrum for $B_{ext} = 0.19$T, $\alpha \approx \pi/2$ at $\Delta = 0.25\kappa$. Probing at the point of maximum contrast (f_Q) results in high-fidelity spin-photon correlations and single-shot readout (inset, $F = 0.92$). (c) SiV spin coherence time $T_2(N = 64) > 1.5$ ms with dynamical decoupling. (inset) Fast microwave Rabi driving of the SiV spin.

SiV resonance near 737nm. An external field B_{ext} lifts the degeneracy of the SiV spin-$\frac{1}{2}$ sub-levels, creating spin-dependent reflection: photons at the frequency of maximum contrast (f_Q) are reflected from the cavity only when the SiV is in a specific spin state ([Fig. 6.2(a)], $|\uparrow\rangle$). In previous works, spin readout of the SiV was performed with B_{ext} parallel to the SiV symmetry axis, where the spin-conserving transitions are highly cycling [165]. The high collection efficiency into a tapered fiber allows for fast single-shot readout of the SiV even in a misaligned field [Fig. 6.2(b)], which is necessary for the nuclear spin control described below. We observe a readout fidelity of $F = 0.92$ in 13 s

even when only a few (~ 10) photons are scattered.

We next demonstrate that the SiV spin in a nanocavity is a suitable quantum memory. Microwave pulses at $f_{\uparrow\downarrow} = 6.7\,\text{GHz}$ coherently manipulate the SiV spin qubit. The resulting Rabi oscillations, which can be driven in excess of $80\,\text{MHz}$ while maintaining acceptable sample temperatures (chapter 7.7.1), are shown in the inset of Fig. 6.2(c). These rotations are used to probe the coherence properties of the spin via dynamical decoupling sequences [Fig. 6.2(c)] [351, 352]. We measure the coherence time of the SiV inside the nanocavity to be $T_2 > 1.5\,\text{ms}$ and scale with the number of decoupling pulses as $T_2 \propto N^{2/3}$. The coherence scaling observed here differs from that observed in bulk diamond [165], and is similar to NVs near surfaces [353]. This suggests that SiV memory in nanostructures is limited by an electron spin bath, for example residing near the surface of the nanostructure or resulting from implantation-induced damage (chapter 7.8).

6.3 Spin-photon entanglement

We now combine the efficient spin-photon interface and control over the SiV spin state to demonstrate heralded storage of photonic qubit states in the spin-memory, a key feature of a network node [346]. Fig. 6.3(a) outlines the experimental scheme, where photonic qubits are prepared using time-bin encoding and mapped onto the SiV spin. In our experiments, the SiV is first initialized into a superposition state $|\rightarrow\rangle \propto |\uparrow\rangle + |\downarrow\rangle$

103

by optical pumping followed by a microwave $\frac{\pi}{2}$-pulse. A pair of weak coherent pulses separated by $\delta t = 30\,\text{ns}$ at frequency f_Q are then sent to the cavity. The single photon sub-space corresponds to an incoming qubit state $|\Psi_i\rangle \propto \beta_e\,|e\rangle + \beta_l\,|l\rangle$, where $|e\rangle$ ($|l\rangle$) denotes the presence of a photon in the early (late) time-bin. As a photon can only be reflected from the device if the SiV is in state $|\uparrow\rangle$ [Fig. 6.2(a)], particular components of the initial product state can be effectively "carved out" [348]. We invert the SiV spin with a π-pulse between the arrival of the two time bins at the cavity, such that a photon detection event indicates that the final state has no $|e\uparrow\rangle$ or $|l\downarrow\rangle$ component. This leaves the system in the final spin-photon entangled state $|\Psi_f\rangle \propto \beta_e\,|e\downarrow\rangle + \beta_l\,|l\uparrow\rangle$. The reflected photon enters a time-delay interferometer, where one arm passes through
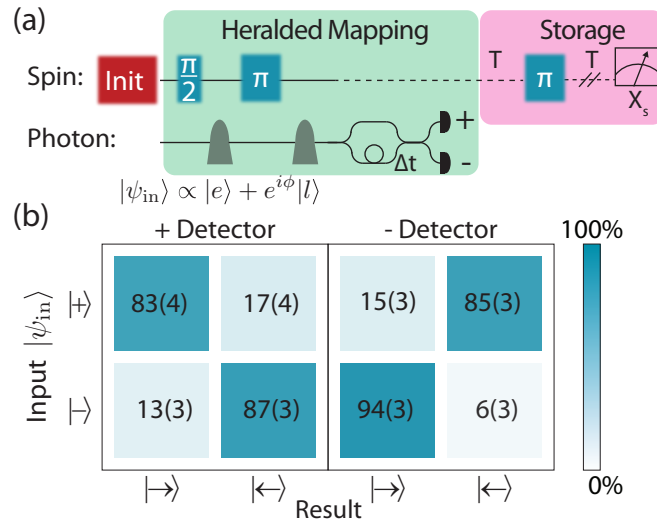
Figure 6.3: (a) Schematic for heralded photon storage. After photonic qubit is reflected off the cavity, an X measurement on the photon heralds successful state transfer which is stored for $2T = 20\,\text{s}$. (b) Spin-photon storage fidelity. The state $|\pm\rangle = |\downarrow\rangle \pm |\uparrow\rangle$ is mapped onto the SiV, with average fidelity $\mathcal{F} = 87(6)\%$.

a delay line of length δt, allowing the two time-bins to interfere and erase which-time-bin information. As can be seen by expressing the final state in the corresponding photon basis:

$$|\psi\rangle_f \propto |+\rangle \left(\beta_e |\downarrow\rangle + \beta_l |\uparrow\rangle\right) + |-\rangle \left(\beta_e |\downarrow\rangle - \beta_l |\uparrow\rangle\right), \tag{6.1}$$

a detection event on either the '+' or '−' arm of the interferometer represents a measurement in the X-basis ($|\pm\rangle \propto |e\rangle \pm |l\rangle$), effectively teleporting the initial photonic state onto the electron (up to a known local rotation). We experimentally verify generation of the entangled state $|\psi\rangle_f$ for input states $|\psi\rangle_i = |\pm\rangle$ by measuring spin-photon correlations (chapter 7.9), and use it to extract a teleportation fidelity of 0.92(6).

After detection of the heralding photon, we store the teleported photonic states (initially prepared in $\{|+\rangle$ or $|-\rangle\}$) in spin memory for 20 s by applying an additional decoupling π-pulse on the SiV spin. The overall fidelity of teleportation and storage is $F = 0.87(6)$ after corrected for readout errors [Fig. 6.3(b)]. The quantum storage time can be extended by additional decoupling sequences [Fig. 6.2(c)], enabling entanglement distribution up to a T_2-limited range of 500 km.

6.4 Coherent control of a multi-qubit register

In order to extend this range and to enable more generic quantum communication protocols, we next demonstrate a two-qubit register based on the cavity coupled SiV electronic spin and a nearby ^{13}C nuclear memory. The ^{13}C isotope of carbon is a spin-

$\frac{1}{2}$ nucleus which has $\sim 1\%$ natural abundance in diamond, and is known to exhibit exceptional coherence times [19]. While direct radio-frequency manipulation of nuclear spins is impractical due to heating concerns (chapter 7.10.4), control over ^{13}C spins can be achieved by adapting electron mediated techniques developed for nitrogen vacancy (NV) centers [231, 247, 246, 354]. The physical principle of the SiV-^{13}C interaction is depicted in Fig. 6.4(a). The SiV generates a spin-dependent magnetic field $\mathbf{B}_{\mathrm{SiV}}$ at the position of the ^{13}C, which is located a few lattice sites away. This is described by a hyperfine interaction Hamiltonian:

$$\hat{H}_{\mathrm{HF}} = \hbar A_\parallel \frac{\hat{S}_z}{2}\frac{\hat{I}_z}{2} + \hbar A_\perp \frac{\hat{S}_z}{2}\frac{\hat{I}_x}{2} \tag{6.2}$$

where $\hat{S}_{z,x}$ ($\hat{I}_{z,x}$) are the Pauli operators for the electron (nuclear) spin, and $A_{\parallel,\perp}$ are the coupling parameters related to the parallel and perpendicular components of B_{SiV} with respect to the bias field B_{ext} [247, 354, 355]. Hyperfine interactions manifest themselves in spin-echo measurements as periodic resonances [247], shown in Fig. 6.4(b) for an XY8-2 decoupling sequence $\pi/2 - (\tau - \pi - \tau)^{16} - \pi/2$, where τ is the free evolution time. The coherence envelope for this sequence is $T_2(N = 16) = 603\,\mathrm{s}$ [Fig. 6.4(b), upper panel].

For weakly coupled ^{13}C ($A_\perp \ll \omega_l$, and $A_\parallel \ll \omega_l$, as used in this letter), the positions of the resonances [247]

$$\tau_k \approx \frac{2k+1}{2\omega_l}\left(1 - \frac{1}{2}\left(\frac{A_\perp}{2\omega_l}\right)^2\right), \tag{6.3}$$

106

where ω_l is the larmor frequancy of a bare ^{13}C, are insensitive to specific ^{13}C hyperfine parameters at first order, rendering them indistinguishable at early times ($\tau_k \ll 4\,\text{s}$, [Fig. 6.4(b), red inset]). Individual ^{13}C can be isolated at longer times [247] (chapter 7.10), and are used to engineer gates between a single ^{13}C and the SiV [Fig. 6.4(b), green inset].[1] The fundamental two-qubit gate associated with such interaction is a conditional $\pm\pi/2$ rotation of the ^{13}C-spin around the X axis ($R_x^{\pm\pi/2}$), which is a maximally entangling gate. Together with unconditional rotations of the nuclear spin (which are also generated via dynamical decoupling sequences), and MW rotations on the SiV, these sequences form a universal set of gates for the register [247].

We characterize the ^{13}C via Ramsey spectroscopy [Fig. 6.4(c)]. The nuclear spin is initialized and read out via the optically addressable SiV spin by transferring population between the SiV and ^{13}C (chapter 7.10). Depending on the SiV state before the Ramsey sequence, we observe oscillations of the nuclear spin at its eigenfrequencies $\omega_{\uparrow,\downarrow}^2 = \left(\omega_l \pm A_\parallel/2\right)^2 + (A_\perp/2)^2)$, allowing us to determine the hyperfine parameters $\{\omega_l, A_\parallel, A_\perp\} = 2\pi\{2.0, 0.70, -0.35\}\text{MHz}$. This coherence persists for $T_2^* > 2\,\text{ms}$ (chapter 7.7), and can be further extended to $T_2 > 0.2\,\text{s}$ by applying a single dynamical decoupling π-pulse on the nucleus, demonstrating the exceptional memory of the ^{13}C nuclear spin [Fig. 6.4(d)].

We benchmark the two-qubit register by demonstrating an SiV-controlled X-gate

---

[1]This is in contrast with the NV center, which is a spin-1 system and therefore features a linear shift of the resonances with coupling strength $A_\parallel$ in the $S = \{0, -1\}$ sub-system.
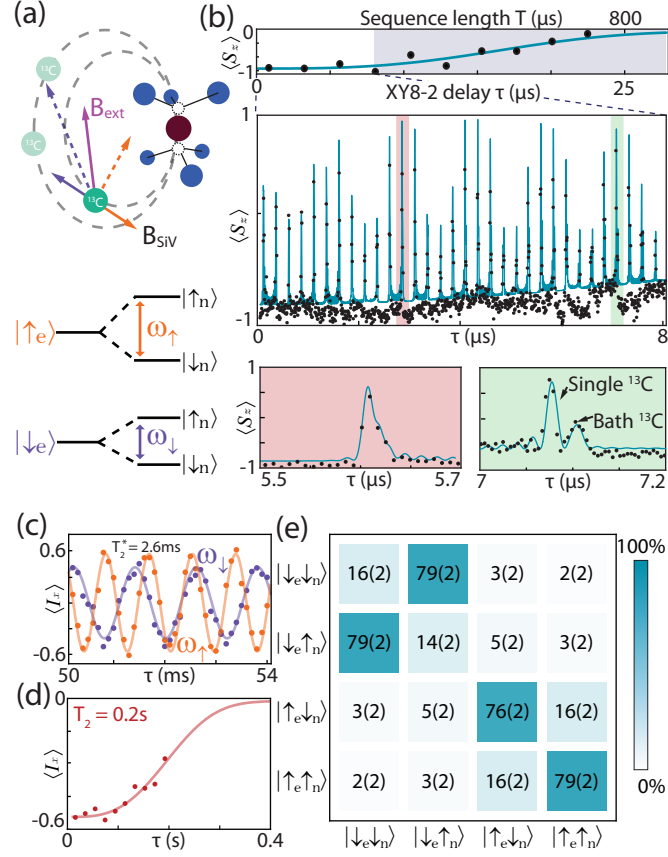
Figure 6.4: (a) Schematic of an SiV coupled to nearby ^{13}C nuclear spins. Orange (purple) vectors are conditional fields when the SiV is in state $|\uparrow\rangle$ ($|\downarrow\rangle$). (b) XY8-2 spin-echo. (Top) envelope for spin-echo shows a $T_2(N = 16) = 603$ s. XY8-2 at early times (Center) exhibits collapses in signal due to interaction with nuclear spins. Single ^{13}C cannot be identified at early times (red inset), but separate from the bath at long times (green inset). (c) Ramsey measurement on the ^{13}C nuclear spin. The nuclear spin precesses at a different Larmor frequency depending on whether the SiV is prepared in $|\uparrow\rangle$ (orange) or $|\downarrow\rangle$ (purple). Coherent oscillations persist for $T_2^* > 2$ ms (chapter 7.10). (d) Spin echo on ^{13}C, revealing $T_2 > 0.2$ s (e) Reconstructed amplitudes for a CNOT gate transfer matrix.

(CNOT) on the ^{13}C-spin by combining a $R_x^{\pm\pi/2}$ with an unconditional nuclear $\pi/2$ rotation (chapter 7.10.3). This gate results in a spin flip of the ^{13}C only if the SiV spin is in the state $|\downarrow\rangle$ [Fig. 6.4(e)]. We use this gate to prepare a Bell state by initializing the

register in $|\downarrow\downarrow\rangle$, and applying a $\pi/2$-rotation gate on the SiV spin followed by a CNOT gate. Correlation measurements yield a concurrence of $\mathcal{C} = 0.22(9)$ corresponding to a Bell state fidelity of $F = 0.59(4)$ after correcting for readout errors (appendix C.4.3).

6.5 CONCLUSION

Our experiments demonstrate the first prototype of a nanophotonic quantum network node combining all necessary ingredients in a single physical system. We emphasize that both spin-photon and spin-spin experiments are performed in the same device under identical conditions (cavity detuning and bias field), thereby providing simultaneous demonstration of all key requirements for a network node.

The main limitation on the demonstrated fidelities are related to the specific ^{13}C in the proximity of the SiV, requiring an unfavorable alignment of the external magnetic field in order to isolate a single ^{13}C. Specifically, the fidelity of two-qubit gates is limited by residual coupling to bath nuclei, SiV decoherence during the gate operations, and under/over-rotations of the nuclear spin arising from the granularity of spin-echo sequences. To reduce these errors, fine-tuned adaptive pulse sequences can be used to enhance sensitivity to specific nearby ^{13}C, and tailor the rotation angle and axis of rotation [356, 357]. Alternatively, replacing gold with superconducting microwave coplanar waveguides will significantly reduce ohmic heating, and allow direct radio-frequency control of nuclear spins. These improvements could also enable the realization of a deter-

ministic two-qubit register based on ^{29}SiV, which contains both electronic and nuclear spins in a single defect [252] (chapter 7).

The fidelity of the heralded photon storage is limited primarily by single shot readout and imperfect critical coupling of the cavity. The improvements of the nuclear spin control mentioned above would allow for working in an external magnetic field aligned to the SiV axis, which would improve readout fidelity from $F \sim 0.90$ (reported here) to 0.99 [76] (chapter 7). The impedance mismatch of the cavity used in this experiment also gives rise to residual reflections which are not entangled with the SiV. Over-coupled cavities enable the use of a SiV spin-dependent phase flip for reflected photons, improving both the fidelity and success probability of spin-photon interactions.

In conjunction with recent advances in controlling emitter inhomogeneity via electromechanical tuning [245], these techniques should allow for chip-scale fabrication of quantum network nodes, laying the groundwork for the realization of scalable quantum repeater [46, 80] architectures. The ability to store quantum information in highly coherent ^{13}C nuclei, as well as the opportunity to extend these results to other group-IV color-centers, may open up the possibility of operating such nodes at temperatures > 1 K [88, 89, 167, 180]. Finally, the efficient quantum network node demonstrated in this Letter could enable generation of multi-dimensional cluster states of many photons, which could facilitate realization of novel, ultra-fast one-way quantum communication architectures [143].

7

Operating principles of an

SiV-nanocavity quantum network node

7.1 Introduction

Quantum networks have the potential to enable a plethora of new technologies including secure communication, enhanced metrology, and distributed quantum computing [42, 61, 63, 68, 80]. Such networks require nodes which perform quantum processing on a small register of interconnected qubits with long coherence times. Distant nodes are connected by efficiently interfacing qubits with optical photons that can be coupled into an optical fiber [Fig. 7.1(a)].

The prevailing strategy for engineering an efficient, coherent optical interface is that

111
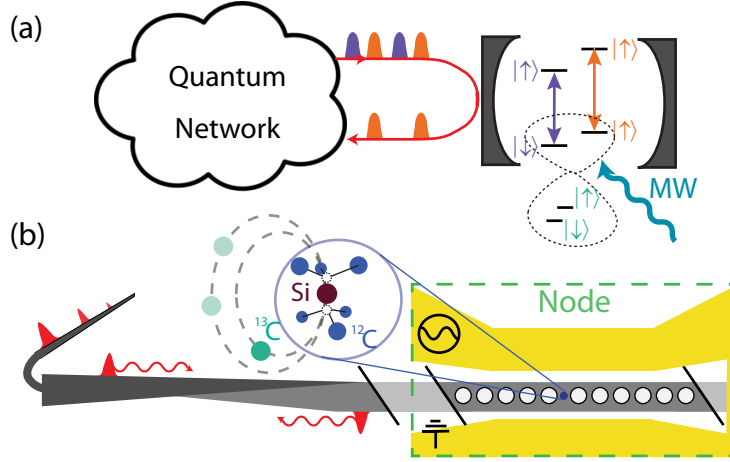
Figure 7.1: (a) Schematic of a quantum network. Nodes consisting of several qubits are coupled together via an optical interface. (b) A quantum network node based on the SiV. SiV centers and ancilla ^{13}C are incorporated into a nanophotonic device and addressed with a coupled fiber and microwave coplanar waveguide.

of cavity quantum electrodynamics (QED), which enhances the interactions between atomic quantum memories and photons [16, 94, 305, 332, 346]. Nanophotonic cavity QED systems are particularly appealing, as the tight confinement of light inside optical nanostructures enables strong, high-bandwidth qubit-photon interactions [87, 323, 339]. In practice, nanophotonic devices also have a number of technological advantages over macroscopic optical cavities, as they can be fabricated en-masse and interfaced with on-chip electronics and photonics, making them suitable for scaling up to large-scale networks [16, 349]. While strong interactions between single qubits and optical photons have been demonstrated in a number of cavity QED platforms [16, 17, 163, 231, 332, 350], no single realization currently meets all of the requirements of a quantum network node.

112

Simultaneously achieving high-fidelity, coherent control of multiple long-lived qubits inside of a photonic structure is a major outstanding challenge.

Recent work has established the silicon-vacancy color-center in diamond (SiV) as a promising candidate for quantum networking applications [76, 165, 167, 343, 244, 358]. The SiV is an optically active point defect in the diamond lattice [178, 179]. Its D_{3d} inversion symmetry results in a vanishing permanent electric dipole moment of the ground and excited states, rendering the transition insensitive to electric field noise typically present in nanostructures [86]. Recent work has independently shown that SiV centers in nanostructures display strong interactions with single photons [76] and that SiV centers at temperatures below $100\,\mathrm{mK}$ (achievable in dilution refrigerators) exhibit long coherence times [165, 193]. While these results indicate the promising potential of the SiV center for future quantum network nodes, significant technical challenges must be overcome in order to combine these ingredients.

In this paper, we outline the practical considerations and approaches needed to build a quantum network node with SiV centers in nanophotonic diamond cavities coupled to ancillary nuclear spins [Fig. 7.1(b)] (chapter 6). Section 7.2 describes recent improvements to the fabrication techniques used to create and incorporate SiV centers into high-quality factor, critically-coupled nanophotonic cavities with an efficient fiber-optical interface. Section 7.3 describes the millikelvin experimental apparatus and several common experimental protocols. Section 7.4 describes the SiV level structure and electronic transitions, illusutrating the interplay of strain and magnetic field in enabling

113

both coherent control of– and a photonic interface for– SiV spins. Sections 7.6, 7.7 and 7.8 outline experimental implementations of optical and microwave control of SiV centers, and use this control to create electron-photon Bell states with high fidelity in section 7.9. Section 7.10 introduces techniques for coupling to additional qubits consisting of naturally occuring ^{13}C in diamond. We describe our method for initializing and reading out these nuclear spins via the SiV, coherent control of ^{13}C with microwave and radio-frequency driving, probe the coherence of these nuclei, and finally entangle the SiV with a nearby ^{13}C and demonstrate electron-nuclear Bell states.

7.2 Nanophotonic device fabrication

7.2.1 Device design

The devices used in these experiments integrate nanophotonic cavities, implanted SiV centers, and microwave coplanar waveguides onto a single diamond chip. Here we present the fabrication process used to realize such devices.

Typically, high-quality photonic crystal resonators are fabricated from 2-D membranes, which tightly confine light due to total internal reflection off of material boundaries. Difficulties in growing high-purity, single-crystal diamond films on non-diamond substrates are one of the key challenges to fabricating such resonators in diamond [359]. As a result, nanophotonic diamond structures must be etched out of bulk diamond, which requires non-traditional etching techniques. In particular, two methods

114
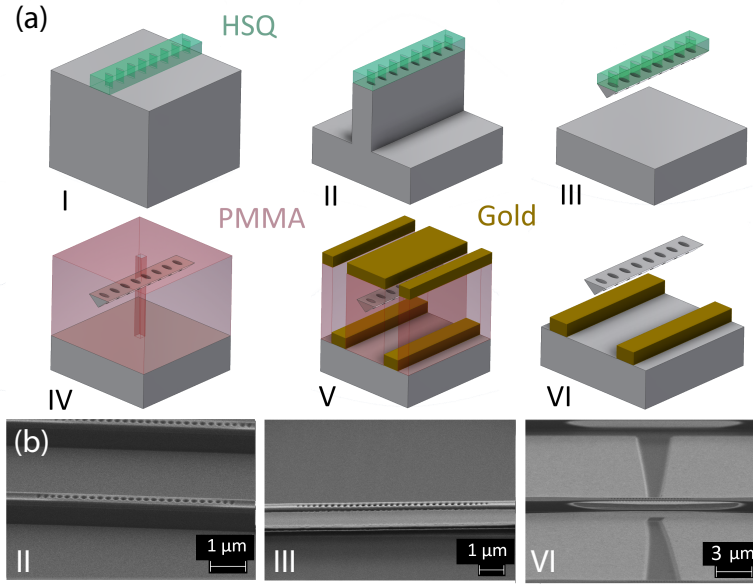
Figure 7.2: (a) Schematic of the nanofabricataion process used to produce devices. I: Titanium-HSQ mask is patterned using EBL. II: Pattern is transferred onto diamond using top down O_2 RIE. III: Angled IBE is used to separate structures from substrate. IV: Devices are covered in PMMA and implantation aperatures are formed using EBL. Device are then cleaned, implanted, and annealed. V: PMMA is used in a litoff procedure to pattern gold microwave striplines. VI: Final devices are cleaned and prepared for experiment. (b) Scanning electron micrographs corresponding to steps II, III, and VI in the fabricaton procedure.

have emerged for creating freestanding diamond nanostructures: Isotropic undercutting [268, 292] and angled ion-beam etching (IBE) [289]. In this work, we use the latter technique, resulting in freestanding, triangular-cross-section waveguides.

Preliminary design of the nanophotic structures are described in appendix C.1, and are optimized to maximize atom-photon interaction while maintaining high waveguide coupling. To take advantage of the scalable nature of nanofabrication, these optimized devices are patterned in sets of roughly 100 with slightly modified fabrication parameters. The overall scale of all photonic crystal cavity parameters are varied between

different devices on the same diamond chip to compensate for fabrication errors (which lead to unexpected variations in the resonator frequency and quality-factor). Due to these errors, roughly one in six cavities are suitable for SiV experiments. Fortunately, hundreds of devices are made in a single fabrication run, ensuring that every run yields many usable devices.

The diamond waveguide region (as opposed to the photonic crystal cavity region [Appendix. C.1]) has two distinguishing features. First, thin support structures are placed periodically along the waveguide and are used to suspend the structures above the substrate. These supports are portions of the waveguide which are adiabatically tapered to be $\sim 30\%$ wider than the rest of the waveguide, and take longer to etch away during the angled etch process. By terminating the etch after normal waveguide regions are fully etched through, these wide sections become $\sim 10\,\mathrm{nm}$ thick supports which tether the waveguide structures to the substrate while minimizing scattered loss from guided modes. Second, one end of the waveguide structure is adiabatically tapered into free-space [184]. These tapers are formed by a linear taper of the waveguide down to less than $50\,\mathrm{nm}$ wide over a $10\,\mathrm{m}$ length. This tapered region can be coupled to a similarly tapered optical fiber, allowing structures to efficiently interface with a fiber network (chapter 7.3). This tapered end of the waveguide is the most fragile portion of the structure, and can break after repeated fiber coupling attempts. This is often what limits the total measurement lifetime of a device.

The number of devices (and thus the relative yield of the fabrication process) is limited

116

by the maximum packing density on the diamond chip. This is primarily limited by the need to accommodate 10 m wide microwave coplanar waveguides (CPWs) between devices, which are patterned directly onto the diamond surface to efficiently control SiV spins using microwaves. Simulations (Sonnet Inc) of prospective design geometries ensure that the CPW is impedance matched with our 50 feed lines, which minimizes scattered power from the waveguides. Tapers in the CPW near the center of the cavity regions concentrate current and increase the amplitude of the microwave field near the SiVs, and CPWs are terminated with a short in order to ensure a magnetic field maximum along the device.

7.2.2 DEVICE FABRICATION

Fabrication of the diamond structures proceeds as described in ref. [184] with the notable modification that the angled etch is conducted not with a Faraday cage loaded inside a reactive ion etching chamber, but instead with an IBE. The Faraday cage technique offered the benefit of simplicity and accessibility—requiring only that the reactive ion etching chamber in question was large enough to accommodate the cage structure—but suffered from large fluctuations in etch rate across the surface of the sample, as well as between different fabrication runs, due to imperfections in the Faraday cage mesh. These irregularities could be partially compensated for by repeatedly repositioning and rotating the cage with respect to sample during the etch, but this process proved to be laborious and imprecise. Instead, IBE offers collimated beams of ions several cm in

117

diameter, leading to almost uniform etch rates across the several mm diamond chip. This technique allowed for consistent fabrication of cavities with $Q > 10^4$, $V < 0.6[\lambda/(n = 2.4)]^3$, and resonances within $\sim 10\,\mathrm{nm}$ of SiV optical frequencies.

Once the diamond cavities are fabricated [Fig. 7.2(a I-III)], SiV centers must be incorporated. To ensure the best possible atom-photon interaction rate (chapter 7.6), SiVs should be positioned at the cavity mode maximum. Ideally, this requires implantation accuracy of better than $50\,\mathrm{nm}$ in all 3 dimensions due to the small mode volume ($\sim 0.5[\lambda/(n = 2.4)]^3$) of the cavities used. In the past, implantation of silicon ions (which form SiV centers following a high-temperature anneal) was done using focused ion-beam implantation, but this technique required specialized tools and lacked the accuracy necessary for maximally efficient mode coupling [87]. Instead, we adapt the standard masked implantation technique and use commercial foundaries for ion implantation.

For the implantation process, we repeatedly spin and bake MMA EL11 and PMMA C4 (Microchem) to cover the nanophotonic cavities completely with polymer resist. We then spin-coat a conductive surface layer of Espacer (Showa Denko). An E-beam lithography (EBL) tool then aligns with large markers underneath the polymer layer, allowing it to expose an area surrounding smaller, high-resolution alignment markers on the diamond. The exposed regions are developed in a 1:3 mixture of MIBK:IPA. Espacer is again spin-coated, and a second EBL write can be done, aligned to the high-resolution markers. Based on these alignment markers, holes of less than $65\,\mathrm{nm}$ diameter (limited

118

by the resolution of PMMA resist) are patterned onto the center of the photonic crystal cavity which, after subsequent development, act as narrow apertures to the diamond surface [Fig. 7.2(a IV)]. The rest of the diamond surface is still covered in sufficiently thick PMMA to prevent ions from reaching masked portions of the device. Diamonds are then sent to a commercial foundry (Innovion) where they are implanted with silicon ions at the appropriate energy and dose [Fig. 7.2 (b)]. Annealing in a home-built vacuum furnace at $\sim 1400\,\mathrm{K}$ converts these implanted ions into SiV centers [86, 360].

CPWs are fabricated using a liftoff process similar to that used to create masked implantation windows. The most notable difference is an additional oxygen plasma descum after development to remove PMMA residue from the surface. Following development, a $10\,\mathrm{nm}$ titanium film serves as an adhesion layer for a $250\,\mathrm{nm}$ thick gold CPW [Fig. 7.2 (a V)]. Liftoff is performed in heated Remover PG (Microchem) [Fig. 7.2 (a VI)]. The metal thicknesses used here are chosen to improve adhesion of the gold, as well as prevent absorption of cavity photons by the metallic CPW. We observe that the cavity quality factor significantly degrades with gold films $> 300\,\mathrm{nm}$. Due to ohmic heating, which can degrade the coherence properties of SiV spins (chapter 7.7, the length of the CPW is constrained to address a maximum of roughly 6 devices.

Future improvements in diamond device performance will be predicated on improvements of the fabrication technology. Device quality factors are currently limited by deviations in device cross section caused by imperfect selectivity of the HSQ hard mask to oxygen etching. Replacing this mask with a sufficiently smooth metal mask could

result in improved etch selectivity and device performance. Isotropic undercut etching could also lead to improved control over device cross sections and facilitate more sophisticated device geometries [292, 361] at the cost of reduced control over isotropically etched surface roughness. Various techniques exist for the formation of smaller implantation apertures [209, 362], but these techniques are difficult to use in conjunction with implantation into completed nanophotonic devices. Finally, the use of superconducting striplines could reduce heating, which would enable the CPW to potentially address all devices on the diamond chip and allow for faster driving of SiV spin and nuclear transitions (chapter 7.7, 7.10).

7.3 Experimental Setup

Experiments are performed in a home-built photonic-probe setup inside of a dilution refrigerator (DR, BlueFors BF-LD250) [Fig. 7.3(a)]. The diamond substrate is mounted to a gold-plated copper sample holder via indium soldering below the mixing chamber in the bore of a (6,1,1) T superconducting vector magnet (American Magnetics Inc.) anchored to the 4 K stage. A thermal link between the device and the mixing chamber plate is provided by gold-plated copper bars, as well as oxygen-free copper braids (Copper Braid Products), ensuring maximal thermal conductivity between the mixing chamber plate and the sample, which reaches a base temperature of roughly 60 mK. We address single nanophotonic devices via a tapered optical fiber, which can be coupled
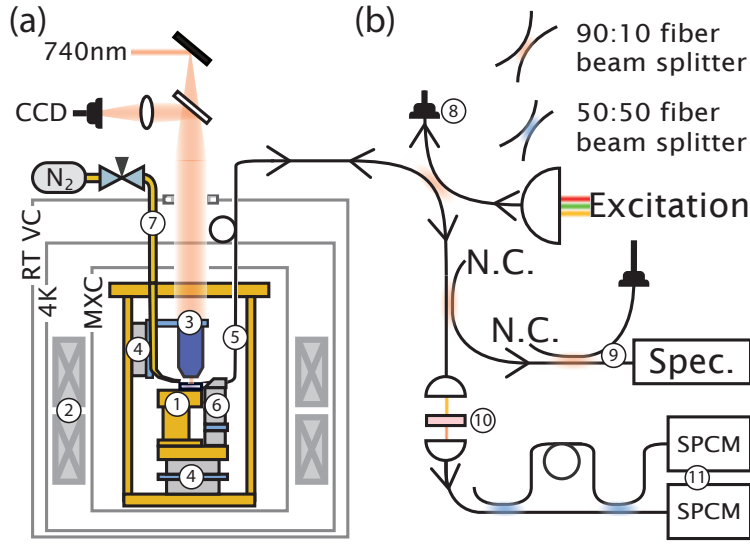
Figure 7.3: (a) Experiment schematic. Devices ① are mounted in the bore of a SC magnet ② inside of a dilution refrigerator, and imaged with wide-field imaging ③ and piezo steppers ④. Devices are addressed with a tapered optical fiber ⑤ positioned using a second set of piezo steppers ⑥. Cavities are tuned using a nitrogen ⑦. (b) Fiber network used to probe devices. Excitation light is monitored ⑧ and sent to the device. Collected light is monitored ⑨ and filtered ⑩ then sent to one or several SPCMs ⑪. N.C. indicates no connection.

in-situ with collection efficiencies exceeding 90% [184]. The tapered fiber is mounted to a 3-axis piezo stepper (ANPx101, ANPz101), and imaged in free-space by an $8f$ wide-field scanning confocal microscope which focuses onto a cryo-compatible objective (Attocube LT-APO-VISIR). This setup allows for coupling to several cavities during a single cooldown.

Once coupled, the cavity resonance is red-shifted via nitrogen gas condensation [76]. A copper tube is weakly thermalized with the $4\,\mathrm{K}$ plate of the DR and can be heated above $80\,\mathrm{K}$ in order to flow N_2 gas onto the devices. This gas condenses onto the photonic crystal, modifying its refractive index and red-shifting the cavity resonance.

121

When the copper tube is not heated, it thermalizes to 4 K, reducing the blackbody load on the sample and preventing undesired gas from leaking into the vacuum chamber.

After red-tuning all devices in this way, each cavity can be individually blue-tuned by illuminating the device with a $\sim$100 W broadband laser via the tapered fiber, locally heating the device and evaporating nitrogen. This laser-tuning can be performed very slowly to set the cavity resonance with a few GHz. The cavity tuning range exceeds 10 nm without significantly degrading the cavity quality factor, and is remarkably stable inside the DR, with no observable drift over several months of measurements.

In previous work [76], SiVs were probed in transmission via the free-space confocal microscope focused onto a notch opposing the tapered fiber. Mechanical vibrations arising from the DR pulse tube ($\sim$1 m pointing error at the sample position) result in significant fluctuations in power and polarization of incoupled light. In this work, we demonstrate a fully integrated solution by utilizing the same tapered fiber to both probe the device and collect reflected photons. This approach stabilizes the excitation path and improves the efficiency of the atom-photon interface, allowing for deterministic interactions with single itinerant photons. High-contrast reflection measurements are enabled by the high-cooperativity, critically-coupled atom-cavity system. Resonant light is sent via the fiber network [Fig. 7.3(b)] and reflected off of the target device. We pick off a small fraction ($\sim$ 10%) of this signal and use it to monitor the wide-band reflection spectrum on a spectrometer (Horiba iHR-550) as well as calibrate the coupling efficiency to the nanocavity. The remaining reflection is then routed either directly to

122

a single-photon counting module (SPCM, Excelitas SPCM-NIR), or into a time-delay interferometer for use in spin-photon experiments (chapter 7.9).

7.4 Optimal strain regimes for SiV spin-photon experiments

Similar to other solid state emitters [159, 363], the SiV is sensitive to local inhomogeneity in the host crystal. In the case of the SiV, which has D_{3d} symmetry, the dominant perturbation is crystal strain. In this section, we describe the effects of strain on the SiV spin and optical properties, and how they can enable efficient microwave and optical control of SiV centers inside nanostructures.

The SiV electronic structure is comprised of spin-orbit eigenstates split by spin-orbit interactions. Optical transitions connect the ground state manifold (LB, UB) and excited state manifold (LB', UB') [Fig. 7.4(a)]. In a DR, phonon absorption $LB \to UB$ (and $LB' \to UB'$) is supressed, resulting in thermal polarization into LB.

We consider the ground state SiV Hamiltonian with spin-orbit and strain interactions,

in the combined orbital and spin basis $\{|e_y \uparrow\rangle, |e_y \downarrow\rangle, |e_x \uparrow\rangle, |e_x \downarrow\rangle\}$ [179, 244]

$$\mathcal{H}_{SiV} = \mathcal{H}_{SO} + \mathcal{H}_{\text{strain}} \tag{7.1}$$

$$= \begin{pmatrix} \alpha - \beta & 0 & \gamma - i\lambda & 0 \\ 0 & \alpha - \beta & 0 & \gamma + i\lambda \\ \gamma + i\lambda & 0 & \alpha + \beta & 0 \\ 0 & \gamma - i\lambda & 0 & \alpha + \beta \end{pmatrix} \tag{7.2}$$

where α corresponds to axial strain, β and γ correspond to transverse strain, and λ is the strength of spin-orbit interaction. Diagonalizing this reveals the orbital character of the lower branch:

$$LB \propto \begin{cases} |e_x \uparrow\rangle - \frac{1+\sqrt{1+(\gamma/\beta)^2+(\lambda/\beta)^2}}{\gamma/\beta - i\lambda/\beta} |e_y \uparrow\rangle \\ |e_x \downarrow\rangle - \frac{1-\sqrt{1+(\gamma/\beta)^2+(\lambda/\beta)^2}}{\gamma/\beta - i\lambda/\beta} |e_y \downarrow\rangle \end{cases} \tag{7.3}$$

We investigate these electronic levels in the context of the SiV as a spin-photon interface.

124

7.5 Effects of strain on the SiV qubit states

In the limit of zero crystal strain, the orbital factors simplify to the canonical form [179]

$$LB = \begin{cases} |e_+ \downarrow\rangle \\[2mm] |e_- \uparrow\rangle \end{cases} \tag{7.4}$$

In this regime, the spin-qubit has orthogonal electronic orbital and spin components. As result, one would need to simultaneously drive an orbital and spin flip to manipulate the qubit, which is forbidden for direct microwave driving alone. Thus, in the low strain regime, two-photon optical transitions between the qubit states, already demonstrated at millikelvin temperatures in [343], are likely necessary to realize a SiV spin qubit.

In the high strain limit ($\sqrt{\beta^2 + \gamma^2} \gg \lambda$), these orbitals become

$$LB = \begin{cases} (\cos(\theta/2)|e_x\rangle - \sin(\theta/2)|e_y\rangle) \otimes |\downarrow\rangle \\[2mm] (\cos(\theta/2)|e_x\rangle - \sin(\theta/2)|e_y\rangle) \otimes |\uparrow\rangle \end{cases} \tag{7.5}$$

where $\tan(\theta) = \frac{\beta}{\gamma}$. In this regime, the ground state orbital components are identical, and the qubit states can be described by the electronic spin degree of freedom only. As such, the magnetic dipole transition between the qubit states is now allowed and can be efficiently driven with microwaves.

In addition to determining the efficiency of qubit transitions, the spin-orbit nature of

the SiV qubit states also determines its susceptibility to external fields. In an externally applied magnetic field, LB splits due to magnetic moments associated with both spin– and orbital– angular momenta. This splitting is parameterized by an effective g-tensor which, for a fixed angle between the external field and the SiV symmetry axis, can be simplified to an effective g-factor: $\mu \, g \, B_{\text{ext}}/h = f_{\uparrow\downarrow}$. In the limit of large strain, the orbital component of the two LB wavefunctions converge, and g trends towards that of a free electron (g = 2). As a result, the qubit states behave akin to a free-electron in the high strain regime, and there is no dependence of g on external field angle or small perturbations in crystal strain.

While it is difficult to probe β or γ directly, they relate to the energy difference between UB and LB via $\Delta_{\text{gs}} = 2\sqrt{\beta_{\text{gs}}^2 + \gamma_{\text{gs}}^2 + \lambda_{\text{gs}}^2}$ [Fig. 7.4(a)]. From this, we extract $\sqrt{\beta^2 + \gamma^2}$, given the known value of $\lambda_{\text{gs}} =$46 GHz [178, 179, 252]. Numerically diagonalizing the SiV Hamiltonian using the extracted values for β and γ closely matches the measured ground state splitting, both as a function of applied field magnitude and angle [Fig. 7.4(b)].

7.5.1 Effects of strain on the SiV spin-photon interface

Strain also plays a crucial role in determining the optical interface to the SiV spin qubit. The treatment shown above can be repeated for the excited states, with the caveat that the parameters β, γ, and λ are different in the excited state manifold as compared to the ground state manifold [244]. These differences give rise to a different

126
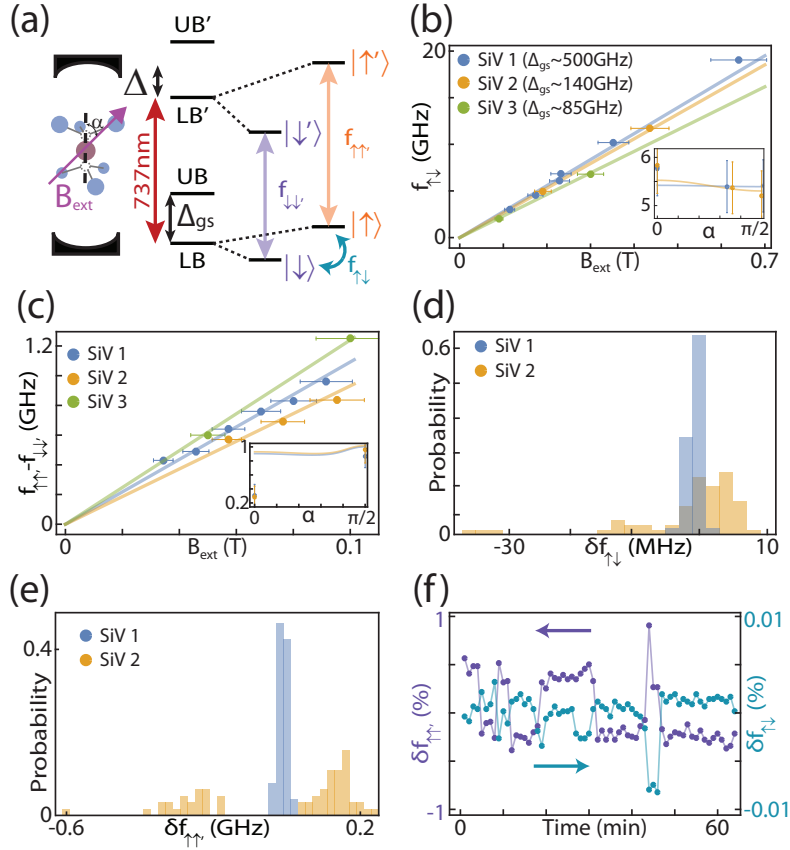
Figure 7.4: (a) SiV level diagram. Optical transitions $f_{\uparrow\uparrow'}, f_{\downarrow\downarrow'} \sim 737\,\mathrm{nm}$ are coupled to a nanophotonic cavity with mean detuning Δ. Microwaves at frequency $f_{\uparrow\downarrow}$ drive rotations in the lower branch (LB). (b) Qubit frequency $f_{\uparrow\downarrow}$ for differently strained emitters. Modeled splitting for ground state g-factors $g_{gs1} = 1.99, g_{gs2} = 1.89, g_{gs3} = 1.65$ (solid lines) based on independent measurements of Δ_{gs}. (inset) Angle dependence of $f_{\uparrow\downarrow}$. Solid lines are predictions using the same model parameters. (c) Optical splitting $f_{\uparrow\uparrow'} - f_{\downarrow\downarrow'}$. Fits extract excited state g-factors $g_{es1} = 1.97, g_{es2} = 1.83, g_{es3} = 1.62$ (solid lines). (inset) Angle dependence of $f_{\uparrow\uparrow'} - f_{\downarrow\downarrow'}$. (d) Histogram of MW transition frequency for two different emitters. (e) Histogram of Optical transition frequency for two different emitters. (f) Simultaneous measurement of $f_{\uparrow\downarrow}$ and $f_{\uparrow\uparrow'}$ reveals correlations between optical and microwave spectral diffusion for emitter 2.

g-factor in the excited state (g_{es}). If the strain is much larger than both $\lambda_{gs} = 46\,\mathrm{GHz}$ and $\lambda_{es} = 255\,\mathrm{GHz}$, then $g_{gs} \approx g_{es} \approx 2$. In this case, the two spin-cycling transition frequencies $f_{\uparrow\uparrow'}$ and $f_{\downarrow\downarrow'}$ are identical, and the only spin-selective optical transitions are

the dipole-forbidden spin-flipping transitions $f_{\uparrow\downarrow'}$ and $f_{\downarrow\uparrow'}$.

Under more moderate strain, the difference $\delta g = |g_{es} - g_{gs}|$ splits the degenerate optical transitions $f_{\uparrow\uparrow'}$ and $f_{\downarrow\downarrow'}$, making them spin-selective as well. Due to differences in the anisotropic g-tensor in the ground and excited states, δg depends on the orientation of the magnetic field as well, and is minimized in the case of a $\langle 111 \rangle$-aligned field [Fig 7.4(c), inset]. In such an external field aligned with the SiV symmetry axis, optical transitions become highly spin-conserving [165], allowing many photons to scatter without altering the SiV spin state. This high cyclicity enables high-fidelity single-shot readout of the spin state (chapter 6.2), even without high collection efficiencies [165]. This makes working with the spin-cycling transitions highly desirable, at the expense of a reduced ability to resolve spin-selective transitions for a given field magnitude. The need to resolve individual transitions suggests an optimal strain regime where $\sqrt{\beta_{gs}^2 + \gamma_{gs}^2} \gg \lambda_{gs}$, while $\sqrt{\beta_{es}^2 + \gamma_{es}^2} \lesssim \lambda_{es}$, where one can independently address $f_{\uparrow\uparrow'}$ and $f_{\downarrow\downarrow'}$ [Fig. 7.4(c)].

7.5.2 Effects of strain on SiV stability

Despite the SiV's symmetry-protected optical transitions, spectral diffusion of the SiV has been observed in many experiments [86, 194] (but still much smaller compared to emitters without inversion symmetry, for example, nitrogen-vacancy centers [82, 364]). While the exact nature of this diffusion has not been studied in depth, it is often attributed to the second-order Stark effect or strain fluctuations, both of which affect the energies of SiV orbital wavefunctions. In this paper, we also observe significant

128

fluctuations of the spin qubit frequency.

As can be seen in reference [244], for an appropriately low static strain value, fluctuating strain can give rise to fluctuations in the g-tensor of the ground state, causing spectral diffusion of the qubit frequency $f_{\uparrow\downarrow}$ [Fig. 7.4(d)]. Since g_{gs} asymptotically approaches 2 as the static strain increases [244], the qubit susceptibility to this fluctuating strain is reduced in the case of highly strained SiV centers, resulting in a more stable qubit.

While spectral diffusion of the optical transition should not saturate in the same way as diffusion of the microwave transition, we observe qualitatively different spectral diffusion properties for different emitters [Fig. 7.4(e) and Fig. 7.5]. SiV 1 ($\Delta_{gs} = 500\,\mathrm{GHz}$) displays slow drift of the optical line which is stable to $<100\,\mathrm{MHz}$ over many minutes. We do not observe significant fluctuations ($> 500\,\mathrm{kHz}$) of the microwave transition for this SiV. On the other hand, SiV 2 ($\Delta_{gs} = 140\,\mathrm{GHz}$) drifts over a wider range, and also exhibits abrupt jumps between several discrete frequencies.

We simultaneously record the optical transition and qubit frequency for SiV 2 and observe correlations between the two frequencies [Fig. 7.4(f)], indicating that they could arise from the same environmental perturbation. In Appendix C.2, we calculate the qubit and optical transition frequencies using the strain Hamiltonian (eq. 7.2) and find that both correlations and absolute amplitudes of spectral diffusion can simultaneously be explained by strain fluctuations on the order of 1% [Appendix C.2].

In this work we rely on static strain, likely resulting from damage induced by ion

129
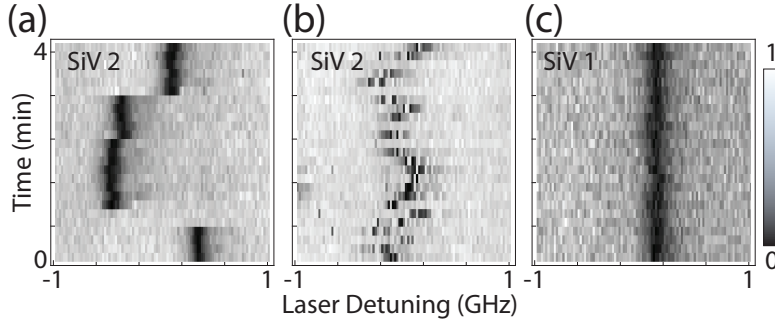
Figure 7.5: (a) Spectral diffusion of SiV 2. We observe slow spectral wandering as well as spectral jumps. (b) Applying a short green repumping pulse before every measurement significantly speeds up the timescale for spectral diffusion. (c) Spectral diffusion of SiV 1 in nanostructures. Line is stable to below 100 MHz over many minutes. Scale bar indicates normalized SiV reflection signal.

implantation and nanofabrication, and select for spectrally stable SiVs with appropriate strain profiles. This is characterized by first measuring Δ_{gs} in zero magnetic field at 4 K by exciting the optical transition $LB \rightarrow LB'$ and measuring emission from the $LB' \rightarrow UB$ on a spectrometer. We use this to screen for SiVs with $\Delta_{gs} >100\,\text{GHz}$ to ensure efficient MW driving of the spin qubit. We further apply a static external magnetic field and measure spectral stability properties as well as $f_{\uparrow\uparrow'} - f_{\downarrow\downarrow'}$ to guarantee a good spin-photon interface. We measured ~ 10 candidate emitters, and found 4 which satisfy all of the necessary criteria for spin-photon experiments.

7.5.3 MITIGATING SPECTRAL DIFFUSION

In order to couple SiV centers to a quantum network, electronic transitions must be stabilized with respect to a probe laser. We note that such spectral diffusion is a

universal challenge for solid-state quantum systems [82, 365, 366]. In the case of the SiV center, spectral diffusion can be seen explicitly in figure 7.5(a), where the optical transition frequency can either drift slowly (central region), or undergo large spectral jumps. As this diffusion can be larger than the SiV linewidth, any given instance of an experiment could have the probe laser completely detuned from the atomic transition, resulting in a failed experiment.

There are several possible solutions to mitigate this spectral diffusion. First, exploiting a high-cooperativity interface, one can Purcell-broaden the optical linewidth (chapter 7.6) to exceed the spectral diffusion [87]. Second, a high collection efficiency can be used to read out the optical position faster than the spectral diffusion. The frequency can then be probabilistically stabilized by applying a short laser pulse at $520\,\mathrm{nm}$ which dramatically speeds up the timescale of spectral diffusion, [75, 76] [Fig. 7.5(b)]. Alternatively this signal could be used to actively stabilize the line using strain-tuning [245]. From the observations in figure 7.4(f), this technique should mitigate spectral diffusion of both the optical and spin transitions. Strain tuning also offers the capability to control the DC strain value, which has important effects on qubit properties as discussed previously, and enables tuning multiple SiV centers to a common network operation frequency. As such, this tunability will likely be an important part of future quantum networking technologies based on SiV centers.

The severity of spectral diffusion is different for different emitters however, and this control is not always necessary, especially for proof-of-principle experiments with a small

131

number of emitters. For SiV 1, the main SiV used in the following sections, and the SiV used in chapter 6, we find almost no spectral diffusion, with optical transitions stable over many minutes [Fig. 7.5(c)]. This is an ideal configuration, as experiments can be performed without any need to verify the optical line position.

7.6 Regimes of cavity-QED for SiV spin-photon interfaces

Efficient spin-photon interactions are enabled by incorporating SiV centers into nanophotonic cavities. In this section, we describe SiV-cavity measurements in several regimes of cavity QED, and comment on their viability for spin-photon experiments.

7.6.1 Spectroscopy of cavity-coupled SiVs

We measure the spectrum of the atom-cavity system at different atom-cavity detunings in order to characterize the device and extract key cavity QED parameters [Fig. 7.6(a)]. The reflection spectrum of a two-level system coupled to a cavity is modeled by solving the frequency response of the standard Jaynes-Cummings Hamiltonian using input-output formalism for a cavity near critical coupling [94]:

$$\mathcal{R}(\omega) = \left| 1 - \frac{2\kappa_l}{i(\omega - \omega_c) + \kappa_{\text{tot}} + g^2/(i(\omega - \omega_a) + \gamma)} \right|^2, \tag{7.6}$$

where κ_l is the decay rate from the incoupling mirror, κ_{tot} is the cavity linewidth, $\omega_c(\omega_a)$ is the cavity (atom) resonance frequency, g is the single-photon Rabi frequency, and γ

132
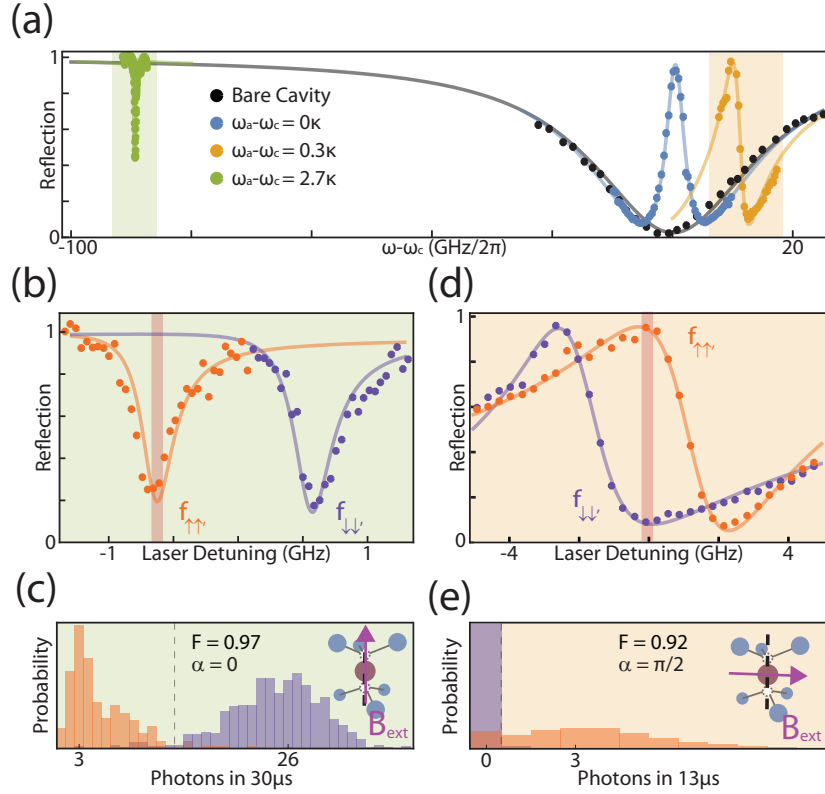
Figure 7.6: (a) SiV-cavity reflection spectrum at several detunings. The bare cavity spectrum (black) is modulated by the presence of the SiV. When the atom cavity detuing is small (Blue, orange), high-contrast, broad features are the result of Purcell enhanced SiV transitions. Far from the cavity resonance (green), interaction results in narrow SiV-assisted transmission channels. (b) Spin-dependent reflection for large SiV-cavity detuning $\Delta \approx -3\kappa$, $B_{\text{ext}} = 0.35\,\text{T}$. In this regime, SiV spin states can be individually addressed. (c) Probing either transmission dip results in high-fidelity single-shot readout in an aligned field ($F = 0.97$, threshold on detecting 13 photons). (d) Spin-dependent reflection near resonance $\Delta \approx 0.5\kappa$, $B_{\text{ext}} = 0.19\,\text{T}$. Dispersive lineshapes allow for distinguishable reflection spectra from both SiV spin states. (e) A probe at the frequency of maximum contrast (f_Q) can determine the spin state in a single shot in a misaligned field($F = 0.92$, threshold on detecting > 1 photon).

is the bare atomic linewidth. Interactions between the SiV optical transition and the

nanophotonic cavity result in two main effects. First, the SiV center can modulate the

reflection spectrum of the bare cavity, as seen in the colored curves of figure 7.6(a).

133

Second, the coupling to the cavity can broaden the linewidth of the SiV based on the Purcell effect:

$$\Gamma \approx \gamma + 4g^2/\kappa \frac{1}{1 + 4(\omega_c - \omega_a)^2/\kappa^2}$$

When the cavity is far detuned from the atomic transition $|\omega_c - \omega_a| \equiv \Delta > \kappa$ [Fig. 7.6(a), green], Purcell enhancement is negligible and the cavity and atomic linewidths $\kappa, \gamma = 2\pi \times \{33, 0.1\}$ GHz are estimated. When the cavity is on resonance with the atom ($\Delta = 0$), we fit (7.6) using previously estimated values of κ and γ to extract $g = 2\pi \times 5.6$ GHz. Together, these measurements allow us to determine the atom-cavity cooperativity $C = 4g^2/\kappa\gamma = 38$. Importantly, interactions between the SiV and single photons becomes deterministic when $C > 1$.

As mentioned in section (chapter 7.4), we would like to make use of spectrally resolved spin conserving optical transitions ($f_{\uparrow\uparrow'}, f_{\downarrow\downarrow'}$) to build a spin-photon interface using the SiV. Here, we make this criteria more explicit: $f_{\uparrow\uparrow'}$ and $f_{\downarrow\downarrow'}$ can be resolved when $|f_{\uparrow\uparrow'} - f_{\downarrow\downarrow'}| \gtrsim \Gamma$.

7.6.2 Cavity QED in the detuned regime

In the detuned regime ($\Delta > \kappa$), $\Gamma \approx \gamma$, and narrow atom-like transitions are easily resolved under most magnetic field configurations, including when the field is aligned with the SiV symmetry axis [Fig. 7.6(b)]. In this case (chapter 7.4) [165], optical transitions are highly spin-conserving, and many photons can be collected allowing for

high-fidelity single-shot readout of the SiV spin state ($F = 0.97$) [Fig. 7.6(c)]. Rapid, high-fidelity, non-destructive single-shot readout can enable projective-readout based initialization: after a single measurement of the SiV spin state, the probability of a measurement-induced spin flip is low, effectively initializing the spin into a known state.

While this regime is useful for characterizing the system, the maximum fidelity of spin-photon entanglement based on reflection amplitude is limited. As seen in figure 7.6(b), the contrast in the reflection signal between an SiV in $|\uparrow\rangle$ (orange) vs. $|\downarrow\rangle$ (purple) is only $\sim 80\%$, implying that in 20% of cases, a photon is reflected from the cavity independent of the spin state of the SiV, resulting in errors. We note that the residual 20% of reflection can be compensated by embedding the cavity inside an interferometer at the expense of additional technical stabilization challenges, discussed below.

7.6.3 Cavity QED near resonance

Tuning the cavity onto the atomic resonance ($\Delta \approx 0$) dramatically improves the reflection contrast [Fig. 7.6(a) (blue curve)]. Here, we observe nearly full contrast of the reflection spectrum due to the presence of the SiV. Unfortunately, this is associated with a broadened atomic linewidth ($\Gamma = \gamma(1 + C) \sim 4\,\text{GHz}$). While it is, in principle, still possible to split the atomic lines by going to higher magnetic fields, there are several technical considerations which make this impractical. Large magnetic fields ($|B_{\text{ext}}| > 0.5\,\text{T}$) correspond to large qubit frequencies ($f_{\uparrow\downarrow}$), which can induce spontaneous qubit decay due to phonon emission ($|\uparrow\rangle \rightarrow |\downarrow\rangle$), as well as increased local heating of the device from

135

microwave dissipation, both of which reduce the SiV spin coherence time rendering it ineffective as a quantum memory.

At intermediate detunings ($0 < \Delta < \kappa$), the SiV resonance is located on the cavity slope and results in high-contrast, spin-dependent Fano lineshapes which exhibit sharp features smaller than Γ [Fig. 7.6(a), orange curve]. By working at an optimal B_{ext} where the peak of one spin transition is overlapped by the valley of the other, the best features of the resonant and far-detuned regimes are recovered [Fig. 7.6(e)]. Probing the system at the point of maximum contrast ($f_Q \approx (|f_{\uparrow\uparrow'} - f_{\downarrow\downarrow'}|)/2$, contrast $> 90\%$) enables single-shot readout of the SiV spin state for an arbitrary field orientation, even when transitions are not cycling [Fig. 7.6(f)].

This demonstrates an optical regime of cavity QED where we simultaneously achieve high-contrast readout while maintaining spin-dependent transitions. In this regime, we still expect residual reflections of about 10%, which end up limiting spin-photon entanglement fidelity. This infidelity arises because the cavity is not perfectly critically coupled ($\kappa_l \neq \kappa_{tot}/2$), and can in principle be solved by engineering devices that are more critically coupled. Alternatively, this problem can be addressed for any cavity by interfering the signal with a coherent reference to cancel unwanted reflections. In this case, one would have to embed the cavity in one arm of a stabilized interferometer. This is quite challenging, as it involves stabilizing $\sim 10\,\text{m}$ long interferometer arms, part of which lie inside the DR (and experience strong vibrations from the pulse-tube cryocooler).

136

A fundamental issue with critically coupled cavities is that not all of the incident light is reflected from the device. If the spin is not initialized in the highly-reflecting state, photons are transmitted and not recaptured into the fiber network. Switching to overcoupled (single-sided) cavities, where all photons are reflected with a spin-dependent phase, could improve both the fidelity and efficiency of spin-photon entanglement. Once again, however, measurement of this phase would require embedding the cavity inside of a stabilized interferometer. As such, the un-compensated reflection amplitude based scheme employed here is the most technically simple approach to engineering spin-photon interactions.

7.7   Microwave spin control

While the optical interface described in previous sections enables high-fidelity initialization and readout of the SiV spin qubit, direct microwave driving is the most straightforward path towards coherent single-qubit rotations. Typically, microwave manipulation of electron spins requires application of significant microwave power. This presents a challenge, as SiV spins must be kept at local temperatures below $500\,\mathrm{mK}$ in order to avoid heating-related dephasing. In this section, we implement coherent microwave control of SiV centers inside nanostructures at temperatures below $500\,\mathrm{mK}$.
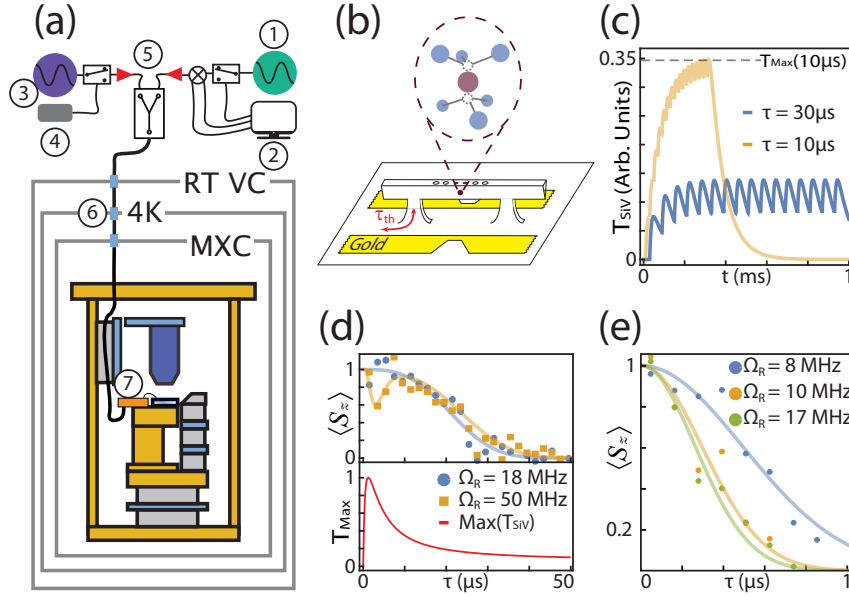
Figure 7.7: (a) Experimental schematic for microwave control. The amplitude and phase of a CW microwave source ① are modulated via a microwave switch and IQ mixer controlled externally by an AWG ②. A CW radio frequency source ③ is controlled using a digital delay generator ④. Both signals are amplified by 30dB amplifiers ⑤ before entering the DR. 0dB cryo-attenuators ⑥ thermalize coax cables at each DR stage, ultimately mounted to a PCB ⑦ on the sample stage and delivered to the devices. (b) Schematic depicting microwave-induced heating of devices. (c) Modeled temperature at the SiV from a dynamical decoupling sequence. At long τ, device cools down between each decoupling pulse, resulting in low temperatures. At short τ, devices are insufficiently cooled, resulting in a higer max temperature ($T_{\max}$). (d) Effects of microwave heating on SiV coherence time. (Top panel) At high Rabi frequencies, SiV coherence is temporarily reduced for small τ. (Bottom panel) The local temperature ($T_{\max}$) at the SiV calculated by taking the maximum value of the plots in figure (c). (e) Hahn-echo for even lower Rabi frequencies, showing coherence times that scale with microwave power

7.7.1 Generating microwave single-qubit gates

The SiV spin is coherently controlled using amplitude and phase controlled microwave pulses generated by a Hittite signal generator (HMC-T2220). A target pulse sequence is loaded onto an arbitrary waveform generator (Tektronix AWG 7122B), which uses a

digital channel to control a fast, high-extinction MW-switch (Custom Microwave Components, CMCS0947A-C2), and the analog channels adjust the amplitude and phase via an IQ-mixer (Marki, MMIQ-0416LSM). The resulting pulse train is subsequently amplified (Minicircuits, ZVE-3W-183+) to roughly 3 W of power, and sent via a coaxial cable into the dilution refrigerator. At each cryogenic flange, a 0 dB attenuator is used to thermalize the inner and outer conductors of the coaxial line while minimizing microwave dissipation. The signal is then launched into a coplanar waveguide on a custom-built circuit board (Rogers4003C, Bay Area Circuits) so it can be wire-bonded directly to the diamond chip (chapter 7.2, Fig. 7.7(c)). The qubit frequency ($f_{\downarrow\uparrow}$) is measured by its optically detected magnetic resonance spectrum (ODMR) identically to the method described in [165]. We observe ODMR from 2 GHz to 20 GHz (corresponding to fields from 0.1 T to 0.7 T), implying that microwave control of SiV centers in this configuration is possible at a wide variety of external field magnitudes. This allows the freedom of tuning the field to optimize other constraints, such as for resolving spin transitions (chapter 7.6) and identifying ancillary nuclear spins (chapter 7.10).

Once the qubit frequency has been determined for a given field, single-qubit gates are tuned up by measuring Rabi oscillations. The frequency of these oscillations scales with the applied microwave power $\Omega_R \sim \sqrt{P}$ and determines the single-qubit gate times. We can perform π-pulses (R_ϕ^π) in under 12 ns, corresponding to a Rabi frequency exceeding 80 MHz (chapter 6.2). This coherent control is used to implement pulse-error correcting dynamical decoupling sequences, either CPMG-N sequences of the form

139

$R_x^{\pi/2} - \left(\tau - R_y^{\pi} - \tau\right)^N - R_x^{\pi/2} = x - (Y)^N - x$ [367] or XY8-N sequences of the form $x - (XYXYYXYX)^N - x$ [368]. Sweeping the inter-pulse delay τ measures the coherence time T_2 of the SiV.

7.7.2 EFFECTS OF MICROWAVE HEATING ON COHERENCE

As mentioned in sections 7.3 and 7.4, thermally induced T_1 relaxation can dramatically reduce SiV coherence times. To explain this phenomenon, we model the nanobeam as a $1D$ beam weakly coupled at two anchor points to a uniform thermal bath [Fig. 7.7(b)]. Initially, the beam is at the steady-state base temperature of the DR. A MW pulse instantaneously heats the bath, and the beam rethermalizes on a timescale τ_{th} set by the thermal conduction of diamond and the beam geometry. Once the pulse ends, this heat is extracted from the beam on a similar timescale. By solving the time-dependent 1-D heat equation, we find that the change in temperature at the SiV caused by a single pulse (starting at time t_0) scales as $T_{\mathrm{SiV}} \propto (e^{-(t-t_0)/\tau_{\mathrm{th}}} - e^{-9(t-t_0)/\tau_{\mathrm{th}}})$. We take the sum over N such pulses to model the effects of heating from a dynamical-decoupling sequence of size N.

At early times ($\tau < \tau_{\mathrm{th}}$), the SiV does not see the effects of heating by the MW line, and coherence is high. Similarly, at long times ($\tau \gg \tau_{\mathrm{th}}$) a small amount of heat is able to enter the nanostructure and slightly raise the local temperature, but this heat is dissipated before the next pulse arrives [Fig. 7.7(c), blue curve]. At intermediate timescales however, a situation can arise where the nanobeam has not fully dissipated

140

the heat from one MW pulse before the second one arrives [Fig. 7.7(c), orange curve]. We plot the maximum temperature as seen by the SiV as a function of pulse spacing [Fig. 7.7(d), lower panel], and observe a spike in local temperature for a specific inter-pulse spacing τ, which depends on τ_{th}. Dynamical-decoupling sequences using high Rabi frequency pulses reveal a collapse in coherence at a similar time [Fig. 7.7(d), upper panel]. This collapse disappears at lower Rabi frequencies, suggesting that it is associated with heating-related dephasing. We fit this collapse to a model where the coherence time T_2 depends on temperature [193], and extract the rate of heating $\tau_{\text{th}} = 70\,\text{s}$.

Typically, faster π-pulses improve measured spin coherence by minimizing finite-pulse effects and detuning errors. Unfortunately, as seen above, faster pulses require higher MW powers which cause heating-related decoherence in our system. We measure Hahn-echo at lower MW powers [fig. 7.7(e)], and find MW heating limits T_2 even at $\Omega_R \sim 10\,\text{MHz}$. For applications where long coherence is important, such as electron-nuclear gates (chapter 7.10, we operate at an optimal Rabi frequency $\Omega_R = 2\pi\times10\,\text{MHz}$ where nuclear gates are as fast as possible while maintaining coherence for the entire gate duration. For applications such as spin-photon entangling gates where fast gates are necessary (chapter 7.9), we operate at higher Rabi frequencies $\Omega_R = 2\pi\times80\,\text{MHz}$ at the cost of reduced coherence times.

Heating related effects could be mitigated by using superconducting microwave waveguides. This approach would also enable the fabrication of a single, long superconducting waveguide that could simultaneously address all devices on a single chip. However, it

141

is still an open question whether or not superconducting waveguides with appropriate critical temperature, current, and field properties can be fabricated around diamond nanostructures.

7.8 INVESTIGATING THE NOISE BATH OF SiVs IN NANOSTRUCTURES

At low temperatures, the coherence time of SiV centers drastically depends on the surrounding spin bath, which can differ from emitter to emitter. As an example, we note that the T_2 of two different SiV centers in different nanostructures scales differently with the number of applied decoupling pulses [Fig. 7.8(a)]. Surprisingly, the coherence time of SiV 2 does not scale with the number of applied pulses, while the coherence time of SiV 1 does scale as $T_2(N) \propto N^{2/3}$. Notably, both scalings are different as compared to what was previously measured in bulk diamond: $T_2(N) \propto N^1$ [165]. In this section, we probe the spin bath of these two SiVs in nanostructures to investigate potential explanations for the above observations.

In order to investigate the poor coherence of SiV 2, we perform double electron-electron resonance (DEER) spectroscopy [369] to probe the spin bath surrounding this SiV. We perform a Hahn-echo sequence on the SiV, and sweep the frequency of a second microwave pulse (taking the RF path in figure 7.7(a)), contemporaneous with the echoing SiV π-pulse [Fig. 7.8(b), upper panel]. If this second pulse is resonant with a spin bath coupled to the SiV, the bath can flip simultaneously with the SiV, leading

142
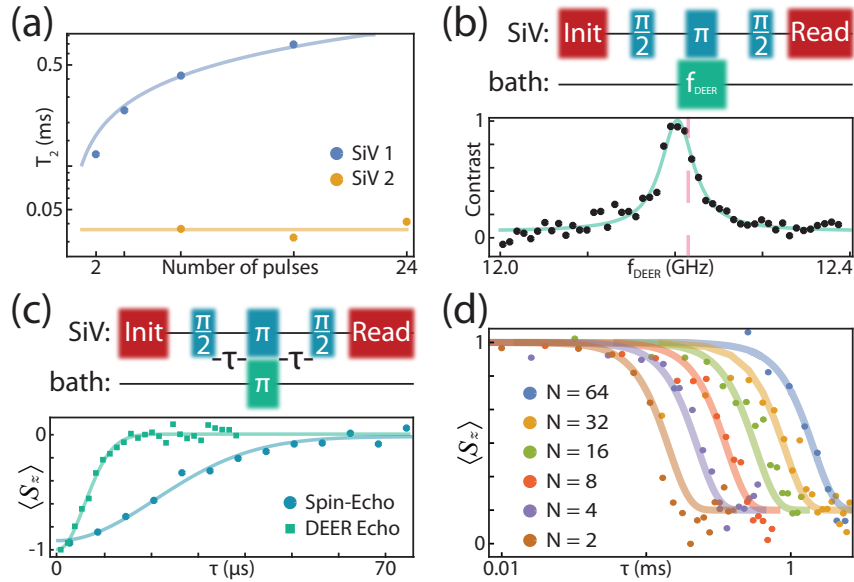
Figure 7.8: (a) T2 scaling for two different SiVs. SiV 2 exhibits no scaling with number of pulses ($T_{2,\mathrm{SiV2}}$ =30 s). (b) DEER ESR on SiV 2. Vertical red line is the expected frequency of a g = 2 spin based on our ability to determine the applied external field (Typically to within 10%). (c) DEER Echo on SiV 2. $T_{2,DEER}$ =10 s. (d) Dynamical-decoupling on SiV 1. Data points are T_2 measurements used in part (a, blue curve), and solid lines are a noise model consisting of two Lorentzian noise baths.

to increased sensitivity to noise from the bath [Fig. 7.8(b), lower panel]. We observe a significant reduction of coherence at a frequency consistent with that of a free-electron spin bath ($\mathrm{g_{bath}} = 2$) (resonance expected at 12(1) GHz).

Next, we repeat a standard Hahn-echo sequence where a π-pulse resonant with this bath is applied simultaneously with the SiV echo pulse (DEER echo). The coherence time measured in DEER echo is significantly shorter than for standard spin-echo, indicating that coupling to this spin bath is a significant source of decoherence for this SiV. One possible explanation for the particularly severe bath surrounding this SiV is a thin

143

layer of alumina (Al_2O_3) deposited via atomic layer deposition on this device in order to tune cavities closer to the SiV transition frequency. The amorphous oxide layer–or its interface with the diamond crystal–can be host to a large number of charge traps, all located within $\sim 50\,nm$ of this SiV. Unfortunately, we could not measure this device without alumina layer due to our inability to gas-tune the nanophotonic cavity close enough to the SiV resonance (chapter 7.3).

These observations are further corroborated by DEER measurements in SiV 1, where the alumina layer was not used (only N_2 was used to tune this cavity). In this device, we observe longer coherence times which scale $T_2(N) \propto N^{2/3}$, as well as no significant signatures from $g_{bath} = 2$ spins using DEER spectroscopy. We fit this scaling to a model consisting of two weakly-coupled spin baths [Fig. 7.8(d), Appendix. C.3], and extract bath parameters b_1 =5 kHz, τ_1 =1 s, b_2 =180 kHz, τ_2 =1 ms, where b corresponds to the strength of the noise bath, and τ corresponds to the correlation time of the noise [352, 353].

While the source of this noise is an area of future study, we find that the b_2 term (likely due to bulk impurities) is the dominant contribution towards decoherence in the system [Appendix. C.3]. Removing this term from the model results in coherence times up to a factor of 1000 times larger than measured values. Higher-temperature [86] or *in situ* [370] annealing could potentially mitigate this source of decoherence by eliminating paramagnetic defects such as vacancy clusters. Additionally, by accompanying Si implantation with electron irradiation [371], SiV centers could be created more efficiently,

and with reduced lattice damage. Finally, working with isotopically purified diamond samples with very few ^{13}C, a spin-1/2 isotope of carbon, could also result in a reduced spin bath [165], [Appendix. C.3].

7.9 SPIN-PHOTON ENTANGLEMENT

The previous sections characterize the SiV as an efficient spin-photon interface and a quantum memory with long-lived coherence. Here, we combine these two properties to demonstrate entanglement between a spin qubit and a photonic qubit. The mechanism for generating entanglement between photons and the SiV can be seen in figure 7.6(b,d): Depending on the spin state of the SiV, photons at the probe frequency are either reflected from the cavity and detected, or are transmitted and lost.

7.9.1 GENERATING TIME-BIN QUBITS

We begin by explaining our choice of time-bin encoding for photonic qubits. One straightforward possibility is to use the Fock state of the photon. However, it is extremely challenging to perform rotations on a Fock state, and photon loss results in an error in the computational basis. Another, perhaps more obvious possibility is to use the polarization degree of freedom. While the SiV spin-photon interface is not polarization selective (both spin states couple to photons of the same polarization), one could consider polarization based spin-photon entangling schemes already demonstated

145

in nanophotonic systems [112, 113]. However, this requires embedding the nanostructure inside of a stabilized interferometer, which has a number of challenges (chapter 7.6). In addition, it requires careful fabrication of overcoupled, single-sided cavities (unlike the critically coupled diamond nanocavities used here [chapter 7.2]). As such, we believe time-bin encoding is a natural choice given the critically-coupled SiV-cavity interface described here (chapter 7.6).

These qubits are generated by passing a weak coherent laser though a cascaded AOM, amplitude-EOM, and phase-EOM. The time-bins are shaped by an AWG-generated pulse on the amplitude-EOM, and are chosen to be much narrower than the delay δt between time bins. We can choose to prepare arbitrary initial photonic states by using the phase-EOM to imprint an optional phase shift to the second bin of the photonic qubit. Since we use a laser with Poissonian photon number statistics, we set the average photon number $\langle n_{ph} \rangle = 0.008 \ll 1$ using the AOM to avoid events where two photons are incident on the cavity.

Using this encoding, measurements in a rotated basis (X-basis) become straightforward. We send the time-bin qubit into an actively stabilized, unbalanced, fiber-based, Mach-Zender interferometer, where one arm passes through a delay line of time δt. With 25% probability, $|e\rangle$ enters the long arm of the interferometer and $|l\rangle$ enters the short arm, and the two time bins interfere at the output. Depending on the relative phase between the two bins, this will be detected on only one of the two arms of the interferometer output [Fig. 7.3(b)], corresponding to a measurement in the X basis of

146

$|\pm\rangle$.

7.9.2 SPIN-PHOTON BELL STATES

We prepare and verify the generation of maximally entangled Bell states between the SiV and a photonic qubit using the experimental sequence depicted in figure 7.9(a). First, the SiV is initialized into a superposition state $|\rightarrow\rangle = 1/\sqrt{2}(|\uparrow\rangle + |\downarrow\rangle)$. Then photons at frequency f_Q (chapter 7.6) are sent to the cavity, corresponding to an incoming photon state $|+\rangle = 1/\sqrt{2}(|e\rangle + |l\rangle)$, conditioned on the eventual detection of only one photon during the experiment run. Before any interactions, this state can be written as an equal superposition: $\Psi_0 = |\rightarrow\rangle \otimes |+\rangle = 1/2(|e\uparrow\rangle + |e\downarrow\rangle + |l\uparrow\rangle + |l\downarrow\rangle)$. The first time bin is only reflected from the cavity if the the SiV is in state $|\uparrow\rangle$, effectively carving out $|e\downarrow\rangle$ in reflection [348]. A π-pulse on the SiV transforms the resulting state to $\Psi_1 = 1/\sqrt{3}(|e\downarrow\rangle + |l\downarrow\rangle + |l\uparrow\rangle)$. Finally, reflection of the late time-bin off of the cavity carves out the state $|l\downarrow\rangle$, leaving a final entangled state $\Psi_2 = 1/\sqrt{2}(|e\downarrow\rangle + |l\uparrow\rangle)$. To characterize the resulting state, we perform tomography on both qubits in the Z and X bases [Fig. 7.9(a)].

In order to enable high-bandwidth operation and reduce the requirements for laser and interferometric stabilization in generating and measuring time-bin qubits, it is generally beneficial to set δt as small as possible. The minimum δt is determined by two factors: First, each pulse must be broad enough in the time-domain (narrow enough in the frequency domain) so that it does not distort upon reflection off of the device.

147
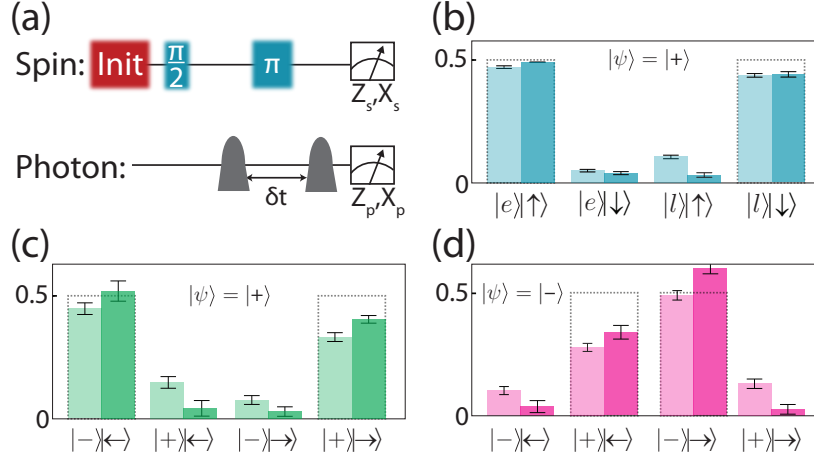
Figure 7.9: (a) Experimental sequence for generating and verifying spin-photon entanglement. A time-bin encoded qubit is reflected by the cavity, and both the SiV and the photonic qubits are measured in the Z and X bases. (b) Spin-photon correlations measured in the Z-Z basis. Light (dark) bars are before (after) correcting for known readout error associated with single-shot readout of the SiV. (c) Spin-photon correlations measured in the X-X basis. Bell-state preparation fidelity of $F \geq 0.89(3)$ and a concurrence $\mathcal{C} \geq 0.72(7)$. (d) Preparation of second spin-photon Bell state. Changing the phase of the incoming photonic qubit prepares a Bell-state with inverted statistics in the X basis.

From figure 7.6(d), the reflection specturm is roughly constant over a $\sim 100\,\mathrm{MHz}$ range, implying that $\sim$ nanosecond pulses are sufficient. The second consideration is that a microwave π-pulse must be placed between the two pulses. In this experiment, we drive fast (12 ns) π-pulses. As such, we set $\delta t = 30\,\mathrm{ns}$ and use 5 ns optical pulses to satisfy these criteria.

7.9.3 SPIN-PHOTON ENTANGLEMENT MEASUREMENTS

For Z-basis measurements, photons reflected from the cavity are sent directly to a SPCM and the time-of-arrival of the time-bin qubit is recorded. Afterwards, the SiV is read

out in the Z-basis (chapter 7.6). Single-shot readout is calibrated via a separate measurement where the two spin-states are prepared via optical pumping and read out, and the fidelity of correctly determining the $|\uparrow\rangle$ ($|\downarrow\rangle$) state is $F_\uparrow = 0.85$ ($F_\downarrow = 0.84$), limited by the large 0 component of the geometric distribution which governs photon statistics for spin-flip systems (chapter 7.6). In other words, since we work in a misaligned field in this experiment, the probability of a spin flip is high, making it somewhat likely to measure 0 photons regardless of initial spin state. Even before accounting for this known error [Appendix. C.4], we observe clear correlations between the photonic and spin qubits [Fig. 7.9(b), light-shading]. Error bars for these correlation histograms (and the following fidelity calculations) are estimated by statistical bootstrapping, where the scattered photon histograms (post-selected on the detection of $|e\rangle$ or $|l\rangle$) are randomly sampled in many trials, and the variance of that ensemble is extracted.

Measurements in the X-basis are performed similarly. The photon is measured through an interferometer as described above, where now the detector path information is recorded for the overlapping time-bin. After a $R_y^{\pi/2}$ pulse on the SiV, the scattered photon histograms again reveal significant correlations between the '+' and '-' detectors and the SiV spin state [fig. 7.9(c)]. By adding a π-phase between the early and late time bins, we can prepare an orthogonal Bell state. Measured correlations of this state are flipped in the X-basis [Fig. 7.9(d)].

Measurements of this Bell state in the Z- and X-bases are used to estimate a lower bound on the fidelity: $F = \langle\Psi^+|\rho|\Psi^+\rangle \geq 0.70(3)$ ($F \geq 0.89(3)$ after correcting for

149

readout errors) [Appendix. C.4]. The resulting entangled state is quantified by its concrrence $\mathcal{C} \geq 0.42(6)$ ($\mathcal{C} \geq 0.79(7)$ after correcting for readout errors) [Appendix. C.4]. This high-fidelity entangled state between a photonic qubit and a quantum memory is a fundamental resource for quantum communication [80] and quantum computing schemes [68], and can be used, for example, to demonstrate heralded storage of a photonic qubit into memory (chapter 6.3).

7.10 CONTROL OF SiV-^{13}C REGISTER

While demonstrations of a quantum node with a single qubit is useful for some protocol, nodes with several interacting qubits enable a wider range of applications, including quantum repeaters [46]. In this section, we introduce additional qubits based on ^{13}C naturally occurring in diamond (chapter 7.8).

7.10.1 COUPLING BETWEEN THE SiV AND SEVERAL ^{13}C

For all of the emitters investigated in section 7.7, we observe collapses in the echo signal corresponding to entanglement with nearby nuclear spins [Fig. 7.10(a)]. As the diamond used in this work has 1% ^{13}C (chapter 7.8), we typically observe several such nuclei, with all of their resonances overlapping due to their second-order sensitivity to hyperfine coupling parameters (chapter 6.4). Consequently, during a spin echo sequence the SiV entangles with many nuclei, quickly losing coherence and resulting in a collapse to $\langle S_z \rangle =$

150

0 [Fig. 7.10(a), left side]. If single ^{13}C can be addressed however, this entanglement results in coherent population transfer and echo collapses which can, in some cases, completely flip the SiV spin state ($\langle S_z \rangle = \pm 1$). This entanglement forms the basis for quantum gates [Fig. 7.10(a), right side]. These gates can be tuned by changing the alignment of B_{ext} with respect to the hyperfine coupling tensor, or by using different timings. Unfortunately, as a result of the complicated nuclear bath for this device, a majority of field orientations and amplitudes only show collapses to $\langle S_z \rangle = 0$. The highest fidelity nuclear gates demonstrated here are based on echo resonances with the largest contrast which, crucially, were not commensurate with an aligned field. Thus, in this device, single ^{13}C could only be isolated at the cost of lower SSR fidelity (chapter 7.6).

7.10.2 Initializing the nuclear spin

Once a single nuclear spin is identified, resonances in spin-echo form the building block for quantum gates. For example, a complete flip of the SiV is the result of the nuclear spin rotating by π conditionally around the axes $\pm$X ($\mathcal{R}^{\pi}_{\pm x, \text{SiV}-\text{C}}$), depending on the state of the SiV. We can vary the rotation angle of this pulse by choosing different spacings τ between pulses [Fig. 7.10(a)], or by using different numbers of π-pulses. We find a maximally entangling gate ($\mathcal{R}^{\pi/2}_{\pm x, \text{SiV}-\text{C}}$) by applying $N = 8$ π-pulses separated by $2\tau = 2 \times 2.859\,\mu$s. This can be visualized on the Bloch sphere in figure 7.10(b), where the state of the SiV (orange or purple) induces different rotations of the ^{13}C.

A similarly constructed entangling gate ($\mathcal{R}^{\phi}_{\vec{n_\uparrow},\vec{n_\downarrow}}$, discussed in Appendix C.5) is used to coherently map population from the SiV onto the nuclear spin or map population from the nuclear spin onto the SiV [Fig. 7.10(c)]. The fidelity of these gates is estimated by polarizing the SiV, mapping the population onto the ^{13}C, and waiting for $T \gg T_2^*$ (allowing coherence to decay) before mapping the population back and reading out [Fig. 7.10(d)]. We find that we can recover 80% of the population in this way, giving us an estimated initialization and readout fidelity of $F = 0.9$.

Based on the contrast of resonances in spin-echo (also 0.9), this is likely limited by entanglement with other nearby ^{13}C for this emitter, as well as slightly sub-optimal choices for τ and N. Coupling to other ^{13}C results in population leaking out of our two-qubit register, and can be improved by increasing sensitivity to single ^{13}C, or by looking for a different emitter with a different ^{13}C distribution. The misaligned external field further results in slight misalignment of the nuclear rotation axis and angle of rotation, and can be improved by employing adapted control sequences to correct for these errors [356, 357].

7.10.3 Microwave control of nuclear spins

As demonstrated above, control of the ^{13}C via composite pulse sequences on the SiV is also possible. A maximally entangling gate has already been demonstrated and used to initialize the ^{13}C, so in order to build a universal set of gates, all we require are unconditional single-qubit rotations. This is done following reference [247], where un-
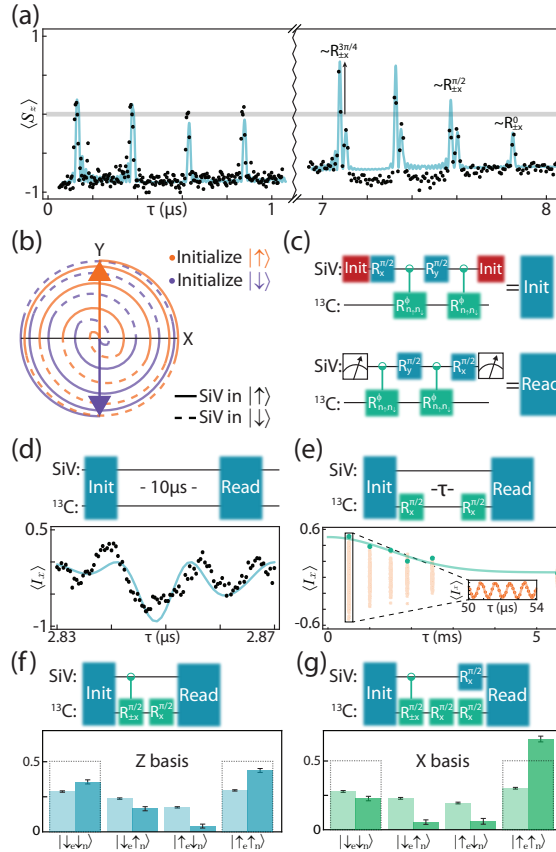
Figure 7.10: (a) XY8-2 spin echo sequence reveals coupling to nuclear spins. (Left panel) Collapses $\langle S_x \rangle = 0$ at short times indicate coupling to many nuclei. (Right panel) Collapses $\langle S_x \rangle \neq 0$ at long times indicate conditional gates on a single nuclear spin. (b) Trajectory of ^{13}C on the Bloch sphere during a maximally entangling gate. Orange (purple) lines correspond to the SiV initially prepared in state $|\uparrow\rangle$ ($|\uparrow\rangle$); transitions from solid to dashed lines represent flips of the SiV electronic spin during the gate. (c) Maximally entangling gates of the form $\mathcal{R}^{\phi}_{\vec{n}_\uparrow,\vec{n}_\downarrow}$ are used to initialize and readout the two-qubit register. (d) Tuning up an initialization gate. Inter-pulse spacing τ for Init and Read gates are swept to maximize polarization. Solid line is the modeled pulse sequence using the hyperfine parameters extracted from (a). (e) Nuclear Ramsey measurement. Driving the ^{13}C using composite gates on the SiV reveals $T_2^* = 2.2$ ms. (Inset) Orange points are coherent oscillations of the Ramsey signal due to hyperfine coupling to the SiV. (f) Electron-nuclear correlations measured in the ZZ-basis. Light (dark) bars are before (after) correcting for known errors associated with reading out the SiV and ^{13}C. (g) Electron-nuclear correlations measured in the XX-basis. We estimate a Bell state preparation fidelity of $F \geq 0.59(4)$ and a concurrence $\mathcal{C} \geq 0.22(9)$.

153

conditional nuclear rotations occur in spin-echo sequences when the inter-pulse spacing τ is halfway between two collapses. For the following gates, we use an unconditional $\pi/2$-pulse composed of 8 π-pulses separated by $\tau = 0.731\,\mathrm{s}$.

We use this gate to probe the coherence time T_2^* of the ^{13}C. After mapping population onto the nuclear spin, the SiV is re-initialized, and then used to perform unconditional $\pi/2$-rotations on the ^{13}C [Fig. 7.10(d)]. Oscillations in the signal demonstrate Larmor precession of the nucleus at a frequency determined by a combination of the external field as well as ^{13}C-specific hyperfine interactions (chapter 6.4), which are seen as the orange data points in figure 7.10(d). The green envelope is calculated by fitting the oscillations and extracting their amplitude. The decay of this envelope T_2^* =2.2 ms shows that the ^{13}C has an exceptional quantum memory, even in the absence of any dynamical decoupling.

We characterize the fidelity of our conditional and unconditional nuclear gates by generating and reading out Bell states between the SiV and ^{13}C [Appendix. C.4]. First, we initialize the 2-qubit register into one of the 4 eigenstates: $\{|\uparrow_e\uparrow_N\rangle, |\uparrow_e\downarrow_N\rangle, |\downarrow_e\uparrow_N\rangle, |\downarrow_e\downarrow_N\rangle\}$, then perform a $\pi/2$-pulse on the electron to prepare a superposition state. Afterward, a CNOT gate, comprised of an unconditional $\pi/2$ pulse followed by a maximally entangling gate, prepares one of the Bell states $|\Psi_\pm\rangle, |\Phi_\pm\rangle$ depending on the initial state [Fig. 7.10 (e,f)]. Following the analysis outlined in appendix C.4, we report an error corrected fidelity of $F \geq 0.59(4)$ and $\mathcal{C} \geq 0.22(9)$, primarily limited by our inability to initialize the ^{13}C (chapter 6.4).

7.10.4 Radio-frequency driving of nuclear spins

The previous section demonstrated a CNOT gate between SiV and ^{13}C using composite MW pulses. This approach has several drawbacks. First, the gate fidelity is limited by our ability to finely tune the rotation angle of the maximally entangled gate which can not be done in a continuous fashion [see Fig. 7.11(a)]. Second, this gate requires a specific number of MW pulses and delays between them, making the gate duration (~ 50 s in this work) comparable to the SiV coherence time. Finally, this scheme relies on a second order splitting of individual ^{13}C resonances to resolve individual ones; residual coupling to additional ^{13}C limits the fidelity for a pulse sequence of given total length.

Direct RF control [167] would be a simple way to make a fast and high-fidelity CNOT gate since it would require a single RF π-pulse on a nuclear spin transition [372]. Furthermore, since the nuclear spin transition frequencies depend on the hyperfine coupling to leading order, these pulses could have higher ^{13}C selectivity and potentially shorter gate duration.

We use the RF port inside the DR (chapter 7.7) to apply RF pulses resonant with nuclear spin transitions. Figure 7.10(a) shows RF Rabi oscillations of the nuclear spin. Since the ^{13}C gyromagnetic ratio is about 3 orders of magnitude smaller compared to the SiV spin, RF driving is much less efficient than MW one and requires much more power. To investigate local heating of the SiV (chapter 7.7) we measured the SiV spin coherence contrast in spin-echo sequence right after applying off-resonant RF

155
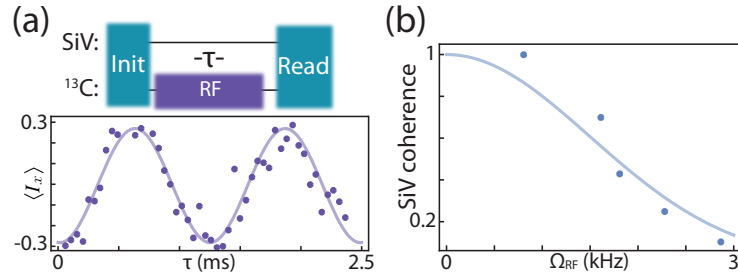
Figure 7.11: (a) RF Rabi oscillations. Applying an RF tone directly drives nuclear rotations of a coupled ^{13}C. (b) SiV coherence in the presence of an RF drive. As the strength of the RF drive is increased, local heating from the CPW reduces the SiV T_2.

pulse of 100 s at different power (calibrated via RF rabi oscillations) [Figure 7.10(b)]. Unfortunately, Even modest Rabi frequencies ($\Omega_{\mathrm{RF}} \sim 1\,\mathrm{kHz}$) result in 20% loss in SiV coherence. Replacing the gold CWG used in this work by superconducting ones may solve heating issue and make RF driving practically useful.

7.11 Conclusion

The SiV center in diamond has rapidly become a leading candidate to serve as the building block of a future quantum network. In this work, we describe the underlying technical procedures and optimal parameter regimes necessary for utilizing the SiV-nanocavity system as a quantum network node. In particular, we discuss the effect of static and dynamic strain on the properties of the SiV spin qubit and its optical interface, with direct application to quantum networking experiments. We demonstrate techniques for coherently controlling and interfacing SiV spin qubits inside of nanophotonic structures at millikelvin temperatures to optical photons. Finally, we identify and

156

coherently control auxiliary nuclear spins, forming a nanophotonic two-qubit register.

The work presented here and in the complementary letter (chapter 6) illustrates the path towards the realization of a first-generation quantum repeater based on SiV centers inside diamond nanodevices. We note that a key ingredient enabling future, large-scale experiments involving several solid-state SiV-nanocavity nodes will be the incorporation of strain tuning onto each device [245]. Precise tuning of both the static and dynamic strain can overcome the limitations of inhomogeneous broadening and spectral diffusion, and enable scalable fabrication of quantum repeater nodes (chapter 7.4).

8

Experimental demonstration of memory-enhanced quantum communication

The ability to communicate quantum information over long distances is of central importance in quantum science and engineering [42]. While some applications of quantum communication such as secure quantum key distribution (QKD) [28, 373] are already being successfully deployed [29, 30, 56, 374], their range is currently limited by photon losses and cannot be extended using straightforward measure-and-repeat strategies without compromising unconditional security [49]. Alternatively, quantum repeaters

[46], which utilize intermediate quantum memory nodes and error correction techniques, can extend the range of quantum channels. However, their implementation remains an outstanding challenge [53, 94, 110, 122, 127, 375, 376], requiring a combination of efficient and high-fidelity quantum memories, gate operations, and measurements. Here we use a single solid-state spin memory integrated in a nanophotonic diamond resonator [76, 77, 184] to implement asynchronous photonic Bell-state measurements, a key component of quantum repeaters. In a proof-of-principle experiment, we demonstrate high-fidelity operation that effectively enables quantum communication at a rate that surpasses the ideal loss-equivalent direct-transmission method while operating at megahertz clock speeds. These results represent a significant step towards practical quantum repeaters and large-scale quantum networks [62, 68].

8.1 Introduction

Efficient, long-lived quantum memory nodes are expected to play an essential role in extending the range of quantum communication [46], as they enable asynchronous quantum logic operations, such as Bell-state measurements (BSM), between optical photons. Such an asynchronous BSM is central to many quantum communication protocols, including the realization of scalable quantum repeaters [46] with multiple intermediate nodes. Its elementary operation can be understood by considering a specific implementation of quantum cryptography [377, 378] illustrated in Fig. 8.1a. Here two remote

159

communicating parties, Alice and Bob, try to agree on a key that is secure against potential eavesdroppers. They each send a randomly chosen photonic qubit $\{|\pm x\rangle, |\pm y\rangle\}$ encoded in one of two conjugate bases (X or Y) across a lossy channel to an untrusted central node (Charlie), who performs a BSM and reports the result over an authenticated public channel. After a number of iterations, Alice and Bob publicly reveal their choice of bases to obtain a correlated bit string (sifted key) from the cases when they used a compatible basis. A potentially secure key can subsequently be distilled provided the BSM error rate is low enough.

While a photonic BSM can be implemented with linear optics and single photon detectors, in this "direct-transmission" approach, the BSM is only successful when photons from Alice and Bob arrive simultaneously. Thus, when Alice and Bob are separated by a lossy fiber with a total transmission probability $p_{\mathrm{A}\rightarrow\mathrm{B}} \ll 1$, Charlie measures photon coincidences with probability also limited by $p_{\mathrm{A}\rightarrow\mathrm{B}}$, leading to a fundamental bound [49] on the maximum possible distilled key rate of $R_{\max} = p_{\mathrm{A}\rightarrow\mathrm{B}}/2$ bits per channel use for an unbiased basis choice [29]. While linear optical techniques to circumvent this bound are now being actively explored [379], they offer only limited improvement and cannot be scaled beyond a single intermediate node.

Alternatively, this bound can be surpassed using a quantum memory node at Charlie's location. In this approach, illustrated in Fig. 8.1, the state of Alice's photon is stored in the heralded memory while awaiting receipt of Bob's photon over the lossy channel. Once the second photon arrives, a BSM between Alice's and Bob's qubits yields a
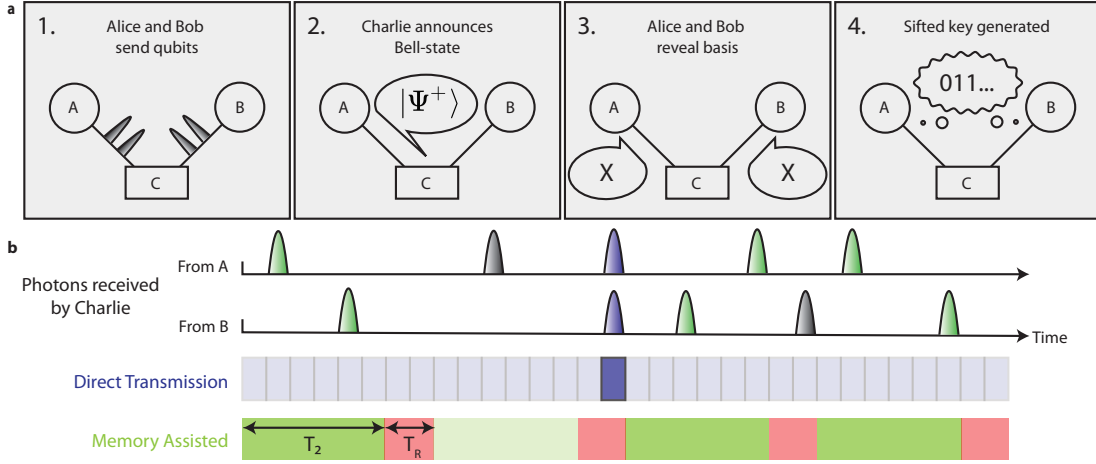
Figure 8.1: Concept of memory-enhanced quantum communication. a, Quantum communication protocol. Alice and Bob send qubits encoded in photons to a measurement device (Charlie) in between them. Charlie performs a BSM and announces the result. After verifying which rounds Alice and Bob sent qubits in compatible bases, a sifted key is generated. **b,** Illustration of memory-enhanced protocol. Photons arrive at Charlie from A and B at random times over a lossy channel, and are unlikely to arrive simultaneously (indicated in purple), leading to a low BSM success rate for direct transmission. Despite overhead time T_R associated with operating a quantum memory (red), a BSM can be performed between photons that arrive at Charlie within memory coherence time T_2, leading to higher success rates (green). BSM successes and failures are denoted by dark and light shaded windows respectively for both approaches.

distilled key rate that for an ideal memory scales as [380] $R_s \propto \sqrt{p_{\text{A}\rightarrow\text{B}}}$, potentially leading to substantial improvement over direct transmission.

8.2 Efficient nanophotonic quantum node

In this work we realize and use a quantum node that enables BSM rates exceeding those of an ideal system based on linear optics. We focus on the demonstration and characterization of the BSM node, leaving the implementation of source-specific technical components of full-scale QKD systems, such as decoy states [381], basis biasing [382],

161

a finite key error analysis [383], and a physical separation of Alice and Bob for future work. Our realization is based on a single silicon-vacancy (SiV) color-center integrated inside a diamond nanophotonic cavity [76, 77, 184] (Fig. 8.2a). Its key figure-of-merit, the cooperativity [94] C, describes the ratio of the interaction rate with individual cavity photons compared to all dissipation rates. A low mode volume $(0.5(\lambda/n)^3)$, high quality factor (2×10^4), and nanoscale positioning of SiV centers enable an exceptional $C = 105 \pm 11$. Cavity photons at $737\,\mathrm{nm}$ are critically coupled to a waveguide and adiabatically transferred into a single-mode optical fiber [184] that is routed to superconducting nanowire single-photon detectors, yielding a full system detection efficiency of about 85% (appendix D.3). The device is placed inside a dilution refrigerator, resulting in electronic spin quantum memory [77] time $T_2 > 0.2\,\mathrm{ms}$ at temperatures below $300\,\mathrm{mK}$.

The operating principle of the SiV-cavity based spin-photon interface is illustrated in Fig. 8.2. Spin dependent modulation of the cavity reflection at incident probe frequency f_0 (Fig. 8.2b) results in the direct observation of electron spin quantum jumps (Fig. 8.2c, inset), enabling nondestructive single-shot readout of the spin state (Fig. 8.2c) in 30 s with fidelity $F = 0.9998^{+0.0002}_{-0.0003}$. Coherent control of the SiV spin qubit ($f_Q \approx$ $12\,\mathrm{GHz}$) is accomplished using microwave fields delivered via an on-chip gold coplanar waveguide [77]. We utilize both optical readout and microwave control to perform projective feedback-based initialization of the SiV spin into the $|\downarrow\rangle$ state with a fidelity of $F = 0.998 \pm 0.001$. Spin-dependent cavity reflection also enables quantum logic

162
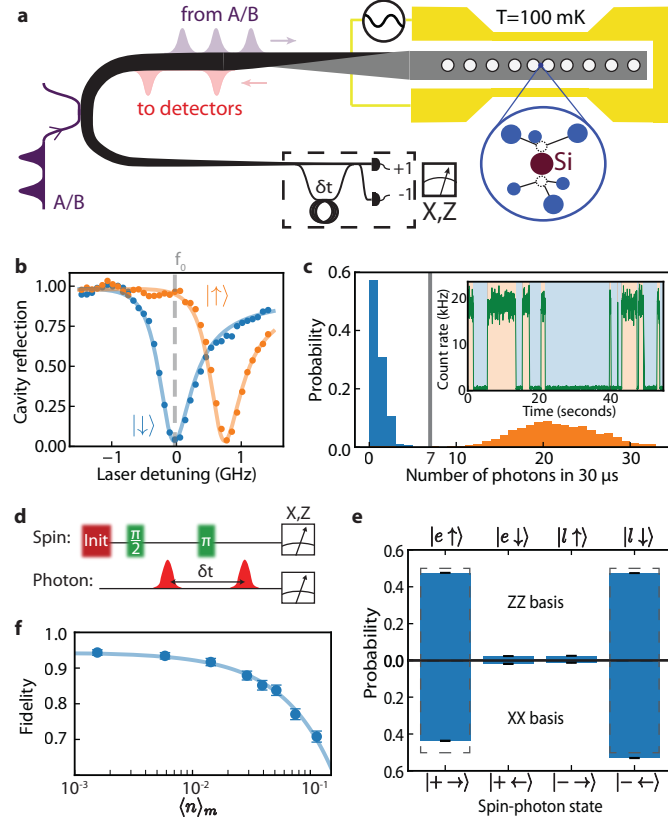
Figure 8.2: Realization of heralded spin-photon gate. a, Schematic of memory-assisted implementation of Charlie's measurement device. Weak pulses derived from a single laser simulate incoming photons from Alice and Bob (purple). Reflected photons (red) are detected in a heralding setup (dashed box). **b,** Reflection spectrum of memory node, showing spin-dependent device reflectivity. **c,** Histogram of detected photon numbers during a 30 s laser pulse, enabling single-shot readout based on a threshold of 7 photons. (Inset) Electron spin quantum jumps under weak illumination. **d,** Schematic of spin-photon quantum logic operation used to generate and verify spin-photon entangled state. **e,** Characterization of resulting spin-photon correlations in the ZZ and XX bases. Dashed bars show ideal values. **f,** Measured spin-photon entanglement fidelity as a function of $\langle n \rangle_m$, the average incident photon number during each initialization of the memory. All error bars represent 1 standard deviation.

operations between an incoming photonic time-bin qubit, defined by a phase-coherent

pair of attenuated laser pulses, and the spin memory [77, 113]. We characterize this

by using the protocol illustrated in Fig. 8.2d to generate the spin-photon entangled

163

state $(|e\uparrow\rangle + |l\downarrow\rangle)/\sqrt{2}$ conditioned on successful reflection of an incoming single photon with overall heralding efficiency $\eta = 0.423 \pm 0.004$ (appendix D.3). Here, $|e\rangle$ and $|l\rangle$ denote the presence of a photon in an early or late time-bin separated by $\delta t = 142\,\text{ns}$ respectively. We characterize the entangled state by performing measurements in the joint spin-photon ZZ and XX bases (Fig. 8.2e), implementing local operations on the reflected photonic qubit with a time-delay interferometer (Fig. 8.2a, dashed box). By lowering the average number of photons $\langle n \rangle_m$ incident on the device during the SiV memory time, we reduce the possibility that an additional photon reaches the cavity without being subsequently detected, enabling high spin-photon gate fidelities for small $\langle n \rangle_m$ (Fig. 8.2f). For $\langle n \rangle_m = 0.002$ we measure a lower bound on the fidelity [77] of the spin-photon entangled state of $F \geq 0.944 \pm 0.008$, primarily limited by residual reflections from the $|\downarrow\rangle$ state.

8.3 Asynchronous Bell-state measurements

This spin-photon logic gate can be directly used to herald the storage of an incoming photonic qubit by interferometrically measuring the reflected photon in the X basis [77]. To implement a memory-assisted BSM, we extend this protocol to accommodate a total of N photonic qubit time-bins within a single initialization of the memory (Fig. 8.3a). Each individual time-bin qubit is encoded in the relative amplitudes and phases of a pair of neighboring pulses separated by δt. Detection of a reflected photon heralds the arrival

164

of the photonic qubit formed by the two interfering pulses without revealing its state [77]. Two such heralding events, combined with subsequent spin-state readout in the X basis, constitute a successful BSM on the incident photons. This can be understood without loss of generality by restricting input photonic states to be encoded in the relative phase ϕ between neighboring pulses with equal amplitude: $(|e\rangle + e^{i\phi}|l\rangle)/\sqrt{2}$ (Fig. 8.3b). Detection of the first reflected photon in the X basis teleports its quantum state onto the spin, resulting in the state $(|\uparrow\rangle + m_1 e^{i\phi_1}|\downarrow\rangle)/\sqrt{2}$, where $m_1 = \pm 1$ depending on which detector registers the photon [77]. Detection of a second photon at a later time within the electron spin T_2 results in the spin state $(|\uparrow\rangle + m_1 m_2 e^{i(\phi_1 + \phi_2)}|\downarrow\rangle)/\sqrt{2}$. The phase of this spin state depends only on the sum of the incoming phases and the product of their detection outcomes, but not the individual phases themselves. As a result, if the photons were sent with phases that meet the condition $\phi_1 + \phi_2 \in \{0, \pi\}$, a final measurement of the spin in the X basis ($m_3 = \pm 1$) completes an asynchronous BSM, distinguishing two of the four Bell-states based on the total parity $m_1 m_2 m_3 = \pm 1$ (appendix D.5).

This approach can be directly applied to generate a correlated bit-string within the protocol illustrated in Fig. 8.1a. We analyze the system performance by characterizing the overall quantum-bit error rate (QBER) [29, 377] for $N = 124$ photonic qubits per memory initialization. We use several random bit strings of incoming photons from $\{|\pm x\rangle, |\pm y\rangle\}$ and observe strong correlations between the resulting BSM outcome and the initial combination of input qubits for both bases (Fig. 8.3c). Using this method, we estimate the average QBER to be $E = 0.116 \pm 0.002$ for all combinations of random

165
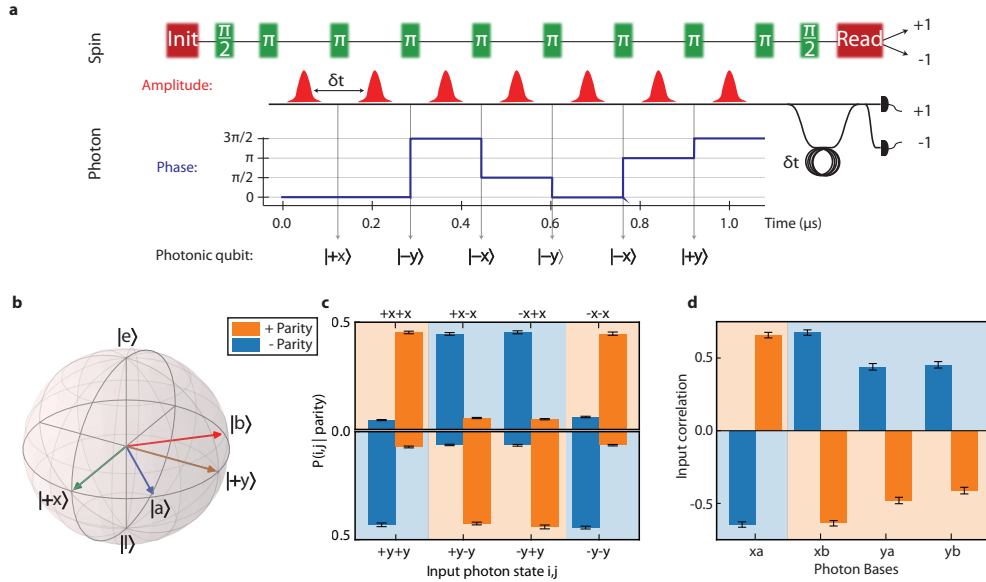
Figure 8.3: Asynchronous Bell-state measurements using quantum memory. a, Example sequence with $N = 6$ photonic qubits sent in a single memory time. Microwave π pulses (green) are interleaved with incoming optical pulses. Photons have fixed amplitude (red) and qubits are defined by the relative phases between subsequent pulses (blue). **b,** Bloch sphere representation of input photonic time-bin qubits used for characterization. **c,** Characterization of asynchronous BSM. Conditional probabilities for Alice and Bob to have sent input states (i, j) given a particular parity outcome for input states in the X (top) and Y (bottom) bases. **d,** Bell test using the CHSH inequality. Conditioned on the BSM outcome, the average correlation between input photons is plotted for each pair of bases used (appendix D.8). Shaded backgrounds denote the expected parity. All error bars represent 1 standard deviation.

bit strings measured, significantly below the limit of $E_i = 0.146$, which could provide

security against individual attacks [29] (note that the measured error rate is also well

below the minimum average QBER [377] of $E_{lo} = 0.125$ achievable using a linear optics

BSM with weak coherent pulse inputs, see appendix D.8). In our experiment, the QBER

is affected by technical imperfections in the preparation of random strings of photonic

qubits. We find specific periodic patterns of photonic qubits to be less prone to these

effects, resulting in a QBER as low as $E = 0.097 \pm 0.006$, which falls within the threshold corresponding to unconditional security [373] of $E_u = 0.110$ with a confidence level of 0.986 (appendix D.8). We further verify security by testing the Bell-CHSH inequality [53] using input states from four different bases, each separated by an angle of 45° (appendix D.8). We find that the correlations between input photons (Fig. 8.3d) violate the Bell-CHSH inequality $S_\pm \leq 2$, observing $S_+ = 2.21 \pm 0.04$ and $S_- = 2.19 \pm 0.04$ for positive and negative BSM parity results respectively. This result demonstrates that this device can be used for quantum communication that is secured by Bell's theorem.

8.4 BENCHMARKING QUANTUM MEMORY ADVANTAGE

In order to benchmark the performance of memory-assisted quantum communication, we model an effective channel loss by reducing the mean photon number $\langle n \rangle_p$ incident on the device per photonic qubit. Assuming that Alice and Bob emit roughly one photon per qubit, this yields an effective channel transmission probability $p_{A \to B} = \langle n \rangle_p^2$, resulting in the maximal distilled key rate $R_{\max}$ per channel use for the direct transmission approach [377], given by the red line in Fig. 8.4. We emphasize that this is a theoretical upper bound for a linear optics based BSM, assuming ideal single-photon sources and detectors and balanced basis choices. The measured sifted key rates of the memory-based device are plotted as open circles in Fig. 8.4. Due to the high overall heralding efficiency and the large number of photonic qubits per memory time (up to $N = 504$), the memory-

167

assisted sifted key rate exceeds the capability of a linear-optics based BSM device by a factor of 78.4 ± 0.7 at an effective channel loss of about 88 dB.

In practice, errors introduced by the quantum memory node could leak information to the environment, reducing the quality and potential security of the sifted key [373]. A shorter secure key can be recovered from a sifted key with finite QBER using classical error correction and privacy amplification techniques. The fraction of distilled bits r_s that can be secure against individual attacks rapidly diminishes [29] as the QBER approaches $E_i = 0.147$. For each value of the effective channel loss, we estimate the QBER and use it to compute r_s, enabling extraction of distilled key rates R_S, plotted in black in Fig. 8.4. Even after error-correction, we find that the memory-assisted distilled key rate outperforms the ideal limit for the corresponding direct-transmission implementation by a factor of up to $R_S/R_{\max} = 4.1 \pm 0.5$ (± 0.1 systematic uncertainty, for $N = 124$). We further find that this rate also exceeds the fundamental bound on repeaterless communication [49] $R_S \leq 1.44 p_{A \to B}$ with a statistical confidence level of 99.2% ($^{+0.2\%}_{-0.3\%}$ systematic uncertainty, see appendix D.8). Despite experimental overhead time associated with operating the device (T_R in Fig. 8.1b), the performance of the memory-assisted BSM node (for $N = 248$) is competitive with an ideal unassisted system running at a $4\,\mathrm{MHz}$ average clock rate (appendix D.7).

168
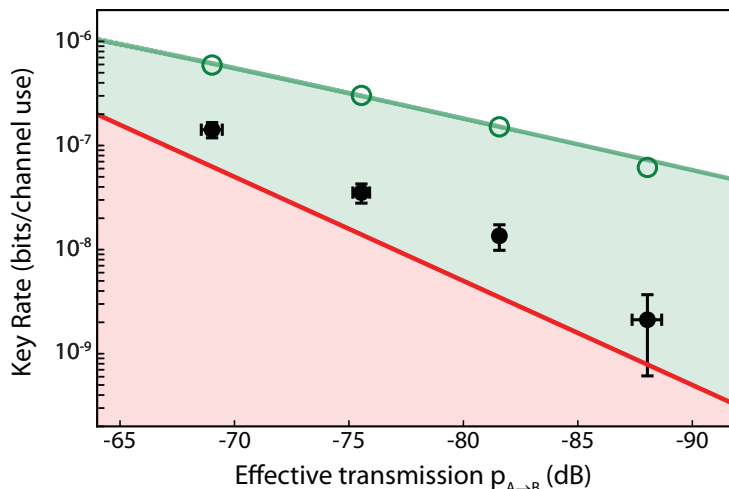
Figure 8.4: Performance of memory-assisted quantum communication. Log-log plot of key rate in bits per channel use versus effective channel transmission ($p_{A\to B} = \langle n \rangle_p^2$, where $\langle n \rangle_p$ is the average number of photons incident on the measurement device per photonic qubit). Red line: theoretical maximum for loss-equivalent direct transmission experiment. Green open circles: experimentally measured sifted key rate (green line is the expected rate). To ensure optimal operation of the memory, $\langle n \rangle_m = \langle n \rangle_p N \approx 0.02$ is kept constant (appendix D.6). From left to right, points correspond to $N = \{60, 124, 248, 504\}$. Black filled circles: distilled key rates R_S using memory device. Vertical error bars are given by the 68% confidence interval and horizontal error bars represent the standard deviation of the systematic power fluctuations.

8.5 Outlook

These experiments demonstrate a form of quantum advantage allowed by memory-based communication nodes and represent a crucial step towards realizing functional quantum repeaters. Several important technical improvements will be necessary to apply this advance for practical long-distance quantum communication. First, this protocol must be implemented using truly independent, distant communicating parties. Additionally, frequency conversion from telecommunications wavelengths to 737 nm, as well as low-loss

169

optical elements used for routing photons to and from the memory node, will need to be incorporated. Finally, rapid generation of provably secure keys will require implementation of decoy-state protocols [381], biased bases [382], and finite-key error analyses [383], all compatible with the present approach. With these improvements, our approach is well-suited for deployment in real-world settings. It does not require phase stabilization of long-distance links and operates efficiently in the relevant regime of $p_{A \to B} \approx$ 70 dB, corresponding to about 350 km of telecommunications fiber. Additionally, a single device can be used at the center of a star network topology [384], enabling quantum communication between several parties beyond the metropolitan scale.

Furthermore, the present approach can be extended along several directions. The use of long-lived ^{13}C nuclear spin qubits could eliminate the need to operate at low total $\langle n \rangle_m$ and would provide longer storage times, potentially enabling hundred-fold enhancement of BSM success rates [77, 122]. Recently implemented strain-tuning capabilities [245] should allow for operation of many quantum nodes at a common network frequency. Unlike linear-optics based alternatives [379], the approach presented here can be extended to implement the full repeater protocol, enabling a polynomial scaling of the communication rate with distance [46]. Finally, the demonstrated multi-photon gate operations can also be adapted to engineer large cluster-states of entangled photons [385], which can be utilized for rapid quantum communication [144]. Implementation of these techniques could enable the realization and applications of scalable quantum networks [42] beyond QKD, ranging from non-local quantum metrology [62] to modular

170

quantum computing architectures [68].

9

Conclusion and outlooks

The realization of a large-scale quantum network is an immense scientific and technological challenge. In this thesis, we presented a series of experiments aimed at addressing this challenge using a platform based on environmentally insensitive color-centers embedded in diamond nanophotonic structures [50, 74–78]. We showed that color-centers with inversion symmetry could be incorporated into nanoscale structures that enable extremely strong atom-photon coupling strengths without sacrificing optical coherence properties. The resulting devices are nonlinear at the level of single photons, enabling the first observation of optical photon-mediated interactions between two emitters. By developing techniques for simultaneous optical access to and coherent microwave control of color-center spins at millikelvin temperatures, we realized a nanophotonic quantum memory node which for the first time satisfies all of the key requirements of a

172

quantum network node. These advances culminated in the first experimental realization of memory-enhanced quantum communication, signaling the maturity of diamond nanophotonic devices for functional quantum networks.

The progress described here lays the foundation for three major near-term experiments, each of which should have a significant impact of the field of quantum information science. First, a quantum communication experiment identical to the one described in chapter 8 distributed over metropolitan-scale links, incorporating elements such as efficient frequency conversion [111, 386] and timing synchronization, demonstrates the promise of integration of quantum memories into practical metropolitan links [387]. Second, recent (soon to be published) progress involving high-fidelity multi-qubit operation, combined with newly developed quantum gates between emitters with different resonance frequencies, can be used to implement rapid entanglement distribution and purification between remote nodes [120, 121]. Once high fidelity entanglement can be distributed rapidly enough, it can be used for implementation of device-independent quantum key distribution [34, 55], which is a clear application of quantum technology that cannot be achieved by any classical means. Finally, efficient photon outcoupling and coherent nuclear spin control, combined with (soon to be published) deterministic generation of pulse-shaped single-photons, will enable generation of trains of entangled cluster states of photons [141, 142, 388, 389], which are the base resource for measurement-based quantum computing and rapid one-way quantum communication protocols [47, 385]. By increasing optical coupling efficiencies, such experiments could

open up the field of loss-tolerant all-photonic quantum information processing [48, 135], a potentially more resource-efficient approach for scaling up quantum computers and networks. All three of these promising near-term experiments demonstrate the immense potential of the platform presented here for future quantum optical technologies.

Despite this remarkable progress, key practical challenges must be addressed before quantum network nodes can be deployed on a large scale [390]. Quantum network nodes must be made compatible with high-bandwidth, long-distance networks. This will require several advances across quantum information science and engineering. Protocols for the rapid distribution, purification, and application of entanglement will need to be implemented and tested. In parallel, major advances to hardware, including nanofabricated devices, cryogenic systems, high-frequency control electronics, stable laser systems, and efficient optical interconnects, will be required to continue such developments.

One necessary advance beyond the work presented here is the integration of nuclear spin memories with quantum networking protocols to enable entanglement purification and error correction, mentioned briefly above [79, 122]. Radio-frequency control of ^{13}C and ^{29}Si nuclear spins will be required to perform high fidelity single and two-qubit operations required for such schemes. While initial results towards constructing multi-qubit registers in diamond are promising (chapter 6) [19], reliable and scalable control of such registers in cryogenic conditions will require development of lower loss (ideally superconducting) on-chip control electronics. Advances in fabrication of type-II superconductors, such as Nb and NbTiN, which can potentially deliver high critical currents

174

in the presence of large external magnetic fields [391, 392], as well as incorporation with existing diamond nanofabrication techniques will be leveraged to enable these advances.

Once bandwidth limitations of individual quantum memories are saturated, efficient channel multiplexing will need to be incorporated into quantum networking protocols, including frequency-domain multiplexing [393] and rapid photon routing to multiple physical devices operating in parallel on-chip [235]. Improvements in diamond fabrication techniques, including a transition to rectangular cross-section devices compatible with on-chip photon routing and incorporation of DC electrodes for strain tuning [245] will help to facilitate experiments with several emitters in a single cryostat. Advances in permanent and robust fiber packaging of nanophotonic samples will also be required to improve yields of such efforts. For compatibility with long-distance fiber networks, efficient frequency conversion to and from telecommunications wavelengths is also needed. Recent advances in the nanofabrication of nonlinear optical materials such as lithium niobate [394] can be leveraged to enable efficient frequency modulators and shifters, switches, and frequency converters essential for many of these tasks.

While these advances would increase the density of qubits per node, improvements in laboratory control equipment are needed to reduce the cost per node, and allow for reliable, automated operation, making large-scale deployment of quantum networks feasible. Current experiments are conducted with general purpose laboratory tools which are expensive and not tailored for the application at hand. Customized, miniaturized cryostats that are optimized for a combination of cost, cryogenic resources, cooling

175

power, base temperature, and peripheral support will need to be specially designed for such quantum network nodes. Lasers, optics, and electronic control systems such as microwave sources, arbitrary waveform generators, and time-taggers will need to be integrated into dedicated packages with convenient, stable, and scalable software interfaces. Quantum network technologies can borrow from recent advances in highly packaged control systems currently being developed in industry for quantum computers, but will need further customization, such as the implementation of distributed clock synchronization equipment and distributed client-server control software architectures.

In addition to these technical efforts, some of the main challenges in scaling and deploying quantum network nodes may be addressed with more fundamental research and spectroscopy. Different materials systems (see chapter 3.3.3) might offer unique advantages over the diamond nanophotonic platform presented here. Emerging systems, such as defects in silicon, are not yet well understood or established as spin-photon interfaces. However, such a platform might be able to solve a number of challenges, such as the ability to operate at comparatively higher temperatures, or the ability to use more mature fabrication techniques. For this reason, fundamental research and spectroscopy is needed to continue to identify, characterize, and test emerging systems as candidates for quantum network nodes that may be easier to operate in the long-term.

The combination of serious technical challenges and fundamental research remaining on the path to quantum networks raises the question: should we fully pursue the SiV-nanophotonic platform, or search for an improved materials system before tackling the

176

formidable engineering challenges described above? The knowledge and tools acquired by continuing to study and apply the SiV-cavity system, ranging across quantum optics, materials science, condensed-matter physics, nanofabrication, and electrical engineering, will be essential to the construction of future quantum networks, regardless of which materials platform is used in the end. The experiments presented in this thesis are evidence of just that; the rapid transition from the basic physical characterization presented in chapters 4 and 5 to system-level application of the same types of devices for novel quantum communication protocols (chapter 8) was enabled by decades of understanding and progress in the quantum control of related platforms, including the quantum control of NV center and ^{13}C spins in diamond [19, 81], as well as self-assembled quantum dots in nanofabricated GaAs photonic crystals [17, 395]. The techniques developed for those platforms were directly applied in the experiments presented in this thesis; similarly, experimental progress with the SiV center in diamond will be used in the construction of next-generation quantum networking technology. At the same time, the advances presented in this thesis would not have been possible without spending several years to address serious technical advances in areas such nanofabrication and cryogenic experimentation techniques. Therefore, the work presented in this thesis provides evidence for a multi-faceted approach towards realizing quantum networks: one in which engineering progress should be prioritized and leveraged to explore state-of-the-art quantum networking protocols with silicon-vacancy centers, while fundamental materials research continues in parallel.

A

Supporting material for chapter 4

A.1 Experimental setup

All experiments at $T = 5\,\mathrm{K}$ are performed in a modified liquid helium flow probestation (Desert Cryogenics model TTP4). We use a dual-axis scanning galvonometer mirror system (Thorlabs GVS012) and a high NA objective (Olympus 100x 0.90 NA) to deliver light via free-space in the experiments presented in Fig. 4.1-4.4, S1 [87]. We use a 520 nm diode laser (Thorlabs LP520-SF15) for off-resonant continuous-wave excitation [Fig. 4.1(b) and Fig. 4.2(c)] and a pulsed 532 nm laser (PicoQuant PDL 800-B) to perform lifetime measurements [Fig. 4.2(d) and Fig. A.1]. We employ sum-frequency generation using a nonlinear crystal (ADVR KTP), mixing $\sim 980\,\mathrm{nm}$ laser light from a Ti:Sapphire laser (M-Squared SolsTiS-2000-PSX-XF) and 1550 nm

laser light from an external cavity diode laser (Thorlabs SFL 1550P) in a fiber-based wavelength division multiplexer (Thorlabs WD202A-APC). The output fiber is cleaved and coupled to a waveguide in the nonlinear crystal, which has $\sim 1\,\mathrm{nm}$ bandwidth. We tune the frequency of the Ti:Sapphire laser to modulate the frequency of the $\sim 600\,\mathrm{nm}$ light. The wavelength is recorded on a high resolution wavemeter (High Finesse WS7) with $10\,\mathrm{MHz}$ resolution and $50\,\mathrm{MHz}$ accuracy.

GeV centers are incorporated into devices at low density using $^{74}\mathrm{Ge}^+$ ion implantation (Innovion Corporation, $10^9\ \mathrm{Ge}^+/\ \mathrm{cm}^2$ at an energy of $275\,\mathrm{keV}$) and subsequent high temperature annealing at $1200\,^\circ\mathrm{C}$ in vacuum. Waveguides are oriented along the $\langle 110 \rangle$ axis of the diamond. Confocal microscopy is used to collect light in the experiments presented in Fig. 4.1(b), Fig. 4.2(d), and Fig. A.1. In all other experiments, light in the waveguide is collected using a tapered optical fiber [184]. Technical details on fiber coupling and calibration of coupling efficiency are given in the supplementary materials of [87]. Single photons are detected on an avalanche-photodiode (APD - Excelitas SPCM-ARQH).

A.2 GeV-waveguide coupling efficiency

We define the GeV-waveguide coupling efficiency β as the probability for the GeV to emit a photon into the waveguide mode per excitation. To estimate β, we measure the saturation of ZPL fluorescence from a single GeV center in a waveguide [Fig. 4.2(b)].

We fit to a two-level model of saturation $D = D_{max}I/(I + I_{sat})$ where D and D_{max} are the detected and maximum possible detected intensities respectively, and I and I_{sat} are the applied and saturation intensities respectively. This predicts a maximum detected count rate of $D_{max} = 0.79 \pm .02$ Mcps.

Since we filter for ZPL photons (Semrock FF01-605/15-25), we collect roughly 60% of the total emission spectrum given by the ZPL branching ratio [195]. We only collect the photons emitted into the direction of the tapered fiber, resulting in another factor of 0.5. Next we account for coupling to the tapered fiber (~ 0.5), transmission through two 90:10 beamsplitters (Thorlabs TW670R2A2) in the fiber network (~ 0.8), and re-collimation into fiber after a spectral filter (Semrock TLP01-628-25x36, free space-fiber coupling efficiency ~ 0.8). We send the light to an APD which has detector quantum efficiency ~ 0.6 at $\lambda = 600$ nm.

The maximum single-photon detection rate is given by one photon per excited state lifetime (6.6 ± 0.3 ns), yielding a rate of about 160 Mcps. Accounting for all of the factors described above, we expect a count rate of ~ 8 Mcps assuming the GeV emits every photon into the waveguide mode. From the maximum detection rate ~ 0.8 Mcps, we can place a lower bound on the probability of emission into the waveguide $\beta \geq 0.1$.

This is lower than the simulated value for β in the designed nanostructure, which is roughly 0.7 (Lumerical). The angle of the GeV dipole with respect to the waveguide and improper placement of the GeV with respect to the waveguide mode maximum likely limit the GeV-waveguide coupling in this experiment. We also note that this is a lower

bound for β, since we do not account for time spent in unknown dark states such as different charge states of the GeV center.

A.3 Linewidth measurements

In Fig. 4.3(a) we measure the linewidth of transition 1-3 [Fig. 4.1(b)] at $T = 5\,$K for a single GeV in a waveguide using photoluminescence excitation (PLE) spectroscopy. The frequency of the excitation laser is scanned over the resonance several times, and fluorescence in the phonon sideband (PSB) is sent to an APD. We sum the different line-scans without correcting for background or spectral diffusion shifts of the line-position. We fit a Lorentzian to the integrated data in the main text and find a full-width at half maximum of $\gamma/(2\pi) = 72.8 \pm 1.4\,$MHz, where the error given is the fit error to the data.

We note that the measurement of narrow GeV resonances in waveguides is not limited to this single GeV center. For a total of 6 different GeV centers in waveguides, we observe an average linewidth of 100 ± 28 MHz at $T = 5\,$K. While further work is needed to establish reliable statistics for GeV linewidths, these results demonstrate the reproducibility of narrow GeV optical transitions in nanostructures. Additionally, PLE spectroscopy of GeV centers in bulk diamond at $T = 2.2\,$K, carried out in [180], demonstrates a narrow $42\,$MHz line that is stable over long timescales.

We measure the excited state lifetime to extract the lifetime-limited linewidth for the GeV center described in the main text using pulsed off-resonant $532\,$nm excitation.

181

We record the decay of ZPL fluorescence in the time-domain using fast acquisition electronics (PicoQuant HydraHarp 400) and fit to a bi-exponential model that accounts for the sharp background from the strong laser pulse with the first exponent, and the lifetime of the GeV excited state with the second exponent. This is the same technique used to determine GeV lifetimes in Fig. 4.2(d). For this GeV, we measure a lifetime $\tau_0 = 6.1 \pm 0.2$ ns, shown in Fig. A.1. From this measurement we extract a lifetime-broadened linewidth of $\gamma_0/(2\pi) = 26 \pm 1$ MHz.

We probe the contribution of phonon relaxation between orbital sublevels to the optical transition linewidth of several GeV centers for temperatures between $T = 35\,\mathrm{K}$ and $T = 350\,\mathrm{K}$ [Fig. 4.3(a) inset] using off-resonant $520\,\mathrm{nm}$ excitation and recording the linewidth on a spectrometer (Horiba iHR550 with Synapse CCD and 1800 gr/mm, resolution 0.025 nm). The transition linewidth scales as T^3 (see main text for fit details). The T^3 fit implies that a two-phonon process is the dominant broadening mechanism at $T > 50\,\mathrm{K}$, similar to the case of the SiV [193]. We note that at temperatures $T > 100\,\mathrm{K}$, the line is too broad to resolve the fine structure exactly, and we measure collective features from transitions C and D. For $T > 200\,\mathrm{K}$, all four lines merge to give one linewidth. These imperfections only modify the measured linewidth by a small multiplicative factor, and the T^3 fit remains effective.
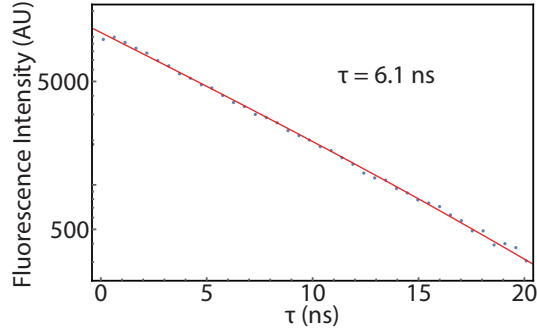
Figure A.1: Lifetime measurement of the GeV used for Fig. 4.3-4.5 in the main text. Pulsed 532 nm excitation is applied. ZPL fluorescence is plotted on a log scale as a function of time τ from pulse leading edge.

A.4 Optical Rabi oscillation measurements

In order to probe optical relaxation dynamics at higher resonant excitation intensities, we utilize an active preselection sequence. We first probe the resonance with a weak resonant pulse, and detect scattered PSB photons on an APD. Using a fast counter on a field-programmable gate-array (Lattice Diamond MachXO2HE), we determine if the GeV satisfies the resonance condition based on whether or not the GeV scatters more photons than a user-defined threshold. If the GeV is not on resonance, we apply a strong 520 nm pulse which further speeds up spectral diffusion, randomizing the resonance position. We then repeat the procedure until the GeV scatters the threshold number of photons and is determined to be on resonance. By optimizing the power and duration of the various pulses as well as the photon detection threshold, we can maintain an experimental duty cycle of $\sim 50\%$ while remaining on resonance.

183

We utilize this sequence to measure optical Rabi oscillations with the same GeV center described in the PLE measurement in Fig. 4.3(a). Once we determine that the GeV is on resonance, we apply a strong 40 ns resonant pulse and measure the fluorescence on the PSB in the time-domain [Fig. 4.3(b)] using fast acquisition electronics. We fit to the data using a two-level model of exponentially decaying oscillations of the form $(g/2)\Theta(t-t_0)(1-\mathcal{C}\exp\left(-|t-t_0|/\tau_{Rabi}\right)\cos\left(2\pi\Omega(t-a)\right))$. Here g is an amplitude normalization factor, $\Theta(t-t_0)$ is a step function at a time $t = t_0$ of the pulse leading edge, $\mathcal{C}$ is the contrast of Rabi oscillations, τ_{Rabi} is the decay constant of Rabi oscillations, and Ω is the Rabi frequency. For the measurement shown in the main text, we obtain $\mathcal{C} = 0.71 \pm 0.03$, $\Omega = 310 \pm 2$ MHz, and $\tau_{Rabi} = 6.59 \pm 0.02$ ns.

We repeat this measurement and fitting protocol at various temperatures up to $T = 10$ K, at which point the Rabi oscillations decay too fast to resolve and fit effectively. We measure τ_{Rabi} as a function of temperature and plot the Rabi oscillation decay rate $\gamma_{Rabi}/(2\pi) = 1/(2\pi\tau_{Rabi})$ as a function of temperature [Fig. 4.3(b) inset]. At low temperatures ($T < 10$ K) the decay rate of Rabi oscillations scales linearly with temperature. We fit to a linear model $\gamma_{Rabi}/(2\pi) = h + kT$ and obtain $h = -7.0 \pm 1.3$ MHz, and $k = 6.6 \pm 0.2$ MHz/K. The linear dependence of Rabi oscillation decay indicates that the transition is primarily broadened by a single phonon process at low temperatures between $T = 5$ K and $T = 10$ K, again similar to the case of the SiV [193].

For all temperature measurements, temperature is measured using a diode (Lakeshore DT-670A-CU) mounted to the sample holder. As a result, we do not probe the local

temperature of the diamond nanostructure, potentially resulting in a small systematic temperature shift ($\sim 1\,\mathrm{K}$) for all reported values. We note that this does not influence the linear and cubic scalings of Rabi oscillation decay and linewidth at low and high temperatures respectively.

A.5 GeV-waveguide cooperativity

We calculate the cooperativity using the measured extinction in Fig. 4.4(b) following [321]. The measurement is taken at $I/I_{sat} \sim 0.02$, satisfying the condition for low power ($\Omega_c/\Gamma \ll 1$ in [321]). In this limit, the transmitted intensity on resonance ($\mathcal{T}$) is related to the cooperativity by $\mathcal{T} \approx (1+C)^{-2}$. We fit a Lorentzian to the transmission data to extract a measured extinction of $18 \pm 1\%$, corresponding to $\mathcal{T} = 0.82 \pm 0.01$, yielding a cooperativity of $C = 0.10 \pm 0.01$, as reported in the main text.

We note that this is a lower bound on the cooperativity, since this formula for cooperativity is for a two-level system. Finite thermal occupation of the upper branch of the ground state [state 2 in Fig. 4.1(b)] reduces the measured extinction. One can approach the expected extinction of a two level system by polarizing the system in state 1 using optical pumping [87]. The presence of additional levels also reduces the measured extinction due to the branching ratios of different transitions (e.g. transition 2-3 and the PSB). Line-broadening mechanisms discussed above also reduce the system cooperativity. Furthermore, the same factors limiting the waveguide-GeV coupling β

also limit the cooperativity in this experiment.

The quantum efficiency, QE, is defined as the ratio of the radiative decay γ_{rad}, to the total excited state decay γ_0 [183]. Because $\Gamma_{1D} < \gamma_{rad}$ and $\gamma_0 < \Gamma'$ due to the ZPL branching ratio and line-broadening, the cooperativity naturally places a lower bound on the quantum efficiency: $C = \Gamma_{1D}/\Gamma' < \gamma_{rad}/\gamma_0 = QE$. From the measurement in Fig. 4.4(b), we extract $C > 0.1$. Accounting for additional measured factors that reduce the cooperativity, but not the quantum efficiency, such as line-broadening beyond the lifetime limit ($26\,\mathrm{MHz}/73\,\mathrm{MHz} \sim 0.4$) and the branching ratio into the ZPL (~ 0.6), we can place a tighter lower bound on the quantum efficiency $QE > 0.4$.

A.6   Homodyne measurement

In this measurement, we excite through one port of a $90:10$ beamsplitter connected to the tapered fiber, sending 10% of the near resonant excitation laser light to the diamond waveguide. We collect light through the fiber on the adjacent 90% port of the beamsplitter. The detected ZPL field consists of interference between two fields: a local oscillator field $\mathbf{E}_{LO}$ arising from partial reflection of the driving laser from the Bragg mirror and resonance fluorescence $\mathbf{E}_{RF}$ stimulated by the driving field.

The diamond waveguide has two orthogonal polarization modes (TE and TM) [266], which in principle can be treated independently. We neglect higher order waveguide modes which couple weakly to the fiber. The relative weights between $\mathbf{E}_{RF}$ and $\mathbf{E}_{LO}$

will differ for the two modes depending on their projections onto GeV dipole axis and the reflectivities of TE and TM fields from the Bragg mirror. The relative phases between the fields will also differ for TE and TM inputs due to the difference in waveguide group velocity for the TE and TM modes, allowing us to vary the phase by changing the input polarization.

Instead of treating the two modes separately, we consider an intuitive single-mode interference picture where $E_{RF} = \alpha S(\Delta) E_{LO} e^{i\phi}$. Here α and ϕ are free parameters that characterize the relative weight and phase of the two fields. $S(\Delta) = (1 - 2i\Delta/\gamma)^{-1}$ accounts for the Lorentzian resonance fluorescence spectrum for a given drive detuning Δ and transition full-width γ. In this model, the detected intensity is proportional to $|1 + \alpha S(\Delta) e^{i\phi}|^2$. We fit this model to the data presented in Fig. 4.5(b) of the main text leaving α and ϕ as free, continuous parameters ($\alpha \in [0, 1]$ and $\phi \in [0, 2\pi)$). Using this technique, we determine relative phases $\phi = (0.98 \pm 0.02)\pi$ for the absorptive profile (orange) and $\phi = (1.66 \pm 0.01)\pi$ for the dispersive profile (blue). Intuitively, a relative phase of π $(3\pi/2)$ produces the typical absorptive (dispersive) Lorentzian lineshape evident in the measured interference spectrum.

We note that the single-mode model is an incomplete description of the homodyne measurement. We treat the problem of single-mode interference with a tunable relative phase because the two-mode problem introduces several additional free-parameters, and the single-mode picture captures the essential interference phenomenon present in the homodyne measurement. Additionally, there exist higher order terms resulting from in-

187

teractions between the reflected field and the GeV center, as well as GeV self-interaction arising from the mirror. These terms are suppressed by the mirror reflectivity $R < 0.25$ and can in principle be incorporated into the model by redefining α and ϕ. We neglect these higher order terms to preserve the simple physical interpretations of α and ϕ as the relative weight and phase between two fields.

To demonstrate the single-photon nonlinearity, we measure the photon statistics of the output field under a drive field with polarization that produces destructive interference ($\phi \sim \pi$). We split the output field on a $50 : 50$ beamsplitter and measure time dependent correlations using fast acquisition electronics. The total acquisition time for this measurement was ~ 5 hours. We postselect coincidence events that occur within 10 ms intervals for which the detected intensity is below 15% of the steady state detuned value, ensuring that we include only data for which the drive field is nearly resonant with the GeV center ($\sim 25\%$ duty cycle). We fit to the data using a single exponential of the form $1 + he^{-t/\tau_b}$ to obtain the reported bunching $g^{(2)}(0) = 1 + h = 1.09 \pm 0.03$ decaying on a timescale $\tau_b = 6.2 \pm 2.7$ ns, close to the GeV excited state lifetime.

B

Supporting material for chapter 5

B.1 EXPERIMENTAL SETUP

B.1.1 CONFOCAL MICROSCOPY INSIDE A DILUTION REFRIGERATOR

All experiments are carried out in a dilution refrigerator (DR: BlueFors BF-LD250) with

free-space optical access (see Fig. B.1). To perform scanning confocal microscopy, we use

a dual-axis scanning galvonometer mirror system (Thorlabs GVS012), two concatenated

$4f$ lens systems ($f_1 = f_3 = 25\,\mathrm{cm}$, $f_2 = 30\,\mathrm{cm}$, $f_4 = 20\,\mathrm{cm}$) consisting of anti-reflection

coated, 40 mm-diameter cemented achromatic doublets (VIS-NIR, Edumund Optics)

and a vacuum- and cryo-compatible objective (Attocube LT-APO-VISIR, $\mathrm{NA} = 0.82$)

to deliver light to the diamond nanodevice. Light reflected from the sample through

the microscope is partially reflected by a 33:67 pellicle beam splitter to a CCD camera

for imaging.

A 6-1-1 T superconducting vector magnet (American Magnetics Inc.) is mounted below the mixing chamber (MXC) and thermally linked to the 4 K plate of the DR. The magnet is operated in persistent current mode to maximize the stability of the applied field used for Zeeman splitting of the SiV spin states. The diamond substrate containing the nanodevices is soldered with indium to a copper sample stage and placed inside the magnet bore. A temperature sensor (Lake Shore Cryotronics, RX-102B-CB) is attached to the sample holder and measures a base temperature of 85 mK.

The objective lens is mounted on a piezoelectric stepper (Attocube ANPx311) via an L-bracket. We use the stepper to move the objective to adjust the focus. The sample stage sits directly beneath the objective, next to an aluminum mount which holds the tapered tip of the optical fiber, through which light exits (and, in some experiments, enters) the DR. The fiber holder is mounted on a stack of 3-axis piezoelectric steppers ($2\times$ Attocube ANPx101, $1\times$ Attocube ANPz101). These steppers are used to position the fiber relative to the nanodevice, allowing us to maximize the coupling efficiency to the tapered diamond waveguide and couple to multiple devices without bringing the DR above 4 K or exchanging the sample. The sample stage and fiber mount stepper stack are both on the copper science plate, which is attached to a separate stack of x- and y-axis piezoelectric steppers ($2\times$ Attocube ANPx311) on top of the base plate. These steppers are used for simultaneous positioning of both the sample stage and the fiber mount relative to the microscope objective.

190
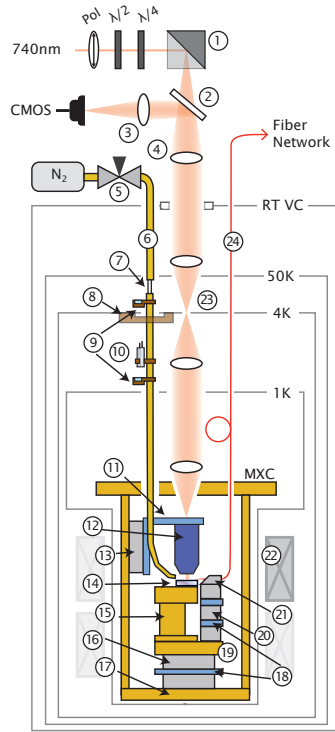
Figure B.1: Schematic of the confocal microscope inside a dilution refrigerator (DR). RT VC: Outer vacuum can at room temperature; 50K: 50 K plate; 4K: 4 K plate; 1K: 1 K plate; MXC: Mixing chamber plate; CMOS: CMOS camera; Pol, $\lambda/2$, $\lambda/4$: Polarizer, half-wave plate, quarter-wave plate; 1: dual-axis scanning galvonometer mirror system (Thorlabs GVS012); 2: 33:67 pellicle beam splitter; 3: achromatic lens ($f = 10$ cm); 4: 40 mm diameter achromatic lenses ($f_1 = f_3 = 25$ cm, $f_2 = 30$ cm, $f_4 = 20$ cm); 5: tunable leak valve (VAT Series 211 DN 16 No. 21124-KE0X-000); 6: Copper tube which delivers the N_2 for gas tuning (see sec. B.1.4); 7: PTFE thermal break; 8: copper thermal link; 9: temperature sensors (Lake Shore DT-670); 10: resistive cartridge heater (Lake Shore HTR-50); 11: objective L-bracket; 12: vacuum- and cryo-compatible objective (Attocube LT-APO-VISIR, NA = 0.82, focal length = 2.87 mm); 13: piezoelectric stepper (Attocube ANPx311) which adjusts the focus of the objective; 14: diamond substrate containing nanodevice; 15: sample stage; 16: piezoelectric steppers (Attocube ANPx311) which position the stage and fiber mount laterally; 17: base plate; 18: aluminum thermalization plates; 19: science plate; 20: piezoelectric steppers (Attocube: $2\times$ ANPx101, $1\times$ ANPz101) which position the fiber mount; 21: fiber mount; 22: 6-1-1 T superconducting vector magnet with persistent switches (American Magnetics Inc. MAxes); 23: 10 mm aperture at 4 K plate of the DR; 24: single-mode fiber (S630-HP). All parts shown in brown or gold are copper (C101). All parts shown in light blue are aluminum (Al 6061).

The base plate is connected to the MXC via thick copper beams which provide a thermal connection as well as a rigid mechanical link, minimizing vibrations propagating mostly from the pulse tube and hence reducing the pointing error of the confocal microscope to approximately $1\,\mu$m in amplitude. The sample stage, objective L-bracket and aluminum thermalization plates (inserted between neighboring base steppers) are also thermally anchored to the MXC via connection to the base plate by oxygen-free copper braids (Copper Braid Products, not shown in Fig. B.1). This ensures rapid thermalization of the entire sample stage setup and inhibits slow mechanical drift of the fiber and objective during the experiment.

B.1.2 EXCITATION AND READOUT OF THE DIAMOND NANODEVICE

A full description of the diamond nanodevice design, properties, and fabrication are presented elsewhere [184]. The nanodevice consists of a 1D photonic crystal cavity symmetrically coupled to a waveguide. The waveguide has two ports. The first port is a notch that couples free-space light entering from the confocal microscope into the waveguide. Light entering through this path is used for resonant excitation of the SiV and cavity modes and comes from narrowband lasers [Newport TLB-6711, M-Squared SolsTiS-2000-PSX-XF and a home-built external-cavity diode laser (Opnext Diode HL7302MG, Littrow configuration)]. In some experiments (see appendix B.7.1), these lasers are modulated using an electro-optic phase modulator (EOSPACE model PM-0S5-10-PFA-PFA-740-SUL) with microwave sources (MW: Agilent 83732B and Hittite HMC-T2220)

to generate additional optical frequencies. The second port is the tapered end of the nanobeam waveguide, which is contacted to the tapered tip of a single mode optical fiber. The coupled fiber is then used to collect light from the cavity mode propagating out of the waveguide. Our techniques for chemically fabricating the tapered fiber and performing the coupling are described in previous works [87, 184]. We also apply pulses from a 520 nm diode laser (Thorlabs LP520-SF15) via the tapered fiber, as shown in Fig. B.2, for charge-state control of the SiV (described in detail in appendix B.7.1).

B.1.3 Fiber-based photon collection and polarization control

A fiber-based optical network (Fig. B.2) is used to efficiently collect light transmitted through the waveguide. In this section, we discuss the use of this fiber network to measure the coupling efficiency of the tapered optical fiber to the diamond waveguide, to control the polarization of the input and output light in the fiber, and to measure the broadband response of the diamond nanocavity.

To couple the tapered fiber to the waveguide, we first send light from a supercontinuum light source (NKT Photonics SuperKExtreme) into the fiber network. The input light is spectrally filtered to an approximately 10 nm range around the SiV ZPL wavelength (Semrock FF01-740/13-25) and then sent into a 90:10 fiber beamsplitter, with 90% of the light sent to a calibration photodiode, and the remaining 10% sent into the diamond waveguide through the tapered fiber contact. The light reflected from the cavity is then split by two other 90:10 beam splitters, which send 1% of the final output

193
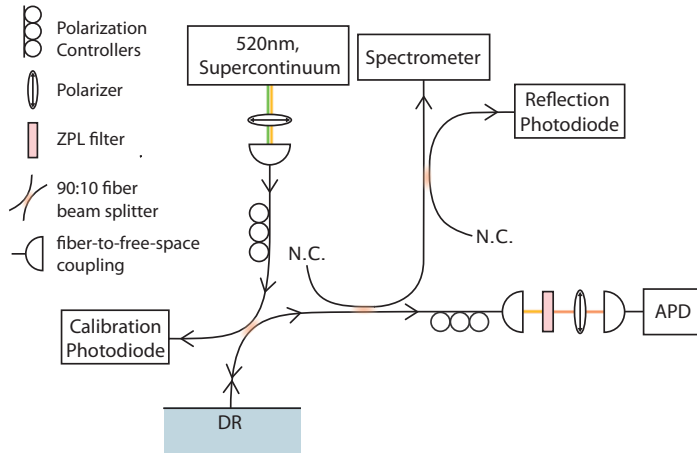
Figure B.2: Schematic of the fiber network used for efficient collection of light from the diamond waveguide. The polarization of the input and output light of the diamond nanocavity inside the DR is tuned via separate sets of polarizers and polarization controllers. The fiber-waveguide coupling efficiency is measured by splitting the light entering and exiting the DR to a calibration photodiode and a reflection photodiode, respectively, and comparing the two signals. The collected light is filtered through a narrowband filter (Semrock FF01-740/13-25) centered around the SiV ZPL wavelength before being detected. N.C. indicates no connection.

light to a reflection photodiode. The efficiency of the coupling between the fiber and the tapered end of the waveguide is calculated by comparing the incoming power and the reflected power measured from the two photodiodes. For this experiment, the frequency of the light is within the stopband of the photonic crystal cavity, and the polarization of the light is adjusted so that it couples only to the correct mode of the device (see below). Therefore, the light should be perfectly reflected. Imperfections in either of these areas will cause us to underestimate the coupling efficiency. For the experiments in this paper, we infer a fiber-waveguide coupling efficiency of approximately 50%.

We measure a transmission efficiency of approximately 10% along the fiber collection path, which accounts for losses from beam splitters, four fiber splices with an average efficiency of 80% per splice and the free-space frequency-filtering stage. With the fiber-waveguide coupling efficiency of around 50% described above and an SPCM efficiency of around 50%, the total detection efficiency of light from the diamond nanocavity is approximately 2.5%.

The waveguide supports two polarization modes: a transverse-electric-like (TE) mode corresponding to the cavity polarization and an orthogonal transverse-magnetic-like (TM) mode with no spectrally-similar cavity resonance. We tune the polarizations of both the input and output fields to address the TE mode of the device. The input resonant-excitation light beam consists of light from different narrowband lasers joined via fiber-based beamsplitters, and couples from free space into the waveguide. We control the polarization of this input field using a polarizer, half wave-plate, and a quarter wave-plate placed in the beam path as shown in Fig. B.1.

Polarization control of the output light transmitted through the diamond waveguide is achieved using the fiber network: First, light propagating out from the diamond waveguide couples to the tapered optical fiber which exits the DR. The light then passes through a polarizer and a set of polarization controllers before being filtered to a frequency range around the ZPL via a bandpass filter (Semrock FF01-740/13-25) in free-space and coupled back into a fiber and collected by a single-photon counting module ("SPCM"; Excelitas SPCM-NIR). By tuning the polarizer and polarization controllers

195

while monitoring the photon detection rate, we can minimize the detection rate at a frequency far detuned from the cavity resonance, where a non-zero spectrally-flat background signal indicates transmission of the TM mode. As a result, the relative signal from the cavity (TE) mode of interest is maximized.

We can also use the fiber network to perform characterization of the spectrum of the diamond nanocavity via reflection. For low-resolution characterization of the diamond nanocavity, light from the broadband supercontinuum laser (with no spectral filtering) is sent in from the fiber for non-resonant excitation of the system. A separate polarizer and set of polarization controllers tune the polarization of this input light to selectively address the nanocavity mode. Reflected light from the cavity is coupled back into the tapered fiber and collected through the fiber and sent to a spectrometer (Horiba iHR550 with Synapse CCD and $1800\,\mathrm{gr/mm}$) with a spectral resolution of $0.025\,\mathrm{nm}$.

B.1.4   Gas tuning of the nanocavity resonance

We tune the resonance wavelength of the diamond nanocavity by depositing solid N_2 on the diamond waveguide to change its refractive index. As shown in Fig. B.1, N_2 gas is extracted from a reservoir at atmospheric pressure via a tunable leak valve (VAT Series 211 DN 16 No. 21124-KE0X-000) into a copper tube. A vacuum gauge attached to the top of the tube is used to read out the pressure of the gas inside the tube. The tube extends into the DR and terminates at the sample stage, where N_2 exits and deposits onto the diamond nanocavity. To start the N_2 deposition, the temperature of the tube

196

is increased by applying power of around $10\,\text{W}$ to a heater resistor, attached to the tube directly below the $4\,\text{K}$ stage, and monitored by several temperature sensors (Lake Shore DT-670SD) placed along the tube. As the temperature of the tube increases, the pressure inside the tube, monitored on the vacuum gauge, initially rises. When the tube reaches a temperature of roughly 80-100 K near the $4\,\text{K}$ plate, the pressure reaches a maximum and then starts to decrease. At this time, residual frozen N_2 has unclogged inside the tube and begins to flow out and deposit onto the nanodevice. We then open the leak valve to let more N_2 into the tube while monitoring the cavity spectrum, and close the leak valve once we have observed a satisfactory shift in the cavity resonance wavelength. The leak rate is on the order of 10^{-2} mbar L/s, corresponding to a cavity resonance tuning rate of approximately 0.01 nm/s. The leak rate can be adjusted in real time to control the tuning rate. The heater is then switched off and the system equilibrates.

Crucially, the copper tube has a weak but non-negligible thermal link to the $4\,\text{K}$ plate, while being thermally isolated from the room-temperature environment via a PTFE thermal break below the $50\,\text{K}$ plate (see Fig. B.1). The copper tube is also carefully thermally isolated from the components of the experiment that are below $4\,\text{K}$. Therefore, when the heater is off, the tube equilibriates to around $4\,\text{K}$. Since this is well below the N_2 freezing point, N_2 cannot leak out of the tube. Thus, after gas tuning, the cavity resonance wavelength experiences no drift and has been measured to be stable (to within $5\,\text{GHz}$ or better) over several weeks.

197

While deposition of N_2 on the device increases the resonance wavelength, the amount of N_2 can also be reduced to incrementally decrease the resonance wavelength. This is done using the supercontinuum laser, which is typically used for low-resolution cavity spectra measurements through the tapered fiber connected to the diamond waveguide as described in appendix B.1.3. By applying this laser at higher power, we heat up the nanobeam and thus evaporate the deposited N_2. We can therefore tune the resonance wavelength of the cavity in both directions while simultaneously monitoring the cavity spectrum on the spectrometer.

B.2   Model for two SiV centers inside an optical cavity

To theoretically describe the transmission measurements described in Figures 1, 2, and 4 of the main text, we model the steady-state response of the SiV-cavity system in the linear regime using a non-Hermitian effective Hamiltonian. This approach accounts for photon loss through the cavity (decay rate κ) and through spontaneous emission (γ_i for SiV i). Because there is no distinction in this formalism between photon loss and pure dephasing of the optical excited state, the γ_i include all sources of decay and decoherence

for these states.[1] Recalling the Tavis-Cummings Hamiltonian for the N-emitter case,

$$H_{\text{TC,N}}/\hbar = \omega_c \hat{a}^\dagger \hat{a} + \sum_i^N \omega_i \hat{\sigma}_i^\dagger \hat{\sigma}_i + \sum_i^N g_i \left(\hat{a}^\dagger \hat{\sigma}_i + \hat{\sigma}_i^\dagger \hat{a} \right) \tag{B.1}$$

we write a non-Hermitian two-emitter Tavis-Cummings Hamiltonian [396]:

$$\hat{H}_{\text{TC}} = \left(\omega_c + \Delta - \frac{\delta}{2} - i\frac{\gamma_1}{2} \right) \hat{\sigma}_1^\dagger \hat{\sigma}_1 + \left(\omega_c + \Delta + \frac{\delta}{2} - i\frac{\gamma_2}{2} \right) \hat{\sigma}_2^\dagger \hat{\sigma}_2 + \left(\omega_c - i\frac{\kappa}{2} \right) \hat{a}^\dagger \hat{a}$$
$$+ \left[\hat{a}^\dagger \left(g_1 \hat{\sigma}_1 + g_2 \hat{\sigma}_2 \right) + h.c. \right] \tag{B.2}$$

where ω_c is the frequency of the cavity, Δ is the detuning between the center-of-mass frequency of the two SiVs $(\omega_1 + \omega_2)/2$ and the cavity mode, $\delta = \omega_1 - \omega_2$ is the detuning between the two SiVs and g_j is the single-photon Rabi frequency for SiV $j \in \{1, 2\}$. The operators $\hat{a}$ and $\hat{\sigma}_j$ are the annihilation operators for the cavity and SiV j excitations. The spectrum of this Hamiltonian gives the bright and dark state energies *e.g.* the red and blue lines in Fig. 5.4D, E.

To calculate the transmission of the system, we use the input-output formalism[397] to solve for the dynamics of the cavity field $\hat{a}$:

$$\dot{\hat{a}}(t) = -i \left[\hat{H}_{\text{TC}}, \hat{a}(t) \right] + \sqrt{\kappa_a} \hat{a}_{in}(t) + \sqrt{\kappa_b} \hat{b}_{in}(t) - \frac{1}{2}(\kappa_a + \kappa_b)\hat{a}(t), \tag{B.3}$$

---

[1]Note that for consistency with the literature, we have taken γ_i to be the *energy* decay rate, which therefore enters with a factor of $\frac{1}{2}$ in the non-Hermitian Hamiltonian (Eqn. B.2) for the field amplitudes. However, this means that pure dephasing at a rate γ_d should be included as $\gamma_i \to \gamma_i + 2\gamma_d$.
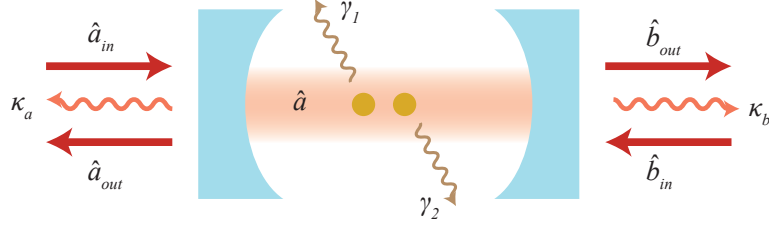
Figure B.3: Visual representation of the cavity input fields $\hat{a}_{in}$ and $\hat{b}_{in} = 0$, cavity output fields $\hat{b}_{out}$ and $\hat{a}_{out}$, intra-cavity field $\hat{a}$, cavity decay κ_a and κ_b and SiV i decoherence (including decay) γ_i.

Here, we have defined $\hat{a}_{\rm in}$ and $\hat{b}_{\rm in}$ as the input fields on either side of the cavity with $\kappa_{\rm a}$ and $\kappa_{\rm b}$ as the corresponding cavity energy decay rates and thus the total decay rate $\kappa = \kappa_{\rm a} + \kappa_{\rm b}$. See Fig. B.3. (In Eqn. B.3, we do not include the cavity decay term $i\kappa\hat{a}^\dagger\hat{a}$ in $H_{\rm TC}$ since this term is already included via $\kappa_{a,b}$.) We write down the equations of motion in the frequency domain, using

$$\hat{a}(t) = \int d\omega e^{-i\omega t}\hat{a}(\omega) \tag{B.4}$$

to arrive at:

$$
\begin{aligned}
-i\omega\hat{a}(\omega) &= \left(-i\omega_c - \frac{\kappa_{\rm a} + \kappa_{\rm b}}{2}\right)\hat{a} + \sqrt{\kappa_{\rm a}}\hat{a}_{\rm in} + \sqrt{\kappa_{\rm b}}\hat{b}_{\rm in} - ig_1\sigma_1 - ig_2\sigma_2 \\
-i\omega\hat{\sigma}_j(\omega) &= \left(-i\left(\omega_c + \Delta + (-1)^j\frac{\delta}{2}\right) - \frac{\gamma_j}{2}\right)\hat{\sigma}_j - ig_j^*\hat{a}
\end{aligned}
\tag{B.5}
$$

Eliminating the SiV degrees of freedom and solving for the cavity mode gives:

200

$$\hat{a}(\omega) = \frac{\sqrt{\kappa_a}\hat{a}_{in}(\omega) + \sqrt{\kappa_b}\hat{b}_{in}(\omega)}{D}, \tag{B.6}$$

where we have defined

$$D \equiv i(\omega_c - \omega) + \frac{\kappa_a + \kappa_b}{2} - \left(\frac{|g_1|^2}{-i\left(\omega_c - \omega + \Delta - \frac{\delta}{2}\right) - \frac{\gamma_1}{2}} + \frac{|g_2|^2}{-i\left(\omega_c - \omega + \Delta + \frac{\delta}{2}\right) - \frac{\gamma_2}{2}} \right). \tag{B.7}$$

In our case of interest, $\langle \hat{b}_{in} \rangle = 0$, and the transmission coefficient is $t = \langle \hat{b}_{out} \rangle / \langle \hat{a}_{in} \rangle$. Using the input-output relations $\hat{a}_{out} + \hat{a}_{in} = \sqrt{\kappa_a}\hat{a}$ and $\hat{b}_{out} + \hat{b}_{in} = \hat{b}_{out} = \sqrt{\kappa_b}\hat{a}$, we have

$$t(\omega) = \frac{\sqrt{\kappa_b \kappa_a}}{D}, \tag{B.8}$$

and thus the transmission intensity for the cavity field $T(\omega) = |t(\omega)|^2$ is,

$$T(\omega) = \frac{\kappa_a \kappa_b}{|D|^2} \tag{B.9}$$

This transmission response is accurate in both the resonant and detuned regime and agrees with numerical solutions of the master equation to better than a few percent. However, to more accurately model the spectra measured in the experiment, we additionally include a background term corresponding to the leakage of coherent laser light

into our detection path, resulting in a measured transmission intensity of

$$T(\omega) = |t(\omega) + Ae^{i\phi}|^2 \tag{B.10}$$

where A and ϕ are the amplitude and phase of the of the background field. This coherent background term, which has a flat frequency spectrum corresponding to, for example, transmission of the TM cavity mode which is imperfectly filtered out, is necessary to account for the lineshapes we observe, which do not agree perfectly with the prediction from Eqn. B.9. Addition of an incoherent background term does not appreciatively improve the agreement between the model and experiment. The solid curves in Figs. 5.1, 5.2 and 5.4 in the main text are all generated via this model.

B.3   SINGLE-SIV MEASUREMENTS

B.3.1   VERIFICATION OF SINGLE SIV CENTERS

In order to verify that the two emitters used in the measurements described in the main text are indeed single emitters, we separately measure the second-order correlation function $g^{(2)}(\tau)$ of the light transmitted via each of the two SiV-like dressed states (polaritons) in the dispersive regime ($\Delta > \kappa$). Here, τ is the delay time between detection of the second and first photon. We measure under conditions where the two SiVs are far detuned from one another ($\delta \sim 2\pi \times 5\,\mathrm{GHz}$), allowing us to measure one SiV at
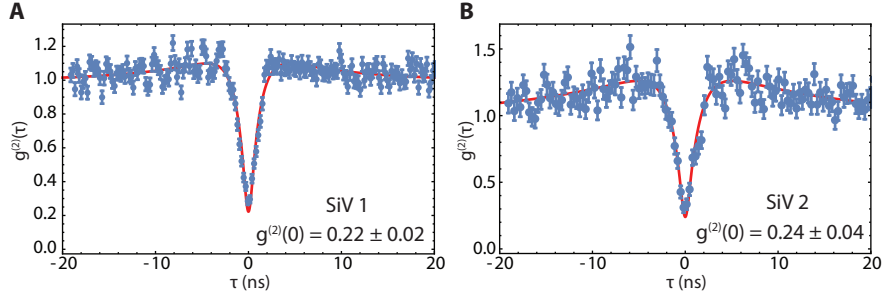
Figure B.4: Verification of single emitters. Photon autocorrelation function $g^{(2)}(\tau)$ for SiV 1 **(A)** and SiV 2 **(B)** in the main text. Error bars are given by shot noise, and red solid lines are a fit to a model given by a double-exponential convolved with a Gaussian of $350\,\mathrm{ps}$ width to account for finite APD timing resolution. From the fits, we extract timescales for antibunching and bunching $\{\tau_{a1}, \tau_{a2}, \tau_{b1}, \tau_{b2}\} = \{1.0, 1.3, 7.7, 13.4\}$ ns.

a time with negligible effects from their interaction. In this regime, each single SiV is only slightly dressed by the cavity mode, and acts as a transmission channel for single photons far detuned from cavity resonance. Therefore, in the ideal case, we expect $g^{(2)}(\tau = 0) \approx 0$ in transmission for single SiV-like polaritons. As explained below, a background field or limited cooperativity can increase the measured value of $g^{(2)}(0)$, but a value of $g^{(2)}(0) < 0.5$ confirms that the measured field corresponds to a single-photon emitter.

We employ an active preselection sequence described in detail in appendix B.7.1 in order to ensure initialization of each SiV in the correct charge and frequency state. These measurements are done at zero magnetic field when the spin sublevels are degenerate and only a single laser is needed to continuously scatter photons from a single SiV. The SiV-like polariton is probed in transmission and the transmitted light is split on a beamsplitter and sent to two SPCMs. Photon detection times are logged using fast

203

acquisition hardware (PicoQuant HydraHarp 400). We construct a histogram as a function of τ and normalize it to the background signal at long time delays.

We measure $g^{(2)}(0) = 0.22 \pm 0.02$ and $g^{(2)}(0) = 0.24 \pm 0.04$ in transmission on resonance with SiV 1 and SiV 2 respectively (Fig. B.4) with an SiV-cavity center-of-mass detuning of $\Delta = 2\pi \times 156\,\mathrm{GHz}$ at a sample temperature of $5\,\mathrm{K}$. No background subtraction or postselection is used. We measure bunching on a timescale significantly longer than the excited state lifetime for both SiVs, likely due to optical pumping into the metastable higher-energy orbital branch of the ground state [87, 179]. The finite value of $g^{(2)}(0)$ primarily arises from the coherent laser background, which is minimized relative to the single-photon transmission when the SiV is excited in the linear regime (low laser power).

B.3.2 EXTRACTION OF CAVITY QED PARAMETERS

In this section, we describe the measurements used to extract the cavity QED parameters (g, κ, γ). We extract $\kappa = 2\pi \times 48\,\mathrm{GHz}$, the cavity decay rate, by fitting the cavity spectrum to a Lorentzian when it is detuned from the SiV resonance by more than 5 cavity linewidths (Fig. B.5A). The measured cavity linewidth κ can change after the gas-tuning process, where the cavity loss rate can increase due to scattering or absorption introduced by the deposited material. This effect is not perfectly reproducible and may depend on the details of the gas deposition process. As a result, κ can vary by tens of perecent between different experiments. In order to account for this, we measure the

full cavity spectrum before each experiment and use the corresponding measured cavity linewidth as κ in the model for that particular experiment.

We extract $\gamma_1 = 2\pi \times 0.19\,\text{GHz}$, the bare (not cavity-enhanced) linewidth of the SiV, by fitting a Lorentzian to the transmission spectrum near the resonance of SiV 1 when the cavity is detuned by $\Delta = 6.8\kappa$ (Fig. B.5C). Note that this linewidth is a factor of two greater than the lifetime-limited linewidth of $\gamma_0 = 2\pi \times 0.094\,\text{GHz}$. In this measurement, extra care was taken to reduce the laser linewidth and power in order to prevent broadening of the measured SiV linewidth from either power broadening or spectral diffusion. Although the linewidth of SiV 2 was not measured carefully in this regime, we measured nearly-identical linewidths for the two SiVs (*cf.* Fig. 5.2A or Fig. 5.4B) at a variety of detunings, suggesting that $\gamma_1 \approx \gamma_2$. We extract $g_1 \approx g_2 = 2\pi \times 7.3\,\text{GHz}$, the single-photon Rabi frequencies for SiV 1 and SiV 2, by fitting Eqn. B.10 to the measurement in the bottom panel of Fig. 5.1C of the main text with the other CQED parameters fixed. In this fit we also leave the coherent background parameters free, obtaining $A = 0.37$ and $\phi = 0.21$.

The increased cooperativity in the present work compared to previous work [87] can be traced primarily to three factors: a slight increase in the cavity quality factor (8400 vs. 7400), an approximately sixfold decrease in the mode volume ($\sim$0.5 vs. $\sim$3) and a $\sim 50\%$ reduction in the SiV linewidth (190 MHz vs 300 MHz). Small variations in the SiV position in both works can also lead to some variation in the cooperativities.

In the future, the cooperativity achieved in this work can be increased in a number
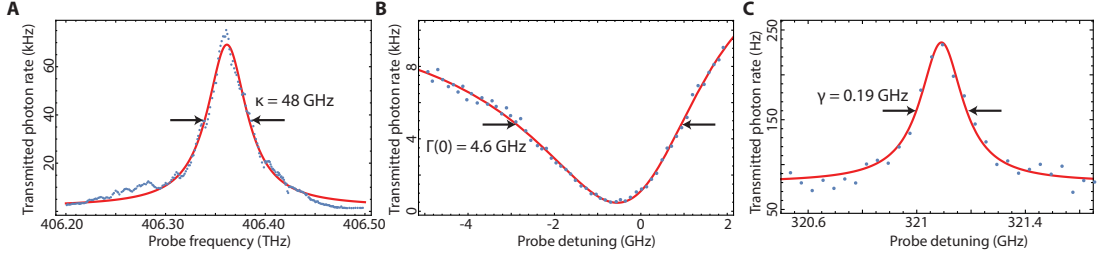
Figure B.5: Measurement of cavity and emitter linewidths (A) Typical measurement of cavity transmission spectrum far detuned from the emitter resonance, used to extract κ. **(B)** Lorentzian with coherent background (see appendix B.2) fit to on-resonance cavity transmission near SiV 1. The data (blue points) are the same as in the lower panel of Fig. 5.1C of the main text. **(C)** Linewidth measurement of SiV 1 when the cavity is $\sim 6.8\kappa$ detuned from the SiV resonance.

of ways. First, the cavity quality factor can be increased by several orders of magnitude with improved photonic crystal design and fabrication, in particular by improving masking and etching processes that currently lead to inhomogeneity in the holes defining the photonic crystal cavity [266]. At least another 30-50% reduction in the mode volume can be achieved through better photonic crystal cavity design [263]. A similar improvement in the implantation accuracy is possible either by tighter focus (and increased alignment accuracy) of the focused ion beam or by moving to a masked-implantation technique [398]. Finally, an increased understanding of the sources of spectral diffusion could allow us to reduce the SiV linewidth through, for example, new methods for materials processing. This could lead to an reduction in the linewidth (and therefore a proportional increase in the cooperativity) by a factor of up to two. Other color centers in diamond with a higher quantum efficiency [75] offer a similar benefit.

B.3.3 ADDITIONAL FACTORS INFLUENCING THE CAVITY TRANSMISSION SPEC-
TRUM

In the linear regime at $\Delta = 0$ the transmission through the cavity is given by $T \approx (1 + C)^{-2}$ (*cf.* Eqn. B.9). For the cooperativity $C = 23$ inferred here, the expected on-resonance transmission is $T = 0.002$, corresponding to a single-SiV cavity extinction of $\Delta T/T = 99.8\%$. This is more than the roughly 95% extinction demonstrated in Fig. 5.1C of the main text. This discrepancy is primarily due to imperfect polarization of the laser field. For our device (*cf.* appendix B.1.3), the TM polarization has high transmission, resulting in the addition of a coherent background that limits the transmission contrast $\Delta T/T$. This background is accounted for in Eq. B.10, which fits the data in Fig. fig:photon-systemC well. Additional factors that could contribute to the background include improper charge-state initialization (blinking) and slow-timescale (non-Markovian) broadening of the line beyond $\gamma = 2\pi \times 0.19\,\mathrm{GHz}$ due to spectral diffusion [87, 86]. This measurement was done at low laser power (see appendix B.4.1-B.4.2) to minimize these effects. The model including the coherent background term (Eqn. B.10) also accurately predicts the measured spectra in the dispersive regime. For example, the solid line shown in Fig. 5.1D of the main text is a fit to Eqn. B.10 with the background amplitude and phase as the only free parameters (for the exact cavity QED parameters and atom cavity detuning in this fit, see appendix B.4.4). According to this fit, the background amplitude is 11% of the amplitude of the SiV-cavity signal

($A = 0.35$ and $\phi = 0.88$). The observed resonance lineshape is therefore set by interference between these three channels: the SiV, the cavity, and the coherent background field. For example, the asymmetric, Fano-like lineshape at around -20 GHz in Fig. 5.1C arise from interference between the cavity and SiV fields.

We also note that since both the input and output fields are each independently filtered through a polarizer, the transmission contrast in the dispersive regime can be artificially enhanced through cross-polarization effects. While our model does not account for the two polarization modes independently, as would be necessary to completely describe the transmission signal due to this effect, our single-mode model fits the measured transmission spectra well with reasonable extracted background amplitudes.

B.4 Two-SiV transmission measurements in zero magnetic field

B.4.1 Charge-state control of SiV centers

Continuous resonant excitation of an SiV results in its eventual ionization (blinking) [87, 86]. The ionization timescale varies among SiV centers, but at low laser powers this timescale is much longer than the time needed to measure the transmission spectrum corresponding to an SiV. This timescale can be reduced by increasing the resonant laser power, allowing us to selectively ionize a particular SiV by applying high laser power on resonance with that SiV. We can therefore ionize one of a pair of nearly-resonant SiV centers into its optically-inactive charge state and, in this way, measure the spectrum

208

corresponding to transmission from a single SiV even when there are multiple SiV centers present (gray data in Fig. 5.2A). SiV centers can then be reinitialized with high fidelity ($\sim 80\%$) into the optically active charge state by applying a $520\,\mathrm{nm}$ laser pulse. With both SiV centers initialized in the correct charge state, we measure the two-SiV spectrum (black data in Fig. 5.2A). Because the charge state is stable over timescales longer than a single run of the experiment, we can also post-select for runs in the experiment where the two SiV centers are in the desired charge state. For more information about charge-state control of the SiV, see section 4 of the supplemental materials of Ref. [87].

B.4.2 SPECTRAL HOPPING OF SiV CENTERS

The SiV optical transition frequency can also drift as a function of time (spectral diffusion) [86]. While these dynamics vary from emitter to emitter, for the SiV centers studied here, we find that spectral diffusion occurs primarily in discrete spectral jumps on a timescale that increases with reduced resonant (and off-resonant repump) laser powers. For all measurements of the two-SiV system at zero magnetic field (Fig. 5.2), we work at laser intensities where the spectral diffusion timescale is much slower than the measurement timescale. In other words, we can obtain several high signal-to-noise transmission spectra before a spectral jump occurs. For example, the data in the case of two interacting SiV centers (black curves in Fig. 5.2A, B) were each acquired over roughly 1 minute, in which time there was no measurable spectral hopping.

SiV centers can also undergo significant spectral jumps when the sample is warmed up

to room temperature and then cooled down again (thermally cycled). This means that after thermal cycling the setup, the same SiV centers can have resonance frequencies that differ on the order of $\sim 5\,\mathrm{GHz}$. This is a much larger frequency scale than the typical slow, laser-induced spectral hopping described above ($\sim 1\,\mathrm{GHz}$). As an example, the experiments in Fig. 5.2 and Fig. 5.4 of the main text were performed with the same pair of SiV centers (also labelled as SiV A and B in Fig. 5.1C of the main text). The average SiV-SiV detuning in Fig. 5.2 is $\delta \sim 1\,\mathrm{GHz}$, whereas the average SiV-SiV detuning (at zero magnetic field) in Fig. 5.4 is $\delta \sim 5\,\mathrm{GHz}$ due to this type of spectral jump. Understanding and limiting sources of spectral diffusion is an important task for future work. However, the frequency scales of all spectral hopping processes are still smaller than or comparable to the frequency tuning range of the magnetic field tuning technique demonstrated here ($\sim 5\,\mathrm{GHz}$) and the Raman tuning technique demonstrated previously [87] ($\sim 20\,\mathrm{GHz}$).

B.4.3 Bright and dark state linewidth measurements

The spectral hopping of SiV centers provides an opportunity to measure the interacting two-SiV spectra as a function of splitting between the bright and dark states by simply integrating for a long time period and binning spectra into individual sets in which no spectral hop has occured. For the measurement presented in the inset of Fig. 5.2B, we do this over the course of roughly 12 hours and fit each binned spectrum to a double Lorentzian model (see Fig. B.6B for some example spectra at different bright-dark

210

splittings). To produce the plot shown in the inset of Fig. 5.2B, we bin each set of spectra based on the frequency difference between peaks obtained from the fit and plot the average width of the left (red) and right (blue) peaks in each bin. The error bars are the standard deviation within each bin. The gray dashed line and shaded region represent the mean and standard deviation of the single-SiV (that is, where the other SiV is ionized) linewidths obtained from single Lorentzian fits.

B.4.4 Cavity QED parameters for the two-SiV measurements in zero magnetic field

We determine the atom-cavity detuning Δ relative to the center-of-mass frequency of the two SiV centers using a Lorentzian fit to the spectrum shown in Fig. B.6A ($\Delta = 2\pi \times 79$ GHz) for the measurements in Fig. 5.2A and the inset of Fig. 5.2. Using the same technique after tuning the cavity to the opposite side of the SiV resonance (for measurement in main panel of Fig. 5.2B), we estimate an SiV-cavity detuning of $\Delta = 2\pi \times -55$ GHz. The cavity spectrum during these experiments ($\kappa = 2\pi \times 30$ GHz) was measured to be slightly narrower than in the measurements presented in Fig. 5.1 (see appendix B.3.2).

Based on these cavity spectra and the measurements described in appendix B.3, the following cavity QED parameters for the coupled SiV-cavity system are kept fixed: $\{g_1, g_2, \kappa, \gamma_1, \gamma_2\} = 2\pi \times \{7.3, 7.3, 30, 0.19, 0.19\}$ GHz yielding $C = 37$ for these SiV centers. As explained above, we set $\Delta = 2\pi \times 79$ GHz for Fig. 5.2A and the inset of

211
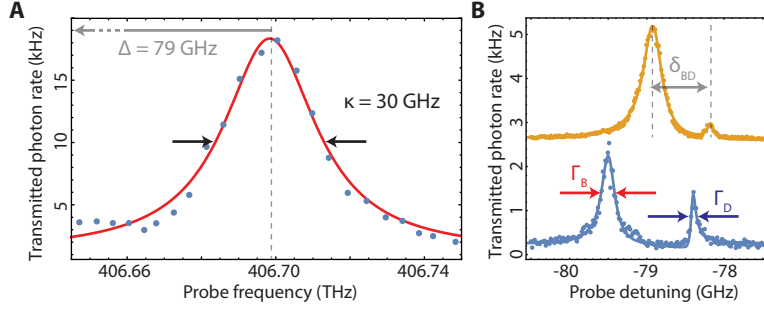
Figure B.6: Two-SiV measurement in zero magnetic field (A) Measurement of cavity linewidth (κ) and detuning from SiV (Δ) for the measurements presented in Fig. 5.1D, 5.2 of the main text. The solid red line is a Lorentzian fit. **(B)** Example 2-SiV transmission spectra at different bright-dark state detunings (δ_{SD}). The solid lines are a bi-Lorentzian fit with coherent background, and are used to extract δ_{SD} and the superradiant (bright) and subradiant (dark) state linewidths, Γ_S and Γ_D, plotted in the inset of Fig. 5.3B in the main text.

Fig. 5.2B and $\Delta = 2\pi \times -55$ GHz for the main panel of Fig. 5.2B. The solid gray curves in Fig. 5.2A are single-SiV spectra obtained from Eqn. B.10 by setting either g_1 or g_2 to zero. From these fits we extract the SiV-SiV detuning $\delta = 2\pi \times 0.56$ GHz (and background parameters of $\{A, \phi\} = \{0.33, -0.78\}$ and $\{0.34, -0.69\}$ for SiVs 1 and 2 respectively).

With Δ and δ fixed, we fit the two-SiV spectrum shown in black in Fig. 5.2A to Eqn. B.10 with only the background terms as free parameters to obtain the solid black curve, which agrees well with the data (and yields background parameter estimates of $A = 0.31$ and $\phi = -0.76$). The close agreement between theory and experiment also validates our independently measured g_i and γ_i. Since individual ionized control spectra similar to the gray data in Fig. 5.2A were not taken for the data shown in the main panel of Fig. 5.2B, δ was left as a free parameter for the fit shown in black in Fig.

5.2B, and was determined to be $\delta = 2\pi \times 2\,\text{GHz}$, which is different from the measured value of δ at the other cavity detuning due to the spectral diffusion process described in appendix B.4.2. We also obtain background parameters $A = 0.54$ and $\phi = 1.38$ for this fit.

The solid lines in the inset of Fig. 5.2B are calculated with the above SiV-cavity parameters at the SiV-cavity detuning $\Delta = 2\pi \times 79\,\text{GHz}$, but at various δ. We first calculate the energy difference between the superradiant (bright) and subradiant (dark) states as a function of SiV-SiV detuning (using the real part of the eigenvalues of $\hat{H}_{\text{TC}}$). We then calculate the $|S\rangle$ and $|D\rangle$ state linewidths (the imaginary eigenvalues of $\hat{H}_{\text{TC}}$ arising from the non-Hermitian terms) as a function of SiV-SiV detuning. This allows us to plot the theoretical bright and dark state linewidths as a function of bright and dark state energy difference, which is the parameter determined from the fitting procedure described in appendix B.4.3 above. The solid curves in the inset of Fig. 5.2 are predictions from the independently-measured cavity QED parameters (*cf.* appendix B.3.2) with no free parameters. This is because in the linear regime, the bright and dark state linewidths do not depend on the signal amplitude, laser power or background, which are the only free parameters in most of the other fits.
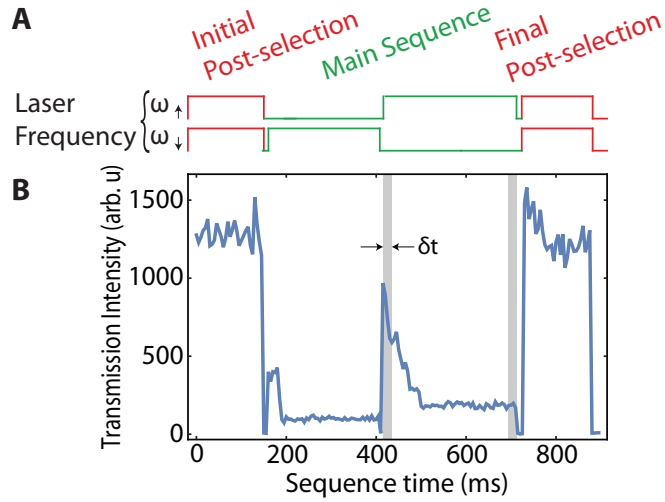
Figure B.7: Pulse sequence for single-shot spin readout. **(A)** Pulse sequence used to measure single-shot readout and **(B)** transmission intensity as a function of time for the corresponding pulse sequence. The spin is initialized into $|\uparrow\rangle$ via optical pumping on $\omega_\downarrow$ and read out via optical pumping on $\omega_\uparrow$ (green sequences). The fidelity is calculated by comparing one time bin δt at the beginning and end of the readout pulse (gray regions). Post-selection pulses (red) are used to ensure the experiment was initialized correctly.

B.5 FIDELITY CALCULATION FOR SINGLE-SHOT READOUT OF THE SiV SPIN

We read out the SiV spin state in the dispersive regime by measuring the spin-dependent transmission (Fig. 5.3). Note that the measurements shown in Fig. 5.3 are performed with a different SiV in the same device as the measurements shown in Fig. 5.2 and Fig. 5.4 of the main text. The full experimental pulse sequence is shown in Fig. B.7. The main sequence consists of a pulse at frequency $\omega_\downarrow$ which initializes the spin in $|\uparrow\rangle$ via optical pumping and a readout pulse at $\omega_\uparrow$. We build a histogram of photons in the initial time bin of duration δt, when the state is assumed to be $|\uparrow\rangle$, as well as in the final time bin of duration δt, after the system has been pumped into $|\downarrow\rangle$. These histograms

214

represent the distribution of photon numbers we expect to observe in a single run of the experiment. Since these histograms are well separated, we can define a threshold photon number n such that if the initial time bin δt we detect more (fewer) than n photons, the state is $|\uparrow\rangle$ ($|\downarrow\rangle$). We numerically optimize our choice for δt and n to maximize the single-shot readout fidelity:

$$\mathcal{F} = \mathrm{Max}_{n,\delta t}\{(1 - \sum_{m=n}^{\infty} P_{\downarrow}(m,\delta t)) + (1 - \sum_{1}^{m=n} P_{\uparrow}(m,\delta t))\}/2. \qquad \text{(B.11)}$$

To account for SiV blinking and spectral diffusion (see sec. B.4), we use pre-sequence and post-sequence pulses to confirm that the SiV is at the correct frequency and in the correct charge state. Simultaneously applying two laser fields at frequencies $\omega_{\uparrow}$ and $\omega_{\downarrow}$ allows us to continuously scatter photons from the SiV without optical pumping, giving a high transmission intensity when the SiV is in the correct state. We use this pulse both at the start of the experiment (to ensure we start in the correct state) and at the end (to ensure the readout itself did not ionize the SiV).

The optimal fidelity occurs at $\delta t = 7\,\mathrm{ms}$ and $n = 34$. Without post-selection, the $|\uparrow\rangle$ histogram is bimodal, limiting the readout fidelity to 89%. With post-selection, the lower lobe of the histogram is removed, and the reported fidelity $\mathcal{F} = 96.8\%$ is achieved. This fidelity is not strictly the readout fidelity, but rather the combined initialization and readout fidelity. In fact, the fidelity is predominately limited by the non-zero overlap of the spin-cycling transitions used in the experiment, which can result in off-resonant

pumping limiting the initialization of the spin into $|\uparrow\rangle$. Based on the measured splitting, we expect a maximum initialization and readout fidelity of 97.4%.

B.6 Spin-dependent SiV-cavity transmission on cavity resonance

In the main text Fig. 5.3, we demonstrated a spin-dependent modulation of the SiV-cavity transmission response in the dispersive regime and used this effect to achieve single-shot readout of the SiV spin. We can perform a similar experiment in the resonant-cavity regime. In this regime, the SiV optical transitions are Purcell-broadened, so we apply a magnetic field of $6.5\,\mathrm{kG}$ approximately orthogonal to the SiV axis such that the splitting between the Purcell-enhanced spin transitions is maximized. We then initialize the SiV in either $|\downarrow\rangle$ or $|\uparrow\rangle$ via optical pumping (Fig. B.7A). We probe the cavity at frequency $\omega_\uparrow$, which is resonant with both the cavity and the $|\uparrow\rangle \to |\uparrow'\rangle$ transition (Fig. B.7B). When the spin is prepared in the state $|\downarrow\rangle$, the probe field at $\omega_\uparrow$ is detuned from the SiV transition and is transmitted (red curve). When the spin is prepared in $|\uparrow\rangle$, it couples to the probe field at frequency $\omega_\uparrow$ and the incoming light is reflected (blue curve). [186]. We observe a maximum spin-dependent transmission contrast of 80%, limited by spectral overlap between the two spin transitions. The memory time of this modulation ($50\,\mu\mathrm{s}$) is limited by the cyclicity of the spin-conserving optical transition addressed by the probe pulse in this highly off-axis field.

216
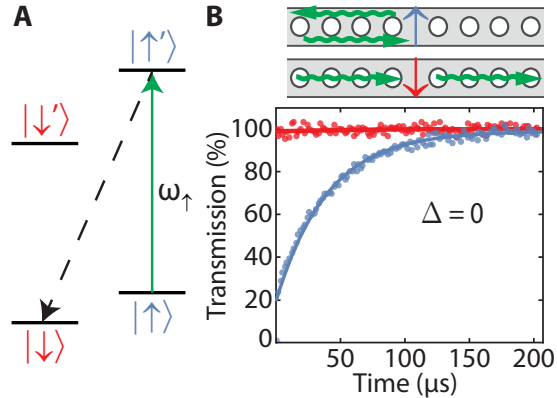
Figure B.8: Switching of the cavity transmission on resonance (A) Simplified level structure of the SiV in a magnetic field. An optical transition at frequency $\omega_\uparrow$ (green arrow) is used to initialize the SiV spin into $|\downarrow\rangle$ by optical pumping via a spin-flipping transition (dashed line). Conversely, pumping at frequency $\omega_\downarrow$ (not shown) initializes the spin into $|\uparrow\rangle$. **(B)** Spin-dependent optical switching on cavity resonance. State $|\downarrow\rangle$ is not coupled to the probe field at frequency $\omega_\uparrow$ which is therefore transmitted (red). Initialization into $|\uparrow\rangle$ results in reflection of the probe field (blue). The maximum spin-dependent contrast is 80%.

B.7   TWO-SiV TRANSMISSION MEASUREMENTS IN NONZERO MAGNETIC FIELDS

B.7.1   SiV FREQUENCY STABILIZATION BASED ON ACTIVE PRESELECTION

SiV optical transitions are narrow and stable for timescales long enough to enable the measurements described in Fig. 5.1-5.3 of the main text. In order to achieve stable optical transitions over longer timescales, we use an active preselection sequence for the measurements described in Fig. 5.4 of the main text. This preselection technique effectively fixes the optical transition frequencies of the emitters to desired frequencies at the expense of a slight reduction in duty cycle.

In order to cycle photons continuously from both SiV centers in a magnetic field, we

apply two tones simultaneously at frequencies $\omega_{\uparrow/\downarrow,i}$ for SiV i (giving four total optical frequencies). To achieve this, each SiV has one spin transition addressed by a separate resonant laser, with each laser modulated by an EOM to produce a sideband at the transition frequency of the other spin-dependent transition. For example, lasers at $\omega_{\uparrow,1}$ and $\omega_{\downarrow,2}$ have corresponding sidebands $\omega_{\downarrow,1}$ and $\omega_{\uparrow,2}$. Each SiV is separately addressed for 1 ms and the number of transmitted photons is recorded using a field-programmable gate array (Lattice Diamond MachXO2).

We set a photon number threshold based on observed photon count rates for these SiV centers under conditions similar to those used in the experiment. If the threshold photon number is exceeded for both SiV centers, we proceed with the experiment (typical duration: $\sim 50\,\mathrm{ms}$). If not, we apply a relatively strong ($\sim 1\,\mu\mathrm{W}$) 520 nm laser pulse for $100\,\mu\mathrm{s}$ to induce spectral hopping of the SiV optical frequencies. Using this technique, we are able to measure with duty cycle $\sim 50\%$ and measure linewidths ($\sim 0.5\,\mathrm{GHz}$) that are significantly narrower than the long-timescale integrated linewidth of the SiV centers without any preselection ($\sim 2\,\mathrm{GHz}$). The gray data in Fig. 5.4B are an example of narrow lines measured using this preselection sequence.

B.7.2 ZEEMAN SPLITTING CALIBRATION

We determine the frequencies of all spin-selective transitions $\omega_{\uparrow/\downarrow,i}$ as a function of magnetic field at a sample temperature of 5 K. A complete description of the magnetic-field dependence of the SiV optical transitions can be found elsewhere [179]. At temperatures

218

above 500 mK where the relevant phonon modes are populated, working in a magnetic field misaligned with respect to the SiV symmetry axis yields a relatively short spin population relaxation rate $T_1 \sim 100$ ns in contrast to the $50\,\mu$s for a similarly misaligned field at 85 mK (Fig. 5.3B) [165]. As a result, optical pumping from a single laser at $\omega_{\uparrow/\downarrow}$ is minimal, allowing us to scatter photons at a sufficient rate to easily observe all spin transitions $\omega_{\uparrow/\downarrow,i}$ in transmission spectrum with a single laser (in other words, with no repumping laser). We measure the transmission spectra around SiV centers 1 and 2 at various magnetic fields from 0 kG to 8 kG. For an example calibration transmission spectrum at 5 K (taken in a different device), see Fig. B.9A.

B.7.3 SPIN-DEPENDENT MEASUREMENT OF THE TWO-SIV TRANSMISSION SPECTRA

For the measurements presented in Fig. 5.4, at each magnetic field value we first probe the response of SiV 1 alone by applying Ω_1 continuously (to ensure initialization in $|\uparrow_1\rangle$ via optical pumping) and scanning Ω_p across the resonance. Although Ω_1 is applied continuously at $\omega_{\downarrow,1}$, we only scatter photons continuously when Ω_p is on resonance with $\omega_{\uparrow,1}$ due to optical pumping into state $|\uparrow_1\rangle$ from Ω_1. We then repeat the same measurement for SiV 2, applying Ω_2 and scanning Ω_p. One example dataset is shown in gray in Fig. 5.4B. The individual transmission spectra are then normalized to the laser background to compensate for slight differences in laser power and summed (incoherently) at each field to produce the data shown in Fig. 5.4C. At each field, we fit

219

a Lorentzian to the single-spin spectra to determine the center frequency of the spin-selective transitions. The solid gray lines in Fig. 5.4C are linear fits to the extracted center frequencies as a function of magnetic field.

To study the two-spin interacting system, we apply Ω_1 and Ω_2 continuously to ensure spin initialization in $|\uparrow_1\rangle |\downarrow_2\rangle$ and measure the transmission spectrum of Ω_p. Again, we normalize the data at each field to the background, which is primarily set by the stronger pump lasers Ω_1 and Ω_2. An example spectrum at a single magnetic field is shown in black in Fig. 5.4B, and the full avoided crossing (transmission spectra as a function of magnetic field) is shown in Fig. 5.4D. In all measurements (single SiV and two-SiV), we adjust our laser intensities such that Ω_1 and Ω_2 are roughly 3 times larger than Ω_p, so that each SiV spin is polarized in the desired spin state (spin polarization $P \sim |\Omega_{1,2}/\Omega_p|^2 \sim 90\%$).

B.7.4 Cavity QED parameters for the two-SiV measurements in a non-zero magnetic field

Despite our use of the preselection sequence described in appendix B.7.1, SiV optical transitions are broadened non-radiatively beyond the linewidth $2\pi \times 0.19$ GHz measured on short timescales without preselection. Although this broadening has both Markovian and non-Markovian sources, to good approximation it can simply be included as an increased decoherence rate contributing to γ. Note that this approximation leads us to underestimate the SiV-cavity cooperativity.

We determine the SiV-polariton linewidth (and by extension, γ) under preselection using the single-spin transmission spectra plotted in Fig. 5.4C. By fitting Lorentzians to the individual spectra at each magnetic field (*cf.* gray data in Fig. 5.4B), we determine the mean single-SiV linewidths to be $\{\Gamma_1(\Delta), \Gamma_2(\Delta)\} = 2\pi \times \{0.77 \pm 0.14, 0.58 \pm 0.12\}$ GHz. We measure a cavity linewidth $\kappa = 2\pi \times 39$ GHz and SiV-cavity detuning $\Delta = 2\pi \times 109$ GHz during this measurement (not shown; see Fig. B.6A for an example measurement) and fix $g_1 = g_2 = 2\pi \times 7.3$ GHz as determined before. From the Purcell-enhanced linewidths and these known cavity-QED parameters, we can extract the bare SiV linewidth γ

$$\gamma_i = \Gamma_i(\Delta) - \frac{4g^2}{\kappa} \frac{1}{1 + 4\Delta^2/\kappa^2}, \tag{B.12}$$

yielding $\{\gamma_1, \gamma_2\} = 2\pi \times \{0.6, 0.42\}$ GHz over long timescales under preselection. We use the complete cavity QED parameters $\{g_1, g_2, \kappa, \gamma_1, \gamma_2\} = 2\pi \times \{7.3, 7.3, 39, 0.6, 0.42\}$ GHz to calculate the eigenvalues of $\hat{H}_{TC}$ at various 2-SiV detunings δ (extracted from Fig. 5.4C) which are the bright and dark state energies (solid red and blue curves in Fig. 5.4D, E). We note that these are computed using no free parameters.

In order to compare the measured data to a theoretical prediction for the full avoided-crossing transmission spectrum shown in Fig. 5.4E, we also need to include in our model effects arising from imperfect polarization P into the desired spin state ($P \sim 0.9$, see appendix B.7.2) and laser background (see appendix B.2). We calculate the transmission spectrum with imperfect polarization $T_P(\omega)$ by computing a weighted average of

transmission spectra:

$$T_P(\omega) = P^2 T(\omega) + P(1-P)T_1(\omega) + (1-P)PT_2(\omega) + (1-P)^2 T_0(\omega), \qquad \text{(B.13)}$$

where $T(\omega)$, $T_1(\omega)$, $T_2(\omega)$ and $T_0(\omega)$ are all given by Eqn. B.10 with $\{g_1, g_2\}$ set to $2\pi \times$ $\{7.3, 7.3\}$, $\{7.3, 0\}$, $\{0, 7.3\}$ and $\{0, 0\}$ GHz respectively. At each field we fit Eqn. B.13 to the two-spin transmission data with only the background amplitude and phase as free parameters (for an example fit, see solid black curve in Fig. 5.4B, which has background parameter estimates $A = 0.54$, $\phi = -0.30$). We determine an average background amplitude and phase ($A = 0.56$ and $\phi = -0.47$) over all magnetic fields (data in Fig. 5.4D) and use these average values in our model. We then use Eqn. B.13 at various δ (which are determined at each magnetic field based on the linear fits shown in Fig. 5.4C) with the above cavity QED parameters, $P = 0.9$ and estimated background parameters to produce the theoretical avoided-crossing transmission spectrum shown in Fig. 5.4E.

B.7.5 Measurement of collective-state formation in an independent device

We also measure the formation of superradiant and subradiant states with a pair of SiV centers located in a different device on the same diamond chip. A transmission spectrum at $5\,\mathrm{K}$ near both SiV and cavity resonance is shown in Fig. B.9A. From

this measurement, we extract Purcell enhanced linewidths of $\{\Gamma_1(0), \Gamma_2(0)\} = 2\pi \times \{1.78, 2.43\}$ GHz. To measure the cavity mediated interaction between these SiV centers, we work at an atom-cavity detuning of $\Delta = 2\pi \times 70$ GHz. To demonstrate that we can bring spin-selective transitions from each SiV into resonance, we first measure the transmission spectrum of all transitions at a temperature of $5\,$K Fig. B.9C as a magnetic field oriented roughly orthogonal to the SiV center's symmetry axis is ramped from $0\,$kG to $6.7\,$kG. In this measurement, the spins are unpolarized, which allows us to see all spin-preserving transitions without a second pumping field. However, this random polarization causes us to average over the different combination of spin states (*e.g.* $P \sim 0.5$ in Eqn. B.13), limiting the visibility of the cavity-mediated interaction.

As evident from the data Fig. B.9C, there is no significant spectral diffusion for this pair of SiV centers, and we therefore choose not to implement the preselection sequence described in appendix B.7.1. Instead, to ensure proper initialization of both SiV centers into the correct charge state, we simply apply a $\sim 1\,\mu$W green pulse every $\sim 5\,$ms[87]. At a temperature of $85\,$mK, the spins can be polarized by applying pump lasers Ω_1 and Ω_2. By polarizing the spins individually, we measure the single SiV linewidths over long timescales under this periodic green illumination (similar to gray data in Fig. 5.4B): $\{\Gamma_1(\Delta), \Gamma_2(\Delta)\} = 2\pi \times \{0.65, 1.01\}$ GHz (Fig. B.9B). Using the SiV linewidth data in Fig. B.9A and Fig. B.9B, the measured cavity linewidth (not shown) and Eqn. B.12, we can extract the full cavity QED parameters: $\{g_1, g_1, \kappa, \gamma_1, \gamma_2\} = 2\pi \times \{5.7, 6.4, 85, 0.23, 0.49\}$ GHz.

Fig. B.9D shows the spectrum of the two interacting spins at $85\,$mK (with both

223
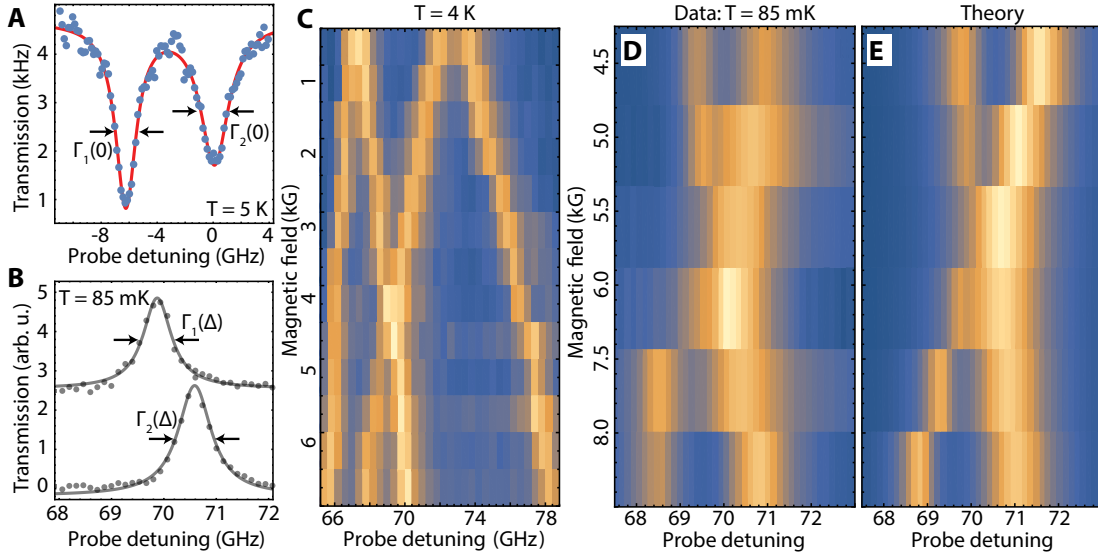
Figure B.9: SiV-SiV interaction measurement in a different device (A) Transmission spectrum near cavity resonance ($\Delta \sim 0\,\text{GHz}$). The red line shows a Bi-Lorentzian fit used to extract the Purcell-enhanced linewidths $\Gamma_1(0)$ and $\Gamma_2(0)$. **(B)** Single SiV linewidth measurements at $85\,\text{mK}$ in a magnetic field oriented roughly $70°$ (similar to the gray data in Fig. 5.4B). The lower data is taken at $B = 6.6\,\text{kG}$ and is used to extract $\Gamma_1(\Delta)$ and the upper data (shifted vertically for clarity) is taken at $B = 8.3\,\text{kG}$ and is used to extract $\Gamma_2(\Delta)$. **(C)** Zeeman calibration transmission spectrum taken as from $0\,\text{kG}$ to $6.7\,\text{kG}$ roughly orthogonal to the SiV symmetry axis. **(D)** Spin dependent SiV-SiV interaction at $T = 85\,\text{mK}$ with both SiVs initialized into spin states that couple to the probe field taken as a function of magnetic field oriented roughly $70°$ from the SiV symmetry axis. **(E)** Theoretical SiV-SiV interaction spectrum for the cavity parameters given in the text, assuming spin polarization of 90% (see appendix B.7.4).

pump fields Ω_1 and Ω_2 applied), taken as a function of the magnitude of an external

magnetic field oriented roughly $70°$ from the SiV symmetry axis. Note that this is a

slightly different orientation compared to the field used in the calibration data in (Fig.

B.9C), hence the two SiV centers tune in and out of resonance at a different magnetic

field magnitude in (Fig. B.9D). Although the avoided crossing is not as well resolved

as in Fig. 5.4D of the main text due to the lower cooperativities (7 and 4) of these SiV

centers, the formation of superradiant and subradiant states near the two-SiV resonance is evident from the enhanced intensity and broader linewidth of the superradiant state that remains on the positive-frequency side of the density plot in Fig. B.9D. The theoretical spectrum (Fig. B.9E) is calculated as in appendix B.7.4 and shows good agreement with the measured data.

C

Supporting material for chapter 7

C.1 Nanophotonic cavity design

We simulate and optimize our nanophotonic structures to maximize atom-photon interactions while maintaining high waveguide coupling, which ensures good collection efficiency for the devices. In particular, this requires optimizing the device quality-factor to mode volume ratio, the relative rates of scattering into waveguide modes, and the size and shape of the optical mode. Each of these quantities are considered in a three-step simulation process (FDTD, Lumerical). We first perform a coarse parameter sweep over all possible unit cells which define the photonic crystal gemometry and identify families of bandgap-generating structures. These structures are the starting point for a gradient ascent optimization procedure, which results in generating high quality-

factor, low mode volume resonators. Finally, the generated designs are modified to ensure efficient resonator-waveguide coupling.

Optimization begins by exploring the full parameter space of TE-like bandgap generating structures within our waveguide geometry. For hole-based cavities [Fig. C.1(a)], this sweep covers a 5-dimensional parameter space: The lattice constant of the unit cell (a), the hole size and aspect ratio (H_x and H_y), the device etch angle (θ) and the waveguide width (w). Due to the size of this parameter space, we start by performing a low-resolution sweep over all parameters, with each potential design simulated by a single unit cell with the following boundary conditions: 4 perfectly matched layer (PML) boundary conditions in the transverse directions and 2 Bloch boundary conditions in the waveguide directions. The band structure of candidate geometries are determined by sweeping the effective k-vector of the Bloch boundary condition and identifying allowed modes. Using this technique, families of similar structures with large bandgaps near the SiV transition frequency are chosen for further simulation. Each candidate photonic crystal is also inspected for the position of its optical mode maximum, ensuring that it has first-order modes concentrated in the center of the diamond, where SiVs will be incorporated [Fig. C.1(b)].

The second step is to simulate the full photonic crystal cavity design, focused in the regions of parameter space identified in step one. This is done by selecting a fixed θ, as well as a total number of unit cells that define the structure, then modifying the bandgap of the photonic crystal with a defect region to form a cavity mode. We define

227
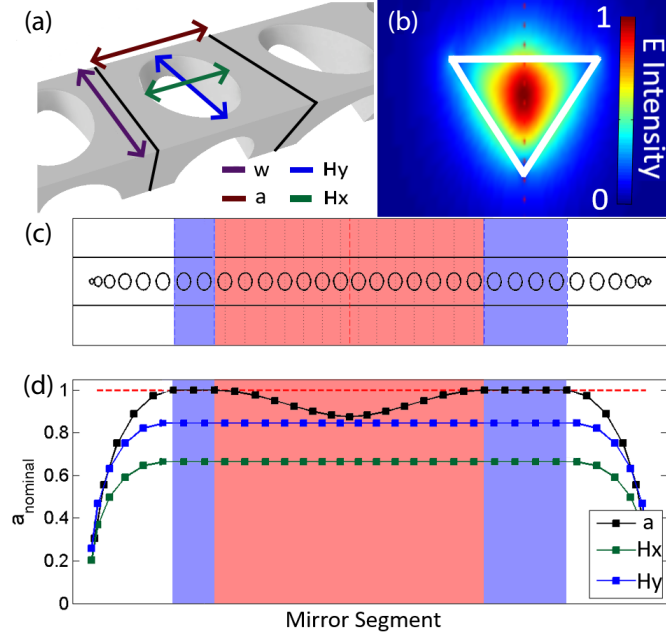
Figure C.1: (a) Unit cell of a photonic crystal cavity (bounded by black lines). H_x and H_y define the size and aspect ratio of the hole, a determines the lattice constant, and w sets the waveguide width. (b) Electric field intensity profile of the TE mode inside the cavity, indicating strong confinement of the optical mode inside the waveguide. (c) Schematic of photonic crystal design. Blue shaded region is the bandgap generating structure, red shaded region represents the cavity structure. (d) Plot of a, H_x, and H_y for the cavity shown in (c), showing cubic taper which defines the cavity region. All sizes are shown in fractions of a_{nominal}, the unperturbed lattice constant.

this defect using a cubic tapering of one (or several) possible parameters:

$$A(x) = 1 - d_{\mathrm{max}}|2x^3 - 3x^2 + 1| \tag{C.1}$$

where A is the relative scale of the target parameter(s) at a distance x from the cavity center, and d_{max} is the defect depth parameter. Photonic Crystal cavities with multi-parameter defects are difficult to reliably fabricate, therefore, devices used in this work

228

have cavity defect geometries defined only by variations in the lattice constant. The cavity generated by this defect is scored by simulating the optical spectrum and mode profile and computing the scoring function F:

$$F = \min(Q, Q_{\text{cutoff}})/(Q_{\text{cutoff}} \times V_{\text{mode}}) \tag{C.2}$$

Where Q is the cavity quality-factor, $Q_{\text{cutoff}} = 5 \times 10^5$ is an estimated maximum realizable Q based on fabrication constraints, and V_{mode} is the cavity mode volume. Based on this criteria, we employ a gradient ascent process over all cavity design parameters (except θ and the total number of unit cells) until F is maximized, or a maximum number of iterations has occurred. Due to the complexity and size of the parameter space, a single iteration of this gradient ascent is unlikely to find the optimal structure. Instead, several candidates from each family of designs found in step one are explored, with the best moving on to the final step of the simulation process. These surviving candidates are again checked to ensure confinement of the optical mode in the center of the cavity structure and to ensure that the structures fall within the tolerances of the fabrication process.

The final step in the simulation process is to modify the optimized designs to maximize resonator-waveguide coupling. This is done by removing unit cells from the input port of the device, which decreases the overall quality-factor of the devices in exchange for better waveguide damping of the optical field. Devices are once again simulated and

229

analyzed for the fraction of light leaving the resonator through the waveguide compared to the fraction scattering into free-space. The number of unit cells on the input port is then optimized for this ratio, with simulations indicating that more than 95% of light is collected into the waveguide. In practice, fabrication defects increase the free-space scattering rate, placing resonators close to the critically-coupled regime. Finally, the waveguide coupling fraction is increased by appending a quadratic taper to both ends of the devices such that the optical mode is transferred adiabatically from the photonic crystal region into the diamond waveguide. This process produces the final cavity structure used for fabrication [Fig. C.1(c)].

C.2 Strain-induced frequency fluctuations

In this Appendix we calculate changes the SiV spin-qubit frequency and optical transition frequency arising from strain fluctuations. We start with the Hamiltonian for SiV

in an external magnetic field B_z aligned along trhe SiV symmetry axis [179, 244]:

$$H = -\lambda \begin{pmatrix} 0 & 0 & i & 0 \\ 0 & 0 & 0 & -i \\ -i & 0 & 0 & 0 \\ 0 & i & 0 & 0 \end{pmatrix} + \underbrace{\begin{pmatrix} \alpha - \beta & 0 & \gamma & 0 \\ 0 & \alpha - \beta & 0 & \gamma \\ \gamma & 0 & \beta & 0 \\ 0 & \gamma & 0 & \beta \end{pmatrix}}_{\text{strain}} +$$

$$\underbrace{q\gamma_L B_z \begin{pmatrix} 0 & 0 & i & 0 \\ 0 & 0 & 0 & i \\ -i & 0 & 0 & 0 \\ 0 & -i & 0 & 0 \end{pmatrix}}_{\text{orbital Zeeman}} + \underbrace{\frac{\gamma_S B_z}{2} \begin{pmatrix} 1 & 0 & 0 & 0 \\ 0 & -1 & 0 & 0 \\ 0 & 0 & 1 & 0 \\ 0 & 0 & 0 & -1 \end{pmatrix}}_{\text{spin Zeeman}}, \quad (C.3)$$

where the first matrix underbrace is labeled spin-orbit,

where λ is a spin-orbit coupling constant, $\gamma_L = \mu_B$ and $\gamma_S = 2\mu_B$ are Landé g-factors of the orbital and spin degrees of freedom (μ_B the Bohr magneton), $q = 0.1$ is a Ham reduction factor of the orbital momentum [179], and α, β, γ are local strain parameters which can be different for the ground and excited sates [Sec. 7.4]. As measuring the exact strain parameters is challenging [Sec. 7.4] we assume only one non-zero component in this tensor (ϵ_{zx}) in order to simplify our calculations. In this case, strain parameters

are:

$$\beta = f_{\text{g(e)}}\epsilon_{zx}, \tag{C.4}$$

$$\alpha = \gamma = 0, \tag{C.5}$$

where $f_{\text{g(e)}} = 1.7 \times 10^6 \, (3.4 \times 10^6) \, \text{GHz/strain}$ [244] for the ground (excited) state and the GS splitting is:

$$\Delta_{GS} = 2\sqrt{\lambda_g^2 + \beta^2}, \tag{C.6}$$

where $\lambda_g \approx 25 \, \text{GHz}$ is the SO-constant for the ground state. Next, we solve this Hamiltonian and investigate how the qubit frequency changes as a function of relative strain fluctuations (ξ):

$$\Delta f_{\text{MW}} = \frac{2 \left(f_{\text{g}}\epsilon_{zx}\right)^2 \lambda_g B_z q \gamma_L}{\left(\left(f_{\text{g}}\epsilon_{zx}\right)^2 + \lambda_g^2\right)^{3/2}} \xi. \tag{C.7}$$

The corresponding change in the optical frequency is:

$$\Delta f_{\text{optical}} = \left(\frac{\left(f_{\text{g}}\epsilon_{zx}\right)^2}{\sqrt{\left(f_{\text{g}}\epsilon_{zx}\right)^2 + \lambda_g^2}} - \frac{\left(f_{\text{e}}\epsilon_{zx}\right)^2}{\sqrt{\left(f_{\text{e}}\epsilon_{zx}\right)^2 + \lambda_e^2}}\right) \xi, \tag{C.8}$$

where $\lambda_e \approx 125 \, \text{GHz}$ is the SO-constant for the excited state.

For SiV 2 [Sec. 7.4] we measured $\Delta_{GS} = 140 \, \text{GHz}$ and find $\epsilon_{zx} = 3.8 \times 10^{-5}$. With $\xi = 1\%$ strain fluctuations, frequencies change by $\Delta f_{\text{MW}} \approx 4 \, \text{MHz}$ and $\Delta f_{\text{optical}} \approx -300 \, \text{MHz}$. This quantitatively agrees with the data presented in [Fig. 7.4(f)].

232

The scaling of $T_2(N) \propto N^{2/3}$ is identical to that found for nitrogen-vacancy centers, where it is assumed that T_2 is limited by a fluctuating electron spin bath [352, 353]. Motivated by DEER measurements with SiV 2, we follow the analysis of ref. [353] to estimate the noise bath observed by SiV 1.

The measured coherence decay is modeled by:

$$\langle S_z \rangle = \text{Exp}\left(-\int d\omega \, S(\omega) \mathcal{F}_N(t,\omega) \right), \tag{C.9}$$

where $S(\omega)$ is the noise power-spectrum of the bath, and $\mathcal{F}_N(t,\omega) = 2\sin(\omega t/2)(1 - \sec(\omega t/2N))^2/\omega^2$ is filter function for a dynamical-decoupling sequence with an even number of pulses [353]. We fit sucessive T_2 echo curves to the functional form $A + Be^{-(t/T_2)^\beta}$, with A, B being free parameters associated with photon count rates, and $\beta = 3$ providing the best fit to the data. This value of β implies a decoherence bath with a Lorentzian noise power-spectrum, $S(\omega, b, \tau) = b^2 \tau/\pi \times 1/(1 + \omega^2 \tau^2)$, where b is a parameter corresponding to the strength of the noise bath, and τ is a parameter corresponding to the correlation time of the noise [352, 353].

Empirically, no one set of noise parameters faithfully reproduces the data for all measured echo sequences. Adding a second source of dephasing $\tilde{S} = S(\omega, b_1, \tau_1) + S(\omega, b_2, \tau_2)$, gives reasonable agreement with the data using parameters $b_1 = 5\,\text{kHz}$,

$\tau_1 = 1\,\text{s}$, $b_2 = 180\,\text{kHz}$, $\tau_2 = 1\,\text{ms}$ [Fig. 7.8(d)]. The two drastically different set of noise parameters for each of the sources can help illuminate the source of noise in our devices.

As explained in the previous section, one likely candidate for this decoherence is a bath of free electrons arising from improper surface termination or local damage caused during nanofabrication, which are known to have correlation times in the $\sim$s range. The SiV studied in this analysis is approximately equidistant from three surfaces: the two nearest holes which define the nanophotonic cavity, and the top surface of the nanobeam [sec: 7.2], all of which are approximately 50 nm away. We estimate a density of $\sigma_{\text{surf}} = 0.067$ spins/nm^2 using:

$$b_1 = \gamma_{\text{SiV}}\langle B_{\text{surf}}\rangle = \frac{\text{g}^2\mu_B^2\mu_0}{\hbar}\frac{1}{4\pi\Sigma d_i^2}\sqrt{\frac{\pi}{4\sigma_{\text{surf}}}} \tag{C.10}$$

where b_1 is the measured strength of the noise bath, g is the electron gyromagnetic ratio, and d_i are the distances to the nearest surfaces. This observation is consistent with surface spin densities measured using NVs [353].

The longer correlation time for the second noise term suggests a different bath, possibly arising from free electron spins inside the bulk diamond. Vacancy clusters, which can persist under annealing even at 1200 C, are known to posses $g = 2$ electron spins, and are one possible candidate for this noise bath [302]. Integrating over d in eq. C.10, we estimate the density of spins required to achieve the measured b_2. We estimate $\rho_{\text{bulk}} \sim 0.53$ spins per nm^3, which corresponds to a doping of 3ppm. Interestingly, this

is nearly identical to the local concentration of silicon incorporated during implantation (most of which is not successfully converted into negatively charged SiV), and could imply implantation-related damage as a possible source of these impurities.

Another possible explanation for this slower bath could be coupling to nuclear spins in the environment. The diamond used in this experiment has a natural abundance of ^{13}C, a spin-1/2 isotope, in concentrations of approximately 1.1%. Replacing $\mu_B \to \mu_N$ in the term for $\langle B \rangle$ gives an estimated nuclear spin density of $\rho_{\text{bulk,N}} = 0.6\%$, only a factor of two different than the expected nuclear spin density.

C.4 Concurrence and Fidelity calculations

C.4.1 Spin-photon concurrence and fidelity calculations

From correlations in the Z- and X-bases, we estimate a lower bound for the entanglement in our system. Following reference [399], we note that the density matrix of our system conditioned on the detection of one photon can be described as:

$$\rho_{ZZ} = 1/2 \begin{pmatrix} p_{e\uparrow} & 0 & 0 & 0 \\ 0 & p_{e\downarrow} & c_{e\downarrow,l\uparrow} & 0 \\ 0 & c_{e\downarrow,l\uparrow}^{\dagger} & p_{l\uparrow} & 0 \\ 0 & 0 & 0 & p_{l\downarrow} \end{pmatrix} \tag{C.11}$$

where p_{ij} are the probabilities of measuring a photon in state i, and the spin in state j. $c_{e\downarrow,l\uparrow}$ represents entanglement between $p_{e\uparrow}$ and $p_{l\downarrow}$. We set all other coherence terms to zero, as they represent negligibly small errors in our system (for example, $c_{e\uparrow,e\downarrow} > 0$ would imply that the SiV was not initialized properly at the start of the measurement). We quantify the degree of entanglement in the system by its concurrence $\mathcal{C}$, which is 0 for seperable states, and 1 for a maximally entangled state [400]:

$$\mathcal{C} = \text{Max}(0, \lambda_0^{1/2} - \sum_{i=1}^{N} \lambda_i^{1/2}), \tag{C.12}$$

where λ_i are the eigenvalues of the matrix $\rho_{ZZ} \cdot \left(\sigma_y \cdot \rho_{ZZ} \cdot \sigma_y^\dagger\right)$, and σ_y is the standard Pauli matrix acting on each qubit basis separately ($\sigma_y = \sigma_{y,\text{ph}} \otimes \sigma_{y,\text{el}}$). While this can be solved exactly, the resulting equation is complicated. Taking only the first-order terms, this can be simplified to put a lower bound on the concurrence:

$$\mathcal{C} \geq 2(|c_{e\downarrow,l\uparrow}| - \sqrt{p_{e\uparrow}p_{l\downarrow}}) \tag{C.13}$$

We measure p direcly in the Z basis, and estimate $|c_{e\downarrow,l\uparrow}|$ by performing measurements in the X basis. A $\pi/2$-rotation on both the photon and spin qubits rotates:

236

$$|e\rangle \to 1/\sqrt{2}(|e\rangle + |l\rangle), \quad |l\rangle \to 1/\sqrt{2}(|e\rangle - |l\rangle)$$

$$|\downarrow\rangle \to 1/\sqrt{2}(|\downarrow\rangle + |\uparrow\rangle), \quad |\uparrow\rangle \to 1/\sqrt{2}(|\downarrow\rangle - |\uparrow\rangle)$$

Afer this transformation, the signal contrast directly measures $c_{e\downarrow,l\uparrow}$:

$$2c_{e\downarrow,l\uparrow} = p_{-,\leftarrow} + p_{+,\rightarrow} - p_{-\rightarrow} - p_{+\leftarrow} \Rightarrow \mathcal{C} \geq 0.42(6) \tag{C.14}$$

Similarly, the fidelity of the entangled state (post-selected on the detection of a photon) can be computed by the overlap with the target Bell state [130]:

$$F = \langle\Psi^+|\rho_{ZZ}|\Psi^+\rangle = (p_{e\uparrow} + p_{l\downarrow} + 2c_{e\downarrow,l\uparrow})/2 \geq 0.70(3) \tag{C.15}$$

C.4.2 Correcting for readout infidelity

Errors arising from single-shot readout incorrectly assign the spin state, results in lower-contrast histograms for spin-photon correlations. We follow the analysis done in ref. [130], and correct for readout errors using a transfer matrix formalism. The measured spin-photon correlations p_{ij} are related to the 'true' populations P_{ij} via:

$$
\begin{pmatrix} p_{e\downarrow} \\ p_{e\uparrow} \\ p_{l\downarrow} \\ p_{l\uparrow} \end{pmatrix} = \begin{pmatrix} F_\downarrow & 1-F_\uparrow & 0 & 0 \\ 1-F_\downarrow & F_\uparrow & 0 & 0 \\ 0 & 0 & F_\downarrow & 1-F_\uparrow \\ 0 & 0 & 1-F_\downarrow & F_\uparrow \end{pmatrix} \begin{pmatrix} P_{e\downarrow} \\ P_{e\uparrow} \\ P_{l\downarrow} \\ P_{l\uparrow} \end{pmatrix}
\tag{C.16}
$$

with $F_\downarrow$, $F_\uparrow$ defined above. After this correction, an identical analysis is performed to calculate the error-corrected histograms [Fig. 7.9(b,c,d) dark-shading]. We find an error-corrected concurrence $\mathcal{C} \geq 0.79(7)$ and fidelity $F \geq 0.89(3)$.

C.4.3 ELECTRON-NUCLEAR CONCURRENCE AND FIDELITY CALCULATIONS

For spin-spin Bell states, in contrast to the spin-photon analysis, we can no longer set any of the off-diagonal terms of the density matrix [eq. C.11] to zero due to the limited ($\sim 90\%$) nuclear initialization fidelity. We note that neglecting these off-diagonal terms can only decrease the estimated entanglement in the system, thus the concurrence can still be written as:

$$
\mathcal{C} \geq 2(|c_{\downarrow\uparrow}| - \sqrt{p_{\uparrow\uparrow}p_{\downarrow\downarrow}})
\tag{C.17}
$$

where the first subscript is the electron spin state, and the second is the nuclear state. We estimate $c_{\downarrow\uparrow}$ again by using the measured populations in an orthogonal basis. In this case, off-diagonal terms add a correction:

238

$$2c_{\downarrow\uparrow} + 2c_{\uparrow\downarrow} = p_{\leftarrow\leftarrow} + p_{\rightarrow\rightarrow} - p_{\leftarrow\rightarrow} - p_{\rightarrow\leftarrow} \tag{C.18}$$

In order for the density matrix to be properly normalized, $c_{\uparrow\downarrow} \leq \sqrt{p_{\uparrow\uparrow}p_{\downarrow\downarrow}}$, giving us the final concurrence:

$$\mathcal{C} \geq p_{\leftarrow\leftarrow} + p_{\rightarrow\rightarrow} - p_{\leftarrow\rightarrow} - p_{\rightarrow\leftarrow} - 4\sqrt{p_{\uparrow\uparrow}p_{\downarrow\downarrow}} \tag{C.19}$$

Additionally, both electron readout error as well as ^{13}C mapping infidelity can misreport the true spin state. As such, the new transfer matrix to correct for this error is:

$$\begin{pmatrix} F_{\downarrow,e}F_{\downarrow,N} & F_{\downarrow,e}(1-F_{\uparrow,N}) & (1-F_{\uparrow,e})F_{\downarrow,N} & (1-F_{\uparrow,e})(1-F_{\uparrow,N}) \\ F_{\downarrow,e}(1-F_{\downarrow,N}) & F_{\downarrow,e}F_{\uparrow,N} & (1-F_{\uparrow,e})(1-F_{\downarrow,N}) & (1-F_{\uparrow,e})F_{\uparrow,N} \\ (1-F_{\downarrow,e})F_{\downarrow,N} & (1-F_{\downarrow,e})(1-F_{\uparrow,N}) & F_{\uparrow,e}F_{\downarrow,N} & F_{\uparrow,e}(1-F_{\uparrow,N}) \\ (1-F_{\downarrow,e})(1-F_{\downarrow,N}) & (1-F_{\downarrow,e})F_{\uparrow,N} & F_{\uparrow,e}(1-F_{\downarrow,N}) & F_{\uparrow,e}F_{\uparrow,N} \end{pmatrix} \tag{C.20}$$

Where $F_{\downarrow,e} \approx F_{\uparrow,e} = 0.85$ and $F_{\downarrow,N} \approx F_{\uparrow,N} = 0.72$. Following this analysis, we report an error-corrected concurrence of $\mathcal{C} \geq 0.22(9)$.

C.4.4 Electron-nuclear CNOT gate

We further characterize the CNOT gate itself as a universal quantum gate. Due to the relatively poor readout fidelity (see above), we do not do this by performing quantum state tomography. Instead, we estimate entries in the CNOT matrix using measurements in only the Z-basis. As a control measurement, we first initialize the two qubits in all possible configurations and read out, averaged over many trials. Next, we initialize the qubits, perform a CNOT gate, and read out, again averaged over many trials, normalized by the control data. Any reduction in contrast after normalization is attributed to the opposite spin state, establishing a system of equations for determining the CNOT matrix. We solve this system of equations, marginalizing over free parameters to determine a MLE estimate for the CNOT transfer matrix, as seen in chapter 6.

C.5 Nuclear initialization and readout

Initialization (and readout) of the ^{13}C spin can be done by mapping population between the SiV spin and the ^{13}C. Following reference [247], we note that Z and X gates are possible with dynamical-decoupling based nuclear gates, thus a natural choice for initialization are gates comprised of both $\mathcal{R}^{\pi/2}_{\pm x,\text{SiV}-\text{C}}$ and $\mathcal{R}^{\pi/2}_{z,\text{SiV}-\text{C}}$, as shown in figure C.2(a) and in reference [247]. We note here that it should be possible to combine the effects of $\mathcal{R}_x$ and $\mathcal{R}_z$ rotations in a single gate, which has the potential of shortening and simplifying the total initialzation gate. One proposed sequence uses the following

240
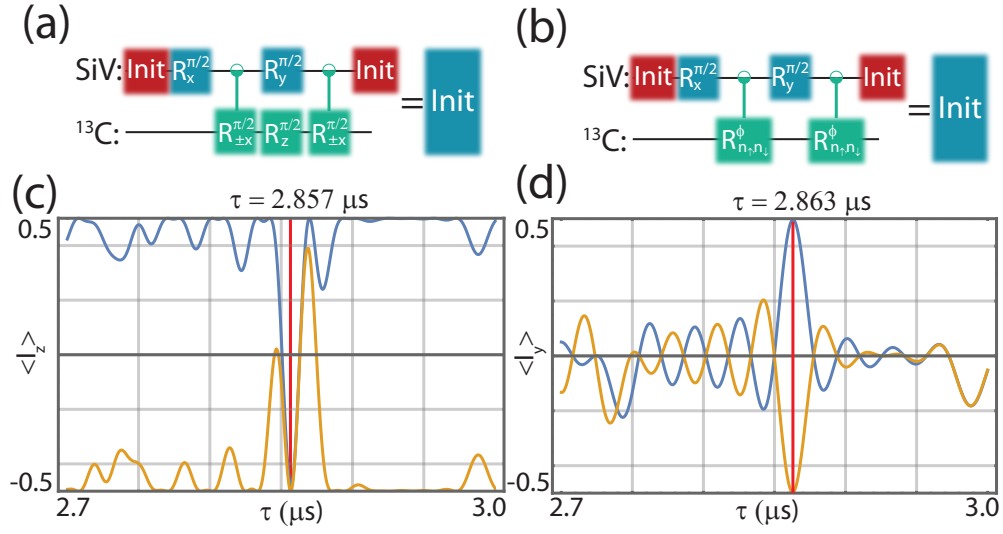
Figure C.2: (a) Original initialization sequence from [247], note $\mathcal{R}_{z,C}^{\pi/2}$ rotation. (b) Simplified initialization sequence used in this work. (c) Simulated performance of the initialization gate from (b) using 8 $\pi-$pulses per each nuclear gate, the initial state is $|\uparrow\uparrow\rangle$ (blue) and $|\uparrow\downarrow\rangle$ (orange). The resonances are narrow compared to (d) due to applying effectively twice more $\pi-$pulses (d) Simulated performance of $\mathcal{R}_{\pm x, \text{SiV}-\text{C}}^{\pi/2}$ gate for 8 $\pi-$pulses for SiV-^{13}C register initialized in $|\uparrow\uparrow\rangle$ (blue) and $|\downarrow\uparrow\rangle$ (orange)

entangling gate:

$$
\mathcal{R}_{\vec{n_\uparrow},\vec{n_\downarrow}}^{\phi} = \begin{pmatrix} (1+i)/2 & i/\sqrt{2} & 0 & 0 \\ i/\sqrt{2} & (1-i)/\sqrt{2} & 0 & 0 \\ 0 & 0 & (1+i)/2 & -i/\sqrt{2} \\ 0 & 0 & -i/\sqrt{2} & (1-i)/2 \end{pmatrix}
$$

$$
= \begin{pmatrix} R_{\Theta=\pi/4}^{\pi/2} R_z^{\pi/2} & 0 \\ 0 & R_{\Theta=\pi/4}^{-\pi/2} R_z^{\pi/2} \end{pmatrix} \quad \text{(C.21)}
$$

241

which corresponds to a rotation on the angle $\phi = 2\pi/3$ around the axes $n_{\uparrow,\downarrow} = \{\pm\sqrt{2}, 0, 1\}/\sqrt{3}$.

The matrix of entire initialization gate [Fig. C.2(b)] built from this gate would then be:

$$\mathrm{Init} = \begin{pmatrix} 0 & 0 & -(1+i)/2 & -1/\sqrt{2} \\ i/\sqrt{2} & -(1+i)/2 & 0 & 0 \\ 0 & 0 & -(1-i)/2 & -i/\sqrt{2} \\ 1/\sqrt{2} & (1-i)/2 & 0 & 0 \end{pmatrix} \tag{C.22}$$

which results in an initialized $^{13}\mathrm{C}$ spin.

To demonstrate this, we numerically simulate a MW pulse sequence using the exact coupling parameters of our $^{13}\mathrm{C}$ (chapter 6) and 8 $\pi-$pulses for each $\mathcal{R}^\phi_{\vec{n_\uparrow},\vec{n_\downarrow}}$ gate. Figure C.2(c) shows that regardless of the initial state, the $^{13}\mathrm{C}$ always ends up in state $|\downarrow\rangle$ (given that the SiV was initialized in $|\uparrow\rangle$). As expected, the timing of this gate ($\tau_{\mathrm{init}} = 2.857\,\mathrm{s}$) is noticeably different from the timing of the $\mathcal{R}^{\pi/2}_{\pm x,\mathrm{SiV-C}}$ gate ($\tau_{\pi/2} = 2.851\,\mathrm{s}$), which occurs at spin-echo resonances [Fig. C.2(d)].

The rotation matrix for this sequence at $\tau = \tau_{\mathrm{init}}$ (with the SiV initialized in $|\uparrow\rangle$) is:

$$\mathcal{R}^\phi_{n_\uparrow} = \begin{pmatrix} 0.55 + 0.51i & 0 + 0.65i \\ 0.65i & 0.55 - 0.52i \end{pmatrix} \tag{C.23}$$

corresponding to a rotation angle $\phi = 0.63\pi$ around the axis $n_\uparrow = \{0.78, 0, 0.62\}$, very close to the theoretical result.

242

Since the experimental fidelities for both initialization gates [Fig. C.2 (a,b)] are similar, we use sequence (b) to make the gate shorter and avoid unnecessary pulse-errors.

D

Supporting material for chapter 8

We perform all measurements in a dilution refrigerator (DR, BlueFors BF-LD250) with a base temperature of 20 mK. The DR is equipped with a superconducting vector magnet (American Magnets Inc. 6-1-1 T), a home-built free-space wide-field microscope with a cryogenic objective (Attocube LT-APO-VISIR), piezo positioners (Attocube ANPx101 and ANPx311 series), and fiber and MW feedthroughs. Tuning of the nanocavity resonance is performed using a gas condensation technique [76]. The SiV-cavity system is optically interrogated through the fiber network without any free-space optics [77]. The operating temperature of the memory node during the BSM measurements was 100-300 mK. We note that similar performance at higher temperatures should be feasible in future experiments leveraging recent developments with heavier group-IV color-centers [88] or highly strained SiV centers [244]. Additional details about the experimental

setup and device fabrication [184, 245, 266, 289] for millikelvin nanophotonic cavity QED experiments with SiV centers are thoroughly described in a separate publication [78].

D.1 Characterization of the nanophotonic quantum memory

A spectrum of the SiV-cavity system at large detuning (248 GHz) allows us to measure the cavity linewidth $\kappa = 21.6 \pm 1.3$ GHz, (Fig. D.1a, blue curve) and natural SiV linewidth $\gamma = 0.123 \pm 0.010$ GHz (Fig. D.1a, red curve). We find spectral diffusion of the SiV optical frequency to be much smaller than γ on minute timescales with an excitation photon flux of less than 1 MHz. Next, we estimate the single-photon Rabi frequency, g, using the cavity reflection spectrum for zero atom-cavity detuning, shown in red in Fig. D.1a. For a resonant atom-cavity system probed in reflection from a single port with cavity-waveguide coupling κ_{wg}, the cavity reflection coefficient [94] as a function of probe detuning Δ_c is given by

$$r(\Delta_c) = \frac{i\Delta_c + \frac{g^2}{i\Delta_c + \frac{\gamma}{2}} - \kappa_{wg} + \frac{\kappa}{2}}{i\Delta_c + \frac{g^2}{i\Delta_c + \frac{\gamma}{2}} + \frac{\kappa}{2}}. \tag{D.1}$$

By fitting $|r(\Delta_c)|^2$ using known values of κ and γ, we obtain the solid red curve in Fig. D.1a which corresponds to a single-photon Rabi frequency $g = 8.38 \pm 0.05$ GHz, yielding the estimated cooperativity $C = \frac{4g^2}{\kappa\gamma} = 105 \pm 11$.

245
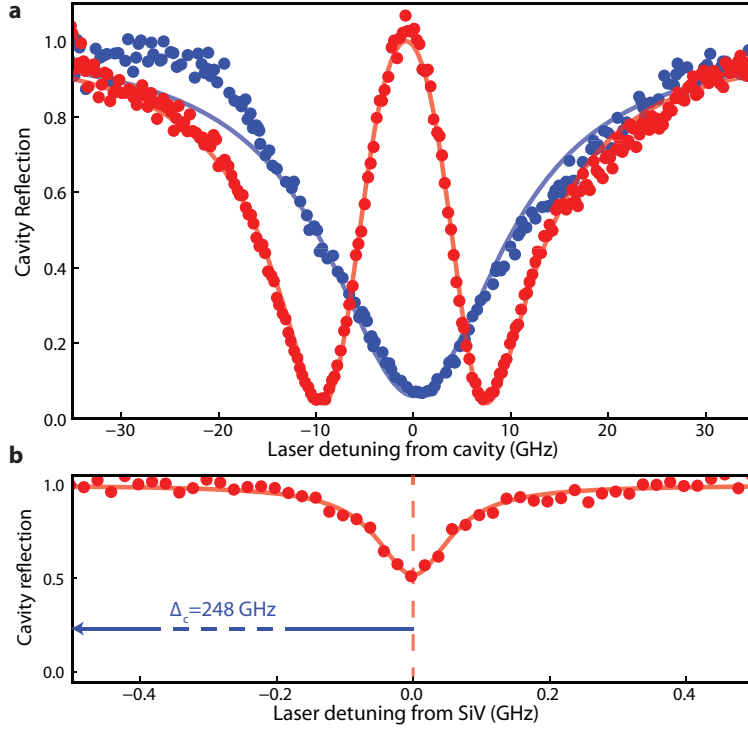
Figure D.1: Characterization of device cooperativity. a, Cavity reflection spectrum far-detuned (blue) and on resonance (red) with SiV center. Blue solid line is a fit to a Lorentzian, enabling extraction of linewidth $\kappa = 21.8\,\text{GHz}$. Red solid line is a fit to a model used to determine the single-photon Rabi frequency $g = 8.38 \pm 0.05$ GHz and shows the onset of a normal mode splitting. **b,** Measurement of SiV linewidth far detuned ($\Delta_c = 248\,\text{GHz}$) from cavity resonance. Red solid line is a fit to a Lorentzian, enabling extraction of natural linewidth $\gamma = 0.123\,\text{GHz}$.

D.2   MICROWAVE CONTROL

We use resonant MW pulses delivered via an on-chip coplanar waveguide (CWG) to coherently control the quantum memory [77, 78]. First, we measure the spectrum of the spin-qubit transition by applying a weak, 10 s-long microwave pulse of variable frequency, observing the optically-detected magnetic resonance (ODMR) spectrum presented in

Fig. D.2a. We note that the spin-qubit transition is split by the presence of a nearby ^{13}C. While coherent control techniques can be employed to utilize the ^{13}C as an additional qubit [77, 78], we do not control or initialize it in this experiment. Instead, we drive the electron spin with strong microwave pulses at a frequency f_Q such that both ^{13}C-state-specific transitions are addressed equally. This also mitigates slow spectral diffusion of the microwave transition [78] of $\sim 100\,$kHz.

After fixing the MW frequency at f_Q we vary the length of this drive pulse (τ_R in Fig. D.2b) and observe full-contrast Rabi oscillations. We choose a π time of $32\,$ns in the experiments in the main text, which is a compromise of two factors: (1) it is sufficiently fast such that we can temporally multiplex between 2 and 4 time-bin qubits around each microwave π pulse and (2) it is sufficiently weak to minimize heating related effects from high microwave currents in resistive gold CWG.
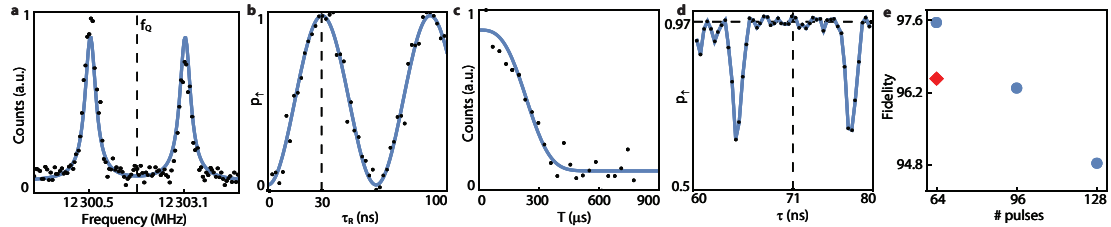
Figure D.2: Microwave characterization of spin-coherence properties. a, ODMR spectrum of the qubit transition at $\sim 12\,$GHz split by coupling to a nearby 13^C. **b,** Rabi oscillations showing π time of $30\,$ns. A π time of $32\,$ns is used for experiments in the main text. **c,** XY8-1 dynamical decoupling signal (unnormalized) as a function of total time T, showing coherence lasting on the several hundred s timescale. **d,** XY8-8 dynamical decoupling signal (normalized) revealing region of high fidelity at relevant value of $2\tau = 142\,$ns. **e,** Fidelity of spin state after dynamical decoupling sequence with varying number of π pulses (N_π), blue points. Red point (diamond) is under illumination with $\langle n \rangle_m = 0.02$.

With known π time we measure the coherence time of the SiV spin qubit under an XY8-1 dynamical decoupling sequence to exceed $200\,\mathrm{s}$ (Fig. D.2c). In the main experiment we use decoupling sequences with more π pulses. As an example, Fig. D.2d shows the population in the $|\uparrow\rangle$ state after XY8-8 decoupling sequence (total $N_\pi = 64$ π pulses) as a function of τ, half of the inter-pulse spacing. For BSM experiments, this inter-pulse spacing, 2τ, is fixed and is matched to the time-bin interval δt. While at some times (e.g. $\tau = 64.5\,\mathrm{ns}$) there is a loss of coherence due to entanglement with the nearby ^{13}C, at $2\tau = 142\,\mathrm{ns}$ we are decoupled from this ^{13}C and can maintain a high degree of spin coherence. Thus we chose the time-bin spacing to be $142\,\mathrm{ns}$. The spin coherence at $2\tau = 142\,\mathrm{ns}$ is plotted as a function N_π in Fig. D.2d, and decreases for large N_π, primarily due to heating related effects [77].

D.3 Fiber network

The schematic of the fiber-network used to deliver optical pulses to and collect reflected photons from the nanophotonic memory device is shown in Fig. D.3b. Photons are routed through the lossy (1%) port of a 99:1 fiber beamsplitter (FBS) to the nanophotonic device. We note that for practical implementation of memory-assisted quantum communication, an efficient optical switch or circulator should be used instead. In this experiment, since we focus on benchmarking the performance of the memory device itself, the loss introduced by this beamsplitter is incorporated into the estimated channel

loss. Reflected photons are collected and routed back through the efficient (99%) port of the FBS and are sent to the time-delay interferometer (TDI) in the heralding setup. The outputs of the TDI are sent back into the dilution refrigerator and directly coupled to superconducting nanowire single photon detectors (SNSPDs, PhotonSpot), which are mounted at the 1K stage and are coated with dielectrics to optimize detection efficiency exactly at 737 nm.

The total heralding efficiency η of the memory node is an important parameter since it directly affects the performance of the BSM for quantum communication experiments. One of the contributing factors is the detection quantum efficiency (QE) of the fiber-coupled SNSPDs. To estimate it we compare the performance of the SNSPDs to the specifications of calibrated conventional avalanche photodiodes single-photon counters (Laser Components COUNT-10C-FC). The estimated QEs of the SNSPDs with this method are as close to unity as we can verify. Additionally, we measure $< 1\%$ reflection from the fiber-SNSPD interface, which typically is the dominant contribution to the reduction of QE in these devices. Thus we assume the lower bound of the QE of the SNSPDs to be $\eta_{\mathrm{QE}} = 0.99$ for the rest of this section. Of course, this estimation is subject to additional systematic errors. However, the actual QE of these detectors would be a common factor (and thus drop out) in a comparison between any two physical quantum communication systems.

Here we use 2 different approaches to estimate η. We first measure the most dominant loss, which arises from the average reflectivity of the critically coupled nanophotonic

249
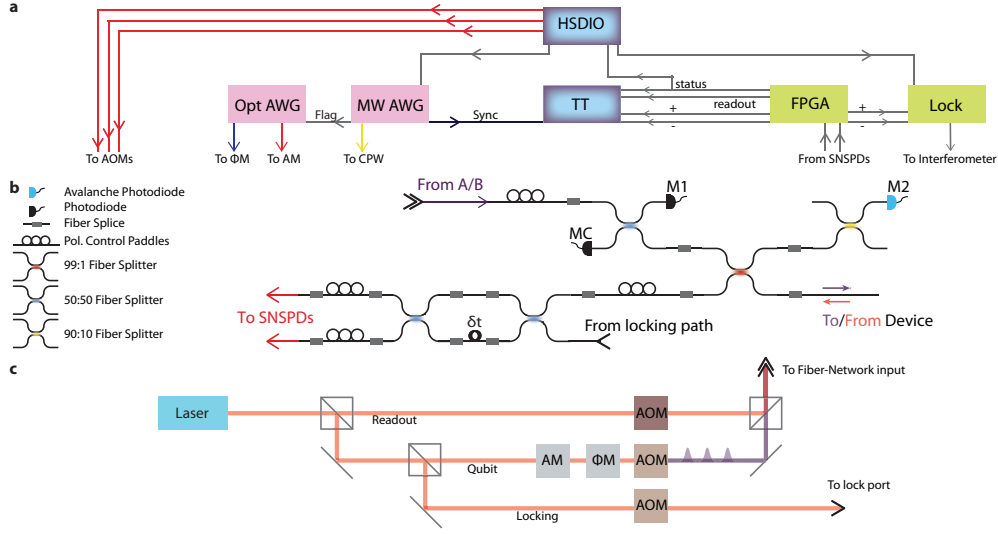
Figure D.3: Experimental schematic. a, Control flow of experiment. Opt (MW) AWG is a Tektronix AWG7122B 5 GS/s (Tektronix AWG70001a 50 GS/s) arbitrary waveform generator used to generate photonic qubits (microwave control signals). All signals are recorded on a time-tagger (TT, PicoQuant HydraHarp 400). **b,** Fiber network used to deliver photons to and collect photons from the memory device, including elements for polarization control and diagnostic measurements of coupling efficiencies. **c,** Preparation of optical fields. The desired phase relation between lock and qubit paths is ensured by modulating AOMs using phase-locked RF sources with a precise 1.8 MHz frequency shift between them.

cavity (Fig. D.1b). While the $|\uparrow\rangle$ state is highly reflecting (94.4%), the $|\downarrow\rangle$ state reflects only 4.1% of incident photons, leading to an average device reflectivity of $\eta_{sp} = 0.493$.

In method (1), we compare the input power photodiode M1 with that of photodiode MC. This estimates a lower-bound on the tapered-fiber diamond waveguide coupling efficiency of $\eta_c = 0.930 \pm 0.017$. This error bar arises from uncertainty due to photodiode noise and does not include systematic photodiode calibration uncertainty. However, we note that if the tapered fiber is replaced by a silver-coated fiber-based retroreflector, this calibration technique extracts a coupling efficiency of $\eta_c^{cal} \approx 0.98$, which is consistent

with the expected reflectivity from such a retroreflector. We independently calibrate the efficiency through the 99:1 fiber beamsplitter and the TDI to be $\eta_f = 0.934$. This gives us our first estimate on the overall heralding efficiency $\eta = \eta_{sp}\eta_c\eta_f\eta_{\mathrm{QE}} = 0.425 \pm 0.008$.

In method (2), during the experiment we compare the reflected counts from the highly-reflecting ($|\uparrow\rangle$) spin-state measured on the SNSPDs with the counts on an avalanche photodiode single photon counting module (M2 in Fig. D.3b) which has a calibrated efficiency of ≈ 0.7 relative to the SNSPDs. From this measurement, we estimate an overall efficiency of fiber-diamond coupling, as well as transmission through all relevant splices and beamsplitters of $\eta_c\eta_f = 0.864 \pm 0.010$. This error bar arises from shot noise on the single photon detectors. Overall, this gives us a consistent estimate of $\eta = \eta_{sp}\eta_c\eta_f\eta_{\mathrm{QE}} = 0.422 \pm 0.005$. Methods (1) and (2), which each have independent systematic uncertainties associated with imperfect photodetector calibrations, are consistent to within a small residual systematic uncertainty, which is noted in the text where appropriate.

D.4 Experimental details of quantum communication experiment

An asynchronous BSM (Fig. 8.3a) relies on (1) precise timing of the arrival of optical pulses (corresponding to photonic qubits [401, 402] from Alice and Bob) with microwave control pulses on the quantum memory and (2) interferometrically stable rotations on reflected time-bin qubits for successful heralding. In order to accomplish (1), all equip-

Step	Process	Duration	Proceed to
1	Lock time-delay interferometer	$200\,\mathrm{ms}$	2
2	Readout SiV	$30\,\mathrm{s}$	If status LOW: 4, else: 3
3	Apply microwave π pulse	$32\,\mathrm{ns}$	2
4	Run main experiment script	$\sim 200\,\mathrm{ms}$	1

Table D.1: High-level experimental sequence. This sequence is programmed into the HSDIO and uses feedback from the status trigger sent from the FPGA (see Fig. D.3a). Main experimental sequence is described in Table D.2. External software with a response time of $100\,\mathrm{ms}$ is also used to monitor the status trigger. If it is HI for $\gtrsim 2\,\mathrm{s}$, the software activates an automatic re-lock procedure which compensates for spectral diffusion and ionization of the SiV center (Methods). Additionally, we keep track of the timing when the TDI piezo voltage rails. This guarantees that the SiV is always resonant with the photonic qubits and that the TDI performs high-fidelity measurements in X basis.

ment used for generation of microwave and optical fields is synchronized by a single device (National Instriuments HSDIO, Fig. D.3a) with programming described in Table D.1, D.2.

In order to accomplish (2), we use a single, narrow linewidth ($< 50\,\mathrm{kHz}$) Ti:Sapphire laser (M Squared SolsTiS-2000-PSX-XF, Fig. D.3b) both for generating photonic qubits and locking the TDI used to herald their arrival. In the experiment, photonic qubits are reflected from the device, sent into the TDI, and detected on the SNSPDs. All detected photons are processed digitally on a field-programmable gate array (FPGA, Fig. D.3a), and the arrival times of these heralding signals are recorded on a time-tagger (TT, Fig. D.3a), and constitute one bit of information of the BSM (m_1 or m_2). At the end of the experiment, a $30\,\mathrm{s}$ pulse from the readout path is reflected off the device, and photons are counted in order to determine the spin state (m_3) depending on the threshold shown in Fig. 8.2c.
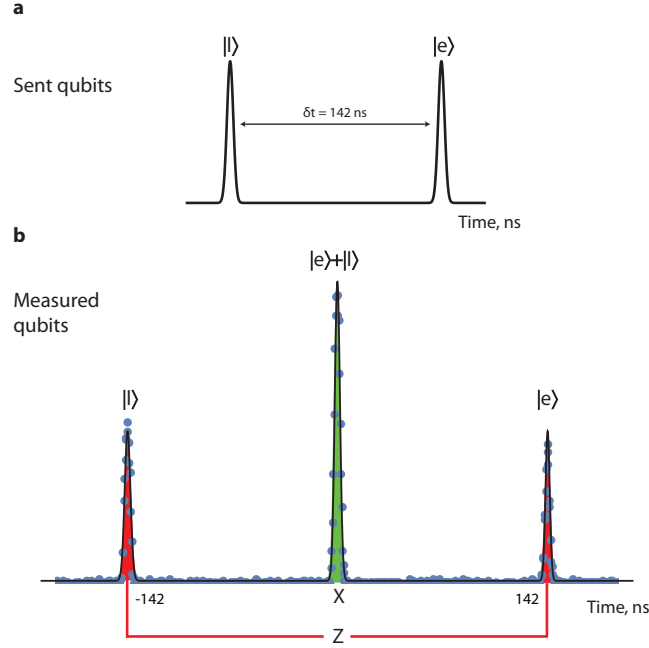
Figure D.4: Measurements on a single time-bin qubit in Z and X bases. a, Example of optical pulses sent for example in the experiment described in Fig. 8.2d. **b,** Time trace of detected photons on + detector when pulses shown in (a) are sent directly into the TDI. The first and last peaks correspond to late and early photons taking the long and short paths of the TDI, which enable measurements in the Z basis $\{|e\rangle, |l\rangle\}$. The central bin corresponds to the late and early components overlapping and interfering constructively to come out of the + port, equivalent to a measurement of the time bin qubit in the $|+x\rangle$ state. A detection event in this same timing window on the - detector (not shown) would constitute a $|-x\rangle$ measurement. In this measurement, the TDI was left unlocked, so we observe no interference in the central window.

To minimize thermal drift of the TDI, it is mounted to a thermally weighted aluminum breadboard, placed in a polyurethane foam-lined and sand filled briefcase, and secured with glue to ensure passive stability on the minute timescale. We halt the experiment and actively lock the interferometer to the sensitive Y-quadrature every $\sim 200\,\mathrm{ms}$ by changing the length of the roughly $28\,\mathrm{m}$ long ($142\,\mathrm{ns}$) delay line with a cylindrical piezo. In order to use the TDI for X-measurements of the reflected qubits, we apply a frequency

Step	Process	Duration	Proceed to
1	Run sequence in Fig. 8.3a for a given N	$10-20$ s	2
2	Readout SiV + report readout to TT	$30\,$s	If status LOW: 1, else: 3
3	Apply microwave π pulse	$32\,$ns	4
4	Readout SiV	$30\,$s	If status LOW: 3, else: 1

Table D.2: Main experimental sequence for memory-enhanced quantum communication. This script is followed until step 1 is run a total of 4000 times, and then terminates and returns to step 1 of Table D.1. The longest step is the readout step, which is limited by the fact that we operate at a photon detection rate of $\sim 1\,$MHz to avoid saturation of the SNSPDs.

shift of $1.8\,$MHz using the qubit AOM, which is $1/4$ of the free-spectral range of the TDI. Since the nanophotonic cavity, the TDI, and the SNSPDs are all polarization sensitive, we use various fiber-based polarization controllers (Fig. D.3b). All fibers in the network are covered with aluminum foil to prevent thermal polarization drifts. This results in an interference visibility of the TDI of $> 99\%$ that is stable for several days without any intervention with lab temperature and humidity variations of $\pm 1°$ C and $\pm 5\%$ respectively.

In order to achieve high-fidelity operations we have to ensure that the laser frequency (which is not locked) is resonant with the SiV frequency f_0 (which is subject to the spectral diffusion [78]). To do that we implement a so-called preselection procedure, described in Table D.1, D.2 and Fig. D.3a. First, the SiV spin state is initialized by performing a projective measurement and applying microwave feedback. During each projective readout, the reflected counts are compared with two thresholds: a "readout" threshold of 7 photons (used only to record m_3), and a "status" threshold of 3 photons. The status trigger is used to prevent the experiment from running in cases when the

laser is no longer on resonance with f_0, or if the SiV has ionized to an optically inactive charge state. The duty cycle of the status trigger is externally monitored and is used to temporarily abort the experiment and run an automated re-lock procedure that locates and sets the laser to the new frequency f_0, reinitailizing the SiV charge state with a 520 nm laser pulse if nececssary. This protocol enables fully automated operation at high fidelities (low QBER) for several days without human intervention.

D.5 Theoretical description of asynchronous Bell state measurement

Here we give a theoretical description of how the sequence depicted in Fig. 8.3a corresponds to an asynchronous BSM between two photonic time-bin qubits. Below, we also describe how this enables the experimental observation of the violation of the Bell-CHSH inequality.

Due to the critical coupling of the nanocavity, the memory node only reflects photons when the SiV spin is in the state $|\uparrow\rangle$. The resulting correlations between the spin and the reflected photons can still be used to realize a BSM between two asynchronously arriving photonic time-bin qubits using an adaptation of the well known proposal of Duan and Kimble for entangling a pair of photons incident on an atom-cavity system [113]. As a result of the critical coupling, we only have access to two of the four Bell states at any time, with the inaccessible Bell states corresponding to photons being

transmitted through the cavity (and thus lost from the detection path). Depending on whether there was an even or odd number of π-pulses on the spin between the arrival of the two heralded photons, we distinguish either the $\{|\Phi_\pm\rangle\}$ or $\{|\Psi_\pm\rangle\}$ states (defined below). For the sake of simplicity, we first describe the BSM for the case when the early time bin of Alice's and Bob's qubits both arrive after an even number of microwave π pulses after its initialization. Thereafter we generalize this result and describe the practical consequences for the quantum communication protocol.

The sequence begins with a $\pi/2$ microwave pulse, preparing the spin in the state $|\psi_i\rangle = (|\uparrow\rangle + |\downarrow\rangle)/\sqrt{2}$. In the absence of a photon at the device, the subsequent microwave π-pulses, which follow an XY8-N type pattern, decouple the spin from the environment and at the end of the sequence should preserve the spin state $|\psi_i\rangle$. However, reflection of Alice's photonic qubit $|A\rangle = (|e\rangle + e^{i\phi_1} |l\rangle)/\sqrt{2}$ from the device results in the entangled spin-photon state $|\psi_A\rangle = (|\uparrow e\rangle + e^{i\phi_1} |\downarrow l\rangle)/\sqrt{2}$. The full system is in the state

$$|\psi_A\rangle = \frac{|+x\rangle\,(|\uparrow\rangle + e^{i\phi_1}\,|\downarrow\rangle) + |-x\rangle\,(|\uparrow\rangle - e^{i\phi_1}\,|\downarrow\rangle)}{2}. \tag{D.2}$$

Regardless of the input photon state, there is equal probability to measure the reflected photon to be $|\pm x\rangle$. Thus, measuring the photon in X basis (through the TDI) does not reveal the initial photon state. After this measurement, the initial state of the photon $|A\rangle$ is teleported onto the spin: $|\psi_{m_1}\rangle = (|\uparrow\rangle + m_1 e^{i\phi_1} |\downarrow\rangle)\sqrt{2}$, where $m_1 = \pm 1$ denotes the detection outcome of the TDI [77]. The quantum state of Alice's photon is

now stored in the spin state, which is preserved by the dynamical decoupling sequence.

Reflection of the second photon $|B\rangle = (|e\rangle + e^{i\phi_2} |l\rangle)\sqrt{2}$ from Bob results in the spin-photon state $|\psi_{m_1,B}\rangle = (|\uparrow e\rangle + m_1 e^{i(\phi_1+\phi_2)} |\downarrow l\rangle)/\sqrt{2}$. This state now has a phase that depends on the initial states of both photons, enabling the photon-photon BSM measurements described below. Rewriting Bob's reflected photon in the X basis, the full system is in the state

$$|\psi_{m_1,B}\rangle = \frac{|+x\rangle (|\uparrow\rangle + m_1 e^{i(\phi_1+\phi_2)} |\downarrow\rangle) + |-x\rangle (|\uparrow\rangle - m_1 e^{i(\phi_1+\phi_2)} |\downarrow\rangle)}{2}. \qquad \text{(D.3)}$$

The second measurement result m_2 once again contains no information about the initial state $|B\rangle$, yet heralds the final spin state $|\psi_{m_1,m_2}\rangle = (|\uparrow\rangle + m_1 m_2 e^{i(\phi_1+\phi_2)} |\downarrow\rangle)$ as described in the main text. When this state lies along the X axis of the Bloch sphere ($\phi_1+\phi_2 = \{0, \pi\}$), the final result of the X basis measurement on the spin state m_3 has a deterministic outcome, dictated by all values of the parameters $\{\phi_1, \phi_2\}$ (known only to Alice and Bob) and $\{m_1, m_2\}$ (which are known to Charlie, but are completely random). Conversely, all information available to Charlie $\{m_1, m_2, m_3\}$ only contains information on the correlation between the photonic qubits, not on their individual states. The resulting truth table for different input states is given in table D.3. For all input states, there is equal probability of measuring ± 1 for each individual measurement m_i. However, the overall parity of the three measurements $m_1 m_2 m_3$ depends on whether or not the input photons were the same, or opposite, for inputs $|A\rangle, |B\rangle \in |\pm x\rangle$ or $|\pm y\rangle$.

257

We now address the fact that the BSM distinguishes either between $\{|\Phi_\pm\rangle\}$ or $\{|\Psi_\pm\rangle\}$ if there was an even or odd number of microwave π pulses between incoming photons respectively. This effect arises because each π pulse in the dynamical decoupling sequence toggles an effective frame change: $Y \leftrightarrow -Y$. The impact on this frame change on the BSM can be seen by writing the pairs of Bell states ($|\Phi_\pm\rangle = (|ee\rangle \pm |ll\rangle)/\sqrt{2}$ and $|\Psi_\pm\rangle = (|el\rangle \pm |le\rangle)/\sqrt{2}$) in the X and Y bases, where we have

$$|\Phi_\pm\rangle^{(X)} = (|+x\rangle |\pm x\rangle + |\mp x\rangle |-x\rangle)/\sqrt{2} \tag{D.4}$$

$$|\Phi_\pm\rangle^{(Y)} = (|+y\rangle |\mp y\rangle + |\pm y\rangle |-y\rangle)/\sqrt{2} \tag{D.5}$$

$$|\Psi_\pm\rangle^{(X)} = (|+x\rangle |\pm x\rangle - |\mp x\rangle |-x\rangle)/\sqrt{2} \tag{D.6}$$

$$|\Psi_\pm\rangle^{(Y)} = i(|+y\rangle |\pm y\rangle - |\mp y\rangle |-y\rangle)/\sqrt{2} \tag{D.7}$$

For X basis inputs, as seen by Eq. D.4 and D.6, switching between $\{|\Phi_\pm\rangle\}$ and $\{|\Psi_\pm\rangle\}$ measurements does not affect the inferred correlation between input photons. For Y basis inputs however, this does result in an effective bit flip in the correlation outcome (see Eq. D.5 and D.7). In practice, Alice and Bob can keep track of each Y photon sent and apply a bit flip accordingly, as long as they have the appropriate timing information about MW pulses applied by Charlie. If Charlie does not give them the appropriate information, this will result in an increased QBER which can be detected.

Alice	Bob	Parity	Bell state
$|+x\rangle$	$|+x\rangle$	$+1$	$|\Phi_+\rangle$
$|+x\rangle$	$|-x\rangle$	-1	$|\Phi_-\rangle$
$|-x\rangle$	$|+x\rangle$	-1	$|\Phi_-\rangle$
$|-x\rangle$	$|-x\rangle$	$+1$	$|\Phi_+\rangle$
$|+y\rangle$	$|+y\rangle$	-1	$|\Phi_-\rangle$
$|+y\rangle$	$|-y\rangle$	$+1$	$|\Phi_+\rangle$
$|-y\rangle$	$|+y\rangle$	$+1$	$|\Phi_+\rangle$
$|-y\rangle$	$|-y\rangle$	-1	$|\Phi_-\rangle$

Table D.3: Truth table of asynchronous BSM protocol, showing the parity (and BSM outcome) for each set of valid input states from Alice and Bob. In the case of Y basis inputs, Alice and Bob adjust the sign of their input state depending on whether it was commensurate with an even or odd numbered free-precession interval, based on timing information provided by Charlie (Supplementary Information).

As an additional remark, this scheme also works for pairs of photons that are not both in the X or Y basis but still satisfy the condition $\phi_1 + \phi_2 = 0$. For example, $|a\rangle$ and $|b\rangle$ from Fig. 8.3b satisfy this condition. In this case, adequate correlations can still be inferred about the input photons, although they were sent in different bases.

Finally, we would like to note that this asynchronous scheme for performing a BSM between two pulses has an important advantage over the synchronous, linear-optical implementation. In the case where Alice and Bob use attenuated laser pulses to encode photonic qubits, which is by far the most technologically simple implementation, there is an inherent QBER of 25% for photons sent in the X and Y bases. This is because the linear-optical implementation relies on the pulses to overlap on a beamsplitter and interfere via the Hong-ou-Mandel effect, which has a finite visibility of 50% for coherent pulses [377]. Intuitively, this finite error arises from a fundamental inability to dis-

tinguish between detection outcomes where two individual single-photons arrived from Alice and Bob versus a two-photon component from either Alice or Bob in the synchronous scheme. In the asynchronous scheme, since pulses do not arrive at the same time from Alice and Bob, this error is mitigated. As a result, for ideal quantum memory operation and sufficiently attenuated laser pulses, the ultimate limit to the QBER is zero.

In order to perform a test of the Bell-CHSH inequality [53], we send input photons equally distributed from all states $\{|\pm x\rangle, |\pm y\rangle, |\pm a\rangle, |\pm b\rangle\}$ (Fig. 8.3b). We select for cases where two heralding events arise from input photons $\{A, B\} = \pm 1$ that are either $45°$ or $135°$ apart from one another. Conditioned on the parity outcome of the BSM (± 1), the Bell-CHSH inequality bounds the correlations between input photons as

$$S_\pm = |\langle A \cdot B \rangle_{xa} - \langle A \cdot B \rangle_{xb} - \langle A \cdot B \rangle_{ya} - \langle A \cdot B \rangle_{yb}| \leq 2, \qquad \text{(D.8)}$$

where the subscripts denote the bases the photons were sent in. The values of each individual term in Eq. D.8, denoted as "input correlations," are plotted in Fig. 8.3d for positive and negative parity outcomes.

D.6 Optimal parameters for asynchronous Bell state measurements

We minimize the experimentally extracted QBER for the asynchronous BSM to optimize the performance of the memory node. The first major factor contributing to QBER is the

scattering of a third photon that is not detected, due to the finite heralding efficiency $\eta = 0.423 \pm 0.04$. This is shown in Fig. 8.2f, where the fidelity of the spin-photon entangled state diminishes for $\langle n \rangle_m \gtrsim 0.02$. At the same time, we would like to work at the maximum possible $\langle n \rangle_m$ in order to maximize the data rate to get enough statistics to extract QBER (and in the quantum communication setting, efficiently generate a key).

To increase the key generation rate per channel use, one can also fit many photonic qubits within each initialization of the memory. In practice, there are 2 physical constraints: (1) the bandwidth of the SiV-photon interface and (2) the coherence time of the memory. We find that one can satisfy (1) at a bandwidth of roughly 50 MHz with no measurable infidelity. For shorter optical pulses (< 10 ns), the spin-photon gate fidelity is reduced. In principle, the SiV-photon bandwidth can be increased by reducing the atom-cavity detuning (here ~ 60 GHz) at the expense of having to operate at higher magnetic fields where microwave qubit manipulation is not as convenient [78].

Even with just an XY8-1 decoupling sequence (number of π pulses $N_\pi = 8$), the coherence time of the SiV is longer than $200\,\mu$s (Fig. D.2c) and can be prolonged to the millisecond range with longer pulse sequences [77]. Unfortunately, to satisfy the bandwidth criteria (1) and to drive both hyperfine transitions (Fig. D.2a), we must use short (32 ns) long π pulses, which cause additional decoherence from ohmic heating [78] already at $N_\pi = 64$ (Fig. D.2e). Due to this we limit the pulse sequences to a maximum $N_\pi = 128$, and only use up to $\approx 20\,\mu$s of the memory time. One solution would be to

261

switch to superconducting microwave delivery. Alternatively, one can use a larger value of τ to allow the device to cool down in between subsequent pulses [78] at the expense of having to stabilize a TDI of larger δt. Working at larger δt also enables temporal multiplexing by fitting multiple time-bin qubits per free-precession interval. In fact, with $2\tau = 142\,\text{ns}$, even given constraint (1) and the finite π time, we can already fit up to 4 optical pulses per free-precession window, enabling a total number of photonic qubits of up to $N = 504$ for only $N_\pi = 128$.

In benchmarking the asynchronous BSM for quantum communication, we optimize the parameters $\langle n \rangle_m$ and N to maximize our enhancement over the direct transmission approach, which is a combination of both increasing N and reducing the QBER, since a large QBER results in a small distilled key fraction r_s. As described in the main text, the effective loss can be associated with $\langle n \rangle_p$, which is the average number of photons per photonic qubit arriving at the device, and is given straightforwardly by $\langle n \rangle_p = \langle n \rangle_m / N$. The most straightforward way to sweep the loss is to keep the experimental sequence the same (fixed N) and vary the overall power, which changes $\langle n \rangle_m$. The results of such a sweep are shown in Fig. D.5a, b. For larger $\langle n \rangle_m$ (corresponding to lower effective channel losses), the errors associated with scattering an additional photon reduce the performance of the memory device.

Due to these considerations, we work at roughly $\langle n \rangle_m \lesssim 0.02$ for experiments in the main text shown in Fig. 8.3 and 8.4, below which the performance does not improve significantly. At this value, we obtain BSM successes at a rate of roughly $0.1\,\text{Hz}$. By
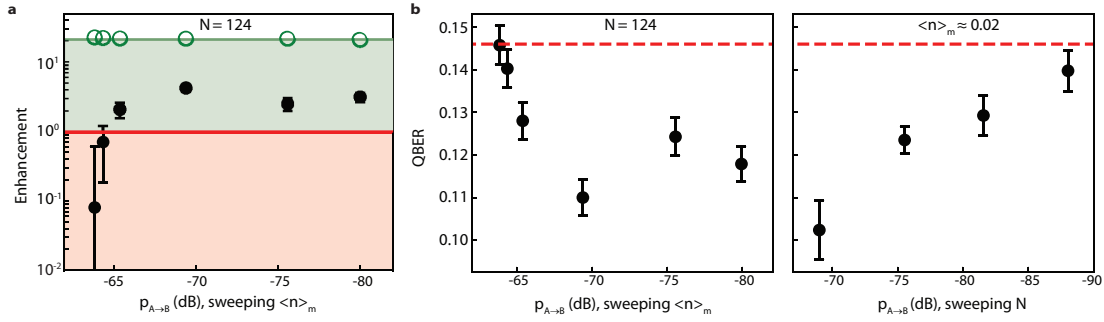
Figure D.5: Performance of memory-device versus of channel loss. a, Enhancement of memory-based approach compared to direct transmission approach, keeping $N = 124$ fixed and varying $\langle n \rangle_m$ in order to vary the effective channel transmission probability $p_{A \to B}$. At high $p_{A \to B}$ (larger $\langle n \rangle_m$), r_s approaches 0 due to increased QBER arising from undetected scattering of a third photon. **b,** (Left) Plot of QBER for same sweep of $\langle n \rangle_m$ shown in **a**. (Right) Plot of QBER while sweeping N in order to vary loss. These points correspond to the same data shown in Fig. 8.4. At lower $p_{A \to B}$ (larger N), microwave-induced heating-related dephasing leads to increased QBER. Vertical error bars are given by the 68% confidence interval and horizontal error bars represent the standard deviation of the systematic power fluctuations.

fixing $\langle n \rangle_m$ and increasing N, we maintain a tolerable BSM success rate while increasing the effective channel loss. Eventually, as demonstrated in Fig. D.5c and in the high-loss data point in Fig. 8.4, effects associated with microwave heating result in errors that again diminish the performance of the memory node for large N. As such, we conclude that the optimal performance of our node occurs for $\langle n \rangle_m \sim 0.02$ and $N \approx 124$, corresponding to an effective channel loss of 69 dB between Alice and Bob, which is equivalent to roughly 350 km of telecommunications fiber.

We also find that the QBER and thus the performance of the communication link is limited by imperfect preparation of photonic qubits. Photonic qubits are defined by sending arbitrary phase patterns generated by the optical AWG to a phase modulator. For an example of such a pattern, see the blue curve in Fig. 8.3a. We use an imper-

263

fect pulse amplifier with finite bandwidth ($0.025 - 700$ MHz), and find that the DC component of these waveforms can result in error in photonic qubit preparation on the few % level. By using a tailored waveform of phases with smaller (or vanishing) DC component, we can reduce these errors. We run such an experiment during the test of the Bell-CHSH inequality. We find that by evaluating BSM correlations from $|\pm a\rangle$ and $|\pm b\rangle$ inputs during this measurement, we estimate a QBER of 0.097 ± 0.006.

Finally, we obtain the effective clock-rate of the communication link by measuring the total number of photonic qubits sent over the course of an entire experiment. In practice, we record the number of channel uses, determined by the number of sync triggers recorded (see Fig. D.3a) as well as the number of qubits per sync trigger (N). We then divide this number by the total experimental time from start to finish ($\sim$ 1-2 days for most experimental runs), including all experimental downtime used to stabilize the interferometer, readout and initialize the SiV, and compensate for spectral diffusion and ionization. For $N = 248$, we extract a clock rate of $1.2\,\mathrm{MHz}$. As the distilled key rate in this configuration exceeds the conventional limit of $p/2$ by a factor of 3.8 ± 1.1, it is competitive with a standard linear-optics based system operating at $4.5^{+1.3}_{-1.2}$ MHz clock rate.

264

D.7 PERFORMANCE OF MEMORY-ASSISTED QUANTUM COMMUNICATION

A single optical link can provide many channels, for example, by making use of different frequency, polarization, or temporal modes. To account for this, when comparing different systems, data rates can be defined on a per-channel-use basis. In a quantum communication setting, full usage of the communication channel between Alice and Bob means that both links from Alice and Bob to Charlie are in use simultaneously. For an asynchronous sequential measurement, typically only half of the channel is used at a time, for example from Alice to Charlie or Bob to Charlie. The other half can in principle be used for a different task when not in use. For example, the unused part of the channel could be routed to a secondary asynchronous BSM device. In our experiment, we can additionally define as a second normalization the rate per channel "occupancy", which accounts for the fact that only half the channel is used at any given time. The rate per channel occupancy is therefore half the rate per full channel use. For comparison, we typically operate at 1.2% channel use and 2.4% channel occupancy.

To characterize the optimal performance of the asynchronous Bell state measurement device, we operate it in the optimal regime determined above ($N = 124$, $\langle n \rangle_m \lesssim 0.02$). We note that the enhancement in the sifted key rate over direct transmission is given by

$$\frac{R}{R_{\max}} = \eta^2 \frac{(N_\pi - 1)(N_\pi - 2)N_{\text{sub}}}{2N_\pi} \tag{D.9}$$

	per channel occupancy	per channel occupancy	per channel use	per channel use
X:Y basis bias	$50:50$	$99:1$	$50:50$	$99:1$
Secure key rate R $[10^{-7}]$	$1.19^{+0.14}_{-0.14}$	$2.33^{+0.28}_{-0.28}$	$2.37^{+0.29}_{-0.28}$	$4.66^{+0.56}_{-0.55}$
$R/R_{\max}$(X:Y)	$2.06^{+0.25}_{-0.25}$	$2.06^{+0.25}_{-0.25}$	$4.13^{+0.50}_{-0.49}$	$4.13^{+0.50}_{-0.49}$
$R/(1.44p_{A\to B})$	$0.71^{+0.09}_{-0.08}$	$1.40^{+0.17}_{-0.17}$	$1.43^{+0.17}_{-0.17}$	$2.80^{+0.34}_{-0.33}$
$1-$confidence level		$1.1^{+0.4}_{-0.3} \times 10^{-2}$	$8^{+3}_{-2} \times 10^{-3}$	$1.3^{+0.5}_{-0.3} \times 10^{-7}$

Table D.4: Quantum-memory-based advantage. Distilled key rates with the asynchronous BSM device and comparison to ideal direct communication implementations, based on the performance of our network node for $N = 124$ and $\langle n \rangle_m \sim 0.02$. Distillable key rates for $E = 0.110 \pm 0.004$ for unbiased and biased basis choice are expressed in a per-channel-occupancy and per-channel-use normalization (Methods). Enhancement is calculated versus the linear optics BSM limit ($R_{\max}(50:50) = p_{A\to B}/2$ for unbiased bases, $R_{\max}(99:1) = 0.98 p_{A\to B}$ with biased bases) and versus the fundamental repeaterless channel capacity [49] ($1.44 p_{A\to B}$). Confidence levels for surpassing the latter bound [49] are given in the final row.

and is independent of $\langle n \rangle_m$ for a fixed number of microwave pulses N_π and optical pulses per microwave pulse N_{sub} and thus fixed $N = N_\pi N_{\text{sub}}$. For low $\langle n \rangle_m$, three photon events become negligible and therefore QBER saturates, such that the enhancement in the distilled key rate saturates as well (Fig. D.5a). We can therefore combine all data sets with fixed $N = 124$ below $\langle n \rangle_m \lesssim 0.02$ to characterize the average QBER of 0.116 ± 0.002 (Fig. 8.3c). The key rates cited in the main text relate to a data set in this series ($\langle n \rangle_m \approx 0.02$), with a QBER of 0.110 ± 0.004. A summary of key rates calculated on a per-channel use and per-channel occupancy basis, as well as comparisons of performance to an ideal linear-optics BSM and the repeaterless bound [49] are given in Table D.4.

Furthermore, we extrapolate the performance of our memory node to include biased input bases from Alice and Bob. This technique enables a reduction of channel uses

where Alice and Bob send photons in different bases, but is still compatible with secure key distribution [382], allowing for enhanced distilled key rates by at most a factor of 2. The extrapolated performance of our node for a bias of 99:1 is also displayed in Table D.4, as well as comparisons to the relevant bounds. We note that basis biasing does not affect the performance when comparing to the equivalent direct-transmission experiment, which is limited by $p_{A \to B}/2$ in the unbiased case and $p_{A \to B}$ in the biased case. However, using biased input bases does make the performance of the memory-assisted approach more competitive with the fixed repeaterless bound [49] of $1.44 p_{A \to B}$.

D.8   ANALYSIS OF QUANTUM COMMUNICATION EXPERIMENT

For each experiment, we estimate the QBER averaged over all relevant basis combinations. This is equivalent to the QBER when the random bit string has all bases occurring with the same probability, (an unbiased and independent basis choice by Alice and Bob). We first note that the QBER for positive and negative parity announcements are not independent. We illustrate this for the example, that Alice and Bob send photons in the X basis. We denote the probability P that Alice sent qubit $|\psi\rangle$, Bob sent qubit $|\xi\rangle$ and the outcome of Charlie's parity measurement is m_C, conditioned on the detection of a coincidence, as $P(\psi_A \cap \xi_B \cap m_C)$. We find for balanced inputs $P(+X_A \cap -X_B) = P(-X_A \cap +X_B)$ that $P(E_{XX}|+_C) = P(E_{XX}|-_C)$ with E_{XX} denoting the occurrence of a bit error in the sifted key of Alice and Bob. We thus find

267

for the posterior probability L for the average QBER for XX coincidences

$$L(P(E_{XX})) = L(P(-_C|+X_A \cap +X_B)) * L(P(+_C|+X_A \cap -X_B))$$

$$* L(P(+_C|-X_A \cap +X_B)) * L(P(-_C|-X_A \cap -X_B)). \quad \text{(D.10)}$$

Note that this expression is independent of the actual distribution of $P(\psi_A \cap \xi_B)$. Here, the posterior probability $L(P(+_C|+X_A \cap -X_B))$ is based on the a binomial likelihood function $P(N_{m_C \cap \psi_A \cap \xi_B}|N_{\psi_A \cap \xi_B}, L)$, where $N_{\mathcal{C}}$ denotes the number of occurrences with condition $\mathcal{C}$. Finally the posterior probability of the unbiased QBER is $L(P(E)) = L(P(E_{XX})) * L(P(E_{YY}))$. All values presented in the text and figures are maximum likelihood values with bounds given by the confidence interval of $\pm 34.1\%$ integrated posterior probability. Confidence levels towards a specific bound (for example, unconditional security [373] are given by the integrated posterior probability up to the bound.

To get the ratio of the distilled distilled key rate with respect to the sifted key rate by (ideal) error correction and privacy amplification, we use the bounds given by difference in information by Alice and Bob with respect to a potential eavesdropper who performs individual attacks: $r_s = I(A, B) - I(A/B, E)^{\max}$ [29]. We use the full posterior probability distribution of QBER (which accounts for statistical and systematic uncertainty in our estimate) to compute the error bar on r_s, and correspondingly, the error bars on the extracted distilled key rates plotted in Fig. 8.4.

References

[1] S. W. Young. *Magnetic resonance imaging: Basic principles.* Raven Press, United States, 1987. URL http://inis.iaea.org/search/search.aspx?orig_q=RN:19077142.

[2] Bernhard Hofmann-Wellenhof, Herbert Lichtenegger, and James Collins. *Global Positioning System. Theory and practice.* February 2001. doi: 10.1007/978-3-7091-6199-9.

[3] Orazio Svelto. Principles of lasers, 2010. URL https://search.library.wisc.edu/catalog/9910103409302121.

[4] Christian Gross and Immanuel Bloch. Quantum simulations with ultracold atoms in optical lattices. *Science*, 357(6355):995, September 2017. doi: 10.1126/science.aal3837. URL http://science.sciencemag.org/content/357/6355/995.abstract.

[5] Manuel Endres, Hannes Bernien, Alexander Keesling, Harry Levine, Eric R. Anschuetz, Alexandre Krajenbrink, Crystal Senko, Vladan Vuletic, Markus Greiner, and Mikhail D. Lukin. Atom-by-atom assembly of defect-free one-dimensional cold atom arrays. *Science*, 354(6315):1024, November 2016. doi: 10.1126/science.aah3752. URL http://science.sciencemag.org/content/354/6315/1024.abstract.

[6] Daniel Barredo, Sylvain de Léséleuc, Vincent Lienhard, Thierry Lahaye, and Antoine Browaeys. An atom-by-atom assembler of defect-free arbitrary two-dimensional atomic arrays. *Science*, 354(6315):1021, November 2016. doi: 10.1126/science.aah3778. URL http://science.sciencemag.org/content/354/6315/1021.abstract.

[7] Colin D. Bruzewicz, John Chiaverini, Robert McConnell, and Jeremy M. Sage. Trapped-ion quantum computing: Progress and challenges. *Applied Physics Reviews*, 6(2):021314, May 2019. doi: 10.1063/1.5088164. URL https://doi.org/10.1063/1.5088164.

[8] S. Debnath, N. M. Linke, C. Figgatt, K. A. Landsman, K. Wright, and C. Monroe. Demonstration of a small programmable quantum computer with atomic qubits.

Nature, 536(7614):63–66, 2016. ISSN 1476-4687. doi: 10.1038/nature18648. URL https://doi.org/10.1038/nature18648.

[9] C. Figgatt, A. Ostrander, N. M. Linke, K. A. Landsman, D. Zhu, D. Maslov, and C. Monroe. Parallel entangling operations on a universal ion-trap quantum computer. *Nature*, 572(7769):368–372, 2019. ISSN 1476-4687. doi: 10.1038/s41586-019-1427-5. URL https://doi.org/10.1038/s41586-019-1427-5.

[10] Pieter Kok and Brendon W. Lovett. *Introduction to Optical Quantum Information Processing*. Cambridge University Press, Cambridge, 2010. doi: 10.1017/CBO9781139193658. URL https://www.cambridge.org/core/books/introduction-to-optical-quantum-information-processing/4CE9A569CAE92B026B2BA041506B9F4B.

[11] Xiaogang Qiang, Xiaoqi Zhou, Jianwei Wang, Callum M. Wilkes, Thomas Loke, Sean O'Gara, Laurent Kling, Graham D. Marshall, Raffaele Santagati, Timothy C. Ralph, Jingbo B. Wang, Jeremy L. O'Brien, Mark G. Thompson, and Jonathan C. F. Matthews. Large-scale silicon quantum photonics implementing arbitrary two-qubit processing. *Nat. Photonics*, 12(9):534–539, September 2018. ISSN 1749-4893. doi: 10.1038/s41566-018-0236-y. URL http://www.nature.com/articles/s41566-018-0236-y/. Number: 9 Publisher: Nature Publishing Group.

[12] M. H. Devoret and R. J. Schoelkopf. Superconducting circuits for quantum information: An outlook. *Science*, 339(6124):1169, March 2013. doi: 10.1126/science.1231930. URL http://science.sciencemag.org/content/339/6124/1169.abstract.

[13] Nissim Ofek, Andrei Petrenko, Reinier Heeres, Philip Reinhold, Zaki Leghtas, Brian Vlastakis, Yehan Liu, Luigi Frunzio, S. M. Girvin, L. Jiang, Mazyar Mirrahimi, M. H. Devoret, and R. J. Schoelkopf. Extending the lifetime of a quantum bit with error correction in superconducting circuits. *Nature*, 536(7617):441–445, 2016. ISSN 1476-4687. doi: 10.1038/nature18949. URL https://doi.org/10.1038/nature18949.

[14] Jarryd J. Pla, Kuan Y. Tan, Juan P. Dehollain, Wee H. Lim, John J. L. Morton, David N. Jamieson, Andrew S. Dzurak, and Andrea Morello. A single-atom elec-

tron spin qubit in silicon. *Nature*, 489(7417):541–545, 2012. ISSN 1476-4687. doi: 10.1038/nature11449. URL https://doi.org/10.1038/nature11449.

[15] X. Mi, M. Benito, S. Putz, D. M. Zajac, J. M. Taylor, Guido Burkard, and J. R. Petta. A coherent spin-photon interface in silicon. *Nature*, 555(7698):599–603, 2018. ISSN 1476-4687. doi: 10.1038/nature25769. URL https://doi.org/10.1038/nature25769.

[16] Peter Lodahl, Sahand Mahmoodian, and Soren Stobbe. Interfacing single photons and single quantum dots with photonic nanostructures. *Rev. Mod. Phys.*, 87(2):347–400, May 2015. ISSN 0034-6861. doi: 10.1103/RevModPhys.87.347. WOS:000354347800001.

[17] Shuo Sun, Hyochul Kim, Glenn S. Solomon, and Edo Waks. A quantum phase switch between a single solid-state spin and a photon. *Nat. Nanotechnol.*, 11 (6):539–544, June 2016. ISSN 1748-3395. doi: 10.1038/nnano.2015.334. URL https://www.nature.com/articles/nnano.2015.334. Number: 6 Publisher: Nature Publishing Group.

[18] Mete Atatüre, Dirk Englund, Nick Vamivakas, Sang-Yun Lee, and Joerg Wrachtrup. Material platforms for spin-based photonic quantum technologies. *Nat. Rev. Mater.*, 3(5):38–51, May 2018. ISSN 2058-8437. doi: 10.1038/s41578-018-0008-9. URL https://www.nature.com/articles/s41578-018-0008-9.

[19] C. E. Bradley, J. Randall, M. H. Abobeih, R. C. Berrevoets, M. J. Degen, M. A. Bakker, M. Markham, D. J. Twitchen, and T. H. Taminiau. A ten-qubit solid-state spin register with quantum memory up to one minute. *Phys. Rev. X*, 9(3): 031045, September 2019. doi: 10.1103/PhysRevX.9.031045. URL https://link.aps.org/doi/10.1103/PhysRevX.9.031045.

[20] Roland Nagy, Matthias Niethammer, Matthias Widmann, Yu-Chen Chen, Péter Udvarhelyi, Cristian Bonato, Jawad Ul Hassan, Robin Karhu, Ivan G. Ivanov, Nguyen Tien Son, Jeronimo R. Maze, Takeshi Ohshima, Öney O. Soykal, Ádám Gali, Sang-Yun Lee, Florian Kaiser, and Jörg Wrachtrup. High-fidelity spin and optical control of single silicon-vacancy centres in silicon carbide. *Nature Commu-*

nications, 10(1):1954, 2019. ISSN 2041-1723. doi: 10.1038/s41467-019-09873-9. URL https://doi.org/10.1038/s41467-019-09873-9.

[21] Charles H. Bennett and David P. DiVincenzo. Quantum information and computation. *Nature*, 404(6775):247–255, 2000. ISSN 1476-4687. doi: 10.1038/35005001. URL https://doi.org/10.1038/35005001.

[22] C. Monroe. Quantum information processing with atoms and photons. *Nature*, 416(6877):238–246, 2002. ISSN 1476-4687. doi: 10.1038/416238a. URL https://doi.org/10.1038/416238a.

[23] Michael A. Nielsen and Isaac L. Chuang. *Quantum Computation and Quantum Information: 10th Anniversary Edition*. Cambridge University Press, 2011.

[24] T. D. Ladd, F. Jelezko, R. Laflamme, Y. Nakamura, C. Monroe, and J. L. O'Brien. Quantum computers. *Nature*, 464(7285):45–53, March 2010. ISSN 1476-4687. doi: 10.1038/nature08812. URL http://www.nature.com/articles/nature08812. Number: 7285 Publisher: Nature Publishing Group.

[25] John Preskill. Quantum Computing in the NISQ era and beyond. *Quantum*, 2: 79, August 2018. ISSN 2521-327X. doi: 10.22331/q-2018-08-06-79. URL https://doi.org/10.22331/q-2018-08-06-79.

[26] C. L. Degen, F. Reinhard, and P. Cappellaro. Quantum sensing. *Rev. Mod. Phys.*, 89(3):035002, July 2017. doi: 10.1103/RevModPhys.89.035002. URL https://link.aps.org/doi/10.1103/RevModPhys.89.035002. Publisher: American Physical Society.

[27] Vittorio Giovannetti, Seth Lloyd, and Lorenzo Maccone. Advances in quantum metrology. *Nature Photonics*, 5(4):222–229, 2011. ISSN 1749-4893. doi: 10.1038/nphoton.2011.35. URL https://doi.org/10.1038/nphoton.2011.35.

[28] Charles H Bennett and Gilles Brassard. Quantum cryptography: Public key distribution and coin tossing. *Proceedings of the IEEE International Conference on Computers, Systems and Signal Processing*, 175:8, 1984. URL https://doi.org/10.1016/j.tcs.2014.05.025.

[29] N. Gisin, G. G. Ribordy, W. Tittel, and H. Zbinden. Quantum cryptography. *Rev. Mod. Phys.*, 74(1):145–195, January 2002. ISSN 0034-6861. doi: 10.1103/RevModPhys.74.145. WOS:000174548700005.

[30] S. Pirandola, U. L. Andersen, L. Banchi, M. Berta, D. Bunandar, R. Colbeck, D. Englund, T. Gehring, C. Lupo, C. Ottaviani, J. L. Pereira, M. Razavi, J. Shamsul Shaari, M. Tomamichel, V. C. Usenko, G. Vallone, P. Villoresi, and P. Wallden. Advances in quantum cryptography. *Adv. Opt. Photon.*, 12(4):1012–1236, Dec 2020. doi: 10.1364/AOP.361502. URL http://aop.osa.org/abstract.cfm?URI=aop-12-4-1012.

[31] P. W. Shor. Algorithms for quantum computation: discrete logarithms and factoring. In *Proceedings 35th Annual Symposium on Foundations of Computer Science*, pages 124–134, 1994. doi: 10.1109/SFCS.1994.365700.

[32] Andrew D. Ludlow, Martin M. Boyd, Jun Ye, E. Peik, and P. O. Schmidt. Optical atomic clocks. *RMP*, 87(2):637–701, June 2015. doi: 10.1103/RevModPhys.87.637. URL https://link.aps.org/doi/10.1103/RevModPhys.87.637.

[33] Artur K. Ekert. Quantum cryptography based on Bell's theorem. *Phys. Rev. Lett.*, 67(6):661–663, August 1991. doi: 10.1103/PhysRevLett.67.661. URL https://link.aps.org/doi/10.1103/PhysRevLett.67.661. Publisher: American Physical Society.

[34] Antonio Acín, Nicolas Brunner, Nicolas Gisin, Serge Massar, Stefano Pironio, and Valerio Scarani. Device-independent security of quantum cryptography against collective attacks. *PRL*, 98(23):230501, June 2007. doi: 10.1103/PhysRevLett.98.230501. URL https://link.aps.org/doi/10.1103/PhysRevLett.98.230501.

[35] Frank Arute, Kunal Arya, Ryan Babbush, Dave Bacon, Joseph C. Bardin, Rami Barends, Rupak Biswas, Sergio Boixo, Fernando G. S. L. Brandao, David A. Buell, Brian Burkett, Yu Chen, Zijun Chen, Ben Chiaro, Roberto Collins, William Courtney, Andrew Dunsworth, Edward Farhi, Brooks Foxen, Austin Fowler, Craig Gidney, Marissa Giustina, Rob Graff, Keith Guerin, Steve Habegger, Matthew P. Harrigan, Michael J. Hartmann, Alan Ho, Markus Hoffmann, Trent Huang, Travis S. Humble, Sergei V. Isakov, Evan Jeffrey, Zhang Jiang, Dvir Kafri, Kostyantyn

273

Kechedzhi, Julian Kelly, Paul V. Klimov, Sergey Knysh, Alexander Korotkov, Fedor Kostritsa, David Landhuis, Mike Lindmark, Erik Lucero, Dmitry Lyakh, Salvatore Mandrà, Jarrod R. McClean, Matthew McEwen, Anthony Megrant, Xiao Mi, Kristel Michielsen, Masoud Mohseni, Josh Mutus, Ofer Naaman, Matthew Neeley, Charles Neill, Murphy Yuezhen Niu, Eric Ostby, Andre Petukhov, John C. Platt, Chris Quintana, Eleanor G. Rieffel, Pedram Roushan, Nicholas C. Rubin, Daniel Sank, Kevin J. Satzinger, Vadim Smelyanskiy, Kevin J. Sung, Matthew D. Trevithick, Amit Vainsencher, Benjamin Villalonga, Theodore White, Z. Jamie Yao, Ping Yeh, Adam Zalcman, Hartmut Neven, and John M. Martinis. Quantum supremacy using a programmable superconducting processor. *Nature*, 574 (7779):505–510, 2019. ISSN 1476-4687. doi: 10.1038/s41586-019-1666-5. URL https://doi.org/10.1038/s41586-019-1666-5.

[36] Han-Sen Zhong, Hui Wang, Yu-Hao Deng, Ming-Cheng Chen, Li-Chao Peng, Yi-Han Luo, Jian Qin, Dian Wu, Xing Ding, Yi Hu, Peng Hu, Xiao-Yan Yang, Wei-Jun Zhang, Hao Li, Yuxuan Li, Xiao Jiang, Lin Gan, Guangwen Yang, Lixing You, Zhen Wang, Li Li, Nai-Le Liu, Chao-Yang Lu, and Jian-Wei Pan. Quantum computational advantage using photons. *Science*, 370(6523):1460, December 2020. doi: 10.1126/science.abe8770. URL http://science.sciencemag.org/content/370/6523/1460.abstract.

[37] Simon J. Devitt, William J. Munro, and Kae Nemoto. Quantum error correction for beginners. *Reports on Progress in Physics*, 76(7):076001, 2013. ISSN 1361-6633. doi: 10.1088/0034-4885/76/7/076001. URL http://dx.doi.org/10.1088/0034-4885/76/7/076001.

[38] Sisi Zhou, Mengzhen Zhang, John Preskill, and Liang Jiang. Achieving the heisenberg limit in quantum metrology using quantum error correction. *Nature Communications*, 9(1):78, 2018. ISSN 2041-1723. doi: 10.1038/s41467-017-02510-3. URL https://doi.org/10.1038/s41467-017-02510-3.

[39] Artur Ekert and Chiara Macchiavello. Quantum error correction for communication. *PRL*, 77(12):2585–2588, September 1996. doi: 10.1103/PhysRevLett.77.2585. URL https://link.aps.org/doi/10.1103/PhysRevLett.77.2585.

274

[40] Peter W. Shor. Scheme for reducing decoherence in quantum computer memory. *PRA*, 52(4):R2493–R2496, October 1995. doi: 10.1103/PhysRevA.52.R2493. URL https://link.aps.org/doi/10.1103/PhysRevA.52.R2493.

[41] Daniel Gottesman, Alexei Kitaev, and John Preskill. Encoding a qubit in an oscillator. *PRA*, 64(1):012310, June 2001. doi: 10.1103/PhysRevA.64.012310. URL https://link.aps.org/doi/10.1103/PhysRevA.64.012310.

[42] H. J. Kimble. The quantum internet. *Nature*, 453(7198):1023–1030, June 2008. ISSN 0028-0836. doi: 10.1038/nature07127. WOS:000256839900044.

[43] Simon J. Devitt, Andrew D. Greentree, Ashley M. Stephens, and Rodney Van Meter. High-speed quantum networking by ship. *Scientific Reports*, 6(1):36163, 2016. ISSN 2045-2322. doi: 10.1038/srep36163. URL https://doi.org/10.1038/srep36163.

[44] Gerd Keiser. *Optical Fiber Communications*. American Cancer Society, 2003. ISBN 9780471219286. doi: https://doi.org/10.1002/0471219282.eot158. URL https://onlinelibrary.wiley.com/doi/abs/10.1002/0471219282.eot158.

[45] Stephanie Wehner, David Elkouss, and Ronald Hanson. Quantum internet: A vision for the road ahead. *Science*, 362(6412):eaam9288, October 2018. ISSN 0036-8075, 1095-9203. doi: 10.1126/science.aam9288. URL http://science.sciencemag.org/content/362/6412/eaam9288. Publisher: American Association for the Advancement of Science Section: Review.

[46] H.-J. Briegel, W. Dür, J. I. Cirac, and P. Zoller. Quantum repeaters: the role of imperfect local operations in quantum communication. *Phys. Rev. Lett.*, 81(26): 5932–5935, December 1998. doi: 10.1103/PhysRevLett.81.5932. URL https://link.aps.org/doi/10.1103/PhysRevLett.81.5932. Publisher: American Physical Society.

[47] Koji Azuma, Kiyoshi Tamaki, and Hoi-Kwong Lo. All-photonic quantum repeaters. *Nat. Commun.*, 6(1):1–7, April 2015. ISSN 2041-1723. doi: 10.1038/ncomms7787. URL https://www.nature.com/articles/ncomms7787. Number: 1 Publisher: Nature Publishing Group.

[48] Johannes Borregaard, Hannes Pichler, Tim Schröder, Mikhail D. Lukin, Peter Lodahl, and Anders S. Sørensen. One-Way Quantum Repeater Based on Near-Deterministic Photon-Emitter Interfaces. *Phys. Rev. X*, 10(2):021071, June 2020. doi: 10.1103/PhysRevX.10.021071. URL https://link.aps.org/doi/10.1103/PhysRevX.10.021071. Publisher: American Physical Society.

[49] Stefano Pirandola, Riccardo Laurenza, Carlo Ottaviani, and Leonardo Banchi. Fundamental limits of repeaterless quantum communications. *Nat. Commun.*, 8 (1):1–15, April 2017. ISSN 2041-1723. doi: 10.1038/ncomms15043. URL https://www.nature.com/articles/ncomms15043/. Number: 1 Publisher: Nature Publishing Group.

[50] M. K. Bhaskar, R. Riedinger, B. Machielse, D. S. Levonian, C. T. Nguyen, E. N. Knall, H. Park, D. Englund, M. Lončar, D. D. Sukachev, and M. D. Lukin. Experimental demonstration of memory-enhanced quantum communication. *Nature*, 580 (7801):60–64, April 2020. ISSN 1476-4687. doi: 10.1038/s41586-020-2103-5. URL https://www.nature.com/articles/s41586-020-2103-5. Number: 7801 Publisher: Nature Publishing Group.

[51] David P. DiVincenzo. The physical implementation of quantum computation. *Fortschritte der Physik*, 48(9-11):771–783, 2000. doi: https://doi.org/10.1002/1521-3978(200009)48:9/11<771::AID-PROP771>3.0.CO;2-E. URL https://onlinelibrary.wiley.com/doi/abs/10.1002/1521-3978%28200009%2948%3A9/11%3C771%3A%3AAID-PROP771%3E3.0.CO%3B2-E.

[52] J. I. Cirac, P. Zoller, H. J. Kimble, and H. Mabuchi. Quantum state transfer and entanglement distribution among distant nodes in a quantum network. *Phys. Rev. Lett.*, 78(16):3221–3224, April 1997. doi: 10.1103/PhysRevLett.78.3221. URL https://link.aps.org/doi/10.1103/PhysRevLett.78.3221. Publisher: American Physical Society.

[53] B. Hensen, H. Bernien, A. E. Dréau, A. Reiserer, N. Kalb, M. S. Blok, J. Ruitenberg, R. F. L. Vermeulen, R. N. Schouten, C. Abellán, W. Amaya, V. Pruneri, M. W. Mitchell, M. Markham, D. J. Twitchen, D. Elkouss, S. Wehner, T. H. Taminiau, and R. Hanson. Loophole-free Bell inequality violation using electron spins separated by 1.3 kilometres. *Nature*, 526(7575):682–686, October 2015.

ISSN 1476-4687. doi: 10.1038/nature15759. URL https://www.nature.com/articles/nature15759.

[54] Lynden K. Shalm, Evan Meyer-Scott, Bradley G. Christensen, Peter Bierhorst, Michael A. Wayne, Martin J. Stevens, Thomas Gerrits, Scott Glancy, Deny R. Hamel, Michael S. Allman, Kevin J. Coakley, Shellee D. Dyer, Carson Hodge, Adriana E. Lita, Varun B. Verma, Camilla Lambrocco, Edward Tortorici, Alan L. Migdall, Yanbao Zhang, Daniel R. Kumor, William H. Farr, Francesco Marsili, Matthew D. Shaw, Jeffrey A. Stern, Carlos Abellán, Waldimar Amaya, Valerio Pruneri, Thomas Jennewein, Morgan W. Mitchell, Paul G. Kwiat, Joshua C. Bienfang, Richard P. Mirin, Emanuel Knill, and Sae Woo Nam. Strong loophole-free test of local realism. *PRL*, 115(25):250402, December 2015. doi: 10.1103/PhysRevLett.115.250402. URL https://link.aps.org/doi/10.1103/PhysRevLett.115.250402.

[55] G. Murta, S. B. van Dam, J. Ribeiro, R. Hanson, and S. Wehner. Towards a realization of device-independent quantum key distribution. *Quantum Science and Technology*, 4(3):035011, 2019. ISSN 2058-9565. doi: 10.1088/2058-9565/ab2819. URL http://dx.doi.org/10.1088/2058-9565/ab2819.

[56] Alberto Boaron, Gianluca Boso, Davide Rusca, Cédric Vulliez, Claire Autebert, Misael Caloz, Matthieu Perrenoud, Gaëtan Gras, Félix Bussières, Ming-Jun Li, Daniel Nolan, Anthony Martin, and Hugo Zbinden. Secure Quantum Key Distribution over 421 km of Optical Fiber. *Phys. Rev. Lett.*, 121(19):190502, November 2018. doi: 10.1103/PhysRevLett.121.190502. URL https://link.aps.org/doi/10.1103/PhysRevLett.121.190502. Publisher: American Physical Society.

[57] Hongjun Zhang, Gaiying Wang, Dong Sun, Xiaowei Li, and Hui Sun. Optical bistability and multistability induced by quantum coherence in diamond germanium-vacancy color centers. *Appl. Optics*, 58(10):2522–2529, April 2019. ISSN 1559-128X. doi: 10.1364/AO.58.002522. WOS:000462833000029.

[58] Mark Hillery, Vladimír Bužek, and André Berthiaume. Quantum secret sharing. *PRA*, 59(3):1829–1834, March 1999. doi: 10.1103/PhysRevA.59.1829. URL https://link.aps.org/doi/10.1103/PhysRevA.59.1829.

[59] Claude Crépeau, Daniel Gottesman, and Adam Smith. Secure multi-party quantum computation. In *Proceedings of the thiry-fourth annual ACM symposium on Theory of computing*, STOC '02, pages 643–652, Montreal, Quebec, Canada, May 2002. Association for Computing Machinery. ISBN 978-1-58113-495-7. doi: 10.1145/509907.510000. URL https://doi.org/10.1145/509907.510000.

[60] J. A. Vaccaro, Joseph Spring, and Anthony Chefles. Quantum protocols for anonymous voting and surveying. *PRA*, 75(1):012333, January 2007. doi: 10.1103/PhysRevA.75.012333. URL https://link.aps.org/doi/10.1103/PhysRevA.75.012333.

[61] Daniel Gottesman, Thomas Jennewein, and Sarah Croke. Longer-baseline telescopes using quantum repeaters. *Phys. Rev. Lett.*, 109(7):070503, August 2012. doi: 10.1103/PhysRevLett.109.070503. URL https://link.aps.org/doi/10.1103/PhysRevLett.109.070503. Publisher: American Physical Society.

[62] E. T. Khabiboulline, J. Borregaard, K. De Greve, and M. D. Lukin. Optical interferometry with quantum networks. *Phys. Rev. Lett.*, 123(7):070504, August 2019. doi: 10.1103/PhysRevLett.123.070504. URL https://link.aps.org/doi/10.1103/PhysRevLett.123.070504. Publisher: American Physical Society.

[63] P. Kómár, E. M. Kessler, M. Bishof, L. Jiang, A. S. Sørensen, J. Ye, and M. D. Lukin. A quantum network of clocks. *Nature Physics*, 10:582 EP –, 06 2014. URL https://doi.org/10.1038/nphys3000.

[64] Joseph F. Fitzsimons. Private quantum computation: an introduction to blind quantum computing and related protocols. *npj Quantum Inf.*, 3(1):1–11, June 2017. ISSN 2056-6387. doi: 10.1038/s41534-017-0025-3. URL https://www.nature.com/articles/s41534-017-0025-3. Number: 1 Publisher: Nature Publishing Group.

[65] Stefanie Barz, Elham Kashefi, Anne Broadbent, Joseph F. Fitzsimons, Anton Zeilinger, and Philip Walther. Demonstration of Blind Quantum Computing. *Science*, 335(6066):303–308, January 2012. ISSN 0036-8075, 1095-9203. doi: 10.1126/science.1214707. URL https://science.sciencemag.org/content/335/6066/303. Publisher: American Association for the Advancement of Science Section: Research Article.

[66] J. I. Cirac, A. K. Ekert, S. F. Huelga, and C. Macchiavello. Distributed quantum computation over noisy channels. *PRA*, 59(6):4249–4254, June 1999. doi: 10.1103/ PhysRevA.59.4249. URL https://link.aps.org/doi/10.1103/PhysRevA.59. 4249.

[67] Liang Jiang, Jacob M. Taylor, Anders S. Sørensen, and Mikhail D. Lukin. Distributed quantum computation based on small quantum registers. *PRA*, 76 (6):062323, December 2007. doi: 10.1103/PhysRevA.76.062323. URL https: //link.aps.org/doi/10.1103/PhysRevA.76.062323.

[68] C. Monroe, R. Raussendorf, A. Ruthven, K. R. Brown, P. Maunz, L.-M. Duan, and J. Kim. Large-scale modular quantum-computer architecture with atomic memory and photonic interconnects. *Phys. Rev. A*, 89(2):022317, February 2014. doi: 10.1103/PhysRevA.89.022317. URL https://link.aps.org/doi/ 10.1103/PhysRevA.89.022317.

[69] Kevin S. Chou, Jacob Z. Blumoff, Christopher S. Wang, Philip C. Reinhold, Christopher J. Axline, Yvonne Y. Gao, L. Frunzio, M. H. Devoret, Liang Jiang, and R. J. Schoelkopf. Deterministic teleportation of a quantum gate between two logical qubits. *Nature*, 561(7723):368–373, 2018. ISSN 1476-4687. doi: 10.1038/ s41586-018-0470-y. URL https://doi.org/10.1038/s41586-018-0470-y.

[70] Youpeng Zhong, Hung-Shen Chang, Audrey Bienfait, Étienne Dumur, Ming-Han Chou, Christopher R. Conner, Joel Grebel, Rhys G. Povey, Haoxiong Yan, David I. Schuster, and Andrew N. Cleland. Deterministic multi-qubit entanglement in a quantum network, 2020.

[71] L. J. Stephenson, D. P. Nadlinger, B. C. Nichol, S. An, P. Drmota, T. G. Ballance, K. Thirumalai, J. F. Goodwin, D. M. Lucas, and C. J. Ballance. High-rate, high-fidelity entanglement of qubits across an elementary quantum network. *PRL*, 124 (11):110501, March 2020. doi: 10.1103/PhysRevLett.124.110501. URL https: //link.aps.org/doi/10.1103/PhysRevLett.124.110501.

[72] D. Stucki, N. Gisin, O. Guinnard, G. Ribordy, and H. Zbinden. Quantum key distribution over 67 km with a plug&play system. *New Journal of Physics*, 4: 41–41, 2002. ISSN 1367-2630. doi: 10.1088/1367-2630/4/1/341. URL http: //dx.doi.org/10.1088/1367-2630/4/1/341.

279

[73] M Sasaki, M Fujiwara, H Ishizuka, W Klaus, K Wakui, M Takeoka, S Miki, T Yamashita, Z Wang, A Tanaka, K Yoshino, Y Nambu, S Takahashi, A Tajima, A Tomita, T Domeki, T Hasegawa, Y Sakai, H Kobayashi, T Asai, K Shimizu, T Tokura, T Tsurumaru, M Matsui, T Honjo, K Tamaki, H Takesue, Y Tokura, J F Dynes, A R Dixon, A W Sharpe, Z L Yuan, A J Shields, S Uchikoga, M Legré, S Robyr, P Trinkler, L Monat, J.-B. Page, G Ribordy, A Poppe, A Allacher, O Maurhart, T Länger, M Peev, and A Zeilinger. Field test of quantum key distribution in the Tokyo QKD Network. *Optics Express*, 19(11):10387–10409, 2011. doi: 10.1364/OE.19.010387. URL http://www.opticsexpress.org/abstract.cfm?URI=oe-19-11-10387.

[74] Erika Janitz, Mihir K. Bhaskar, and Lilian Childress. Cavity quantum electrodynamics with color centers in diamond. *Optica*, 7(10):1232–1252, 2020. doi: 10.1364/OPTICA.398628. URL http://www.osapublishing.org/optica/abstract.cfm?URI=optica-7-10-1232.

[75] M.K. Bhaskar, D.D. Sukachev, A. Sipahigil, R. E. Evans, M. J. Burek, C. T. Nguyen, L. J. Rogers, P. Siyushev, M. H. Metsch, H. Park, F. Jelezko, M. Lončar, and M. D. Lukin. Quantum nonlinear optics with a germanium-vacancy color center in a nanoscale diamond waveguide. *Phys. Rev. Lett.*, 118(22):223603, May 2017. doi: 10.1103/PhysRevLett.118.223603. URL https://link.aps.org/doi/10.1103/PhysRevLett.118.223603.

[76] R. E. Evans, M. K. Bhaskar, D. D. Sukachev, C. T. Nguyen, A. Sipahigil, M. J. Burek, B. Machielse, G. H. Zhang, A. S. Zibrov, E. Bielejec, H. Park, M. Lončar, and M. D. Lukin. Photon-mediated interactions between quantum emitters in a diamond nanocavity. *Science*, 362(6415):662–665, November 2018. ISSN 0036-8075, 1095-9203. doi: 10.1126/science.aau4691. URL https://science.sciencemag.org/content/362/6415/662.

[77] C. T. Nguyen, D. D. Sukachev, M. K. Bhaskar, B. Machielse, D. S. Levonian, E. N. Knall, P. Stroganov, R. Riedinger, H. Park, M. Lončar, and M. D. Lukin. Quantum network nodes based on diamond qubits with an efficient nanophotonic interface. *Phys. Rev. Lett.*, 123(18):183602, October 2019. doi: 10.1103/PhysRevLett.123.183602. URL https://link.aps.org/doi/10.1103/PhysRevLett.123.183602.

[78] C. T. Nguyen, D. D. Sukachev, M. K. Bhaskar, B. Machielse, D. S. Levonian, E. N. Knall, P. Stroganov, C. Chia, M. J. Burek, R. Riedinger, H. Park, M. Lončar, and M. D. Lukin. An integrated nanophotonic quantum register based on silicon-vacancy spins in diamond. *Phys. Rev. B*, 100(16):165428, October 2019. doi: 10.1103/PhysRevB.100.165428. URL https://link.aps.org/doi/10.1103/PhysRevB.100.165428. Publisher: American Physical Society.

[79] L. Childress, J. M. Taylor, A. S. Sørensen, and M. D. Lukin. Fault-tolerant quantum communication based on solid-state photon emitters. *Phys. Rev. Lett.*, 96(7):070504, February 2006. doi: 10.1103/PhysRevLett.96.070504. URL https://link.aps.org/doi/10.1103/PhysRevLett.96.070504. Publisher: American Physical Society.

[80] L. Childress, J. M. Taylor, A. S. Sørensen, and M. D. Lukin. Fault-tolerant quantum repeaters with minimal physical resources and implementations based on single-photon emitters. *Phys. Rev. A*, 72(5):052330, 2005.

[81] L. Childress, M. V. Gurudev Dutt, J. M. Taylor, A. S. Zibrov, F. Jelezko, J. Wrachtrup, P. R. Hemmer, and M. D. Lukin. Coherent dynamics of coupled electron and nuclear spin qubits in diamond. *Science*, 314(5797):281, October 2006. doi: 10.1126/science.1131871. URL http://science.sciencemag.org/content/314/5797/281.abstract.

[82] A. Faraon, C. Santori, Z. Huang, V.M. Acosta, and R.G. Beausoleil. Coupling of nitrogen-vacancy centers to photonic crystal cavities in monocrystalline diamond. *Phys. Rev. Lett.*, 109(3):033604, July 2012. doi: 10.1103/PhysRevLett.109.033604. URL http://link.aps.org/doi/10.1103/PhysRevLett.109.033604.

[83] Ruffin Eley Evans. *An integrated diamond nanophotonics platform for quantum optics*. PhD thesis, 2018.

[84] Christian Hepp. Electronic structure of the silicon vacancy color center in diamond, 2014.

[85] A. Sipahigil, K. D. Jahnke, L. J. Rogers, T. Teraji, J. Isoya, A. S. Zibrov, F. Jelezko, and M. D. Lukin. Indistinguishable Photons from Separated Silicon-Vacancy Centers in Diamond. *Phys. Rev. Lett.*, 113(11):113602, September 2014.

doi: 10.1103/PhysRevLett.113.113602. URL https://link.aps.org/doi/10.1103/PhysRevLett.113.113602. Publisher: American Physical Society.

[86] Ruffin E. Evans, Alp Sipahigil, Denis D. Sukachev, Alexander S. Zibrov, and Mikhail D. Lukin. Narrow-linewidth homogeneous optical emitters in diamond nanostructures via silicon ion implantation. *Phys. Rev. Appl.*, 5(4):044010, April 2016. doi: 10.1103/PhysRevApplied.5.044010. URL https://link.aps.org/doi/10.1103/PhysRevApplied.5.044010. Publisher: American Physical Society.

[87] A. Sipahigil, R. E. Evans, D. D. Sukachev, M. J. Burek, J. Borregaard, M. K. Bhaskar, C. T. Nguyen, J. L. Pacheco, H. A. Atikian, C. Meuwly, R. M. Camacho, F. Jelezko, E. Bielejec, H. Park, M. Loncar, and M. D. Lukin. An integrated diamond nanophotonics platform for quantum-optical networks. *Science*, 354(6314):847–850, November 2016. ISSN 0036-8075. doi: 10.1126/science.aah6875. Place: Washington Publisher: Amer Assoc Advancement Science WOS:000388531900031.

[88] Matthew E. Trusheim, Benjamin Pingault, Noel H. Wan, Mustafa Gündoğan, Lorenzo De Santis, Romain Debroux, Dorian Gangloff, Carola Purser, Kevin C. Chen, Michael Walsh, Joshua J. Rose, Jonas N. Becker, Benjamin Lienhard, Eric Bersin, Ioannis Paradeisanos, Gang Wang, Dominika Lyzwa, Alejandro R-P. Montblanch, Girish Malladi, Hassaram Bakhru, Andrea C. Ferrari, Ian A. Walmsley, Mete Atatüre, and Dirk Englund. Transform-limited photons from a coherent tin-vacancy spin in diamond. *Phys. Rev. Lett.*, 124(2):023602, January 2020. doi: 10.1103/PhysRevLett.124.023602. URL https://link.aps.org/doi/10.1103/PhysRevLett.124.023602. Publisher: American Physical Society.

[89] Matthew E. Trusheim, Noel H. Wan, Kevin C. Chen, Christopher J. Ciccarino, Johannes Flick, Ravishankar Sundararaman, Girish Malladi, Eric Bersin, Michael Walsh, Benjamin Lienhard, Hassaram Bakhru, Prineha Narang, and Dirk Englund. Lead-related quantum emitters in diamond. *Phys. Rev. B*, 99(7):075430, February 2019. doi: 10.1103/PhysRevB.99.075430. URL https://link.aps.org/doi/10.1103/PhysRevB.99.075430.

[90] P. Goy, J. M. Raimond, M. Gross, and S. Haroche. Observation of cavity-enhanced single-atom spontaneous emission. *Phys. Rev. Lett.*, 50(24):1903–1906,

June 1983. doi: 10.1103/PhysRevLett.50.1903. URL https://link.aps.org/doi/10.1103/PhysRevLett.50.1903. Publisher: American Physical Society.

[91] H. J. Kimble. Strong interactions of single atoms and photons in cavity QED. *Phys. Scr.*, T76:127–137, 1998. ISSN 0031-8949. doi: 10.1238/Physica.Topical.076a00127. Place: Bristol Publisher: Iop Publishing Ltd WOS:000075950900019.

[92] H. Mabuchi and A. C. Doherty. Cavity quantum electrodynamics: coherence in context. *Science*, 298(5597):1372–1377, November 2002. ISSN 0036-8075, 1095-9203. doi: 10.1126/science.1078446. URL https://science.sciencemag.org/content/298/5597/1372. Publisher: American Association for the Advancement of Science Section: Special Reviews.

[93] Kerry J. Vahala. Optical microcavities. *Nature*, 424(6950):839–846, August 2003. ISSN 1476-4687. doi: 10.1038/nature01939. URL https://www.nature.com/articles/nature01939. Number: 6950 Publisher: Nature Publishing Group.

[94] Andreas Reiserer and Gerhard Rempe. Cavity-based quantum networks with single atoms and optical photons. *Rev. Mod. Phys.*, 87(4), December 2015. ISSN 0034-6861. doi: 10.1103/RevModPhys.87.1379. Place: College Pk Publisher: Amer Physical Soc WOS:000365886900001.

[95] T. Pellizzari, S. A. Gardiner, J. I. Cirac, and P. Zoller. Decoherence, continuous observation, and quantum computing: a cavity QED model. *Phys. Rev. Lett.*, 75(21):3788–3791, November 1995. doi: 10.1103/PhysRevLett.75.3788. URL https://link.aps.org/doi/10.1103/PhysRevLett.75.3788. Publisher: American Physical Society.

[96] T. E. Northup and R. Blatt. Quantum information transfer using photons. *Nat. Photonics*, 8(5):356–363, May 2014. ISSN 1749-4893. doi: 10.1038/nphoton.2014.53. URL https://www.nature.com/articles/nphoton.2014.53. Number: 5 Publisher: Nature Publishing Group.

[97] J. McKeever, A. Boca, A. D. Boozer, R. Miller, J. R. Buck, A. Kuzmich, and H. J. Kimble. Deterministic generation of single photons from one atom trapped in a cavity. *Science*, 303(5666):1992–1994, March 2004. ISSN 0036-8075, 1095-9203. doi: 10.1126/science.1095232. URL https://science.sciencemag.org/

content/303/5666/1992. Publisher: American Association for the Advancement of Science Section: Report.

[98] Pascale Senellart, Glenn Solomon, and Andrew White. High-performance semiconductor quantum-dot single-photon sources. *Nat. Nanotechnol.*, 12(11):1026–1039, November 2017. ISSN 1748-3395. doi: 10.1038/nnano.2017.218. URL https://www.nature.com/articles/nnano.2017.218.

[99] E. Knill, R. Laflamme, and G. J. Milburn. A scheme for efficient quantum computation with linear optics. *Nature*, 409(6816):46–52, January 2001. ISSN 0028-0836. doi: 10.1038/35051009. WOS:000166175600033.

[100] Pieter Kok, W. J. Munro, Kae Nemoto, T. C. Ralph, Jonathan P. Dowling, and G. J. Milburn. Linear optical quantum computing with photonic qubits. *Rev. Mod. Phys.*, 79(1):135–174, March 2007. ISSN 0034-6861. doi: 10.1103/RevModPhys. 79.135. Place: College Pk Publisher: Amer Physical Soc WOS:000244867600004.

[101] Barak Dayan, A. S. Parkins, Takao Aoki, E. P. Ostby, K. J. Vahala, and H. J. Kimble. A photon turnstile dynamically regulated by one atom. *Science*, 319(5866): 1062–1065, February 2008. ISSN 0036-8075, 1095-9203. doi: 10.1126/science. 1152261. URL https://science.sciencemag.org/content/319/5866/1062. Publisher: American Association for the Advancement of Science Section: Report.

[102] Holger P. Specht, Christian Nolleke, Andreas Reiserer, Manuel Uphoff, Eden Figueroa, Stephan Ritter, and Gerhard Rempe. A single-atom quantum memory. *Nature*, 473(7346):190–193, May 2011. ISSN 0028-0836. doi: 10.1038/nature09997. Place: London Publisher: Nature Publishing Group WOS:000290487200033.

[103] Christoph Clausen, Imam Usmani, Félix Bussières, Nicolas Sangouard, Mikael Afzelius, Hugues de Riedmatten, and Nicolas Gisin. Quantum storage of photonic entanglement in a crystal. *Nature*, 469(7331):508–511, January 2011. ISSN 1476-4687. doi: 10.1038/nature09662. URL https://www.nature.com/articles/nature09662. Number: 7331 Publisher: Nature Publishing Group.

[104] Yi-Hsin Chen, Meng-Jung Lee, I-Chung Wang, Shengwang Du, Yong-Fan Chen, Ying-Cheng Chen, and Ite A. Yu. Coherent optical memory with high storage

efficiency and large fractional delay. *Phys. Rev. Lett.*, 110(8):083601, February 2013. doi: 10.1103/PhysRevLett.110.083601. URL https://link.aps.org/doi/10.1103/PhysRevLett.110.083601. Publisher: American Physical Society.

[105] Alessandro Seri, Andreas Lenhard, Daniel Rieländer, Mustafa Gündoğan, Patrick M. Ledingham, Margherita Mazzera, and Hugues de Riedmatten. Quantum correlations between single telecom photons and a multimode on-demand solid-state quantum memory. *Phys. Rev. X*, 7(2):021028, May 2017. doi: 10.1103/PhysRevX.7.021028. URL https://link.aps.org/doi/10.1103/PhysRevX.7.021028. Publisher: American Physical Society.

[106] B. B. Blinov, D. L. Moehring, L.-M. Duan, and C. Monroe. Observation of entanglement between a single trapped atom and a single photon. *Nature*, 428 (6979):153–157, March 2004. ISSN 1476-4687. doi: 10.1038/nature02377. URL https://www.nature.com/articles/nature02377. Number: 6979 Publisher: Nature Publishing Group.

[107] D. N. Matsukevich, T. Chanelière, M. Bhattacharya, S.-Y. Lan, S. D. Jenkins, T. A. B. Kennedy, and A. Kuzmich. Entanglement of a photon and a collective atomic excitation. *Phys. Rev. Lett.*, 95(4):040405, July 2005. doi: 10.1103/PhysRevLett.95.040405. URL https://link.aps.org/doi/10.1103/PhysRevLett.95.040405. Publisher: American Physical Society.

[108] Jürgen Volz, Markus Weber, Daniel Schlenk, Wenjamin Rosenfeld, Johannes Vrana, Karen Saucke, Christian Kurtsiefer, and Harald Weinfurter. Observation of entanglement of a single photon with a trapped atom. *Phys. Rev. Lett.*, 96 (3):030404, January 2006. doi: 10.1103/PhysRevLett.96.030404. URL https://link.aps.org/doi/10.1103/PhysRevLett.96.030404. Publisher: American Physical Society.

[109] E. Togan, Y. Chu, A. S. Trifonov, L. Jiang, J. Maze, L. Childress, M. V. G. Dutt, A. S. Sørensen, P. R. Hemmer, A. S. Zibrov, and M. D. Lukin. Quantum entanglement between an optical photon and a solid-state spin qubit. *Nature*, 466 (7307):730–734, August 2010. ISSN 1476-4687. doi: 10.1038/nature09256. URL https://www.nature.com/articles/nature09256.

[110] W. B. Gao, P. Fallahi, E. Togan, J. Miguel-Sanchez, and A. Imamoglu. Observation of entanglement between a quantum dot spin and a single photon. *Nature*, 491(7424):426–430, November 2012. ISSN 1476-4687. doi: 10.1038/nature11573. URL https://www.nature.com/articles/nature11573. Number: 7424 Publisher: Nature Publishing Group.

[111] Kristiaan De Greve, Leo Yu, Peter L. McMahon, Jason S. Pelc, Chandra M. Natarajan, Na Young Kim, Eisuke Abe, Sebastian Maier, Christian Schneider, Martin Kamp, Sven Höfling, Robert H. Hadfield, Alfred Forchel, M. M. Fejer, and Yoshihisa Yamamoto. Quantum-dot spin–photon entanglement via frequency downconversion to telecom wavelength. *Nature*, 491(7424):421–425, November 2012. ISSN 1476-4687. doi: 10.1038/nature11577. URL https://www.nature.com/articles/nature11577. Number: 7424 Publisher: Nature Publishing Group.

[112] Tobias Tiecke, J Thompson, Nathalie de Leon, L Liu, Vladan Vuletic, and M Lukin. Nanophotonic quantum phase switch with a single atom. *Nature*, 508: 241–4, April 2014. doi: 10.1038/nature13188.

[113] L.-M. Duan and H. J. Kimble. Scalable photonic quantum computation through cavity-assisted interactions. *Phys. Rev. Lett.*, 92(12):127902, March 2004. doi: 10.1103/PhysRevLett.92.127902. URL https://link.aps.org/doi/10.1103/PhysRevLett.92.127902.

[114] Kristin M. Beck, Mahdi Hosseini, Yiheng Duan, and Vladan Vuletic. Large conditional single-photon cross-phase modulation. *PNAS*, 113(35):9740–9744, August 2016. ISSN 0027-8424. doi: 10.1073/pnas.1524117113. Place: Washington Publisher: Natl Acad Sciences WOS:000383090700040.

[115] Bastian Hacker, Stephan Welte, Gerhard Rempe, and Stephan Ritter. A photon–photon quantum gate based on a single atom in an optical resonator. *Nature*, 536 (7615):193–196, August 2016. ISSN 1476-4687. doi: 10.1038/nature18592. URL https://www.nature.com/articles/nature18592.

[116] Nicolas Sangouard, Christoph Simon, Hugues de Riedmatten, and Nicolas Gisin. Quantum repeaters based on atomic ensembles and linear optics. *Rev. Mod. Phys.*, 83(1):33–80, March 2011. doi: 10.1103/RevModPhys.83.33. URL https:

//link.aps.org/doi/10.1103/RevModPhys.83.33. Publisher: American Physical Society.

[117] Hugues de Riedmatten and Mikael Afzelius. Quantum Light Storage in Solid State Atomic Ensembles. In *Engineering the Atom-Photon Interaction: Controlling Fundamental Processes with Photons, Atoms and Solids*, pages 241–273. Springer, New York, 2015.

[118] William J. Munro, Koji Azuma, Kiyoshi Tamaki, and Kae Nemoto. Inside quantum repeaters. *IEEE J. Sel. Top. Quantum Electron.*, 21(3):78–90, May 2015. ISSN 1558-4542. doi: 10.1109/JSTQE.2015.2392076. Conference Name: IEEE Journal of Selected Topics in Quantum Electronics.

[119] Sreraman Muralidharan, Linshu Li, Jungsang Kim, Norbert Lütkenhaus, Mikhail D. Lukin, and Liang Jiang. Optimal architectures for long distance quantum communication. *Sci. Rep.*, 6(1):1–10, February 2016. ISSN 2045-2322. doi: 10.1038/srep20463. URL https://www.nature.com/articles/srep20463. Number: 1 Publisher: Nature Publishing Group.

[120] Charles H. Bennett, Gilles Brassard, Sandu Popescu, Benjamin Schumacher, John A. Smolin, and William K. Wootters. Purification of noisy entanglement and faithful teleportation via noisy channels. *Phys. Rev. Lett.*, 76(5):722–725, January 1996. doi: 10.1103/PhysRevLett.76.722. URL https://link.aps.org/doi/10.1103/PhysRevLett.76.722. Publisher: American Physical Society.

[121] R. Reichle, D. Leibfried, E. Knill, J. Britton, R. B. Blakestad, J. D. Jost, C. Langer, R. Ozeri, S. Seidelin, and D. J. Wineland. Experimental purification of two-atom entanglement. *Nature*, 443(7113):838–841, October 2006. ISSN 1476-4687. doi: 10.1038/nature05146. URL https://www.nature.com/articles/nature05146. Number: 7113 Publisher: Nature Publishing Group.

[122] N. Kalb, A. A. Reiserer, P. C. Humphreys, J. J. W. Bakermans, S. J. Kamerling, N. H. Nickerson, S. C. Benjamin, D. J. Twitchen, M. Markham, and R. Hanson. Entanglement distillation between solid-state quantum network nodes. *Science*, 356(6341):928–932, June 2017. ISSN 0036-8075, 1095-9203. doi: 10.1126/science.aan0070. URL https://science.sciencemag.org/content/356/6341/928.

287

Publisher: American Association for the Advancement of Science Section: Research Articles.

[123] Charles H. Bennett, Gilles Brassard, Claude Crépeau, Richard Jozsa, Asher Peres, and William K. Wootters. Teleporting an unknown quantum state via dual classical and Einstein-Podolsky-Rosen channels. *Phys. Rev. Lett.*, 70(13):1895–1899, March 1993. doi: 10.1103/PhysRevLett.70.1895. URL https://link.aps.org/doi/10.1103/PhysRevLett.70.1895. Publisher: American Physical Society.

[124] Dik Bouwmeester, Jian-Wei Pan, Klaus Mattle, Manfred Eibl, Harald Weinfurter, and Anton Zeilinger. Experimental quantum teleportation. *Nature*, 390(6660): 575–579, December 1997. ISSN 1476-4687. doi: 10.1038/37539. URL https://www.nature.com/articles/37539. Number: 6660 Publisher: Nature Publishing Group.

[125] C. Cabrillo, J. I. Cirac, P. García-Fernández, and P. Zoller. Creation of entangled states of distant atoms by interference. *Phys. Rev. A*, 59(2):1025–1033, February 1999. doi: 10.1103/PhysRevA.59.1025. URL https://link.aps.org/doi/10.1103/PhysRevA.59.1025. Publisher: American Physical Society.

[126] Sean D. Barrett and Pieter Kok. Efficient high-fidelity quantum computation using matter qubits and linear optics. *Phys. Rev. A*, 71(6):060310, June 2005. doi: 10.1103/PhysRevA.71.060310. URL https://link.aps.org/doi/10.1103/PhysRevA.71.060310. Publisher: American Physical Society.

[127] Chin-Wen Chou, Julien Laurat, Hui Deng, Kyung Soo Choi, Hugues de Riedmatten, Daniel Felinto, and H. Jeff Kimble. Functional quantum nodes for entanglement distribution over scalable quantum networks. *Science*, 316(5829): 1316–1320, June 2007. ISSN 0036-8075, 1095-9203. doi: 10.1126/science.1140300. URL https://science.sciencemag.org/content/316/5829/1316. Publisher: American Association for the Advancement of Science Section: Report.

[128] D. L. Moehring, P. Maunz, S. Olmschenk, K. C. Younge, D. N. Matsukevich, L.-M. Duan, and C. Monroe. Entanglement of single-atom quantum bits at a distance. *Nature*, 449(7158):68–71, September 2007. ISSN 1476-4687. doi: 10.1038/nature06118. URL https://www.nature.com/articles/nature06118. Number: 7158 Publisher: Nature Publishing Group.

[129] Julian Hofmann, Michael Krug, Norbert Ortegel, Lea Gérard, Markus Weber, Wenjamin Rosenfeld, and Harald Weinfurter. Heralded entanglement between widely separated atoms. *Science*, 337(6090):72–75, July 2012. ISSN 0036-8075, 1095-9203. doi: 10.1126/science.1221856. URL https://science.sciencemag.org/content/337/6090/72. Publisher: American Association for the Advancement of Science Section: Report.

[130] H. Bernien, B. Hensen, W. Pfaff, G. Koolstra, M. S. Blok, L. Robledo, T. H. Taminiau, M. Markham, D. J. Twitchen, L. Childress, and R. Hanson. Heralded entanglement between solid-state qubits separated by three metres. *Nature*, 497 (7447):86–90, May 2013. ISSN 1476-4687. doi: 10.1038/nature12016. URL https://www.nature.com/articles/nature12016. Number: 7447 Publisher: Nature Publishing Group.

[131] Aymeric Delteil, Zhe Sun, Wei-bo Gao, Emre Togan, Stefan Faelt, and Ataç Imamoğlu. Generation of heralded entanglement between distant hole spins. *Nat. Phys.*, 12(3):218–223, March 2016. ISSN 1745-2481. doi: 10.1038/nphys3605. URL https://www.nature.com/articles/nphys3605.

[132] R. Stockill, M. J. Stanley, L. Huthmacher, E. Clarke, M. Hugues, A. J. Miller, C. Matthiesen, C. Le Gall, and M. Atatüre. Phase-tuned entangled state generation between distant spin qubits. *Phys. Rev. Lett.*, 119(1):010503, July 2017. doi: 10.1103/PhysRevLett.119.010503. URL https://link.aps.org/doi/10.1103/PhysRevLett.119.010503. Publisher: American Physical Society.

[133] Em Purcell. Spontaneous emission probabilities at radio frequencies. *Phys. Rev.*, 69(11-1):681–681, 1946. ISSN 0031-899X. Place: College Pk Publisher: American Physical Soc WOS:A1946UB26100050.

[134] Christopher J. Axline, Luke D. Burkhart, Wolfgang Pfaff, Mengzhen Zhang, Kevin Chou, Philippe Campagne-Ibarcq, Philip Reinhold, Luigi Frunzio, S. M. Girvin, Liang Jiang, M. H. Devoret, and R. J. Schoelkopf. On-demand quantum state transfer and entanglement between remote microwave cavity memories. *Nat. Phys.*, 14(7):705–710, July 2018. ISSN 1745-2481. doi: 10.1038/s41567-018-0115-y. URL http://www.nature.com/articles/s41567-018-0115-y. Number: 7 Publisher: Nature Publishing Group.

[135] Michael Varnava, Daniel E. Browne, and Terry Rudolph. Loss tolerance in one-way quantum computation via counterfactual error correction. *Phys. Rev. Lett.*, 97 (12):120501, September 2006. doi: 10.1103/PhysRevLett.97.120501. URL https://link.aps.org/doi/10.1103/PhysRevLett.97.120501. Publisher: American Physical Society.

[136] Austin G. Fowler, David S. Wang, Charles D. Hill, Thaddeus D. Ladd, Rodney Van Meter, and Lloyd C. L. Hollenberg. Surface code quantum communication. *Phys. Rev. Lett.*, 104(18):180503, May 2010. doi: 10.1103/PhysRevLett.104.180503. URL https://link.aps.org/doi/10.1103/PhysRevLett.104.180503. Publisher: American Physical Society.

[137] Sreraman Muralidharan, Jungsang Kim, Norbert Lütkenhaus, Mikhail D. Lukin, and Liang Jiang. Ultrafast and fault-tolerant quantum communication across long distances. *Phys. Rev. Lett.*, 112(25):250501, June 2014. doi: 10.1103/PhysRevLett.112.250501. URL https://link.aps.org/doi/10.1103/PhysRevLett.112.250501. Publisher: American Physical Society.

[138] W. J. Munro, A. M. Stephens, S. J. Devitt, K. A. Harrison, and Kae Nemoto. Quantum communication without the necessity of quantum memories. *Nat. Photonics*, 6(11):777–781, November 2012. ISSN 1749-4893. doi: 10.1038/nphoton.2012.243. URL https://www.nature.com/articles/nphoton.2012.243. Number: 11 Publisher: Nature Publishing Group.

[139] Mihir Pant, Hari Krovi, Dirk Englund, and Saikat Guha. Rate-distance tradeoff and resource costs for all-optical quantum repeaters. *Phys. Rev. A*, 95(1):012304, January 2017. doi: 10.1103/PhysRevA.95.012304. URL https://link.aps.org/doi/10.1103/PhysRevA.95.012304. Publisher: American Physical Society.

[140] C. Schön, E. Solano, F. Verstraete, J. I. Cirac, and M. M. Wolf. Sequential generation of entangled multiqubit states. *Phys. Rev. Lett.*, 95(11):110503, September 2005. doi: 10.1103/PhysRevLett.95.110503. URL https://link.aps.org/doi/10.1103/PhysRevLett.95.110503. Publisher: American Physical Society.

[141] Netanel H. Lindner and Terry Rudolph. Proposal for pulsed on-demand sources of photonic cluster state strings. *Phys. Rev. Lett.*, 103(11):113602, September 2009.

290

doi: 10.1103/PhysRevLett.103.113602. URL https://link.aps.org/doi/10.1103/PhysRevLett.103.113602. Publisher: American Physical Society.

[142] I. Schwartz, D. Cogan, E. R. Schmidgall, Y. Don, L. Gantz, O. Kenneth, N. H. Lindner, and D. Gershoni. Deterministic generation of a cluster state of entangled photons. *Science*, 354(6311):434–437, October 2016. ISSN 0036-8075, 1095-9203. doi: 10.1126/science.aah4758. URL https://science.sciencemag.org/content/354/6311/434.

[143] Donovan Buterakos, Edwin Barnes, and Sophia E. Economou. Deterministic generation of all-photonic quantum repeaters from solid-state emitters. *Phys. Rev. X*, 7(4):041023, October 2017. doi: 10.1103/PhysRevX.7.041023. URL https://link.aps.org/doi/10.1103/PhysRevX.7.041023. Publisher: American Physical Society.

[144] Johannes Borregaard, Anders Søndberg Sørensen, and Peter Lodahl. Quantum networks with deterministic spin–photon interfaces. *Adv. Quantum Technol.*, 2 (5-6):1800091, 2019. ISSN 2511-9044. doi: 10.1002/qute.201800091. URL https://onlinelibrary.wiley.com/doi/abs/10.1002/qute.201800091.

[145] Peter Lodahl. Quantum-dot based photonic quantum networks. *Quantum Sci. Technol.*, 3(1):013001, October 2017. ISSN 2058-9565. doi: 10.1088/2058-9565/aa91bb. URL https://doi.org/10.1088%2F2058-9565%2Faa91bb.

[146] Daqing Wang, Hrishikesh Kelkar, Diego Martin-Cano, Dominik Rattenbacher, Alexey Shkarin, Tobias Utikal, Stephan Götzinger, and Vahid Sandoghdar. Turning a molecule into a coherent two-level quantum system. *Nat. Phys.*, 15(5): 483–489, May 2019. ISSN 1745-2481. doi: 10.1038/s41567-019-0436-5. URL https://www.nature.com/articles/s41567-019-0436-5. Number: 5 Publisher: Nature Publishing Group.

[147] Hiroki Takahashi, Ezra Kassa, Costas Christoforou, and Matthias Keller. Strong Coupling of a Single Ion to an Optical Cavity. *Phys. Rev. Lett.*, 124(1):013602, January 2020. doi: 10.1103/PhysRevLett.124.013602. URL https://link.aps.org/doi/10.1103/PhysRevLett.124.013602. Publisher: American Physical Society.

[148] Pascal Kobel, Moritz Breyer, and Michael Köhl. Deterministic spin-photon entanglement from a trapped ion in a fiber Fabry-Perot cavity. *arXiv:2005.09124*, May 2020. URL http://arxiv.org/abs/2005.09124. arXiv: 2005.09124.

[149] David D. Awschalom, Ronald Hanson, Jörg Wrachtrup, and Brian B. Zhou. Quantum technologies with optically interfaced solid-state spins. *Nat. Photonics*, 12 (9):516, September 2018. ISSN 1749-4893. doi: 10.1038/s41566-018-0232-2. URL https://www.nature.com/articles/s41566-018-0232-2.

[150] Tim Schröder, Sara L. Mouradian, Jiabao Zheng, Matthew E. Trusheim, Michael Walsh, Edward H. Chen, Luozhou Li, Igal Bayn, and Dirk Englund. Quantum nanophotonics in diamond. *JOSA B*, 33(4):B65–B83, April 2016. ISSN 1520-8540. doi: 10.1364/JOSAB.33.000B65. URL https://www.osapublishing.org/josab/abstract.cfm?uri=josab-33-4-B65.

[151] Sam Johnson, Philip R. Dolan, and Jason M. Smith. Diamond photonics for distributed quantum networks. *Prog. Quantum Electron.*, 55:129–165, September 2017. ISSN 0079-6727. doi: 10.1016/j.pquantelec.2017.05.003. WOS:000412256500007.

[152] Carlo Bradac, Weibo Gao, Jacopo Forneris, Matthew E. Trusheim, and Igor Aharonovich. Quantum nanophotonics with group IV defects in diamond. *Nat. Commun.*, 10(1):1–13, December 2019. ISSN 2041-1723. doi: 10.1038/s41467-019-13332-w. URL https://www.nature.com/articles/s41467-019-13332-w.

[153] Tian Zhong, Jonathan M. Kindem, John G. Bartholomew, Jake Rochman, Ioana Craiciu, Varun Verma, Sae Woo Nam, Francesco Marsili, Matthew D. Shaw, Andrew D. Beyer, and Andrei Faraon. Optically addressing single rare-earth ions in a nanophotonic cavity. *Phys. Rev. Lett.*, 121(18):183603, October 2018. ISSN 0031-9007. doi: 10.1103/PhysRevLett.121.183603. Place: College Pk Publisher: Amer Physical Soc WOS:000448932900002.

[154] A. M. Dibos, M. Raha, C. M. Phenicie, and J. D. Thompson. Atomic source of single photons in the telecom band. *Phys. Rev. Lett.*, 120(24):243601, June 2018. doi: 10.1103/PhysRevLett.120.243601. URL https://link.aps.org/doi/10.1103/PhysRevLett.120.243601. Publisher: American Physical Society.

[155] Alexander L. Crook, Christopher P. Anderson, Kevin C. Miao, Alexandre Bourassa, Hope Lee, Sam L. Bayliss, David O. Bracher, Xingyu Zhang, Hiroshi Abe, Takeshi Ohshima, Evelyn L. Hu, and David D. Awschalom. Purcell Enhancement of a Single Silicon Carbide Color Center with Coherent Spin Control. *Nano Lett.*, 20(5):3427–3434, May 2020. ISSN 1530-6984. doi: 10.1021/acs.nanolett. 0c00339. URL https://doi.org/10.1021/acs.nanolett.0c00339. Publisher: American Chemical Society.

[156] Lee C. Bassett, Audrius Alkauskas, Annemarie L. Exarhos, and Kai-Mei C. Fu. Quantum defects by design. *Nanophotonics*, 8(11):1867–1888, November 2019. ISSN 2192-8606. doi: 10.1515/nanoph-2019-0211. WOS:000495740200002.

[157] A. M. Zaitsev. *Optical Properties of Diamond: A Data Handbook*. Springer-Verlag, 2001. ISBN 978-3-540-66582-3. doi: 10.1007/978-3-662-04548-0. URL https://www.springer.com/gp/book/9783540665823.

[158] J. R. Maze, A. Gali, E. Togan, Y. Chu, A. Trifonov, E. Kaxiras, and M. D. Lukin. Properties of nitrogen-vacancy centers in diamond: the group theoretic approach. *New J. Phys.*, 13(2):025025, February 2011. ISSN 1367-2630. doi: 10. 1088/1367-2630/13/2/025025. URL https://doi.org/10.1088%2F1367-2630% 2F13%2F2%2F025025. Publisher: IOP Publishing.

[159] M. W. Doherty, N. B. Manson, P. Delaney, and L. C. L. Hollenberg. The negatively charged nitrogen-vacancy centre in diamond: the electronic solution. *New J. Phys.*, 13(2):025019, February 2011. ISSN 1367-2630. doi: 10.1088/1367-2630/13/2/ 025019. URL https://doi.org/10.1088%2F1367-2630%2F13%2F2%2F025019. Publisher: IOP Publishing.

[160] K. Nemoto, M. Trupke, S.J. Devitt, Ashley M. Stephens, Burkhard Scharfenberger, Kathrin Buczak, Tobias Nöbauer, Mark S. Everitt, Jörg Schmiedmayer, and William J. Munro. Photonic architecture for scalable quantum information processing in diamond. *Phys. Rev. X*, 4(3):031022, August 2014. doi: 10.1103/PhysRevX.4.031022. URL https://link.aps.org/doi/10.1103/ PhysRevX.4.031022.

[161] Nicoló Lo Piparo, Mohsen Razavi, and William J. Munro. Memory-assisted quantum key distribution with a single nitrogen-vacancy center. *Phys. Rev. A*, 96

(5):052313, November 2017. doi: 10.1103/PhysRevA.96.052313. URL https://link.aps.org/doi/10.1103/PhysRevA.96.052313. Publisher: American Physical Society.

[162] Filip Rozpedek, Raja Yehia, Kenneth Goodenough, Maximilian Ruf, Peter C. Humphreys, Ronald Hanson, Stephanie Wehner, and David Elkouss. Near-term quantum-repeater experiments with nitrogen-vacancy centers: Overcoming the limitations of direct transmission. *Phys. Rev. A*, 99(5):052330, May 2019. doi: 10.1103/PhysRevA.99.052330. URL https://link.aps.org/doi/10.1103/PhysRevA.99.052330. Publisher: American Physical Society.

[163] W. Pfaff, B. J. Hensen, H. Bernien, S. B. van Dam, M. S. Blok, T. H. Taminiau, M. J. Tiggelman, R. N. Schouten, M. Markham, D. J. Twitchen, and R. Hanson. Unconditional quantum teleportation between distant solid-state quantum bits. *Science*, 345(6196):532–535, August 2014. ISSN 0036-8075, 1095-9203. doi: 10.1126/science.1253512. URL https://science.sciencemag.org/content/345/6196/532. Publisher: American Association for the Advancement of Science Section: Research Article.

[164] Peter C. Humphreys, Norbert Kalb, Jaco P. J. Morits, Raymond N. Schouten, Raymond F. L. Vermeulen, Daniel J. Twitchen, Matthew Markham, and Ronald Hanson. Deterministic delivery of remote entanglement on a quantum network. *Nature*, 558(7709):268–273, June 2018. ISSN 1476-4687. doi: 10.1038/s41586-018-0200-5. URL https://www.nature.com/articles/s41586-018-0200-5. Number: 7709 Publisher: Nature Publishing Group.

[165] D. D. Sukachev, A. Sipahigil, C. T. Nguyen, M. K. Bhaskar, R. E. Evans, F. Jelezko, and M. D. Lukin. Silicon-vacancy spin qubit in diamond: a quantum memory exceeding 10 ms with single-shot state readout. *Phys. Rev. Lett.*, 119(22):223602, November 2017. doi: 10.1103/PhysRevLett.119.223602. URL https://link.aps.org/doi/10.1103/PhysRevLett.119.223602.

[166] Brendon C. Rose, Ding Huang, Zi-Huai Zhang, Paul Stevenson, Alexei M. Tyryshkin, Sorawis Sangtawesin, Srikanth Srinivasan, Lorne Loudin, Matthew L. Markham, Andrew M. Edmonds, Daniel J. Twitchen, Stephen A. Lyon, and Nathalie P. de Leon. Observation of an environmentally insensitive solid-state

spin defect in diamond. *Science*, 361(6397):60–63, July 2018. ISSN 0036-8075, 1095-9203. doi: 10.1126/science.aao0290. URL https://science.sciencemag. org/content/361/6397/60. Publisher: American Association for the Advancement of Science Section: Report.

[167] Mathias H. Metsch, Katharina Senkalla, Benedikt Tratzmiller, Jochen Scheuer, Michael Kern, Jocelyn Achard, Alexandre Tallaire, Martin B. Plenio, Petr Siyushev, and Fedor Jelezko. Initialization and readout of nuclear spins via a negatively charged silicon-vacancy center in diamond. *Phys. Rev. Lett.*, 122(19):190503, May 2019. ISSN 0031-9007. doi: 10.1103/PhysRevLett.122.190503. Place: College Pk Publisher: Amer Physical Soc WOS:000468229900002.

[168] Mark Fox. *Quantum Optics: An Introduction.* Oxford, April 2006. ISBN 978-0-19-856673-1.

[169] Roland Albrecht, Alexander Bommer, Christian Deutsch, Jakob Reichel, and Christoph Becher. Coupling of a single nitrogen-vacancy center in diamond to a fiber-based microcavity. *Phys. Rev. Lett.*, 110(24):243602, June 2013. doi: 10.1103/PhysRevLett.110.243602. URL http://link.aps.org/doi/10.1103/ PhysRevLett.110.243602.

[170] Hanno Kaupp, Christian Deutsch, Huan-Cheng Chang, Jakob Reichel, Theodor W. Hänsch, and David Hunger. Scaling laws of the cavity enhancement for nitrogen-vacancy centers in diamond. *Phys. Rev. A*, 88(5):053812, November 2013. doi: 10.1103/PhysRevA.88.053812. URL http://link.aps.org/doi/10. 1103/PhysRevA.88.053812.

[171] Thomas Grange, Gaston Hornecker, David Hunger, Jean-Philippe Poizat, Jean-Michel Gérard, Pascale Senellart, and Alexia Auffèves. Cavity-funneled generation of indistinguishable single photons from strongly dissipative quantum emitters. *Phys. Rev. Lett.*, 114(19):193601, May 2015. doi: 10.1103/PhysRevLett.114. 193601. URL http://link.aps.org/doi/10.1103/PhysRevLett.114.193601.

[172] Julia Benedikter, Hanno Kaupp, Thomas Huemmer, Yuejiang Liang, Alexander Bommer, Christoph Becher, Anke Krueger, Jason M. Smith, Theodor W. Haensch, and David Hunger. Cavity-enhanced single-photon source based on the silicon-

vacancy center in diamond. *Phys. Rev. Appl.*, 7(2):024031, February 2017. ISSN 2331-7019. doi: 10.1103/PhysRevApplied.7.024031. WOS:000396061000002.

[173] Rasmus HÃžy Jensen, Erika Janitz, Yannik Fontana, Yi He, Olivier Gobron, Ilya P. Radko, Mihir Bhaskar, Ruffin Evans, CÃ©sar Daniel RodrÃguez Rosen-blueth, Lilian Childress, Alexander Huck, and Ulrik Lund Andersen. Cavity-enhanced photon emission from a single germanium-vacancy center in a di-amond membrane. *Phys. Rev. Appl.*, 13(6):064016, June 2020. doi: 10.1103/PhysRevApplied.13.064016. URL https://link.aps.org/doi/10.1103/PhysRevApplied.13.064016. Publisher: American Physical Society.

[174] T. Legero, T. Wilk, A. Kuhn, and G. Rempe. Time-resolved two-photon quantum interference. *Appl. Phys. B*, 77(8):797–802, December 2003. ISSN 1432-0649. doi: 10.1007/s00340-003-1337-x. URL https://doi.org/10.1007/s00340-003-1337-x.

[175] Hannes Bernien, Lilian Childress, Lucio Robledo, Matthew Markham, Daniel Twitchen, and Ronald Hanson. Two-photon quantum interference from separate nitrogen vacancy centers in diamond. *Phys. Rev. Lett.*, 108(4):043604, January 2012. doi: 10.1103/PhysRevLett.108.043604. URL https://link.aps.org/doi/10.1103/PhysRevLett.108.043604. Publisher: American Physical Society.

[176] Marcus W. Doherty, Neil B. Manson, Paul Delaney, Fedor Jelezko, Joerg Wrachtrup, and Lloyd C. L. Hollenberg. The nitrogen-vacancy colour cen-tre in diamond. *Phys. Rep.*, 528(1):1–45, July 2013. ISSN 0370-1573. doi: 10.1016/j.physrep.2013.02.001. Place: Amsterdam Publisher: Elsevier WOS:000321078100001.

[177] Adam Gali. Ab initio theory of the nitrogen-vacancy center in diamond. *Nanophotonics*, 8(11):1907–1943, November 2019. ISSN 2192-8606. doi: 10.1515/nanoph-2019-0154. Place: Berlin Publisher: Walter De Gruyter Gmbh WOS:000495740200004.

[178] Tina Muller, Christian Hepp, Benjamin Pingault, Elke Neu, Stefan Gsell, Matthias Schreck, Hadwig Sternschulte, Doris Steinmüller-Nethl, Christoph Becher, and Mete Atatüre. Optical signatures of silicon-vacancy spins in dia-

mond. *Nat. Commun.*, 5:3328, February 2014. ISSN 2041-1723. doi: 10.1038/ ncomms4328. URL https://www.nature.com/articles/ncomms4328.

[179] Christian Hepp, Tina Müller, Victor Waselowski, Jonas N. Becker, Benjamin Pingault, Hadwig Sternschulte, Doris Steinmüller-Nethl, Adam Gali, Jeronimo R. Maze, Mete Atatüre, and Christoph Becher. Electronic structure of the silicon vacancy color center in diamond. *Phys. Rev. Lett.*, 112(3):036405, January 2014. doi: 10.1103/PhysRevLett.112.036405. URL https://link.aps.org/doi/10. 1103/PhysRevLett.112.036405.

[180] P. Siyushev, M. H. Metsch, Aroosa Ijaz, Jan M. Binder, Mihir K. Bhaskar, Denis D. Sukachev, Alp Sipahigil, Ruffin E. Evans, Christian T. Nguyen, Mikhail D. Lukin, Philip R. Hemmer, Yuri N. Palyanov, Igor N. Kupriyanov, Yuri M. Borzdov, Lachlan J. Rogers, and Fedor Jelezko. Optical and microwave control of germanium-vacancy center spins in diamond. *Phys. Rev. B*, 96(8):081201, August 2017. doi: 10.1103/PhysRevB.96.081201. URL https://link.aps.org/doi/10. 1103/PhysRevB.96.081201.

[181] Alison E. Rugar, Constantin Dory, Shuo Sun, and Jelena Vučković. Characterization of optical and spin properties of single tin-vacancy centers in diamond nanopillars. *Phys. Rev. B*, 99(20):205417, May 2019. doi: 10.1103/PhysRevB.99.205417. URL https://link.aps.org/doi/10.1103/PhysRevB.99.205417.

[182] D. Hunger, T. Steinmetz, Y. Colombe, C. Deutsch, T. W. Hänsch, and J. Reichel. A fiber Fabry–Perot cavity with high finesse. *New J. Phys.*, 12(6):065038, 2010. ISSN 1367-2630. doi: 10.1088/1367-2630/12/6/065038. URL http://stacks. iop.org/1367-2630/12/i=6/a=065038.

[183] Rishi N. Patel, Tim Schröder, Noel Wan, Luozhou Li, Sara L. Mouradian, Edward H. Chen, and Dirk R. Englund. Efficient photon coupling from a diamond nitrogen vacancy center by integration with silica fiber. *Light Sci. Appl.*, 5(2): e16032–e16032, February 2016. ISSN 2047-7538. doi: 10.1038/lsa.2016.32. URL http://www.nature.com/articles/lsa201632/. Number: 2 Publisher: Nature Publishing Group.

[184] Michael J. Burek, Charles Meuwly, Ruffin E. Evans, Mihir K. Bhaskar, Alp Sipahigil, Srujan Meesala, Bartholomeus Machielse, Denis D. Sukachev, Chris-

297

tian T. Nguyen, Jose L. Pacheco, Edward Bielejec, Mikhail D. Lukin, and Marko Loncar. Fiber-coupled diamond quantum nanophotonic interface. *Phys. Rev. Appl.*, 8(2):024026, August 2017. ISSN 2331-7019. doi: 10.1103/PhysRevApplied. 8.024026. WOS:000408360500004.

[185] Haruka Tanji-Suzuki, Ian D. Leroux, Monika H. Schleier-Smith, Marko Cetina, Andrew T. Grier, Jonathan Simon, and Vladan Vuletić. Chapter 4 - Interaction between Atomic Ensembles and Optical Resonators: Classical Description. In *Advances In Atomic, Molecular, and Optical Physics*, volume 60, pages 201–237. Academic Press, January 2011. doi: 10.1016/B978-0-12-385508-4.00004-8.

[186] Edo Waks and Jelena Vuckovic. Dipole induced transparency in drop-filter cavity-waveguide Systems. *Phys. Rev. Lett.*, 96(15):153601, April 2006. doi: 10.1103/PhysRevLett.96.153601. URL https://link.aps.org/doi/10.1103/PhysRevLett.96.153601. Publisher: American Physical Society.

[187] Edo Waks and Jelena Vuckovic. Dispersive properties and large Kerr nonlinearities using dipole-induced transparency in a single-sided cavity. *Phys. Rev. A*, 73(4): 041803, April 2006. doi: 10.1103/PhysRevA.73.041803. URL https://link.aps.org/doi/10.1103/PhysRevA.73.041803. Publisher: American Physical Society.

[188] A. Imamoğlu, D. D. Awschalom, G. Burkard, D. P. DiVincenzo, D. Loss, M. Sherwin, and A. Small. Quantum information processing using quantum dot spins and cavity QED. *Phys. Rev. Lett.*, 83(20):4204–4207, November 1999. doi: 10.1103/PhysRevLett.83.4204. URL https://link.aps.org/doi/10.1103/PhysRevLett.83.4204. Publisher: American Physical Society.

[189] Liang Jiang, J. M. Taylor, Kae Nemoto, W. J. Munro, Rodney Van Meter, and M. D. Lukin. Quantum repeater with encoding. *Phys. Rev. A*, 79(3):032325, March 2009. doi: 10.1103/PhysRevA.79.032325. URL https://link.aps.org/doi/10.1103/PhysRevA.79.032325. Publisher: American Physical Society.

[190] Paul E. Barclay, Kai-Mei C. Fu, Charles Santori, Andrei Faraon, and Raymond G. Beausoleil. Hybrid nanocavity resonant enhancement of color center emission in diamond. *Phys. Rev. X*, 1(1):011007, September 2011. doi: 10.1103/PhysRevX.1.011007. URL https://link.aps.org/doi/10.1103/PhysRevX.1.011007.

[191] Lucio Robledo, Hannes Bernien, Ilse van Weperen, and Ronald Hanson. Control and coherence of the optical transition of single nitrogen vacancy centers in diamond. *Phys. Rev. Lett.*, 105(17):177403, October 2010. doi: 10.1103/PhysRevLett.105.177403. URL https://link.aps.org/doi/10.1103/PhysRevLett.105.177403. Publisher: American Physical Society.

[192] Andreas Dietrich, Kay D. Jahnke, Jan M. Binder, Tokuyuki Teraji, Junichi Isoya, Lachlan J. Rogers, and Fedor Jelezko. Isotopically varying spectral features of silicon-vacancy in diamond. *New J. Phys.*, 16(11):113019, November 2014. ISSN 1367-2630. doi: 10.1088/1367-2630/16/11/113019. URL https://doi.org/10.1088%2F1367-2630%2F16%2F11%2F113019.

[193] Kay D. Jahnke, Alp Sipahigil, Jan M. Binder, Marcus W. Doherty, Mathias Metsch, Lachlan J. Rogers, Neil B. Manson, Mikhail D. Lukin, and Fedor Jelezko. Electron–phonon processes of the silicon-vacancy centre in diamond. *New J. Phys.*, 17(4):043011, April 2015. ISSN 1367-2630. doi: 10.1088/1367-2630/17/4/043011. URL https://doi.org/10.1088%2F1367-2630%2F17%2F4%2F043011. Publisher: IOP Publishing.

[194] L. J. Rogers, K. D. Jahnke, T. Teraji, L. Marseglia, C. Müller, B. Naydenov, H. Schauffert, C. Kranz, J. Isoya, L. P. McGuinness, and F. Jelezko. Multiple intrinsically identical single-photon emitters in the solid state. *Nat. Commun.*, 5 (1):1–6, August 2014. ISSN 2041-1723. doi: 10.1038/ncomms5739. URL https://www.nature.com/articles/ncomms5739.

[195] Yuri N. Palyanov, Igor N. Kupriyanov, Yuri M. Borzdov, and Nikolay V. Surovtsev. Germanium: a new catalyst for diamond synthesis and a new optically active impurity in diamond. *Sci. Rep.*, 5(1):1–8, October 2015. ISSN 2045-2322. doi: 10.1038/srep14789. URL https://www.nature.com/articles/srep14789.

[196] Johannes Görlitz, Dennis Herrmann, Gerg\Ho Thiering, Philipp Fuchs, Morgane Gandil, Takayuki Iwasaki, Takashi Taniguchi, Michael Kieschnick, Jan Meijer, Mutsuko Hatano, Adam Gali, and Christoph Becher. Spectroscopic investigations of negatively charged tin-vacancy centres in diamond. *New J. Phys.*, 22(1):013048, January 2020. ISSN 1367-2630. doi: 10.1088/1367-2630/ab6631. URL https://doi.org/10.1088%2F1367-2630%2Fab6631.

[197] Takayuki Iwasaki, Yoshiyuki Miyamoto, Takashi Taniguchi, Petr Siyushev, Mathias H. Metsch, Fedor Jelezko, and Mutsuko Hatano. Tin-vacancy quantum emitters in diamond. *Phys. Rev. Lett.*, 119(25):253601, December 2017. ISSN 0031-9007. doi: 10.1103/PhysRevLett.119.253601. WOS:000418619100006.

[198] S. Ditalia Tchernij, T. Luehmann, T. Herzig, J. Kuepper, A. Damin, S. Santonocito, M. Signorile, P. Traina, E. Moreva, F. Celegato, S. Pezzagna, I. P. Degiovanni, P. Olivero, M. Jaksic, J. Meijer, P. M. Genovese, and J. Forneris. Single-photon emitters in lead-implanted single-crystal diamond. *ACS Photonics*, 5(12):4864–4871, December 2018. ISSN 2330-4022. doi: 10.1021/acsphotonics.8b01013. WOS:000454463000020.

[199] J. P. Goss, P. R. Briddon, M. J. Rayson, S. J. Sque, and R. Jones. Vacancy-impurity complexes and limitations for implantation doping of diamond. *Phys. Rev. B*, 72(3):035214, July 2005. doi: 10.1103/PhysRevB.72.035214. URL https://link.aps.org/doi/10.1103/PhysRevB.72.035214.

[200] Jason M. Smith, Simon A. Meynell, Ania C. Bleszynski Jayich, and Jan Meijer. Colour centre generation in diamond for quantum technologies. *Nanophotonics*, 8 (11):1889–1906, November 2019. ISSN 2192-8606. doi: 10.1515/nanoph-2019-0196. Place: Berlin Publisher: Walter De Gruyter Gmbh WOS:000495740200003.

[201] J. R. Rabeau, P. Reichart, G. Tamanyan, D. N. Jamieson, S. Prawer, F. Jelezko, T. Gaebel, I. Popa, M. Domhan, and J. Wrachtrup. Implantation of labelled single nitrogen vacancy centers in diamond using N-15. *Appl. Phys. Lett.*, 88(2):023113, January 2006. ISSN 0003-6951. doi: 10.1063/1.2158700. Place: Melville Publisher: Amer Inst Physics WOS:000234606900067.

[202] S. Pezzagna, B. Naydenov, F. Jelezko, J. Wrachtrup, and J. Meijer. Creation efficiency of nitrogen-vacancy centres in diamond. *New J. Phys.*, 12(6):065017, June 2010. ISSN 1367-2630. doi: 10.1088/1367-2630/12/6/065017. URL https://doi.org/10.1088%2F1367-2630%2F12%2F6%2F065017. Publisher: IOP Publishing.

[203] J. O. Orwa, C. Santori, K. M. C. Fu, B. Gibson, D. Simpson, I. Aharonovich, A. Stacey, A. Cimmino, P. Balog, M. Markham, D. Twitchen, A. D. Greentree, R. G. Beausoleil, and S. Prawer. Engineering of nitrogen-vacancy color centers

in high purity diamond by ion implantation and annealing. *J. Appl. Phys.*, 109 (8):083530, April 2011. ISSN 0021-8979. doi: 10.1063/1.3573768. URL https://aip.scitation.org/doi/10.1063/1.3573768.

[204] James F. Ziegler and Jochen P. Biersack. The Stopping and Range of Ions in Matter. In *Treatise on Heavy-Ion Science: Volume 6: Astrophysics, Chemistry, and Condensed Matter*, pages 93–129. Springer US, 1985. ISBN 978-1-4615-8103-1. doi: 10.1007/978-1-4615-8103-1_3. URL https://doi.org/10.1007/978-1-4615-8103-1_3.

[205] J. Meijer, B. Burchard, M. Domhan, C. Wittmann, T. Gaebel, I. Popa, F. Jelezko, and J. Wrachtrup. Generation of single color centers by focused nitrogen implantation. *Appl. Phys. Lett.*, 87(26):261909, December 2005. ISSN 0003-6951. doi: 10.1063/1.2103389. URL https://aip.scitation.org/doi/abs/10.1063/1.2103389.

[206] Margarita Lesik, Piernicola Spinicelli, Sebastien Pezzagna, Patrick Happel, Vincent Jacques, Olivier Salord, Bernard Rasser, Anne Delobbe, Pierre Sudraud, Alexandre Tallaire, Jan Meijer, and Jean-Francois Roch. Maskless and targeted creation of arrays of colour centres in diamond using focused ion beam technology. *Phys. Status Solidi A*, 210(10):2055–2059, October 2013. ISSN 1862-6300. doi: 10.1002/pssa.201300102. Place: Weinheim Publisher: Wiley-V C H Verlag Gmbh WOS:000329299700040.

[207] Syuto Tamura, Godai Koike, Akira Komatsubara, Tokuyuki Teraji, Shinobu Onoda, Liam P. McGuinness, Lachlan Rogers, Boris Naydenov, E. Wu, Liu Yan, Fedor Jelezko, Takeshi Ohshima, Junichi Isoya, Takahiro Shinada, and Takashi Tanii. Array of bright silicon-vacancy centers in diamond fabricated by low-energy focused ion beam implantation. *Appl. Phys. Express*, 7(11):115201, October 2014. ISSN 1882-0786. doi: 10.7567/APEX.7.115201. URL https://iopscience.iop.org/article/10.7567/APEX.7.115201/meta. Publisher: IOP Publishing.

[208] Tim Schröder, Matthew E. Trusheim, Michael Walsh, Luozhou Li, Jiabao Zheng, Marco Schukraft, Alp Sipahigil, Ruffin E. Evans, Denis D. Sukachev, Christian T. Nguyen, Jose L. Pacheco, Ryan M. Camacho, Edward S. Bielejec, Mikhail D. Lukin, and Dirk Englund. Scalable focused ion beam creation of nearly lifetime-limited single quantum emitters in diamond nanostructures. *Nat. Commun.*, 8

(1):1–7, May 2017. ISSN 2041-1723. doi: 10.1038/ncomms15376. URL https://www.nature.com/articles/ncomms15376.

[209] David M. Toyli, Christoph D. Weis, Gregory D. Fuchs, Thomas Schenkel, and David D. Awschalom. Chip-scale nanofabrication of single spins and spin arrays in diamond. *Nano Lett.*, 10(8):3168–3172, August 2010. ISSN 1530-6984. doi: 10.1021/nl102066q. URL https://doi.org/10.1021/nl102066q. Publisher: American Chemical Society.

[210] P. Spinicelli, A. Dréau, L. Rondin, F. Silva, J. Achard, S. Xavier, S. Bansropun, T. Debuisschert, S. Pezzagna, J. Meijer, V. Jacques, and J.-F. Roch. Engineered arrays of nitrogen-vacancy color centers in diamond based on implantation of CN-molecules through nanoapertures. *New J. Phys.*, 13(2):025014, February 2011. ISSN 1367-2630. doi: 10.1088/1367-2630/13/2/025014. URL https://doi.org/10.1088%2F1367-2630%2F13%2F2%2F025014. Publisher: IOP Publishing.

[211] Igal Bayn, Edward H. Chen, Matthew E. Trusheim, Luozhou Li, Tim Schröder, Ophir Gaathon, Ming Lu, Aaron Stein, Mingzhao Liu, Kim Kisslinger, Hannah Clevenson, and Dirk Englund. Generation of ensembles of individually resolvable nitrogen vacancies using nanometer-scale apertures in ultrahigh-aspect ratio planar implantation masks. *Nano Lett.*, 15(3):1751–1758, March 2015. ISSN 1530-6984. doi: 10.1021/nl504441m. URL https://doi.org/10.1021/nl504441m. Publisher: American Chemical Society.

[212] Diego Scarabelli, Matt Trusheim, Ophir Gaathon, Dirk Englund, and Shalom J. Wind. Nanoscale engineering of closely-spaced electronic spins in diamond. *Nano Lett.*, 16(8):4982–4990, August 2016. ISSN 1530-6984. doi: 10.1021/acs.nanolett.6b01692. Place: Washington Publisher: Amer Chemical Soc WOS:000381331900035.

[213] Alison E. Rugar, Haiyu Lu, Constantin Dory, Shuo Sun, Patrick J. McQuade, Zhi-Xun Shen, Nicholas A. Melosh, and Jelena Vučković. Generation of tin-vacancy centers in diamond via shallow ion implantation and subsequent diamond overgrowth. *Nano Lett.*, 20(3):1614–1619, March 2020. ISSN 1530-6984. doi: 10.1021/acs.nanolett.9b04495. URL https://doi.org/10.1021/acs.nanolett.9b04495.

[214] Boris Naydenov, Friedemann Reinhard, Anke Lämmle, V. Richter, Rafi Kalish, Ulrika F. S. D'Haenens-Johansson, Mark Newton, Fedor Jelezko, and Jörg Wrachtrup. Increasing the coherence time of single electron spins in diamond by high temperature annealing. *Appl. Phys. Lett.*, 97 (24):242511, December 2010. ISSN 0003-6951. doi: 10.1063/1.3527975. URL https://aip-scitation-org.ezp-prod1.hul.harvard.edu/doi/full/10.1063/1.3527975. Publisher: American Institute of Physics.

[215] Y. Chu, N.P. de Leon, B.J. Shields, B. Hausmann, R. Evans, E. Togan, M. J. Burek, M. Markham, A. Stacey, A.S. Zibrov, A. Yacoby, D.J. Twitchen, M. Loncar, H. Park, P. Maletinsky, and M.D. Lukin. Coherent optical transitions in implanted nitrogen vacancy centers. *Nano Lett.*, 14(4):1982–1986, April 2014. ISSN 1530-6984. doi: 10.1021/nl404836p. URL https://doi.org/10.1021/nl404836p.

[216] Johannes Lang, Stefan Häußler, Jens Fuhrmann, Richard Waltrich, Sunny Laddha, Jochen Scharpf, Alexander Kubanek, Boris Naydenov, and Fedor Jelezko. Long optical coherence times of shallow-implanted, negatively charged silicon vacancy centers in diamond. *Appl. Phys. Lett.*, 116(6):064001, February 2020. ISSN 0003-6951. doi: 10.1063/1.5143014. URL https://aip.scitation.org/doi/10.1063/1.5143014. Publisher: American Institute of Physics.

[217] S. B. van Dam, M. Walsh, M. J. Degen, E. Bersin, S. L. Mouradian, A. Galiullin, M. Ruf, M. IJspeert, T. H. Taminiau, R. Hanson, and D. R. Englund. Optical coherence of diamond nitrogen-vacancy centers formed by ion implantation and annealing. *Phys. Rev. B*, 99(16):161203, April 2019. doi: 10.1103/PhysRevB.99. 161203. URL https://link.aps.org/doi/10.1103/PhysRevB.99.161203.

[218] Yuri N. Palyanov, Igor N. Kupriyanov, Yuri M. Borzdov, Alexander F. Khokhryakov, and Nikolay V. Surovtsev. High-pressure synthesis and characterization of Ge-doped single crystal diamond. *Cryst. Growth Des.*, 16(6): 3510–3518, June 2016. ISSN 1528-7483. doi: 10.1021/acs.cgd.6b00481. URL https://doi.org/10.1021/acs.cgd.6b00481.

[219] Yuri N. Palyanov, Igor N. Kupriyanov, and Yuri M. Borzdov. High-pressure synthesis and characterization of Sn-doped single crystal diamond. *Carbon*, 143:769–775, March 2019. ISSN 0008-6223. doi: 10.1016/j.carbon.2018.11.084. URL http://www.sciencedirect.com/science/article/pii/S0008622318311175.

[220] Kerem Bray, Blake Regan, Aleksandra Trycz, Rodolfo Previdi, Gediminas Seniuti-nas, Kumaravelu Ganesan, Mehran Kianinia, Sejeong Kim, and Igor Aharonovich. Single crystal diamond membranes and photonic resonators containing germanium vacancy color centers. *ACS Photonics*, 5(12):4817–4822, December 2018. ISSN 2330-4022. doi: 10.1021/acsphotonics.8b00930. WOS:000454463000014.

[221] Kenichi Ohno, F. Joseph Heremans, Lee C. Bassett, Bryan A. Myers, David M. Toyli, Ania C. Bleszynski Jayich, Christopher J. Palmstrøm, and David D. Awschalom. Engineering shallow spins in diamond with nitrogen delta-doping. *Appl. Phys. Lett.*, 101(8):082413, August 2012. ISSN 0003-6951. doi: 10.1063/ 1.4748280. URL https://aip.scitation.org/doi/abs/10.1063/1.4748280. Publisher: American Institute of Physics.

[222] Jonathan C. Lee, David O. Bracher, Shanying Cui, Kenichi Ohno, Claire A. McLellan, Xingyu Zhang, Paolo Andrich, Benjamin Alemán, Kasey J. Russell, Andrew P. Magyar, Igor Aharonovich, Ania Bleszynski Jayich, David Awschalom, and Evelyn L. Hu. Deterministic coupling of delta-doped nitrogen vacancy centers to a nanobeam photonic crystal cavity. *Appl. Phys. Lett.*, 105(26):261101, December 2014. ISSN 0003-6951. doi: 10.1063/1.4904909. URL https://aip-scitation-org.ezp-prod1.hul.harvard.edu/doi/full/ 10.1063/1.4904909. Publisher: American Institute of Physics.

[223] J. Martin, R. Wannemacher, J. Teichert, L. Bischoff, and B. Köhler. Generation and detection of fluorescent color centers in diamond with submicron resolution. *Appl. Phys. Lett.*, 75(20):3096–3098, November 1999. ISSN 0003-6951. doi: 10.1063/1.125242. URL http://aip.scitation.org/doi/10.1063/1.125242. Publisher: American Institute of Physics.

[224] B. Campbell and A. Mainwood. Radiation damage of diamond by electron and gamma irradiation. *Phys. Status Solidi A*, 181(1):99–107, 2000. ISSN 1521-396X. doi: 10.1002/1521-396X(200009)181:1<99::AID-PSSA99> 3.0.CO;2-5. URL https://onlinelibrary.wiley.com/doi/abs/10.1002/ 1521-396X%28200009%29181%3A1%3C99%3A%3AAID-PSSA99%3E3.0.CO%3B2-5.

[225] Claire A. McLellan, Bryan A. Myers, Stephan Kraemer, Kenichi Ohno, David D. Awschalom, and Ania C. Bleszynski Jayich. Patterned formation of highly coherent nitrogen-vacancy centers using a focused electron irradiation technique. *Nano*

Lett., 16(4):2450–2454, April 2016. ISSN 1530-6984. doi: 10.1021/acs.nanolett. 5b05304. URL https://doi.org/10.1021/acs.nanolett.5b05304. Publisher: American Chemical Society.

[226] Yu-Chen Chen, Patrick S. Salter, Sebastian Knauer, Laiyi Weng, Angelo C. Frangeskou, Colin J. Stephen, Shazeaa N. Ishmael, Philip R. Dolan, Sam Johnson, Ben L. Green, Gavin W. Morley, Mark E. Newton, John G. Rarity, Martin J. Booth, and Jason M. Smith. Laser writing of coherent colour centres in diamond. *Nat. Photonics*, 11(2):77–80, February 2017. ISSN 1749-4893. doi: 10.1038/nphoton.2016.234. URL https://www.nature.com/articles/nphoton.2016.234.

[227] Kai-Mei C. Fu, Charles Santori, Paul E. Barclay, Lachlan J. Rogers, Neil B. Manson, and Raymond G. Beausoleil. Observation of the dynamic Jahn-Teller effect in the excited states of nitrogen-vacancy centers in diamond. *Phys. Rev. Lett.*, 103(25):256404, December 2009. doi: 10.1103/PhysRevLett.103.256404. URL https://link.aps.org/doi/10.1103/PhysRevLett.103.256404. Publisher: American Physical Society.

[228] Adam Gali and Jeronimo R. Maze. Ab initio study of the split silicon-vacancy defect in diamond: electronic structure and related properties. *Phys. Rev. B*, 88 (23):235205, December 2013. ISSN 1098-0121. doi: 10.1103/PhysRevB.88.235205. WOS:000328684500004.

[229] Alp Sipahigil. *Quantum optics with diamond color centers coupled to nanophotonic devices*. PhD thesis, May 2017. URL https://dash.harvard.edu/handle/1/40046485.

[230] F. Jelezko and J. Wrachtrup. Single defect centres in diamond: A review. *Phys. Status Solidi A*, 203(13):3207–3225, 2006. ISSN 1862-6319. doi: 10.1002/pssa.200671403. URL https://onlinelibrary.wiley.com/doi/abs/10.1002/pssa.200671403. _eprint: https://onlinelibrary.wiley.com/doi/pdf/10.1002/pssa.200671403.

[231] M. H. Abobeih, J. Cramer, M. A. Bakker, N. Kalb, M. Markham, D. J. Twitchen, and T. H. Taminiau. One-second coherence for a single electron spin coupled to a multi-qubit nuclear-spin environment. *Nat. Commun.*, 9(1):1–8, June 2018. ISSN

2041-1723. doi: 10.1038/s41467-018-04916-z. URL https://www.nature.com/articles/s41467-018-04916-z.

[232] D. M. Toyli, D. J. Christle, A. Alkauskas, B. B. Buckley, C. G. Van de Walle, and D. D. Awschalom. Measurement and control of single nitrogen-vacancy center spins above 600 K. *Phys. Rev. X*, 2(3):031001, July 2012. doi: 10.1103/PhysRevX. 2.031001. URL https://link.aps.org/doi/10.1103/PhysRevX.2.031001.

[233] B. C. Buchler, T. Kalkbrenner, C. Hettich, and V. Sandoghdar. Measuring the quantum efficiency of the optical emission of single radiating dipoles using a scanning mirror. *Phys. Rev. Lett.*, 95(6):063003, August 2005. doi: 10.1103/PhysRevLett.95.063003. URL https://link.aps.org/doi/10.1103/PhysRevLett.95.063003. Publisher: American Physical Society.

[234] Ilya P. Radko, Mads Boll, Niels M. Israelsen, Nicole Raatz, Jan Meijer, Fedor Jelezko, Ulrik L. Andersen, and Alexander Huck. Determining the internal quantum efficiency of shallow-implanted nitrogen-vacancy defects in bulk diamond. *Opt. Express*, 24(24):27715–27725, November 2016. ISSN 1094-4087. doi: 10.1364/OE.24.027715. URL https://www.osapublishing.org/oe/abstract.cfm?uri=oe-24-24-27715.

[235] Noel H. Wan, Tsung-Ju Lu, Kevin C. Chen, Michael P. Walsh, Matthew E. Trusheim, Lorenzo De Santis, Eric A. Bersin, Isaac B. Harris, Sara L. Mouradian, Ian R. Christen, Edward S. Bielejec, and Dirk Englund. Large-scale integration of artificial atoms in hybrid photonic circuits. *Nature*, 583(7815): 226–231, July 2020. ISSN 1476-4687. doi: 10.1038/s41586-020-2441-3. URL http://www.nature.com/articles/s41586-020-2441-3. Number: 7815 Publisher: Nature Publishing Group.

[236] Disheng Chen, Zhao Mu, Yu Zhou, Johannes E. Fröch, Abdullah Rasmit, Carole Diederichs, Nikolay Zheludev, Igor Aharonovich, and Wei-bo Gao. Optical gating of resonance fluorescence from a single germanium vacancy color center in diamond. *Phys. Rev. Lett.*, 123(3):033602, July 2019. doi: 10.1103/PhysRevLett.123.033602. URL https://link.aps.org/doi/10.1103/PhysRevLett.123.033602.

[237] C. Santori, P. E. Barclay, K.-M. C. Fu, R. G. Beausoleil, S. Spillane, and M. Fisch. Nanophotonics for quantum optics using nitrogen-vacancy centers in diamond. *Nanotechnology*, 21(27):274008, June 2010. ISSN 0957-4484. doi: 10.1088/0957-4484/21/27/274008. URL https://doi.org/10.1088%2F0957-4484%2F21%2F27%2F274008. Publisher: IOP Publishing.

[238] Maximilian Ruf, Mark IJspeert, Suzanne van Dam, Nick de Jong, Hans van den Berg, Guus Evers, and Ronald Hanson. Optically coherent nitrogen-vacancy centers in micrometer-thin etched diamond membranes. *Nano Lett.*, 19(6):3987–3992, June 2019. ISSN 1530-6984. doi: 10.1021/acs.nanolett.9b01316. URL https://doi.org/10.1021/acs.nanolett.9b01316.

[239] Lucio Robledo, Lilian Childress, Hannes Bernien, Bas Hensen, Paul F. A. Alkemade, and Ronald Hanson. High-fidelity projective read-out of a solid-state spin quantum register. *Nature*, 477(7366):574–578, September 2011. ISSN 1476-4687. doi: 10.1038/nature10401. URL http://www.nature.com/articles/nature10401. Number: 7366 Publisher: Nature Publishing Group.

[240] Ph Tamarat, T. Gaebel, J. R. Rabeau, M. Khan, A. D. Greentree, H. Wilson, L. C. L. Hollenberg, S. Prawer, P. Hemmer, F. Jelezko, and J. Wrachtrup. Stark shift control of single optical centers in diamond. *Phys. Rev. Lett.*, 97(8):083002, August 2006. ISSN 0031-9007. doi: 10.1103/PhysRevLett.97.083002. Place: College Pk Publisher: American Physical Soc WOS:000240043800019.

[241] L. C. Bassett, F. J. Heremans, C. G. Yale, B. B. Buckley, and D. D. Awschalom. Electrical tuning of single nitrogen-vacancy center optical transitions enhanced by photoinduced fields. *Phys. Rev. Lett.*, 107(26):266403, December 2011. doi: 10.1103/PhysRevLett.107.266403. URL https://link.aps.org/doi/10.1103/PhysRevLett.107.266403. Publisher: American Physical Society.

[242] V. M. Acosta, C. Santori, A. Faraon, Z. Huang, K.-M. C. Fu, A. Stacey, D. A. Simpson, K. Ganesan, S. Tomljenovic-Hanic, A. D. Greentree, S. Prawer, and R. G. Beausoleil. Dynamic stabilization of the optical resonances of single nitrogen-vacancy centers in diamond. *Phys. Rev. Lett.*, 108(20):206401, May 2012. ISSN 0031-9007. doi: 10.1103/PhysRevLett.108.206401. Place: College Pk Publisher: Amer Physical Soc WOS:000304063700010.

[243] Shuo Sun, Jingyuan Linda Zhang, Kevin A. Fischer, Michael J. Burek, Constantin Dory, Konstantinos G. Lagoudakis, Yan-Kai Tzeng, Marina Radulaski, Yousif Kelaita, Amir Safavi-Naeini, Zhi-Xun Shen, Nicholas A. Melosh, Steven Chu, Marko Lončar, and Jelena Vučković. Cavity-enhanced Raman emission from a single color center in a solid. *Phys. Rev. Lett.*, 121(8), August 2018. ISSN 0031-9007, 1079-7114. doi: 10.1103/PhysRevLett.121.083601. URL https://link.aps.org/doi/10.1103/PhysRevLett.121.083601.

[244] Srujan Meesala, Young-Ik Sohn, Benjamin Pingault, Linbo Shao, Haig A. Atikian, Jeffrey Holzgrafe, Mustafa Gündoğan, Camille Stavrakas, Alp Sipahigil, Cleaven Chia, Ruffin Evans, Michael J. Burek, Mian Zhang, Lue Wu, Jose L. Pacheco, John Abraham, Edward Bielejec, Mikhail D. Lukin, Mete Atatüre, and Marko Lončar. Strain engineering of the silicon-vacancy center in diamond. *Phys. Rev. B*, 97(20): 205444, May 2018. doi: 10.1103/PhysRevB.97.205444. URL https://link.aps.org/doi/10.1103/PhysRevB.97.205444. Publisher: American Physical Society.

[245] B. Machielse, S. Bogdanovic, S. Meesala, S. Gauthier, M. J. Burek, G. Joe, M. Chalupnik, Y. I. Sohn, J. Holzgrafe, R. E. Evans, C. Chia, H. Atikian, M. K. Bhaskar, D. D. Sukachev, L. Shao, S. Maity, M. D. Lukin, and M. Lončar. Quantum interference of electromechanically stabilized emitters in nanophotonic devices. *Phys. Rev. X*, 9(3):031022, August 2019. doi: 10.1103/PhysRevX.9.031022. URL https://link.aps.org/doi/10.1103/PhysRevX.9.031022. Publisher: American Physical Society.

[246] M. V. Gurudev Dutt, L. Childress, L. Jiang, E. Togan, J. Maze, F. Jelezko, A. S. Zibrov, P. R. Hemmer, and M. D. Lukin. Quantum register based on individual electronic and nuclear spin qubits in diamond. *Science*, 316(5829): 1312–1316, June 2007. ISSN 0036-8075, 1095-9203. doi: 10.1126/science.1139831. URL https://science.sciencemag.org/content/316/5829/1312. Publisher: American Association for the Advancement of Science Section: Report.

[247] T. H. Taminiau, J. Cramer, T. van der Sar, V. V. Dobrovitski, and R. Hanson. Universal control and error correction in multi-qubit spin registers in diamond. *Nat. Nanotechnol.*, 9(3):171–176, March 2014. ISSN 1748-3395. doi: 10.1038/nnano.2014.2. URL http://www.nature.com/articles/nnano.2014.2. Number: 3 Publisher: Nature Publishing Group.

[248] F. Jelezko, T. Gaebel, I. Popa, A. Gruber, and J. Wrachtrup. Observation of coherent oscillations in a single electron spin. *Phys. Rev. Lett.*, 92(7):076401, February 2004. doi: 10.1103/PhysRevLett.92.076401. URL https://link.aps.org/doi/10.1103/PhysRevLett.92.076401.

[249] B. C. Rose, G. Thiering, A. M. Tyryshkin, A. M. Edmonds, M. L. Markham, A. Gali, S. A. Lyon, and N. P. de Leon. Strongly anisotropic spin relaxation in the neutral silicon vacancy center in diamond. *Phys. Rev. B*, 98(23):235140, December 2018. doi: 10.1103/PhysRevB.98.235140. URL https://link.aps.org/doi/10.1103/PhysRevB.98.235140.

[250] Zi-Huai Zhang, Paul Stevenson, Gergo Thiering, Brendon C. Rose, Ding Huang, Andrew M. Edmonds, Matthew L. Markham, Stephen A. Lyon, Adam Gali, and Nathalie P. de Leon. Optically detected magnetic resonance in the neutral silicon vacancy center in diamond via bound exciton states. *arXiv:2004.12544*, April 2020. URL http://arxiv.org/abs/2004.12544. arXiv: 2004.12544.

[251] Gergő Thiering and Adam Gali. *Ab initio* magneto-optical spectrum of group-IV vacancy color centers in diamond. *Phys. Rev. X*, 8(2):021063, June 2018. ISSN 2160-3308. doi: 10.1103/PhysRevX.8.021063. URL https://link.aps.org/doi/10.1103/PhysRevX.8.021063.

[252] Lachlan J. Rogers, Kay D. Jahnke, Mathias H. Metsch, Alp Sipahigil, Jan M. Binder, Tokuyuki Teraji, Hitoshi Sumiya, Junichi Isoya, Mikhail D. Lukin, Philip Hemmer, and Fedor Jelezko. All-optical initialization, readout, and coherent preparation of single silicon-vacancy spins in diamond. *Phys. Rev. Lett.*, 113 (26):263602, December 2014. doi: 10.1103/PhysRevLett.113.263602. URL https://link.aps.org/doi/10.1103/PhysRevLett.113.263602. Publisher: American Physical Society.

[253] Benjamin Pingault, Jonas N. Becker, Carsten H. H. Schulte, Carsten Arend, Christian Hepp, Tillmann Godde, Alexander I. Tartakovskii, Matthew Markham, Christoph Becher, and Mete Atatüre. All-optical formation of coherent dark states of silicon-vacancy spins in diamond. *Phys. Rev. Lett.*, 113(26):263601, December 2014. doi: 10.1103/PhysRevLett.113.263601. URL https://link.aps.org/doi/10.1103/PhysRevLett.113.263601. Publisher: American Physical Society.

[254] Benjamin Pingault, David-Dominik Jarausch, Christian Hepp, Lina Klintberg, Jonas N. Becker, Matthew Markham, Christoph Becher, and Mete Atatüre. Coherent control of the silicon-vacancy spin in diamond. *Nat. Commun.*, 8(1): 1–7, May 2017. ISSN 2041-1723. doi: 10.1038/ncomms15579. URL http://www.nature.com/articles/ncomms15579/. Number: 1 Publisher: Nature Publishing Group.

[255] Young-Ik Sohn, Srujan Meesala, Benjamin Pingault, Haig A. Atikian, Jeffrey Holzgrafe, Mustafa Gündoğan, Camille Stavrakas, Megan J. Stanley, Alp Sipahigil, Joonhee Choi, Mian Zhang, Jose L. Pacheco, John Abraham, Edward Bielejec, Mikhail D. Lukin, Mete Atatüre, and Marko Lončar. Controlling the coherence of a diamond spin qubit through its strain environment. *Nat. Commun.*, 9(1):1–6, May 2018. ISSN 2041-1723. doi: 10.1038/s41467-018-04340-3. URL https://www.nature.com/articles/s41467-018-04340-3.

[256] Christopher J. Ciccarino, Johannes Flick, Isaac B. Harris, Matthew E. Trusheim, Dirk R. Englund, and Prineha Narang. Strong spin-orbit quenching via the product Jahn-Teller effect in neutral group IV artificial atom qubits in diamond. *arXiv:2001.07743*, January 2020. URL http://arxiv.org/abs/2001.07743. arXiv: 2001.07743.

[257] Isaac Harris, Christopher J. Ciccarino, Johannes Flick, Dirk R. Englund, and Prineha Narang. Group III quantum defects in diamond are stable spin-1 color centers. *arXiv:1907.12548*, July 2019. URL http://arxiv.org/abs/1907.12548. arXiv: 1907.12548.

[258] Keith T. Butler, Daniel W. Davies, Hugh Cartwright, Olexandr Isayev, and Aron Walsh. Machine learning for molecular and materials science. *Nature*, 559(7715): 547–555, July 2018. ISSN 1476-4687. doi: 10.1038/s41586-018-0337-2. URL http://www.nature.com/articles/s41586-018-0337-2. Number: 7715 Publisher: Nature Publishing Group.

[259] Jonathan Schmidt, MÃ¡rio R. G. Marques, Silvana Botti, and Miguel A. L. Marques. Recent advances and applications of machine learning in solid-state materials science. *npj Computational Materials*, 5(1):1–36, August 2019. ISSN 2057-3960. doi: 10.1038/s41524-019-0221-0. URL http://www.nature.com/

articles/s41524-019-0221-0. Number: 1 Publisher: Nature Publishing Group.

[260] John D. Joannopoulos, Steven G. Johnson, Joshua N. Winn, and Robert D. Meade. *Photonic Crystals: Molding the Flow of Light - Second Edition.* Princeton University Press, October 2011. ISBN 978-1-4008-2824-1.

[261] Jacob T. Robinson, Christina Manolatou, Long Chen, and Michal Lipson. Ultrasmall mode volumes in dielectric optical microcavities. *Phys. Rev. Lett.*, 95 (14):143901, September 2005. doi: 10.1103/PhysRevLett.95.143901. URL https://link.aps.org/doi/10.1103/PhysRevLett.95.143901. Publisher: American Physical Society.

[262] Shuren Hu and Sharon M. Weiss. Design of photonic crystal cavities for extreme light concentration. *ACS Photonics*, 3(9):1647–1653, September 2016. doi: 10.1021/acsphotonics.6b00219. URL https://doi.org/10.1021/acsphotonics.6b00219. Publisher: American Chemical Society.

[263] Hyeongrak Choi, Mikkel Heuck, and Dirk Englund. Self-similar nanocavity design with ultrasmall mode volume for single-photon nonlinearities. *Phys. Rev. Lett.*, 118 (22):223605, May 2017. doi: 10.1103/PhysRevLett.118.223605. URL https://link.aps.org/doi/10.1103/PhysRevLett.118.223605. Publisher: American Physical Society.

[264] Camille Papon, Xiaoyan Zhou, Henri Thyrrestrup, Zhe Liu, Søren Stobbe, Rüdiger Schott, Andreas D. Wieck, Arne Ludwig, Peter Lodahl, and Leonardo Midolo. Nanomechanical single-photon routing. *Optica*, 6(4):524–530, April 2019. ISSN 2334-2536. doi: 10.1364/OPTICA.6.000524. URL http://www.osapublishing.org/optica/abstract.cfm?uri=optica-6-4-524. Publisher: Optical Society of America.

[265] A. Femius Koenderink, Andrea Alù, and Albert Polman. Nanophotonics: Shrinking light-based technology. *Science*, 348(6234):516–521, May 2015. ISSN 0036-8075, 1095-9203. doi: 10.1126/science.1261243. URL https://science-sciencemag-org.ezp-prod1.hul.harvard.edu/content/348/6234/516. Publisher: American Association for the Advancement of Science Section: Review.

[266] Michael J. Burek, Yiwen Chu, Madelaine S. Z. Liddy, Parth Patel, Jake Rochman, Srujan Meesala, Wooyoung Hong, Qimin Quan, Mikhail D. Lukin, and Marko Lončar. High quality-factor optical nanocavities in bulk single-crystal diamond. *Nat. Commun.*, 5(1):1–7, December 2014. ISSN 2041-1723. doi: 10.1038/ncomms6718. URL http://www.nature.com/articles/ncomms6718. Number: 1 Publisher: Nature Publishing Group.

[267] Igor Aharonovich and Elke Neu. Diamond nanophotonics. *Adv. Opt. Mater.*, 2(10):911–928, October 2014. ISSN 2195-1071. doi: 10.1002/adom.201400189. WOS:000344172300001.

[268] Behzad Khanaliloo, Matthew Mitchell, Aaron C. Hryciw, and Paul E. Barclay. High-Q/V monolithic diamond microdisks fabricated with quasi-isotropic etching. *Nano Lett.*, 15(8):5131–5136, August 2015. ISSN 1530-6984. doi: 10.1021/acs.nanolett.5b01346. URL https://doi.org/10.1021/acs.nanolett.5b01346.

[269] Matthew Mitchell, David P. Lake, and Paul E. Barclay. Realizing Q > 300 000 in diamond microdisks for optomechanics via etch optimization. *APL Photonics*, 4(1), January 2019. ISSN 2378-0967. doi: 10.1063/1.5053122.

[270] Andrei Faraon, Paul E. Barclay, Charles Santori, Kai-Mei C. Fu, and Raymond G. Beausoleil. Resonant enhancement of the zero-phonon emission from a colour centre in a diamond cavity. *Nat. Photonics*, 5(5):301–305, May 2011. ISSN 1749-4893. doi: 10.1038/nphoton.2011.52. URL https://www.nature.com/articles/nphoton.2011.52. Number: 5 Publisher: Nature Publishing Group.

[271] Birgit J. M. Hausmann, Brendan Shields, Qimin Quan, Patrick Maletinsky, Murray McCutcheon, Jennifer T. Choy, Tom M. Babinec, Alexander Kubanek, Amir Yacoby, Mikhail D. Lukin, and Marko Loncar. Integrated diamond networks for quantum nanophotonics. *Nano Lett.*, 12(3):1578–1582, March 2012. ISSN 1530-6984. doi: 10.1021/nl204449n. Place: Washington Publisher: Amer Chemical Soc WOS:000301406800079.

[272] C. F. Wang, E. L. Hu, J. Yang, and J. E. Butler. Fabrication of suspended single crystal diamond devices by electrochemical etch. *J. Vac. Sci. Technol. B*, 25(3):730–733, April 2007. ISSN 1071-1023. doi: 10.1116/1.2731327.

312

URL https://avs-scitation-org.ezp-prod1.hul.harvard.edu/doi/full/10.1116/1.2731327. Publisher: American Institute of Physics.

[273] Thomas M. Babinec, Jennifer T. Choy, Kirsten J. M. Smith, Mughees Khan, and Marko Loncar. Design and focused ion beam fabrication of single crystal diamond nanobeam cavities. *J. Vac. Sci. Technol. B*, 29(1):010601, January 2011. ISSN 2166-2746. doi: 10.1116/1.3520638. Place: Melville Publisher: A V S Amer Inst Physics WOS:000286679400001.

[274] Igal Bayn, Boris Meyler, Alex Lahav, Joseph Salzman, Rafi Kalish, Barbara A. Fairchild, Steven Prawer, Michael Barth, Oliver Benson, Thomas Wolf, Petr Siyushev, Fedor Jelezko, and Jorg Wrachtrup. Processing of photonic crystal nanocavity for quantum information in diamond. *Diam. Relat. Mater.*, 20(7):937–943, July 2011. ISSN 0925-9635. doi: 10.1016/j.diamond.2011.05.002. URL http://www.sciencedirect.com/science/article/pii/S092596351100166X.

[275] Janine Riedrich-Möller, Laura Kipfstuhl, Christian Hepp, Elke Neu, Christoph Pauly, Frank Mücklich, Armin Baur, Michael Wandt, Sandra Wolff, Martin Fischer, Stefan Gsell, Matthias Schreck, and Christoph Becher. One- and two-dimensional photonic crystal microcavities in single crystal diamond. *Nat. Nanotechnol.*, 7(1):69–74, January 2012. ISSN 1748-3395. doi: 10.1038/nnano.2011.190. URL http://www.nature.com/articles/nnano.2011.190. Number: 1 Publisher: Nature Publishing Group.

[276] Bahram Jalali and Sasan Fathpour. Silicon photonics. *J. Lightwave Technol.*, 24(12):4600–4615, December 2006. ISSN 1558-2213. doi: 10.1109/JLT.2006.885782. Conference Name: Journal of Lightwave Technology.

[277] James E. Butler, Richard L. Woodin, Lawrence Michael Brown, P. Fallon, A. H. Lettington, and John Wickham Steeds. Thin film diamond growth mechanisms. *Philos. Trans. Royal Soc. A*, 342(1664):209–224, February 1993. doi: 10.1098/rsta.1993.0015. URL https://royalsocietypublishing.org/doi/abs/10.1098/rsta.1993.0015. Publisher: Royal Society.

[278] X. Jiang and C. P. Klages. Heteroepitaxial diamond growth on (100) silicon. *Diam. Relat. Mater.*, 2(5):1112–1113, April 1993. ISSN 0925-9635. doi: 10.

1016/0925-9635(93)90282-7. URL `http://www.sciencedirect.com/science/article/pii/0925963593902827`.

[279] M. Schreck, H. Roll, and B. Stritzker. Diamond/Ir/SrTiO3: A material combination for improved heteroepitaxial diamond films. *Appl. Phys. Lett.*, 74(5):650–652, January 1999. ISSN 0003-6951. doi: 10.1063/1. 123029. URL `https://aip-scitation-org.ezp-prod1.hul.harvard.edu/doi/abs/10.1063/1.123029`. Publisher: American Institute of Physics.

[280] Tokuyuki Teraji. Chemical vapor deposition of homoepitaxial diamond films. *Phys. Status Solidi A*, 203(13):3324–3357, 2006. ISSN 1862-6319. doi: 10.1002/pssa.200671408. URL `http://onlinelibrary.wiley.com/doi/abs/10.1002/pssa.200671408`. _eprint: https://onlinelibrary.wiley.com/doi/pdf/10.1002/pssa.200671408.

[281] P. Rath, N. Gruhler, S. Khasminskaya, C. Nebel, C. Wild, and W. H. P. Pernice. Waferscale nanophotonic circuits made from diamond-on-insulator substrates. *Opt. Express*, 21(9):11031–11036, May 2013. ISSN 1094-4087. doi: 10.1364/OE.21.011031. URL `http://www.osapublishing.org/oe/abstract.cfm?uri=oe-21-9-11031`. Publisher: Optical Society of America.

[282] G. S. Sandhu and W. K. Chu. Reactive ion etching of diamond. *Appl. Phys. Lett.*, 55(5):437–438, July 1989. ISSN 0003-6951. doi: 10.1063/1. 101890. URL `https://aip-scitation-org.ezp-prod1.hul.harvard.edu/doi/abs/10.1063/1.101890`. Publisher: American Institute of Physics.

[283] Michael John Burek. *Free-standing nanomechanical and nanophotonic structures in single-crystal diamond*. PhD thesis, January 2016. URL `https://dash.harvard.edu/handle/1/26718746`.

[284] N. R. Parikh, J. D. Hunn, E. McGucken, M. L. Swanson, C. W. White, R. A. Rudder, D. P. Malta, J. B. Posthill, and R. J. Markunas. Single-crystal diamond plate liftoff achieved by ion implantation and subsequent annealing. *Appl. Phys. Lett.*, 61(26):3124–3126, December 1992. ISSN 0003-6951. doi: 10.1063/1.107981. URL `https://aip-scitation-org.ezp-prod1.hul.harvard.edu/doi/abs/10.1063/1.107981`. Publisher: American Institute of Physics.

[285] P. Olivero, S. Rubanov, P. Reichart, B. C. Gibson, S. T. Huntington, J. Rabeau, A. D. Greentree, J. Salzman, D. Moore, D. N. Jamieson, and S. Prawer. Ion-beam-assisted lift-off technique for three-dimensional micromachining of freestanding single-crystal diamond. *Adv. Mater.*, 17(20):2427–2430, 2005. ISSN 1521-4095. doi: 10.1002/adma.200500752. URL http://onlinelibrary.wiley.com/doi/abs/10.1002/adma.200500752. _eprint: https://onlinelibrary.wiley.com/doi/pdf/10.1002/adma.200500752.

[286] Barbara A. Fairchild, Paolo Olivero, Sergey Rubanov, Andrew D. Greentree, Felix Waldermann, Robert A. Taylor, Ian Walmsley, Jason M. Smith, Shane Huntington, Brant C. Gibson, David N. Jamieson, and Steven Prawer. Fabrication of ultrathin single-crystal diamond membranes. *Adv. Mater.*, 20(24):4793–4798, 2008. ISSN 1521-4095. doi: 10.1002/adma.200801460. URL http://onlinelibrary.wiley.com/doi/abs/10.1002/adma.200801460. _eprint: https://onlinelibrary.wiley.com/doi/pdf/10.1002/adma.200801460.

[287] Igal Bayn, Boris Meyler, Joseph Salzman, and Rafi Kalish. Triangular nanobeam photonic cavities in single-crystal diamond. *New J. Phys.*, 13(2):025018, February 2011. ISSN 1367-2630. doi: 10.1088/1367-2630/13/2/025018. URL https://doi.org/10.1088%2F1367-2630%2F13%2F2%2F025018. Publisher: IOP Publishing.

[288] Michael J. Burek, Nathalie P. de Leon, Brendan J. Shields, Birgit J. M. Hausmann, Yiwen Chu, Qimin Quan, Alexander S. Zibrov, Hongkun Park, Mikhail D. Lukin, and Marko Lončar. Free-standing mechanical and photonic nanostructures in single-crystal diamond. *Nano Lett.*, 12(12):6084–6089, December 2012. ISSN 1530-6984. doi: 10.1021/nl302541e. URL https://doi.org/10.1021/nl302541e. Publisher: American Chemical Society.

[289] Haig A. Atikian, Pawel Latawiec, Michael J. Burek, Young-Ik Sohn, Srujan Meesala, Normand Gravel, Ammar B. Kouki, and Marko Lončar. Freestanding nanostructures via reactive ion beam angled etching. *APL Photonics*, 2(5):051301, May 2017. doi: 10.1063/1.4982603. URL https://aip-scitation-org.ezp-prod1.hul.harvard.edu/doi/full/10.1063/1.4982603. Publisher: American Institute of Physics.

[290] Noel H. Wan, Sara Mouradian, and Dirk Englund. Two-dimensional photonic crystal slab nanocavities on bulk single-crystal diamond. *Appl. Phys. Lett.*, 112

(14):141102, April 2018. ISSN 0003-6951. doi: 10.1063/1.5021349. URL https://aip.scitation.org/doi/10.1063/1.5021349.

[291] Behzad Khanaliloo, Harishankar Jayakumar, Aaron C. Hryciw, David P. Lake, Hamidreza Kaviani, and Paul E. Barclay. Single-crystal diamond nanobeam waveguide optomechanics. *Phys. Rev. X*, 5(4):041051, December 2015. doi: 10.1103/PhysRevX.5.041051. URL https://link.aps.org/doi/10.1103/PhysRevX.5.041051. Publisher: American Physical Society.

[292] Sara Mouradian, Noel H. Wan, Tim Schröder, and Dirk Englund. Rectangular photonic crystal nanobeam cavities in bulk diamond. *Appl. Phys. Lett.*, 111(2):021103, July 2017. ISSN 0003-6951. doi: 10.1063/1.4992118. URL https://aip-scitation-org.ezp-prod1.hul.harvard.edu/doi/full/10.1063/1.4992118. Publisher: American Institute of Physics.

[293] Marcell Kiss, Teodoro Graziosi, Adrien Toros, Toralf Scharf, Christian Santschi, Olivier J. F. Martin, and Niels Quack. High-quality single crystal diamond diffraction gratings fabricated by crystallographic etching. *Opt. Express*, 27(21):30371–30379, October 2019. ISSN 1094-4087. doi: 10.1364/OE.27.030371. URL http://www.osapublishing.org/oe/abstract.cfm?uri=oe-27-21-30371. Publisher: Optical Society of America.

[294] Jingyuan Linda Zhang, Shuo Sun, Michael J. Burek, Constantin Dory, Yan-Kai Tzeng, Kevin A. Fischer, Yousif Kelaita, Konstantinos G. Lagoudakis, Marina Radulaski, Zhi-Xun Shen, Nicholas A. Melosh, Steven Chu, Marko Lončar, and Jelena Vučković. Strongly cavity-enhanced spontaneous emission from silicon-vacancy centers in diamond. *Nano Lett.*, 18(2):1360–1365, February 2018. ISSN 1530-6984. doi: 10.1021/acs.nanolett.7b05075. URL https://doi.org/10.1021/acs.nanolett.7b05075. Publisher: American Chemical Society.

[295] B. J. M. Hausmann, I. B. Bulu, P. B. Deotare, M. McCutcheon, V. Venkataraman, M. L. Markham, D. J. Twitchen, and M. Lončar. Integrated high-quality factor optical resonators in diamond. *Nano Lett.*, 13(5):1898–1902, May 2013. ISSN 1530-6984. doi: 10.1021/nl3037454. URL https://doi.org/10.1021/nl3037454. Publisher: American Chemical Society.

[296] Patrik Rath, Svetlana Khasminskaya, Christoph Nebel, Christoph Wild, and Wolfram H. P. Pernice. Grating-assisted coupling to nanophotonic circuits in microcrystalline diamond thin films. *Beilstein J. Nanotechnol.*, 4(1):300–305, May 2013. ISSN 2190-4286. doi: 10.3762/bjnano.4.33. URL https://www.beilstein-journals.org/bjnano/articles/4/33. Publisher: Beilstein-Institut.

[297] Constantin Dory, Dries Vercruysse, Ki Youl Yang, Neil V. Sapra, Alison E. Rugar, Shuo Sun, Daniil M. Lukin, Alexander Y. Piggott, Jingyuan L. Zhang, Marina Radulaski, Konstantinos G. Lagoudakis, Logan Su, and Jelena Vuckovic. Inverse-designed diamond photonics. *Nat. Commun.*, 10, July 2019. ISSN 2041-1723. doi: 10.1038/s41467-019-11343-1.

[298] T. G. Tiecke, K. P. Nayak, J. D. Thompson, T. Peyronel, N. P. de Leon, V. Vuletić, and M. D. Lukin. Efficient fiber-optical interface for nanophotonic devices. *Optica*, 2(2):70–75, February 2015. ISSN 2334-2536. doi: 10.1364/OPTICA.2.000070. URL http://www.osapublishing.org/optica/abstract.cfm?uri=optica-2-2-70. Publisher: Optical Society of America.

[299] Saeed Khan, Sonia M. Buckley, Jeff Chiles, Richard P. Mirin, Sae Woo Nam, and Jeffrey M. Shainline. Low-loss, high-bandwidth fiber-to-chip coupling using capped adiabatic tapered fibers. *APL Photonics*, 5(5):056101, May 2020. doi: 10.1063/1.5145105. URL https://doi.org/10.1063/1.5145105.

[300] F. Pobell. *Matter and Methods at Low Temperatures.* Springer Berlin Heidelberg, 2007. URL https://books.google.com/books?id=mRZ0uPfiWTQC.

[301] H. Bernien. *Control, measurement and entanglement of remote quantum spin registers in diamond.* PhD thesis, 2014.

[302] T Yamamoto, T Umeda, K Watanabe, S Onoda, ML Markham, DJ Twitchen, B Naydenov, LP McGuinness, T Teraji, S Koizumi, et al. Extending spin coherence times of diamond qubits by high-temperature annealing. *Phys. Rev. B*, 88 (7):075206, 2013.

[303] Ali W. Elshaari, Wolfram Pernice, Kartik Srinivasan, Oliver Benson, and Val Zwiller. Hybrid integrated quantum photonic circuits. *Nat. Photonics*, pages

1–14, April 2020. ISSN 1749-4893. doi: 10.1038/s41566-020-0609-x. URL http://www.nature.com/articles/s41566-020-0609-x. Publisher: Nature Publishing Group.

[304] Stephan Ritter, Christian Nölleke, Carolin Hahn, Andreas Reiserer, Andreas Neuzner, Manuel Uphoff, Martin Mücke, Eden Figueroa, Joerg Bochmann, and Gerhard Rempe. An elementary quantum network of single atoms in optical cavities. *Nature*, 484(7393):195–200, April 2012. ISSN 1476-4687. doi: 10.1038/nature11023. URL https://www.nature.com/articles/nature11023.

[305] A. Stute, B. Casabone, B. Brandstätter, K. Friebe, T. E. Northup, and R. Blatt. Quantum-state transfer from an ion to a photon. *Nature Photonics*, 7:219 EP –, 02 2013. URL https://doi.org/10.1038/nphoton.2012.358.

[306] J. D. Thompson, T. G. Tiecke, N. P. de Leon, J. Feist, A. V. Akimov, M. Gullans, A. S. Zibrov, V. Vuletić, and M. D. Lukin. Coupling a Single Trapped Atom to a Nanoscale Optical Cavity. *Science*, 340(6137):1202–1205, June 2013. ISSN 0036-8075, 1095-9203. doi: 10.1126/science.1237125. URL https://science.sciencemag.org/content/340/6137/1202. Publisher: American Association for the Advancement of Science Section: Report.

[307] Juergen Volz, Michael Scheucher, Christian Junge, and Arno Rauschenbeutel. Nonlinear pi phase shift for single fibre-guided photons interacting with a single resonator-enhanced atom. *Nat. Photonics*, 8(12):965–970, December 2014. ISSN 1749-4885. doi: 10.1038/NPHOTON.2014.253. Place: London Publisher: Nature Publishing Group WOS:000345818600017.

[308] Polnop Samutpraphoot, Tamara Đorđević, Paloma L. Ocola, Hannes Bernien, Crystal Senko, Vladan Vuletić, and Mikhail D. Lukin. Strong coupling of two individually controlled atoms via a nanophotonic cavity. *PRL*, 124(6):063602, February 2020. doi: 10.1103/PhysRevLett.124.063602. URL https://link.aps.org/doi/10.1103/PhysRevLett.124.063602.

[309] Manuel Brekenfeld, Dominik Niemietz, Joseph Dale Christesen, and Gerhard Rempe. A quantum network node with crossed optical fibre cavities. *Nat. Phys.*, pages 1–5, April 2020. ISSN 1745-2481. doi: 10.1038/s41567-020-0855-3. URL

http://www.nature.com/articles/s41567-020-0855-3. Publisher: Nature Publishing Group.

[310] Shuo Sun, Jingyuan Linda Zhang, Kevin A. Fischer, Michael J. Burek, Constantin Dory, Konstantinos G. Lagoudakis, Yan-Kai Tzeng, Marina Radulaski, Yousif Kelaita, Amir Safavi-Naeini, Zhi-Xun Shen, Nicholas A. Melosh, Steven Chu, Marko Loncar, and Jelena Vuckovic. Frequency Tunable Single-Photon Emission From a Single Atomic Defect in a Solid. In *2019 CONFERENCE ON LASERS AND ELECTRO-OPTICS (CLEO)*, Conference on Lasers and Electro-Optics, 2019. ISBN 978-1-943580-57-6.

[311] Tian Zhong, Jonathan M. Kindem, John G. Bartholomew, Jake Rochman, Ioana Craiciu, Evan Miyazono, Marco Bettinelli, Enrico Cavalli, Varun Verma, Sae Woo Nam, Francesco Marsili, Matthew D. Shaw, Andrew D. Beyer, and Andrei Faraon. Nanophotonic rare-earth quantum memory with optically controlled retrieval. *Science*, 357(6358):1392, September 2017. doi: 10.1126/science.aan5959. URL http://science.sciencemag.org/content/357/6358/1392.abstract.

[312] L. Huthmacher, R. Stockill, E. Clarke, M. Hugues, C. Le Gall, and M. Atatüre. Coherence of a dynamically decoupled quantum-dot hole spin. *Phys. Rev. B*, 97: 241413, Jun 2018. doi: 10.1103/PhysRevB.97.241413. URL https://link.aps.org/doi/10.1103/PhysRevB.97.241413.

[313] L. Bergeron, C. Chartrand, A. T. K. Kurkjian, K. J. Morse, H. Riemann, N. V. Abrosimov, P. Becker, H.-J. Pohl, M. L. W. Thewalt, and S. Simmons. Silicon-integrated telecommunications photon-spin interface. *PRXQUANTUM*, 1(2):020301, October 2020. doi: 10.1103/PRXQuantum.1.020301. URL https://link.aps.org/doi/10.1103/PRXQuantum.1.020301.

[314] Iacopo Carusotto and Cristiano Ciuti. Quantum fluids of light. *Rev. Mod. Phys.*, 85(1):299, 2013.

[315] Igor Aharonovich, Dirk Englund, and Milos Toth. Solid-state single-photon emitters. *Nat. Photonics*, 10(10):631–641, October 2016. ISSN 1749-4885. doi: 10.1038/NPHOTON.2016.186. WOS:000384951900008.

[316] Peter Christian Maurer, Georg Kucsko, Christian Latta, Liang Jiang, Norman Ying Yao, Steven D Bennett, Fernando Pastawski, David Hunger, Nicholas

Chisholm, Matthew Markham, et al. Room-temperature quantum bit memory exceeding one second. *Science*, 336(6086):1283–1286, 2012.

[317] Uwe Jantzen, Andrea B Kurz, Daniel S Rudnicki, Clemens Schäfermeier, Kay D Jahnke, Ulrik L Andersen, Valery A Davydov, Viatcheslav N Agafonov, Alexander Kubanek, Lachlan J Rogers, and Fedor Jelezko. Nanodiamonds carrying silicon-vacancy quantum emitters with almost lifetime-limited linewidths. *New J. Phys.*, 18(7):073036, 2016. URL http://stacks.iop.org/1367-2630/18/i=7/a=073036.

[318] Ke Li, Yu Zhou, A Rasmita, I Aharonovich, and W B Gao. Nonblinking emitters with nearly lifetime-limited linewidths in cvd nanodiamonds. *Phys. Rev. Appl.*, 6 (2):024010, 2016.

[319] Takayuki Iwasaki, Fumitaka Ishibashi, Yoshiyuki Miyamoto, Yuki Doi, Satoshi Kobayashi, Takehide Miyazaki, Kosuke Tahara, Kay D. Jahnke, Lachlan J. Rogers, Boris Naydenov, Fedor Jelezko, Satoshi Yamasaki, Shinji Nagamachi, Toshiro Inubushi, Norikazu Mizuochi, and Mutsuko Hatano. Germanium-vacancy single color centers in diamond. *Sci. Rep.*, 5(1):1–7, August 2015. ISSN 2045-2322. doi: 10.1038/srep12882. URL https://www.nature.com/articles/srep12882.

[320] Evgenii Alekseevich Ekimov, SG Lyapin, Kirill Nikolaevich Boldyrev, Mikhail Vladislavovich Kondrin, R Khmelnitskiy, Vladimir Aleksandrovich Gavva, Tat'yana Vladimirovna Kotereva, and Marina Nikolaevna Popova. Germanium–vacancy color center in isotopically enriched diamonds synthesized at high pressures. *JETP Lett.*, 102(11):701–706, 2015.

[321] Darrick E. Chang, Anders S. Sørensen, Eugene A. Demler, and Mikhail D. Lukin. A single-photon transistor using nanoscale surface plasmons. *Nat. Phys.*, 3 (11):807–812, November 2007. ISSN 1745-2481. doi: 10.1038/nphys708. URL http://www.nature.com/articles/nphys708. Number: 11 Publisher: Nature Publishing Group.

[322] A. Goban, C.-L. Hung, J. D. Hood, S.-P. Yu, J. A. Muniz, O. Painter, and H. J. Kimble. Superradiance for Atoms Trapped along a Photonic Crystal Waveguide. *Phys. Rev. Lett.*, 115(6):063601, August 2015. doi: 10.1103/PhysRevLett.

115.063601. URL https://link.aps.org/doi/10.1103/PhysRevLett.115.063601. Publisher: American Physical Society.

[323] A. Javadi, I. Sollner, M. Arcari, S. Lindskov Hansen, L. Midolo, S. Mahmoodian, G. Kirsanske, T. Pregnolato, E. H. Lee, J. D. Song, S. Stobbe, and P. Lodahl. Single-photon non-linear optics with a quantum dot in a waveguide. *Nat. Commun.*, 6:8655, Oct 2015. URL http://dx.doi.org/10.1038/ncomms9655.

[324] Asma Khalid, Kelvin Chung, Ranjith Rajasekharan, Desmond WM Lau, Timothy J Karle, Brant C Gibson, and Snjezana Tomljenovic-Hanic. Lifetime reduction and enhanced emission of single photon color centers in nanodiamond via surrounding refractive index modification. *Sci. Rep.*, 5:11179, 2015.

[325] Martin Frimmer, Abbas Mohtashami, and A Femius Koenderink. Nanomechanical method to gauge emission quantum yield applied to nitrogen-vacancy centers in nanodiamond. *Appl. Phys. Lett.*, 102(12):121105, 2013.

[326] M L Goldman, A Sipahigil, M W Doherty, N Y Yao, S D Bennett, M Markham, D J Twitchen, N B Manson, A Kubanek, and M D Lukin. Phonon-induced population dynamics and intersystem crossing in nitrogen-vacancy centers. *Phys. Rev. Lett.*, 114(14):145502, 2015.

[327] Carsten HH Schulte, Jack Hansom, Alex E Jones, Clemens Matthiesen, Claire Le Gall, and Mete Atatüre. Quadrature squeezed photons from a two-level system. *Nature*, 525:222–225, 2015.

[328] Meng Khoon Tey, Zilong Chen, Syed Abdullah Aljunid, Brenda Chng, Florian Huber, Gleb Maslennikov, and Christian Kurtsiefer. Strong interaction between light and a single trapped atom without the need for a cavity. *Nat. Phys.*, 4(12):924–927, 2008.

[329] G Hétet, L Slodička, M Hennrich, and R Blatt. Single atom as a mirror of an optical cavity. *Phys. Rev. Lett.*, 107(13):133002, 2011.

[330] Gert Wrigge, Ilja Gerhardt, Jaesuk Hwang, Gert Zumofen, and Vahid Sandoghdar. Efficient coupling of photons to a single molecule and the observation of its resonance fluorescence. *Nat. Phys.*, 4(1):60–66, 2008.

[331] A N Vamivakas, M Atatüre, J Dreiser, S T Yilmaz, A Badolato, A K Swan, B B Goldberg, A Imamoglu, and M S Ünlü. Strong extinction of a far-field laser beam by a single quantum dot. *Nano Lett.*, 7(9):2892–2896, 2007.

[332] Stephan Welte, Bastian Hacker, Severin Daiss, Stephan Ritter, and Gerhard Rempe. Photon-Mediated Quantum Gate between Two Neutral Atoms in an Optical Cavity. *Phys. Rev. X*, 8(1):011018, February 2018. doi: 10.1103/PhysRevX.8. 011018. URL https://link.aps.org/doi/10.1103/PhysRevX.8.011018. Publisher: American Physical Society.

[333] Andreas Wallraff, David I Schuster, Alexandre Blais, L Frunzio, R-S Huang, J Majer, S Kumar, Steven M Girvin, and Robert J Schoelkopf. Strong coupling of a single photon to a superconducting qubit using circuit quantum electrodynamics. *Nature*, 431(7005):162–167, 2004.

[334] J. Majer, J. M. Chow, J. M. Gambetta, Jens Koch, B. R. Johnson, J. A. Schreier, L. Frunzio, D. I. Schuster, A. A. Houck, A. Wallraff, A. Blais, M. H. Devoret, S. M. Girvin, and R. J. Schoelkopf. Coupling superconducting qubits via a cavity bus. *Nature*, 449(7161):443–447, September 2007. ISSN 1476-4687. doi: 10.1038/ nature06184. URL http://www.nature.com/articles/nature06184. Number: 7161 Publisher: Nature Publishing Group.

[335] M. J. Kastoryano, F. Reiter, and A. S. Sørensen. Dissipative Preparation of Entanglement in Optical Cavities. *Phys. Rev. Lett.*, 106(9):090502, February 2011. doi: 10.1103/PhysRevLett.106.090502. URL https://link.aps.org/doi/10. 1103/PhysRevLett.106.090502. Publisher: American Physical Society.

[336] B Casabone, K Friebe, B Brandstätter, K Schüppert, R Blatt, and TE Northup. Enhanced quantum interface with collective ion-cavity coupling. *Phys. Rev. Lett.*, 114(2):023602, 2015.

[337] René Reimann, Wolfgang Alt, Tobias Kampschulte, Tobias Macha, Lothar Ratschbacher, Natalie Thau, Seokchan Yoon, and Dieter Meschede. Cavity-modified collective rayleigh scattering of two atoms. *Phys. Rev. Lett.*, 114(2): 023601, 2015.

[338] A Laucht, JM Villas-Bôas, Søren Stobbe, N Hauke, F Hofbauer, G Böhm, Peter Lodahl, M-C Amann, M Kaniber, and JJ Finley. Mutual coupling of two semi-

conductor quantum dots via an optical nanocavity. *Phys. Rev. B*, 82(7):075305, 2010.

[339] Hyochul Kim, Deepak Sridharan, Thomas C Shen, Glenn S Solomon, and Edo Waks. Strong coupling between two quantum dots and a photonic crystal cavity using magnetic field tuning. *Opt. Express*, 19(3):2589–2598, 2011.

[340] Shi-Biao Zheng and Guang-Can Guo. Efficient scheme for two-atom entanglement and quantum information processing in cavity qed. *Phys. Rev. Lett.*, 85(11):2392, 2000.

[341] Alisa Javadi, Dapeng Ding, Martin Hayhurst Appel, Sahand Mahmoodian, Matthias Christian Löbl, Immo Söllner, Rüdiger Schott, Camille Papon, Tommaso Pregnolato, Søren Stobbe, et al. Spin–photon interface and spin-controlled photon switching in a nanobeam waveguide. *Nat. Nanotech.*, 13(5):398, 2018.

[342] J. Borregaard, P. Kómár, E. M. Kessler, M. D. Lukin, and A. S. Sørensen. Long-distance entanglement distribution using individual atoms in optical cavities. *Phys. Rev. A*, 92(1):012307, July 2015. doi: 10.1103/PhysRevA.92.012307. URL https://link.aps.org/doi/10.1103/PhysRevA.92.012307. Publisher: American Physical Society.

[343] Jonas N. Becker, Benjamin Pingault, David Groß, Mustafa Gündoğan, Nadezhda Kukharchyk, Matthew Markham, Andrew Edmonds, Mete Atatüre, Pavel Bushev, and Christoph Becher. All-optical control of the silicon-vacancy spin in diamond at millikelvin temperatures. *Phys. Rev. Lett.*, 120(5):053603, January 2018. doi: 10.1103/PhysRevLett.120.053603. URL https://link.aps.org/doi/10.1103/PhysRevLett.120.053603.

[344] Sophia E. Economou, Netanel Lindner, and Terry Rudolph. Optically generated 2-dimensional photonic cluster state from coupled quantum dots. *Phys. Rev. Lett.*, 105(9):093601, August 2010. doi: 10.1103/PhysRevLett.105.093601. URL https://link.aps.org/doi/10.1103/PhysRevLett.105.093601. Publisher: American Physical Society.

[345] A. Stute, B. Casabone, P. Schindler, T. Monz, P. O. Schmidt, B. Brandstätter, T. E. Northup, and R. Blatt. Tunable ion–photon entanglement in an

optical cavity. *Nature*, 485(7399):482–485, May 2012. ISSN 1476-4687. doi: 10.1038/nature11120. URL https://www.nature.com/articles/nature11120. Number: 7399 Publisher: Nature Publishing Group.

[346] Norbert Kalb, Andreas Reiserer, Stephan Ritter, and Gerhard Rempe. Heralded storage of a photonic quantum bit in a single atom. *Phys. Rev. Lett.*, 114:220501, Jun 2015. doi: 10.1103/PhysRevLett.114.220501. URL https://link.aps.org/doi/10.1103/PhysRevLett.114.220501.

[347] Andreas Reiserer, Norbert Kalb, Gerhard Rempe, and Stephan Ritter. A quantum gate between a flying optical photon and a single trapped atom. *Nature*, 508(7495): 237–240, 2014.

[348] Stephan Welte, Bastian Hacker, Severin Daiss, Stephan Ritter, and Gerhard Rempe. Cavity carving of atomic bell states. *Phys. Rev. Lett.*, 118:210503, May 2017. doi: 10.1103/PhysRevLett.118.210503. URL https://link.aps.org/doi/10.1103/PhysRevLett.118.210503.

[349] Sean Molesky, Zin Lin, Alexander Y. Piggott, Weiliang Jin, Jelena Vuckovic, and Alejandro W. Rodriguez. Inverse design in nanophotonics. *Nature Photonics*, 12(11):659–670, 2018. ISSN 1749-4893. doi: 10.1038/s41566-018-0246-9. URL https://doi.org/10.1038/s41566-018-0246-9.

[350] G. Waldherr, Y. Wang, S. Zaiser, M. Jamali, T. Schulte-Herbrüggen, H. Abe, T. Ohshima, J. Isoya, J. F. Du, P. Neumann, and J. Wrachtrup. Quantum error correction in a solid-state hybrid spin register. *Nature*, 506:204 EP –, Feb 2014. URL https://doi.org/10.1038/nature12919.

[351] C. A. Ryan, J. S. Hodges, and D. G. Cory. Robust decoupling techniques to extend quantum coherence in diamond. *Phys. Rev. Lett.*, 105:200402, Nov 2010. doi: 10.1103/PhysRevLett.105.200402. URL https://link.aps.org/doi/10.1103/PhysRevLett.105.200402.

[352] G. de Lange, Z. H. Wang, D. Ristè, V. V. Dobrovitski, and R. Hanson. Universal dynamical decoupling of a single solid-state spin from a spin bath. *Science*, 330 (6000):60–63, October 2010. ISSN 0036-8075, 1095-9203. doi: 10.1126/science. 1192739. URL https://science-sciencemag-org.ezp-prod1.hul.harvard.

edu/content/330/6000/60. Publisher: American Association for the Advancement of Science Section: Report.

[353] B. A. Myers, A. Das, M. C. Dartiailh, K. Ohno, D. D. Awschalom, and A. C. Bleszynski Jayich. Probing surface noise with depth-calibrated spins in diamond. *Phys. Rev. Lett.*, 113(2):027602, July 2014. doi: 10.1103/PhysRevLett.113.027602. URL https://link.aps.org/doi/10.1103/PhysRevLett.113.027602. Publisher: American Physical Society.

[354] Shimon Kolkowitz, Quirin P. Unterreithmeier, Steven D. Bennett, and Mikhail D. Lukin. Sensing distant nuclear spins with a single electron spin. *Phys. Rev. Lett.*, 109:137601, Sep 2012. doi: 10.1103/PhysRevLett.109.137601. URL https://link.aps.org/doi/10.1103/PhysRevLett.109.137601.

[355] L. G. Rowan, E. L. Hahn, and W. B. Mims. Electron-spin-echo envelope modulation. *Phys. Rev.*, 137:A61–A71, Jan 1965. doi: 10.1103/PhysRev.137.A61. URL https://link.aps.org/doi/10.1103/PhysRev.137.A61.

[356] J. Casanova, Z.-Y. Wang, J. F. Haase, and M. B. Plenio. Robust dynamical decoupling sequences for individual-nuclear-spin addressing. *Phys. Rev. A*, 92: 042304, Oct 2015. doi: 10.1103/PhysRevA.92.042304. URL https://link.aps.org/doi/10.1103/PhysRevA.92.042304.

[357] Ilai Schwartz, Jochen Scheuer, Benedikt Tratzmiller, Samuel Müller, Qiong Chen, Ish Dhand, Zhen-Yu Wang, Christoph Müller, Boris Naydenov, Fedor Jelezko, and Martin B. Plenio. Robust optical polarization of nuclear spin baths using hamiltonian engineering of nitrogen-vacancy center quantum dynamics. *Science Advances*, 4(8), 2018. doi: 10.1126/sciadv.aat8978. URL http://advances.sciencemag.org/content/4/8/eaat8978.

[358] Jonas Nils Becker, Johannes Görlitz, Carsten Arend, Matthew Markham, and Christoph Becher. Ultrafast all-optical coherent control of single silicon vacancy colour centres in diamond. *Nat. Commun.*, 7:13512, 2016.

[359] Ernst G. Bauer, Brian W. Dodson, Daniel J. Ehrlich, Leonard C. Feldman, C. Peter Flynn, Michael W. Geis, James P. Harbison, Richard J. Matyi, Paul S. Peercy, Pierre M. Petroff, and et al. Fundamental issues in heteroepitaxy—a department

of energy, council on materials science panel report. *Journal of Materials Research*, 5(4):852–894, 1990. doi: 10.1557/JMR.1990.0852.

[360] C. D. Clark, H. Kanda, I. Kiflawi, and G. Sittas. Silicon defects in diamond. *Phys. Rev. B*, 51:16681–16688, Jun 1995. doi: 10.1103/PhysRevB.51.16681. URL http://link.aps.org/doi/10.1103/PhysRevB.51.16681.

[361] Constantin Dory, Dries Vercruysse, Ki Youl Yang, Neil V. Sapra, Alison E. Rugar, Shuo Sun, Daniil M. Lukin, Alexander Y. Piggott, Jingyuan L. Zhang, Marina Radulaski, Konstantinos G. Lagoudakis, Logan Su, and Jelena Vuckovic. Optimized diamond quantum photonics. *arXiv preprint arXiv:1812.02287*, 2019.

[362] T. Staudacher, F. Ziem, L. Häussler, R. Stöhr, S. Steinert, F. Reinhard, J. Scharpf, A. Denisenko, and J. Wrachtrup. Enhancing the spin properties of shallow implanted nitrogen vacancy centers in diamond by epitaxial overgrowth. *Applied Physics Letters*, 101(21):212401, 2012. doi: 10.1063/1.4767144. URL https://doi.org/10.1063/1.4767144.

[363] J. M. Moison, F. Houzay, F. Barthe, L. Leprince, E. André, and O. Vatel. Self-organized growth of regular nanometer-scale inas dots on gaas. *Applied Physics Letters*, 64(2):196–198, 1994. doi: 10.1063/1.111502. URL https://doi.org/10.1063/1.111502.

[364] D. Riedel, I. Sollner, Brendan J. Shields, Sebastian Starosielec, Patrick Appel, Elke Neu, Patrick Maletinsky, and Richard J. Warburton. Deterministic enhancement of coherent photon generation from a nitrogen-vacancy center in ultrapure diamond. *Phys. Rev. X*, 7(3):031040, September 2017. doi: 10.1103/PhysRevX.7.031040. URL https://link.aps.org/doi/10.1103/PhysRevX.7.031040.

[365] Andreas V. Kuhlmann, Jonathan H. Prechtel, Julien Houel, Arne Ludwig, Dirk Reuter, Andreas D. Wieck, and Richard J. Warburton. Transform-limited single photons from a single quantum dot. *Nature Communications*, 6:8204 EP –, Sep 2015. URL https://doi.org/10.1038/ncomms9204. Article.

[366] C. Neill, A. Megrant, R. Barends, Yu Chen, B. Chiaro, J. Kelly, J. Y. Mutus, P. J. J. O'Malley, D. Sank, J. Wenner, T. C. White, Yi Yin, A. N. Cleland,

and John M. Martinis. Fluctuations from edge defects in superconducting resonators. *Applied Physics Letters*, 103(7):072601, 2013. doi: 10.1063/1.4818710. URL https://doi.org/10.1063/1.4818710.

[367] S. Meiboom and D. Gill. Modified spin-echo method for measuring nuclear relaxation times. *Review of Scientific Instruments*, 29(8):688–691, 1958. doi: 10.1063/1.1716296.

[368] T. Gullion, D.B. Baker, and M.S. Conradi. New, compensated carr-purcell sequences. *Journal of Magnetic Resonance (1969)*, 89(3):479–484, 1990. doi: https://doi.org/10.1016/0022-2364(90)90331-3.

[369] A. D. Milov, A. B. Ponomarev, and Yu D. Tsvetkov. Electron-electron double resonance in electron spin echo: Model biradical systems and the sensitized photolysis of decalin. *Chemical Physics Letters*, 110(1):67–72, 1984. ISSN 0009-2614. URL http://www.sciencedirect.com/science/article/pii/0009261484801487.

[370] R. Kalish and S. Prawer. Graphitization of diamond by ion impact: Fundamentals and applications. *Nuclear Instruments and Methods in Physics Research Section B: Beam Interactions with Materials and Atoms*, 106(1):492 – 499, 1995. ISSN 0168-583X. doi: https://doi.org/10.1016/0168-583X(95)00758-X. URL http://www.sciencedirect.com/science/article/pii/0168583X9500758X. Ion Beam Modification of Materials.

[371] V. M. Acosta, E. Bauch, M. P. Ledbetter, C. Santori, K.-M. C. Fu, P. E. Barclay, R. G. Beausoleil, H. Linget, J. F. Roch, F. Treussart, S. Chemerisov, W. Gawlik, and D. Budker. Diamonds with a high density of nitrogen-vacancy centers for magnetometry applications. *Phys. Rev. B*, 80:115202, Sep 2009. doi: 10.1103/PhysRevB.80.115202. URL https://link.aps.org/doi/10.1103/PhysRevB.80.115202.

[372] Xing Rong, Jianpei Geng, Fazhan Shi, Ying Liu, Kebiao Xu, Wenchao Ma, Fei Kong, Zhen Jiang, Yang Wu, and Jiangfeng Du. Experimental fault-tolerant universal quantum gates with solid-state spins under ambient conditions. *Nature Communications*, 6:8748 EP –, Nov 2015. URL https://doi.org/10.1038/ncomms9748. Article.

[373] Peter W. Shor and John Preskill. Simple proof of security of the BB84 quantum key distribution protocol. *Physical Review Letters*, 85(2):441–444, 2000. ISSN 00319007. doi: 10.1103/PhysRevLett.85.441. URL https://doi.org/10.1103/PhysRevLett.85.441.

[374] Qiang Zhang, Feihu Xu, Yu-Ao Chen, Cheng-Zhi Peng, and Jian-Wei Pan. Large scale quantum key distribution: challenges and solutions [Invited]. *Optics Express*, 26(18):24260–24273, 2018. doi: 10.1364/OE.26.024260. URL https://doi.org/10.1364/OE.26.024260.

[375] Zhen-Sheng Yuan, Yu-Ao Chen, Bo Zhao, Shuai Chen, Jörg Schmiedmayer, and Jian-Wei Pan. Experimental demonstration of a BDCZ quantum repeater node. *Nature*, 454:1098, aug 2008. URL https://doi.org/10.1038/nature07241.

[376] Fumihiro Kaneda, Feihu Xu, Joseph Chapman, and Paul G Kwiat. Quantum-memory-assisted multi-photon generation for efficient quantum information processing. *Optica*, 4(9):1034–1037, sep 2017. doi: 10.1364/OPTICA.4.001034. URL https://doi.org/10.0.5.84/OPTICA.4.001034.

[377] Hoi-Kwong Lo, Marcos Curty, and Bing Qi. Measurement-Device-Independent Quantum Key Distribution. *Physical Review Letters*, 108(13):130503, mar 2012. doi: 10.1103/PhysRevLett.108.130503. URL https://doi.org/10.1103/PhysRevLett.108.130503.

[378] Samuel L Braunstein and Stefano Pirandola. Side-Channel-Free Quantum Key Distribution. *Physical Review Letters*, 108(13):130502, mar 2012. doi: 10.1103/PhysRevLett.108.130502. URL https://doi.org/10.1103/PhysRevLett.108.130502.

[379] M. Minder, M. Pittaluga, G. L. Roberts, M. Lucamarini, J. F. Dynes, Z. L. Yuan, and A. J. Shields. Experimental quantum key distribution beyond the repeaterless secret key capacity. *Nat. Photonics*, 13(5):334–338, May 2019. ISSN 1749-4893. doi: 10.1038/s41566-019-0377-7. URL https://www.nature.com/articles/s41566-019-0377-7. Number: 5 Publisher: Nature Publishing Group.

[380] Christiana Panayi, Mohsen Razavi, Xiongfeng Ma, and Norbert Lütkenhaus. Memory-assisted measurement-device-independent quantum key distribution.

New Journal of Physics, 16(4):43005, 2014. ISSN 1367-2630. doi: 10.1088/ 1367-2630/16/4/043005. URL https://doi.org/10.1088/1367-2630/16/4/ 043005.

[381] Hoi-Kwong Lo, Xiongfeng Ma, and Kai Chen. Decoy State Quantum Key Distribution. *Physical Review Letters*, 94(23):230504, jun 2005. doi: 10.1103/PhysRevLett.94.230504. URL https://link.aps.org/doi/10.1103/ PhysRevLett.94.230504.

[382] Hoi-Kwong Lo, H F Chau, and M Ardehali. Efficient Quantum Key Distribution Scheme and a Proof of Its Unconditional Security. *Journal of Cryptology*, 18(2): 133–165, 2005. ISSN 1432-1378. doi: 10.1007/s00145-004-0142-y. URL https: //doi.org/10.1007/s00145-004-0142-y.

[383] Marcos Curty, Feihu Xu, Wei Cui, Charles Ci Wen Lim, Kiyoshi Tamaki, and Hoi-Kwong Lo. Finite-key analysis for measurement-device-independent quantum key distribution. *Nature Communications*, 5:3732, apr 2014. URL https://doi.org/ 10.1038/ncomms4732.

[384] Eli Biham, Bruno Huttner, and Tal Mor. Quantum cryptographic network based on quantum memories. *Physical Review A*, 54(4):2651–2658, oct 1996. doi: 10.1103/PhysRevA.54.2651. URL https://link.aps.org/doi/10.1103/ PhysRevA.54.2651.

[385] Robert Raussendorf and Hans J. Briegel. A one-way quantum computer. *Phys. Rev. Lett.*, 86(22):5188–5191, May 2001. doi: 10.1103/PhysRevLett.86.5188. URL https://link.aps.org/doi/10.1103/PhysRevLett.86.5188. Publisher: American Physical Society.

[386] Anaïs Dréau, Anna Tchebotareva, Aboubakr El Mahdaoui, Cristian Bonato, and Ronald Hanson. Quantum frequency conversion of single photons from a nitrogen-vacancy center in diamond to telecommunication wavelengths. *Phys. Rev. Applied*, 9(6):064031, June 2018. doi: 10.1103/PhysRevApplied.9.064031. URL https://link.aps.org/doi/10.1103/PhysRevApplied.9.064031. Publisher: American Physical Society.

[387] Darius Bunandar, Anthony Lentine, Catherine Lee, Hong Cai, Christopher M Long, Nicholas Boynton, Nicholas Martinez, Christopher DeRose, Changchen

Chen, Matthew Grein, Douglas Trotter, Andrew Starbuck, Andrew Pomerene, Scott Hamilton, Franco N. C. Wong, Ryan Camacho, Paul Davids, Junji Urayama, and Dirk Englund. Metropolitan Quantum Key Distribution with Silicon Photonics. *Physical Review X*, 8(2):21009, apr 2018. doi: 10.1103/PhysRevX.8.021009. URL https://link.aps.org/doi/10.1103/PhysRevX.8.021009.

[388] Hans J. Briegel and Robert Raussendorf. Persistent entanglement in arrays of interacting particles. *PRL*, 86(5):910–913, January 2001. doi: 10.1103/PhysRevLett.86.910. URL https://link.aps.org/doi/10.1103/PhysRevLett.86.910.

[389] Hannes Pichler, Soonwon Choi, Peter Zoller, and Mikhail D. Lukin. Universal photonic quantum computation via time-delayed feedback. *PNAS*, 114(43):11362–11367, October 2017. ISSN 0027-8424, 1091-6490. doi: 10.1073/pnas.1711003114. URL https://www.pnas.org/content/114/43/11362. Publisher: National Academy of Sciences Section: Physical Sciences.

[390] David Awschalom, Karl K. Berggren, Hannes Bernien, Sunil Bhave, Lincoln D. Carr, Paul Davids, Sophia E. Economou, Dirk Englund, Andrei Faraon, Marty Fejer, Saikat Guha, Martin V. Gustafsson, Evelyn Hu, Liang Jiang, Jungsang Kim, Boris Korzh, Prem Kumar, Paul G. Kwiat, Marko Lončar, Mikhail D. Lukin, David A. B. Miller, Christopher Monroe, Sae Woo Nam, Prineha Narang, Jason S. Orcutt, Michael G. Raymer, Amir H. Safavi-Naeini, Maria Spiropulu, Kartik Srinivasan, Shuo Sun, Jelena Vučković, Edo Waks, Ronald Walsworth, Andrew M. Weiner, and Zhesen Zhang. Development of Quantum InterConnects for Next-Generation Information Technologies. *arXiv:1912.06642*, January 2020. URL http://arxiv.org/abs/1912.06642. arXiv: 1912.06642.

[391] B. T. Matthias, T. H. Geballe, and V. B. Compton. Superconductivity. *RMP*, 35(1):1–22, January 1963. doi: 10.1103/RevModPhys.35.1. URL https://link.aps.org/doi/10.1103/RevModPhys.35.1.

[392] A. M. Campbell and J. E. Evetts. Flux vortices and transport currents in type ii superconductors. *null*, 21(90):199–428, March 1972. ISSN 0001-8732. doi: 10.1080/00018737200101288. URL https://doi.org/10.1080/00018737200101288.

[393] C. A. Brackett. Dense wavelength division multiplexing networks: principles and applications. *IEEE Journal on Selected Areas in Communications*, 8(6):948–964, 1990. ISSN 1558-0008. doi: 10.1109/49.57798.

[394] Mian Zhang, Brandon Buscaino, Cheng Wang, Amirhassan Shams-Ansari, Christian Reimer, Rongrong Zhu, Joseph M. Kahn, and Marko Lončar. Broadband electro-optic frequency comb generation in a lithium niobate microring resonator. *Nature*, 568(7752):373–377, 2019. ISSN 1476-4687. doi: 10.1038/s41586-019-1008-7. URL https://doi.org/10.1038/s41586-019-1008-7.

[395] Dirk Englund, Andrei Faraon, Ilya Fushman, Nick Stoltz, Pierre Petroff, and Jelena Vučković. Controlling cavity reflectivity with a single quantum dot. *Nature*, 450(7171):857–861, December 2007. ISSN 1476-4687. doi: 10.1038/nature06234. URL https://www.nature.com/articles/nature06234. Number: 7171 Publisher: Nature Publishing Group.

[396] Michael Tavis and Frederick W Cummings. Exact solution for an n-molecule—radiation-field hamiltonian. *Physical Review*, 170(2):379, 1968.

[397] C. W. Gardiner and M. J. Collett. Input and output in damped quantum systems: Quantum stochastic differential equations and the master equation. *Phys. Rev. A*, 31:3761–3774, Jun 1985. doi: 10.1103/PhysRevA.31.3761. URL https://link.aps.org/doi/10.1103/PhysRevA.31.3761.

[398] M Schukraft, J Zheng, T Schröder, SL Mouradian, M Walsh, ME Trusheim, H Bakhru, and DR Englund. Invited article: Precision nanoimplantation of nitrogen vacancy centers into diamond photonic crystal cavities and waveguides. *APL Photonics*, 1(2):020801, 2016.

[399] C. W. Chou, H. de Riedmatten, D. Felinto, S. V. Polyakov, S. J. van Enk, and H. J. Kimble. Measurement-induced entanglement for excitation stored in remote atomic ensembles. *Nature*, 438(7069):828–832, 12 2005. URL http://dx.doi.org/10.1038/nature04353.

[400] William K. Wootters. Entanglement of formation of an arbitrary state of two qubits. *Phys. Rev. Lett.*, 80:2245–2248, Mar 1998. doi: 10.1103/PhysRevLett.80.2245. URL http://link.aps.org/doi/10.1103/PhysRevLett.80.2245.

331

[401] Hugues de Riedmatten, Ivan Marcikic, Valerio Scarani, Wolfgang Tittel, Hugo Zbinden, and Nicolas Gisin. Tailoring photonic entanglement in high-dimensional Hilbert spaces. *Physical Review A*, 69(5):50304, may 2004. doi: 10.1103/ PhysRevA.69.050304. URL https://doi.org/10.1103/PhysRevA.69.050304.

[402] Toshihiko Sasaki, Yoshihisa Yamamoto, and Masato Koashi. Practical quantum key distribution protocol without monitoring signal disturbance. *Nature*, 509:475, may 2014. URL https://doi.org/10.1038/nature13303.